Spectroscopic Studies of Evolved Stars and Planetary Nebulae

A thesis submitted to the University of Manchester
for the degree of Doctor of Philosophy
in the Faculty of Engineering and Physical Sciences

2014

By
Christina Louise Smith
School of Physics and Astronomy

Contents

Abstract **17**

Declaration **18**

Copyright **19**

Acknowledgements **20**

Dedication **22**

Supporting Publications **25**

1 Introduction **27**

1.1 Evolution of low-to-intermediate mass stars 27

1.1.1 Early phases 28

1.1.2 Asymptotic giant branch 33

1.1.3 Proto-planetary nebulae and planetary nebulae 35

1.2 Circumstellar chemistry 38

1.2.1 Mixing processes in AGB stars 38

1.2.2 Dust and molecule formation in AGB stars 40

1.2.3 Structure and chemistry of PNe 41

1.3 The s-process 42

1.4 Overview of spectral theory 44

1.4.1 Electronic transitions 44

1.4.2 Rotational and vibrational transitions 46
1.4.3 Radiative transfer 47
1.4.4 Brightness temperature 50
1.4.5 Transitions in two-level systems 51
1.4.6 Maser emission 53
1.5 Thesis outline 54

2 Molecular line survey **57**
2.1 Introduction 57
2.2 Observations 59
2.2.1 Targets 59
2.2.2 Telescope 62
2.2.3 Data reduction and line identification 63
2.3 Line profiles 65
2.3.1 Optically thin limit 68
2.3.2 Optically thick limit 69
2.4 Results 72
2.4.1 Line fitting 73
2.4.2 Detections in individual sources 81
2.5 Analysis 86
2.5.1 Excitation temperatures: population diagram method . . . 86
2.5.2 Column densities 92
2.5.3 Isotopic ratios 94
2.6 Discussion 100
2.6.1 Emission extent 100
2.6.2 Excitation temperatures 100
2.6.3 Source-averaged column densities 101
2.6.4 Isotopic Ratios 103
2.6.5 Evidence for mixing processes 105

2.6.6 J-type stars and A+B grains . . . 106
2.6.7 Uncertainty considerations . . . 108
2.7 Conclusions . . . 109

3 A new HCN maser in IRAS 15082−4808 111
3.1 Introduction . . . 111
3.2 Observations . . . 113
3.2.1 Mopra 2010 . . . 113
3.2.2 Literature and archive data . . . 114
3.3 Analysis . . . 115
3.3.1 Velocity . . . 115
3.3.2 Maser pumping . . . 118
3.3.3 Relation to variability . . . 122
3.3.4 Applications to AGB winds . . . 127
3.3.5 Insights into AGB atmospheres . . . 129
3.4 Conclusions . . . 132

4 Modelling CO in the circumstellar envelope of II Lup 135
4.1 Introduction . . . 135
4.2 The code . . . 136
4.2.1 MCMax . . . 136
4.2.2 GASTRoNOoM . . . 137
4.2.3 ComboCode . . . 139
4.3 The data . . . 140
4.3.1 SED data . . . 141
4.3.2 Spectral line data . . . 142
4.4 Modelling . . . 143
4.4.1 SED modelling . . . 144
4.4.2 SiC feature . . . 145
4.4.3 Spectral Line Modelling . . . 146

4.5 Model sensitivity to input parameters . . . 158
4.5.1 Dust model . . . 158
4.5.2 Line profile sensitivity . . . 162
4.6 Understanding the envelope of II Lup . . . 163
4.6.1 Physical interpretation of the models . . . 163
4.6.2 Insights into the composition and thermodynamics . . . 170
4.6.3 Comparison with literature models . . . 174
4.7 Conclusions . . . 175

5 Zinc abundances of planetary nebulae 177
5.1 Introduction . . . 177
5.2 Observations and data reduction . . . 180
5.2.1 Literature data . . . 184
5.3 Abundance derivation . . . 188
5.3.1 Determination of physical parameters . . . 189
5.3.2 Line emissivities . . . 190
5.3.3 Ionic abundances . . . 192
5.3.4 Ionisation correction factors . . . 192
5.3.5 Elemental abundances . . . 195
5.4 Results . . . 196
5.4.1 Uncertainty considerations . . . 196
5.5 Discussion . . . 199
5.5.1 Metallicity as a function of Galactocentric distance . . . 201
5.6 Conclusions . . . 203

6 Conclusions and further work 207
6.1 Conclusions . . . 207
6.2 Further Work . . . 211

A Mopra spectra **215**

A.1 IRAS 15194-5115 215

A.2 IRAS 15082-4808 224

A.3 IRAS 07454-7112 232

A.4 IC 4406 240

A.5 NGC 6537 249

B Constants and parameters **257**

B.1 Table of constants for Mopra analysis 257

C PACS model spectra **261**

References **270**

List of Tables

1.1 Characteristics of AGB variability subclasses 35

2.1 Source and coordinate list 60
2.2 Details of all detected transitions. 70
2.3 Detected transitions in the AGB star sample 74
2.4 Detected transitions in the PN sample 78
2.5 Excitation temperatures (K) 91
2.6 Column densities (population diagram method). 93
2.7 Column densities of all detected species. 95
2.8 Measured isotopic ratios. 97

3.1 Known HCN 89.087 GHz maser sources. 116

4.1 SED data. 141
4.2 CO line profile data 141
4.3 SED input parameters 145
4.4 Parameters for each of the models discussed 159

5.1 Basic information and literature parameters for each source. . . . 181
5.2 Telluric standards for each source 183
5.3 Abundances of zinc and iron for the new and literature samples. . 197
5.4 Distances and Galactic coordinates for all sources 202

B.1 List of constants used in the Mopra analysis 257

List of Figures

1.1 The HR path followed by a 1 $M_{\odot}$ star 29
1.2 Proton-proton chain 30
1.3 The CNO cycle. 30
1.4 The structure of an AGB star 33
1.5 An example light curve 35
1.6 A selection of planetary nebulae morphologies. 37
1.7 Examples of orbital shapes. 44
1.8 Energy level structure of a simple atom 45
1.9 Pictorial representation of vibrational states 48
1.10 CN energy level structure 49
1.11 Example planck spectra. 50
1.12 Types of transition. 52
1.13 Schematic maser 54

2.1 Presolar grain isotopic abundances 58
2.2 IC 4406 and NGC 6537 61
2.3 Schematic diagram of MOPS. 63
2.4 Line of sight through a CSE 66
2.5 Pictorial representation of each annulus in the integration region . 67
2.6 Line profiles of a CSE 68
2.7 C_2H fitted for hyperfine structure. 82
2.8 $C^{13}CH$ fitted for hyperfine structure. 83

2.9 Silicon isotopic ratios in SiC presolar grains. 107

3.1 HCN 89.087 GHz maser observations at three epochs. 117
3.2 Fitted HCN 88.631 GHz emission line. 119
3.3 SWS spectra of HCN sources (14 μm) 119
3.4 SWS spectra of HCN sources (7 μm) 120
3.5 Variability and maser spectra for IRAS 15082−4808 122
3.6 Variability curves of all HCN maser sources. 123
3.7 CIT 6 maser spectra. 128
3.8 Maser intensity against pulse phase. 128
3.9 Expansion velocity against the upper state energy (K) of vibrational transitions of HCN 130
3.10 Positions of selected shells as a function of time. 131

4.1 ComboCode iterative structure 140
4.2 Plot of all SED data 142
4.3 The best SED model. 146
4.4 Comparison of the SiC feature 147
4.5 APEX model-data comparison for the AC model 148
4.6 Partial PACS model-data comparison for the AC model 149
4.7 PACS model/data intensity comparison in the AC model 149
4.8 Partial PACS model-data comparison for the PE model 150
4.9 PACS model/data intensity comparison in the PE model 151
4.10 APEX model-data comparison for the PE model 151
4.11 AC vs PE model temperature profiles 152
4.12 Low-J line comparison for the DT model 153
4.13 Partial PACS model-data comparison for the DT model 154
4.14 PACS model/data intensity comparison in the DT model 155
4.15 Low-J line model-data comparison for the VM model 156
4.16 Partial PACS model-data comparison for the VM model 156

4.17 PACS model/data intensity comparison in the VM model 157
4.18 SED model parameter sensitivity 161
4.19 Model line profile parameter sensitivity 164
4.20 Dust temperature profiles for both 'best' models. 170
4.21 Dust opacity profiles for both 'best' models. 171
4.22 Gas temperature profiles for both models. 172
4.23 Gas velocity profiles for both models. 173
4.24 CO and ^{13}CO abundance profiles for both models. 173

5.1 Zinc spectra of all sources 185
5.2 *ISO* spectrum of NGC 7027 188
5.3 Fractional ionisation abundance of zinc from CLOUDY models. . . 193
5.4 Fractional ionisation abundance of oxygen from CLOUDY models. 193
5.5 Fractional abundances of O^{++} and Zn^{3+}. 194
5.6 Fractional abundances of a variety of species 195
5.7 Zn/H against Galactocentric distance of sources. 204
5.8 O/Zn against Galactocentric distance of sources. 204

A.1 Mopra spectrum of IRAS 15194-5115. 215
A.2 Mopra spectrum of IRAS 15082-4808. 224
A.3 Mopra spectrum of IRAS 07454-7112. 232
A.4 Mopra spectrum of IC 4406. 240
A.5 Mopra spectrum of NGC 6537. 249

C.1 AC model PACS spectrum 262
C.2 PE model PACS spectrum 264
C.3 DTM model PACS spectrum 266
C.4 VMM model PACS spectrum 268

List of Abbreviations

AC model	APEX Cooling Model
AGB	Asymptotic Giant Branch
AGN	Active Galactic Nuclei
APEX	Atacama Pathfinder Experiment
ASAP	ATNF Spectral Analysis Package
ATNF	Australia Telescope National Facility
C-rich	Carbon-rich
CDMS	Cologne Database for Molecular Spectroscopy
CEL	Collisionally Excited Line
CNO cycle	Carbon-Nitrogen-Oxygen cycle
CSE	Circumstellar Envelope
Dec	Declination
DT model	Discontinuous Temperature model
DU	Dredge Up
E-AGB	Early Asymptotic Giant Branch
GA	Genetic Algorithm
HBB	Hot Bottom Burning
HR diagram	Hertzsprung-Russell diagram
HST	Hubble Space Telescope
IF	Intermediate Frequency
ISO	Infrared Space Observatory
ISW	Interacting Stellar Winds

JCMT	James Clark Maxwell Telescope
JPL	Jet Propulsion Laboratory
LSR	Local Standard of Rest
LTE	Local Thermodynamic Equilibrium
MMIC	Monolithic Microwave Integrated Circuit
MOPS	Mopra Spectrometer
NIST	National Institute of Standards and Technology
O-rich	Oxygen-rich
ORL	Optical Recombination Line
PACS	Photoconductor Array Camera and Spectrometer
PE model	PACS Epsilon Model
PMZ	Partial Mixing Zone
PN	Planetary Nebula
PNe	Planetary Nebulae
PPN	Proto-Planetary Nebula
PPNe	Proto-Planetary Nebulae
RA	Right Ascension
RGB	Red Giant Branch
S-process	Slow Neutron Capture Process
SCUBA	Submillimetre Common-User Bolometer Array
SED	Spectral Energy Distribution
SEST	Swedish-ESO Submillimeter Telescope
SR	Semi-Regular
SWS	Short Wavelength Spectrometer
TDU	Third Dredge Up
TP	Thermal Pulse
TP-AGB	Thermally Pulsing Asymptotic Giant Branch
VM model	Variable Mass-loss Rate Model

The University of Manchester

ABSTRACT OF THESIS submitted by Christina Louise Smith
for the Degree of Doctor of Philosophy and entitled
"Spectroscopic Studies of Evolved Stars and Planetary Nebulae"
September 2014

Evolved stars and planetary nebulae are rich and varied sites of molecule and dust formation. These objects undergo dramatic mass loss which ultimately enriches the interstellar medium. In this thesis, a number of studies, outlined below, have been undertaken to better understand the chemical and physical properties of these diverse objects.

A molecular line survey of a sample of evolved stars and planetary nebulae has been carried out using the Mopra radio telescope, Australia. Transitions with hyperfine structure have been fitted to constrain optical depths. The population diagram method was applied to determine the rotation temperatures of molecules which had multiple transitions available. Column densities have been calculated for all detected species and isotopic ratios measured where possible. The results include the corroboration of the classification of II Lup as a J-type star.

The 89.087 GHz HCN maser was detected in IRAS 15082-4808 for the first time from the aforementioned survey, bringing the total number of detections of this maser to ten. The velocity shift of this maser has been measured at -2.0 ± 0.9 km/s. Drawing on literature data in addition to the survey data, the variation of maser intensity with pulsation phase has been investigated across all sources for the first time. Comparing these masers with model atmospheres constrains the formation region to between 2 and 4 stellar radii.

CO in the circumstellar envelope of II Lup has been modelled using the radiative transfer codes GASTRoNOoM, and ComboCode. The models have demonstrated that a 'standard' smooth model does not satisfactorily reproduce the combined CO observations of PACS, JCMT, Mopra and APEX. Two potential solutions are proposed: a discontinuous temperature model, requiring the presence of an efficient cooling molecule that is most effective in the region 75-200 R*, or a variable mass loss model that requires a factor of ten increase in mass loss in the same region.

Zinc abundances, a proxy for iron abundances, have been determined for a sample of Galactic planetary nebulae using the [Zn IV] 3.625 μm line. O^{++}/O has been shown to be a reliable ionisation correction factor for Zn^{3+} from Cloudy photoionisation models. The majority of the sample are sub-solar in [Zn/H] and enriched in [O/Zn]. Zinc abundances as functions of Galactocentric distance have also been investigated and no evidence for a trend has been found.

Declaration

No portion of the work referred to in this thesis has been submitted in support of an application for another degree or qualification of this or any other university or other institution of learning.

Copyright

Acknowledgements

Firstly, I would like to thank my supervisor, Albert Zijlstra, for the all the time, help and guidance given to me throughout my PhD - I'm really grateful, so just thank you. I would also like to thank Leen Decin, Harriet Dinerstein, Gary Fuller and Robin Lombaert for allowing me to work with them and for answering the many questions that I posed. I'd also like to thank Keith Butler for providing the collisional rate coefficients for Chapter 5, Jane Greaves for discussions on hyperfine structure, Susanne Höfner for allowing the reproduction of Fig. 3.10 and Samira Alharbi for providing the JCMT data in Chapter 4.

There have been many people at JBCA over the years who have made my time here fantastic. There are too many to list you all by name, but special mentions should go to Adam, Iain, Jen, Kerry, Leo, Libby, Liz, Mark, Mike, Steph and my fantastic office mates for all the times they heard: 'so, I've got a question...', 'plunch?' and 'gah!'.

Outside of JBCA, I'd like to thank The Musketeers and The Didsbury Crew, my fabulous housemates, actual and honorary, over the past few years and the girls of Physics Netball for all the giggles, grooving and good times.

To the people who heroically volunteered to proof-read segments of this thesis prior to submission (Aaron, Alastair, Ellie, Emma, Frankie, Jonathan, Leo, Liz, Mike and Maddy) thank you so, so much!

Last, but by no means least, I would like to thank my amazing family for all the unconditional love and support they've given me - I couldn't have done it without you!

This PhD was funded by the Science and Technology Facilities Council. The Mopra radio telescope is part of the Australia Telescope National Facility which is funded by the Commonwealth of Australia for operation as a National Facility managed by CSIRO. This thesis includes observations made with ESO Telescopes at La Silla Paranal Observatory. This thesis also makes use of variable star observations from the AAVSO International Database, contributed by observers worldwide.

This thesis was typeset using LaTeX.

For my parents,
who helped me find my poem.

And for Grandad,
who taught me so much,
the Universe is a little less wonderful without you.

Your head is filled with stars
And star nurseries more real
To you than the distant glow
And swirl of forming words.

Your heart is pulled by the
Solemn, slow swing of spiral
Galaxies defined by
Mathematical mysteries.

And you think that in your
Skyward search for hydrogen
In the Galactic plane,
There is no poetry?

Simply...
You have found your own poem.

— Deborah J Smith

Supporting Publications

Zinc abundances of planetary nebulae

Smith, C. L., Zijlstra, A. A. and Dinerstein, H. L., 2014, MNRAS, 441, 3161

A new HCN maser in IRAS 15082-4808

Smith, C. L., Zijlstra, A. A. and Fuller, G. A., 2014, MNRAS, 440, 172

Modelling CO in the circumstellar envelope of IRAS 15194-5115

Smith, C. L., Zijlstra, A. A., Decin, L. and Lombaert, R., 2012, in Nuclei in the Cosmos (NIC XII)

Chapter 1

Introduction

1.1 Evolution of low-to-intermediate mass stars

Low and intermediate mass stars (up to approximately 8 $M_{\odot}$) are important for Galactic chemical evolution. These stars undergo a very different stellar evolution to their high-mass counterparts: they never reach sufficient temperatures and pressures to induce carbon burning within their cores. Instead, they pass through a phase of evolution known as the asymptotic giant branch (AGB), subsequently becoming a planetary nebula (PN) and eventually a white dwarf.

AGB stars are sites of varied nucleosynthesis, resulting from complex mixing processes, which may be studied through observed surface abundances. As AGB stars pass through this phase of evolution, they shed their outer layers, forming a circumstellar envelope. By measuring elemental and isotopic abundances found within the circumstellar envelope, the history of the star's mass loss, mixing processes and nucleosynthesis can be inferred.

Planetary nebulae are the brightest phase of low-to-intermediate mass stellar evolution. This is also the last phase before a star becomes a white dwarf. Planetary nebulae have a rich and varied chemistry as well as complex morphologies. Elemental, ionic and isotopic abundances shed light on the composition and

history of the precursor star.

This thesis is based upon studies of objects within these two phases (and the transitional phase between). In the following sections, low-to-intermediate mass stellar evolution is outlined in further detail to put these objects, and this thesis, in context.

1.1.1 Early phases

As stars begin their nuclear-burning lives, they join the *main sequence* track on the Hertzsprung-Russell diagram (HR diagram). An example of a HR diagram is shown in Fig. 1.1. These stars are predominantly made up of hydrogen, with some helium and small fractions of heavier elements. Hydrogen is converted into helium within the core of main sequence stars. The majority of hydrogen burning proceeds by either the proton-proton chain (pp chain) or the carbon-nitrogen-oxygen cycle (CNO cycle). These two processes are outlined in Fig. 1.2 and 1.3; further details may be found in Kippenhahn, Weigert & Weiss (2012) and Prialnik (2009).

The main sequence lifetime of a star is dependent upon both its mass and luminosity. The larger the star, the more fuel it has available to power nuclear fusion. However, the larger the star, the higher the luminosity and thus its fuel is consumed more rapidly. The mass-luminosity relation describes how the luminosity of a main sequence star depends upon mass:

$$L \propto M^{\eta}, \tag{1.1}$$

where L is the luminosity of the star, M is the mass and the value of η is dependent upon the star being examined. The average value of η over the whole main sequence track is 3.5 (Kippenhahn & Weigert 1994; Prialnik 2009).

The estimated main-sequence lifetime of any given star is proportional to the mass of the nuclear burning region of the star and inversely proportional to the

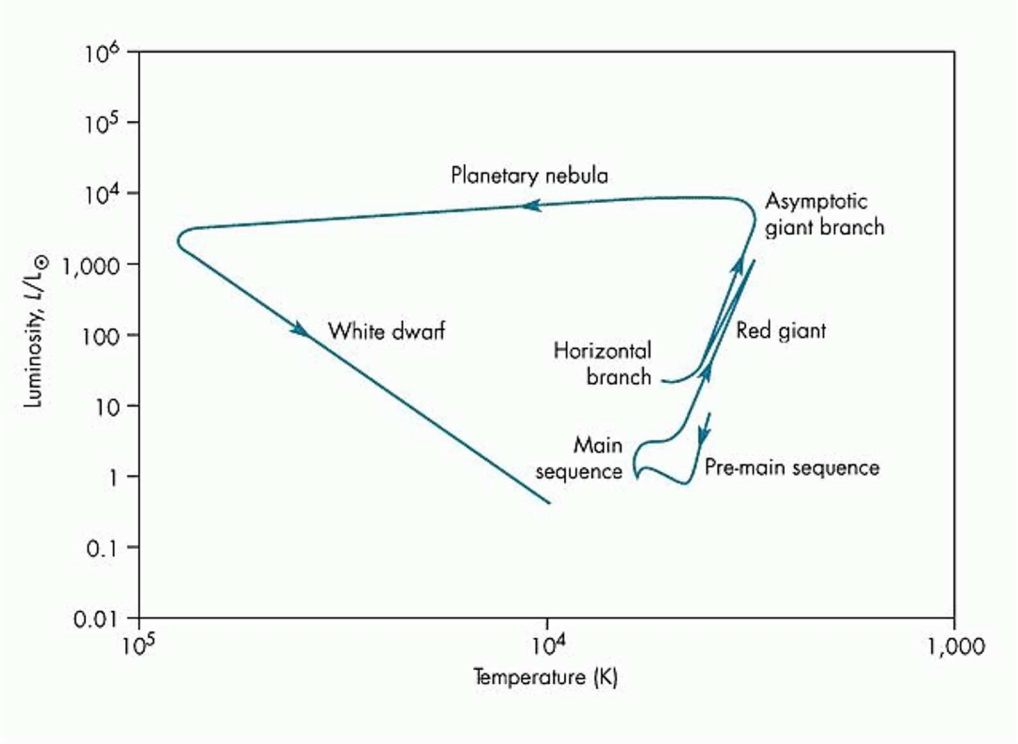

Figure 1.1: Path followed by a 1 $M_\odot$ star of solar metallicity on the Hertzprung-Russell diagram[a].

[a]Image credit:
http://edu-observatory.org/mcc/homework/homework.ch.18-19/HR_diagram_Sun.gif

luminosity. Making the assumption that the mass of the nuclear burning region, M_n, is proportional to the total mass of the star gives:

$$\tau_{MS} \propto \frac{M_n}{L} \propto M^{1-\eta}, \tag{1.2}$$

where τ_{MS} is the main sequence lifetime of the star. Thus the more massive a star, the shorter the time spent on the main sequence. Core-convection alters the internal conditions of the star which can also change its main sequence lifetime.

Main sequence stars exist in a relatively stable state. On any given portion of the star, the pressure exerted by thermal and radiation processes is balanced by the gravitational force being exerted on that portion. This is known as the condition of *hydrostatic equilibrium*.

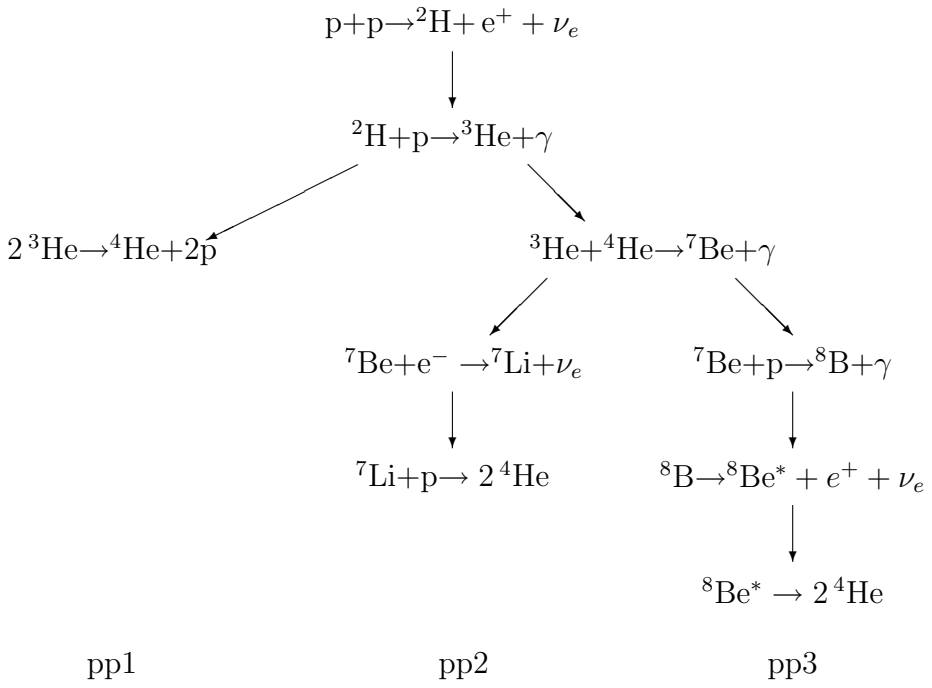

Figure 1.2: The pp chain of nuclear fusion, reactions taken from Adelberger et al. (2010).

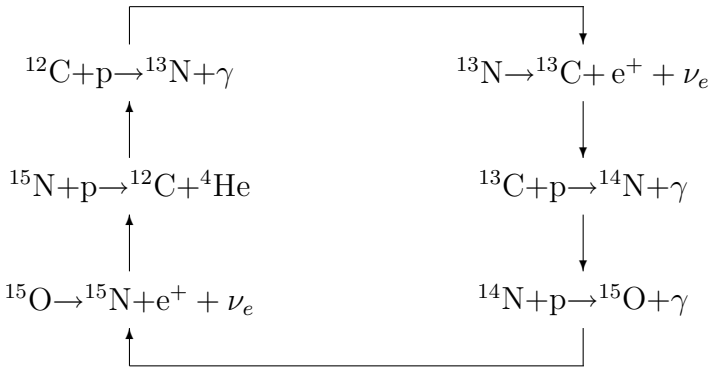

Figure 1.3: The CNO cycle.

When four hydrogen nuclei are converted into a single helium nucleus, assuming the medium behaves as an ideal gas, either the temperature must increase or the pressure and/or volume must decrease ($PV = N\mathrm{k}_B T$; P: pressure, V: Volume, N: number of particles, T: temperature). A decrease in pressure will result in contraction according to the condition of hydrostatic equilibrium. Also, once all core hydrogen has been converted into helium and fusion within the core ceases, reducing the radiation pressure, the core begins to gravitationally contract. These contractions release gravitational potential energy in the form of thermal energy:

$$\zeta E_i + E_g = 0, \tag{1.3}$$

where E_i and E_g are the internal and gravitational energies of the gas. ζ is defined as $(3P)/(u\rho)$ where P, u and ρ are the pressure, internal energy per unit mass and mass density of the gas respectively. For an ideal gas, $\zeta = 2$. Equ. 1.3 is known as the *virial theorem* and in this form assumes a zero surface pressure.

Eventually, the temperature and pressure are sufficiently high to induce hydrogen burning in a shell surrounding the core. The star is then said to have joined the *red giant branch* (RGB). The core continues to contract, causing an increase in temperature and subsequently an increase in energy generation from the H-burning shell due to the strong temperature dependence of the CNO-cycle. At high temperatures, the CNO-cycle dominates hydrogen burning. This increase in energy generation causes an increase in radiation pressure, which leads to envelope expansion. The outer layers of the star cool as they expand, thus appearing redder, and the star becomes almost fully convective (Evans & Murdin 2002). Eventually, the core reaches 10^8 K: helium ignition temperature.

Low mass stars (< 2 M$_\odot$) and intermediate mass stars (2 M$_\odot < M_{\mathrm{star}} < 8$ M$_\odot$) join the next phase of evolution in different ways. Low mass stars have electron degenerate cores at the end of the RGB. Within a degenerate gas, the pressure

is approximately independent of temperature and as helium ignition occurs, the temperature of the core increases. Instead of this causing an increase in pressure, leading to core expansion, cooling and stability, this causes the helium-burning rate to increase. This subsequently increases the temperature and gives rise to a runaway helium-burning effect for a few seconds, during which the 'local luminosity' can reach $\sim 10^{11}$ $L_{\odot}$, known as a *helium flash*. The energy from the helium flash is almost entirely absorbed by the outer layers of the star. Eventually, the increase in core temperature is great enough to cause the electron degeneracy to break down and stable helium burning begins. Intermediate mass stars do not have this degenerate core and thus helium burning begins in these stars without a helium flash. Both low and intermediate mass stars are said to have joined the *horizontal branch* of the HR diagram. From this point, low and intermediate mass stars once again evolve in the same manner.

Horizontal branch stars burn helium predominantly via the triple-α process, producing carbon and oxygen:

$$2\,{}^{4}\mathrm{He} \rightarrow {}^{8}\mathrm{Be} + \gamma,$$

$${}^{8}\mathrm{Be} + {}^{4}\mathrm{He} \rightarrow {}^{12}\mathrm{C} + \gamma.$$

^{8}Be has a very short lifetime and rapidly breaks back down into two ^{4}He (as in the pp-3 chain). In order to produce ^{12}C, the helium must be absorbed almost instantaneously. The resulting carbon can interact with further helium to form oxygen.

Hydrogen continues to be burnt in a shell surrounding the helium-burning core. The core helium burning phase is significantly shorter than the hydrogen burning phase (Herwig 2005) and results in the production of a carbon/oxygen core. Once the core helium burning ceases, the core once again contracts under gravity.

In low and intermediate mass stars, the temperatures remain insufficient to

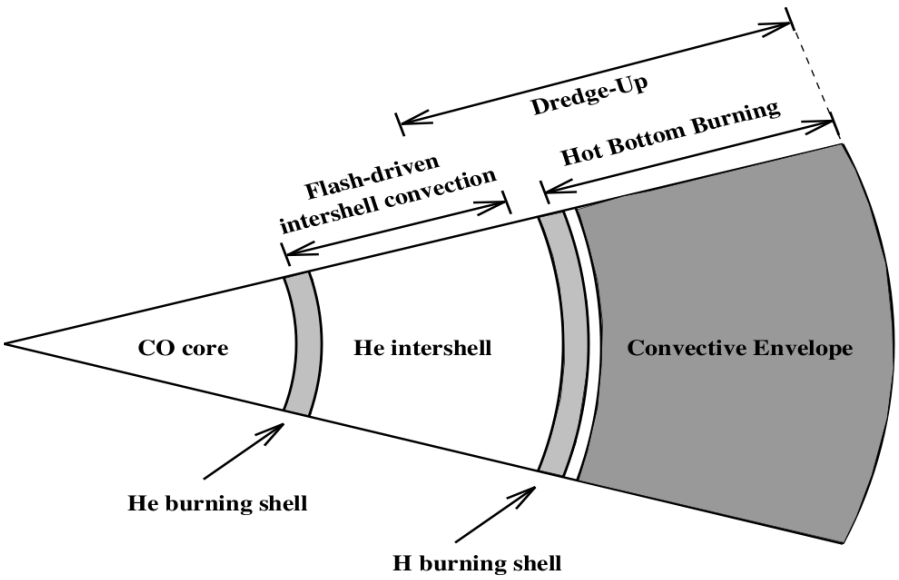

Figure 1.4: Structure of an AGB star (not to scale) from Lattanzio & Boothroyd (1997).

induce carbon burning in the core. Hydrogen and helium burning are able to continue in concentric shells around the C/O core, all surrounded by a hydrogen rich convective envelope, as shown in Fig. 1.4. This phase of evolution is known as the *asymptotic giant branch* (AGB).

1.1.2 Asymptotic giant branch

Throughout this phase of evolution, a star undergoes a large number of changes. The dominance of each of the nuclear burning shells changes as it evolves. Initially, the helium-burning shell provides the main source of luminosity within the star and the star is said to be an *early-AGB star* (E-AGB). The helium burning occurs more rapidly than the hydrogen burning. Thus after a time, the helium shell will have converted the majority of the helium (produced by the previous hydrogen burning phase) into carbon and oxygen, causing the hydrogen-burning shell to become the principle source of luminosity. Eventually, a sufficient amount of helium, produced by the hydrogen-burning shell, accretes onto the helium shell and induces a helium flash-burning phase for a short time, known as a *thermal*

pulse (TP). After this, the star returns to its quiescent H-burning phase. This is a cyclical phenomenon with TPs occurring with a period of 10^4-10^5 years. Stars within this pulsing phase are known as *thermally pulsing AGB stars* (TP-AGB). The effect of thermal pulses on surface abundances will be discussed in Sect. 1.2.1.

Both E-AGB and TP-AGB stars undergo *radial pulsations*, a different phenomenon to TPs, henceforth simply pulsations. These pulsations are related to the dynamics of the envelope rather than the nuclear processes within the star. Pulsations result in observable changes in the luminosity of the star on time periods ranging from 50-2000 days (Zijlstra 2006). An example light curve is shown in Fig. 1.5. Stars undergoing these pulsations are subdivided into three categories, defined by their light curves and spectra: *semi-regular* (SR), *Mira* and *OH/IR* variables. The definition of each type may be found in Table 1.1.

When a star undergoes a pulsation, shocks are sent through the atmosphere of the star, causing compression and heating of the gas. These are prime conditions for the formation of dust grains. Incident photons from the star are absorbed by the grains, leading to at least partial obscuration of the star in the visible region of the spectrum. The absorption causes a gain in momentum for the grain and the absorbed radiation is re-radiated isotropically in the infrared. Momentum from the grains is passed to the surrounding gas by friction. The inner region of the AGB star's atmosphere will move out and fall back with the pulsations, whilst the outer region will not, creating a mass-loss from the star. This results in an outwardly expanding envelope of gas and dust, known as the *circumstellar envelope* (CSE). Interspersed with the normal pulsations, TPs cause sudden bursts of large mass loss, which may account for some of the detached or concentric ring CSEs that have been observed (Zijlstra 2006). The composition of the CSE will reflect the surface abundances of the star at the time of ejection and will vary radially, reflecting the changing surface composition of the star with time, further details of which will be discussed in Sect. 1.2.1.

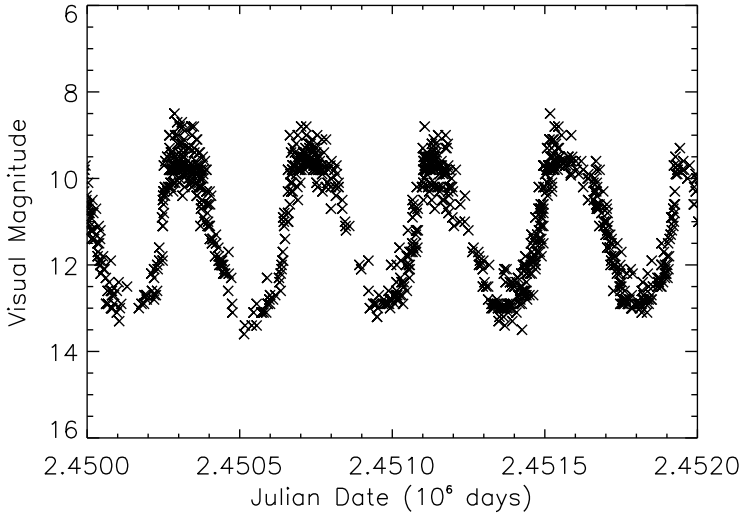

Figure 1.5: An example light curve, based upon V Cyg data from Henden (2013).

Table 1.1: Defining characteristics of the sub-classes of AGB variability. OH/IR stars also exhibit OH masers and are almost entirely obscured in the visible. For further details see Kwon & Suh (2010), Zijlstra (2006) and Xiong, Chen & Gao (1994).

Type	Period (days)	V-band Amplitude (mag)	Regularity
SR	50-100	< 2.5	Irregular
Mira	150-500	> 2.5	Regular
OH/IR	500-2000	> 2.5	Regular

1.1.3 Proto-planetary nebulae and planetary nebulae

A *proto-planetary nebula* (PPN) (also known as a post-AGB star) is a transitional phase between the AGB and *planetary nebula* (PN) phases of evolution. The start of the PPN phase is signalled by a rapidly decreasing rate of mass loss from the star, with the majority of the hydrogen-rich envelope having already been lost, leaving the star with an envelope mass of $\sim 10^{-2}$ $M_{\odot}$ (van Winckel 2003). The degeneracy of the central star increases through this phase and the remnants of the hydrogen envelope exist in a very thin H-burning shell (Kwok 2000; Kwok &

Murdin 2000; Kwok 1993).

In PPNe, the CSE is no longer attached to the surface of the star. The star gradually increases in effective temperature and evolves towards the blue in the HR diagram as it progresses through the PPN stage. The CSE is not yet being ionised by the central star.

The PPN stage is short lived ($\sim 10^3$ yr, Kwok 1993) and not well understood, especially concerning the morphology: how AGB progenitors with spherical outflows evolve into PNe with a variety of morphologies. Examples of PN and their different morphologies are shown in Fig. 1.6. As discussed in Kwok (2000), asymmetric PPN have been observed (e.g. IRAS 17150-3224), some of which may be only a few hundred years out of the AGB phase. There are a number of current theories detailing potential shaping mechanisms, including but not limited to: binary interactions, magnetic fields and fast, collimated winds (e.g. Zijlstra 2007, Balick & Frank 2002, Soker 2006 and references therein).

It is not only the asymmetry that is altered between the AGB and PN phases. The radial structure of the CSE also changes dramatically. AGB stars generally have diffuse CSEs with no visible shell structure. Conversely, PNe have densely packed material arranged in shell-like structures surrounding the central star with a significantly higher outflow velocity than is found in AGB CSEs.

The favoured explanation for this difference in CSE structure is the *interacting stellar winds* (ISW) model. This is caused by a new, fast wind from the star as it begins the PN phase. This newly-ejected fast wind collides with the material ejected during the AGB phase, propels it outwards, and compresses the material into the observed shell structure. This amplifies the asymmetry of the object (Balick & Frank 2002; Kwok 2000).

Once the central star of the PPN reaches approximately 20,000 K, the Lyman continuum photons cause it to ionise the surrounding nebula. This signifies the end of the PPN stage and the beginning of the PN phase. Evolving through this phase, the last remaining portions of hydrogen and helium burning end, leaving

Figure 1.6: A selection of planetary nebulae morphologies. Images courtesy of NASA Astronomy Picture of the Day.

the central star within the nebula as a white dwarf. This will fade and slowly cool, eventually reaching the point where it can no longer light up the surrounding nebula.

1.2 Circumstellar chemistry

1.2.1 Mixing processes in AGB stars

The composition of the CSE of an AGB star reflects the surface abundances of the star at the time of ejection. The surface composition of the star will change with time due to a number of mixing processes. Therefore the composition of the CSE may change with distance from the host star (Habing & Olofsson 2004).

Temporary deepenings of the convective envelope of the star occur when there is a significant change in the nuclear processes occurring within the star. This phenomenon is called a *dredge up* (DU) and brings to the surface the products of nucleosynthesis. Several take place over the course of a star's lifetime.

The *first dredge up* occurs as the star begins to ascend the RGB. At this point, the convective region can reach far enough down to bring products of partial hydrogen burning into the convective envelope and from there to the surface. The *second dredge up* happens at the end of the helium core burning phase in stars with a mass greater than ~ 4 $M_{\odot}$.

The *third dredge up* (TDU) occurs during a thermal pulse during the AGB phase and thus a star may undergo many TDUs. TDUs have a significant effect upon the stellar surface abundance of a number of elements, especially carbon. Initially, an AGB star will have a larger surface abundance (by number) of oxygen than carbon, however with each successive TDU the surface abundance of carbon increases. When a star has a surface abundance ratio C/O ~ 1, an S-type star is said to have formed. At the point where the carbon abundance is greater than the oxygen abundance, a carbon star is said to have been formed. The evolution

of an AGB star is affected very little by the surface C/O abundance ratio, but the gases and dust formed within the CSE will be greatly affected. The mass loss rate of the AGB star is, however, affected by the change in C/O ratio as carbon bearing dust has a higher opacity in general than oxygen-rich dust, leading to more efficient momentum transfer and thus a higher mass loss rate.

Extra mixing, also known as 'cool bottom processing' is a term used to describe a supplementary mixing process that resolves the difference between observed surface abundances of elements such as carbon, oxygen and lithium, and that predicted by stellar evolutionary codes (e.g. Charbonnel 1994).

Extra mixing is well established on the RGB. Karakas, Campbell & Stancliffe (2010) investigated whether this extra mixing was required during the AGB by evolving models from the end of the RGB through the AGB using observed abundance values. Their results were generally inconclusive, not ruling out extra mixing on the AGB, but also noting that this is not the only process that could cause the observed abundance ratios. There are several current theories about the potential process behind extra mixing (e.g. thermohaline mixing, gravity waves, magnetic mixing, rotational mixing). For further details about these theories, see Karakas, Campbell & Stancliffe (2010), Quievy et al. (2009) Busso et al. (2007) and Zahn (1992).

In AGB stars with a mass greater than ~ 4 $M_{\odot}$, during the inter-pulse phase, the convective zone of the envelope reaches deep into the stellar interior and penetrates the H-burning shell. This results in nucleosynthesis occurring at the base of a convection zone, known as *hot bottom burning* (HBB). Species formed in this region are transported up into the convective envelope. This allows some radioactive products to decay within the envelope. This is the case for ^{7}Be, which decays to ^{7}Li, which is subsequently transported to the surface and can lead to the formation of lithium-rich stars. As shown by Blöcker, Herwig & Driebe (2000), the surface abundances of a number of elements, including ^{13}C and ^{14}N, are also affected by HBB. CNO-cycling converts ^{12}C into ^{13}C and ^{14}N, decreasing the

surface abundance of ^{12}C and increasing the surface abundances of ^{13}C and ^{14}N.

Within AGB stars there are radiative and convective regions, but the border between the two is not sharp. In fact the strength of convection decreases gradually over the boundary. This is known as *convective overshoot* and can lead to further mixing in stars than would be obtained in the classic sharp boundary case (Woo & Demarque 2001). This process also affects the abundance of ^{13}C produced in the star.

1.2.2 Dust and molecule formation in AGB stars

The chemistry of an AGB circumstellar envelope is often very rich, incorporating many molecular and dust species. Molecules can be formed in several different areas in the CSE. Some molecules, such as HCN, form in or close to the stellar photosphere (e.g. 10^{13} cm) under high temperature and density conditions. Molecules formed within the central and inner regions of the CSE are destroyed by interstellar UV photons when they reach sufficiently large distances from the central star. This results in the formation of free radicals which are highly reactive and interact with each other or with surrounding molecules. The products of these reactions are often more complex molecules than are found in the inner and central regions (Agúndez et al. 2008; Cherchneff 1996; Olofsson 1997; Habing & Olofsson 2012).

Dust is also able to condense out of the gaseous medium of a circumstellar envelope. The theory of dust formation stems initially from a process called 'nucleation' whereby molecules of the dust-forming species at a sufficient density cluster together, eventually leading to the solid particle or 'seed grain' forming (Patzer 2004). Further molecules adsorb onto the seed grain causing it to grow. This process requires relatively high densities of molecules to be present at sufficiently low temperatures to allow condensation to occur, thus instabilities and shocks in the circumstellar envelope play an important role (e.g. Höfner 2009

and Cuntz & Muchmore 1994). The composition of the grains formed is highly dependent upon the composition of the CSE, specifically the C/O ratio. The eventual dust yield has been shown to be dependent on the metallicity of the star (Ventura et al. 2012).

CO has an important role in shaping the chemistry of AGB CSEs. CO has a high binding energy and thus will preferentially form over other molecules. This gives rise to the 'locking up' of carbon in oxygen-rich (O-rich) CSEs and conversely oxygen in carbon-rich CSEs (C-rich). In C-rich stars this allows a variety of carbon-containing molecules and dust to form, such as SiC_2. In O-rich envelopes, silicates such as pyroxene and olivine ($Mg_xFe_{(1-x)}SiO_3$ and $Mg_{2x}Fe_{2(1-x)}SiO_4$) form.

SiO also has a high binding energy, although slightly lower than that of CO. However, its abundance is predominantly determined by the initial abundance of Si and therefore has a smaller impact on the composition of the CSE than CO (Matsuura et al. 2005; Gail et al. 2009).

1.2.3 Structure and chemistry of PNe

Planetary nebulae, like their AGB progenitors, play host to a variety of gas and dust species, although the high levels of ionising radiation break down many of these in close proximity to the star. Kimura, Gruenwald & Aleman (2012) have constructed a detailed model that examines the structure of and chemical reactions occurring within planetary nebulae. The structure of the nebulae is broken down into four distinct regions: the H^+ dominated region, the H^0 dominated region, the H_2 dominated region and finally the CO dominated region, with the H^+ and CO regions corresponding to the innermost and outermost zones of the nebula envelope respectively. Only the densest planetary nebulae will have sufficient circumstellar material to absorb all the CO-dissociating photons and allow the presence of a CO region. In the 'standard model' nebula of Kimura, Gruenwald

& Aleman (2012) with a hydrogen density of 10^5 cm^{-3}, the CO-dominated region begins at $\sim 1.8 \times 10^{17}$ cm.

Within regions of the envelope that are exposed to the high levels of UV radiation emitted by the star, a large number of atomic and molecular ions form. This environment produces high levels of emission in the form of optical recombination lines (ORL) from a variety of species and transitions. These regions also produce bright transitions in the form of collisionally excited lines (CEL). For further information on collisional and recombination transitions, see Sect. 1.4.5. In the outer regions of a nebula, the envelope is essentially the remnant of the progenitor AGB CSE, and a large number of molecular and dust species can be detected. NGC 7027, for example, has a highly ionised region that is visible in the optical, but also has a large number of molecular species in the outer regions of the envelope which have been detected in the infrared and submillimeter.

1.3 The s-process

A number of different nuclear processes occur over the course of a low-to-intermediate mass star's lifetime. The largest fraction of nucleosynthesis relates to the hydrogen burning (via either the pp chain or CNO cycle) or helium burning (via the triple-α reaction). Despite not producing sufficiently high temperatures and pressures within the core to induce carbon burning, AGB stars can produce heavier elements in moderate amounts by several processes.

The *s-process*, or slow neutron capture process, is the method by which neutrons are captured onto low mass elements in relatively low neutron flux and temperatures (Herwig 2005; Lugaro & van Raai 2008). In fact, the s-process is responsible for the production of approximately half of the elements heavier than iron (Goriely & Siess 2005 and references therein). The neutrons required for this process are produced in one of two ways:

$$^{13}\mathrm{C} + \alpha \rightarrow ^{16}\mathrm{O} + \mathrm{n}$$

or

$$^{22}\mathrm{Ne} + \alpha \rightarrow ^{25}\mathrm{Mg} + \mathrm{n}.$$

The former reaction is the primary production process for neutrons in AGB stars of mass $< 4\ \mathrm{M}_{\odot}$. The latter reaction only becomes dominant at temperatures greater than 300 MK, found in stars of mass $> 4\ \mathrm{M}_{\odot}$. Elements like ^{14}N and ^{13}C can also act as neutron poisons, inhibiting the s-process by absorbing neutrons:

$$^{14}\mathrm{N} + \mathrm{n} \rightarrow ^{14}\mathrm{C} + \mathrm{p},$$

$$^{13}\mathrm{C} + \mathrm{n} \rightarrow ^{14}\mathrm{C} + \gamma,$$

with the latter reaction having a significantly lower reaction cross-section than the former: ^{13}C is a less effective neutron poison.

^{22}Ne can be produced in pulse driven convective zones by consecutive α captures: $^{14}\mathrm{N} \rightarrow ^{18}\mathrm{O} \rightarrow ^{22}\mathrm{Ne}$. The abundance of ^{13}C required for the s-process to occur is greater than that produced in equilibrium by the CNO cycle. In order to reach this abundance, protons from the hydrogen-rich convective envelope must be mixed into the inter-shell region (see Fig. 1.4) after a third dredge up and there are a number of suggested mechanisms for this (see Lattanzio & Lugaro 2005 for further information). ^{13}C is then produced through the absorption of a proton by a ^{12}C nucleus and the subsequent β^{+} decay of the ^{13}N product.

With each TP following the initiation of s-process production, more and more s-process elements are mixed into the convective layers of the star. From there, these are transported to the surface, altering the surface composition of the star with every TP.

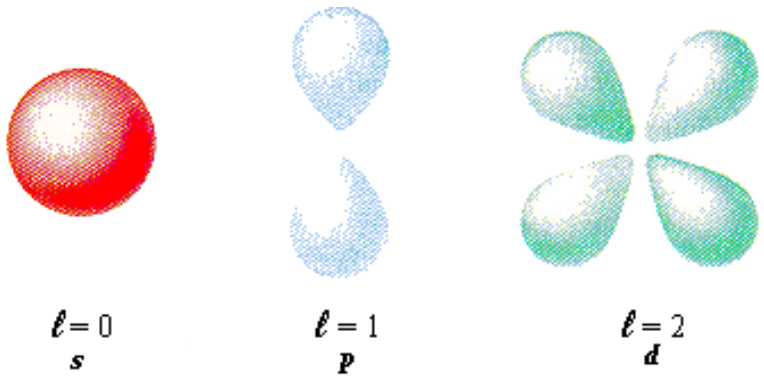

Figure 1.7: Examples of orbital shapes for $l = 0$, 1 and 2. Taken from Bodner Research Web page (2011).

1.4 Overview of spectral theory

1.4.1 Electronic transitions

Four quantum numbers are used to describe the state of an electron. The first, n, is the principle quantum number. In Bohr's theory of atomic structure, electrons can only inhabit certain energy levels (also known as shells or orbitals). The principle quantum number represents the shell inhabited and must be an integer (see Herzberg & Spinks 1944 and Walter 2000 for further details). The azimuthal quantum number, l, represents the shape of an orbital, examples of which are shown in Fig. 1.7, and can take integer values $0 \leq l \leq (n-1)$. m, the magnetic quantum number, represents the orientation of the orbital ellipse and has allowed values $-l \leq m \leq +l$ in integer steps. The final quantum number, s, represents the spin of the electron and can take values of $\pm\frac{1}{2}$.

In a similar fashion to electrons, atoms also may be described by quantum numbers. Four dictate the electronic state of the atom: the principal quantum number, N; the total orbital angular momentum, L, with magnitude equal to any allowed vectorial sum of l; the total spin of the electrons, S, is the vector sum of the individual spins, s, of the electrons; and the total electron angular momentum, J, which may take values $|L-S| \leq J \leq (L+S)$ in integer steps.

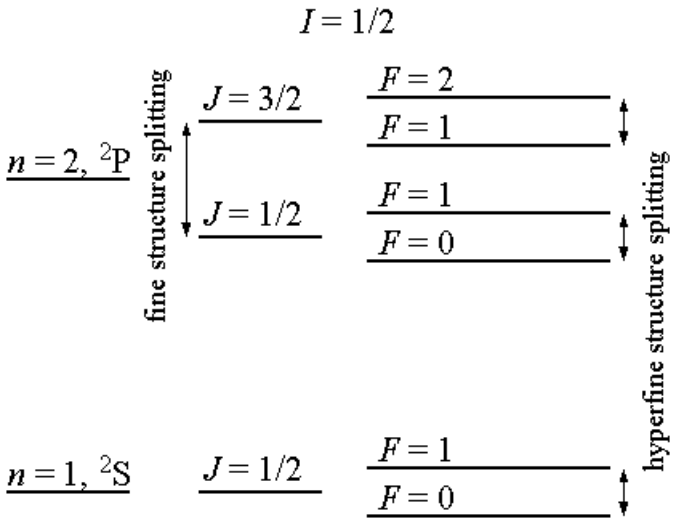

Figure 1.8: Energy level structure of a simple atom, including fine and hyperfine structure[a].

[a]Image credit: *http : //image.absoluteastronomy.com/images/hyperfinestructure.gif*

There are further quantum numbers for atoms: I, dictating the net spin of the nucleus, M, the magnetic quantum number (taking values of $-J \leq M \leq J$ in integer steps) and F, the vector sum of I and J, representing the total momentum of the atom. F may take values of $|J - I| \leq F \leq J + I$ in integer steps.

Interactions between the electron and the nucleus give rise to fine and hyperfine splitting of the levels. Fine splitting is caused by the interaction between the spin of the electron and the orbital angular momentum, represented by J. Therefore, for a particular N, there will be one or more values of J, each one representing a component of fine splitting.

Hyperfine splitting is the result of the interaction of the nuclear spin with the orbiting electrons (represented numerically by F). For a particular N and J, there will be one or more values of F, each one being a component of hyperfine splitting. This is more easily shown diagrammatically, as in Fig. 1.8.

Electrons can be promoted up energy levels in the atom either by absorption of an incident photon or collisional excitation. These excited electrons may decay

to lower states via collisional de-excitation, stimulated emission or spontaneous emission. Further details on transition mechanisms can be found in Sect. 1.4.5.

Looking simply at the physical structure, it could appear that a vast number of transitions are possible. However, many of these are not observed. Selection rules exist for atoms (and ions and molecules) which determine whether a particular transition has a high probability of occurring or a low probability of occurring. These rules, for high probability transitions in simple systems, are:

- $\Delta L = 0, \pm 1$,
- $\Delta l = 1$,
- $\Delta J = 0, \pm 1$ except $J = 0 \rightarrow 0$,
- $\Delta S = 0$,
- $\Delta M = 0 \pm 1$ except $M = 0 \rightarrow J = 0$ if $\Delta J = 0$,

where all quantum numbers are as described previously. Those transitions that conform to the selection rules are known as *allowed transitions* and those that do not are known as *forbidden transitions*. Forbidden transitions, despite their name, can be observed in low-density environments such as planetary nebulae. The mean free path in these low-density environments is sufficiently long that the excited electron has time to decay radiatively. This would not occur elsewhere as the particle would collide with another before the emission were possible (further information about collisional de-excitation can be found in Sect. 1.4.5). In environments like planetary nebulae, these forbidden transitions are often the brightest observed lines.

1.4.2 Rotational and vibrational transitions

Transitions are not restricted solely to electronic transitions in atoms or ions. Rotational and vibrational transitions exist in molecules (in addition to electronic

transitions). Vibrational energy states are caused by the bonding between atoms behaving in a similar manner to a harmonic oscillator. The bond between the two or more molecules may vibrate, stretch or bend. A pictorial representation is shown in Fig. 1.9.

In quantum mechanics, angular momentum of molecules is also quantised, leading to rotational energy levels which may be excited in a similar way to electronic energy levels. For a given electronic state, there is a series of rotational states which may be excited. These rotational energy levels may also undergo fine and hyperfine splitting. The fine splitting is caused by interactions between an electron and the rotation of the molecule (represented, again, by J) and hyperfine structure is caused by the interaction between the nuclear spin and J, represented by F (Milam, Woolf & Ziurys 2009; Skatrud et al. 1983; Chabay & Sherwood 2010; Brown & Carrington 2003). The rotational energy level structure of ^{12}CN is shown in Fig. 1.10 including the fine and hyperfine components.

1.4.3 Radiative transfer

The lines seen in observations are caused by large-scale emission or absorption from regions of gas. As electromagnetic radiation passes through a pocket of material, it may be absorbed and excite vibrational, rotational or electronic states in the atoms, ions or molecules. This causes the intensity of the radiation passing through to decrease:

$$dI = -\kappa_\nu I_\nu ds,$$

where dI_ν is the change in intensity of incident radiation when passing through a volume of material of depth ds, initial intensity at a particular frequency, ν, is given by I_ν and κ is a parameter called the *absorption coefficient* of the material. This dictates the amount of incident radiation absorbed per unit depth of material travelled through (Tielens 2005; Dyson & Williams 1997).

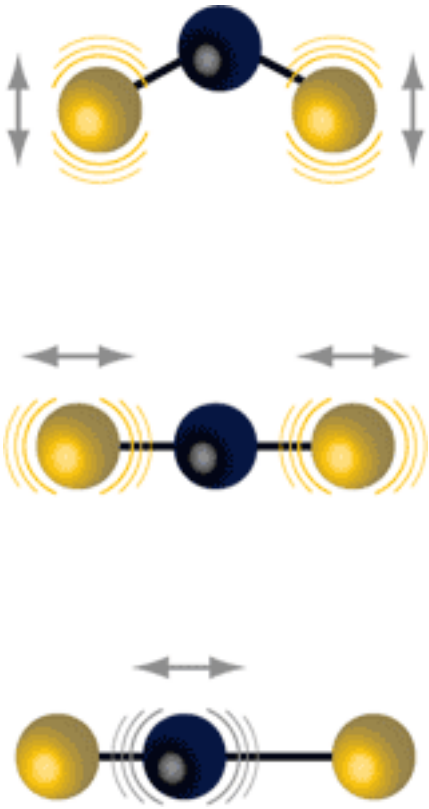

Figure 1.9: Pictorial representation of the different vibrational states possible in a triatomic molecule: the bending modes (upper image), the symmetric stretching modes (middle) and the anti-symmetric stretching modes (lower image)[a].

[a]Image credit: *http : //www.als.lbl.gov/als/science/sci_archive/96vibration.html*

The gas may also undergo emission, parameterised by the following equation:

$$dI_\nu = \epsilon_\nu ds,$$

where ϵ_ν is the emissivity of the material at a given frequency per unit depth.

The net change in intensity of the radiation per unit depth is simply a combination of the two:

$$\frac{dI_\nu}{ds} = \epsilon_\nu - \kappa_\nu I_\nu,$$

and this is known as the *equation of radiative transfer* (Dyson & Williams 1997;

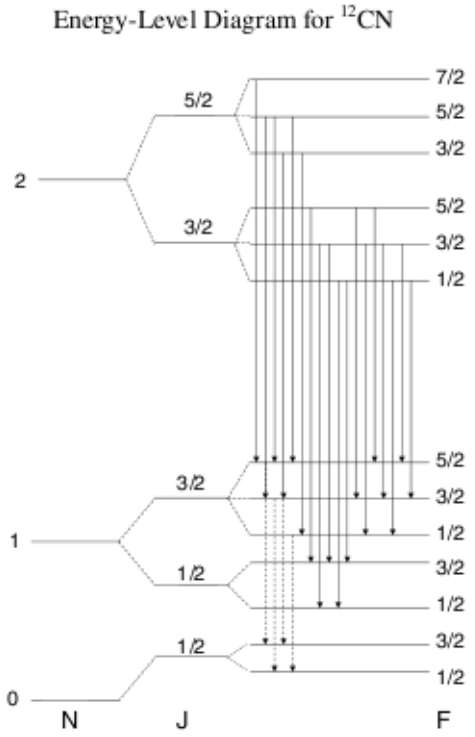

Figure 1.10: Structure of the ^{12}CN rotational line emission, including fine and hyperfine components for the N= 0,1 and 2 levels (Milam, Woolf & Ziurys 2009).

Tielens 2005).

An important factor may be defined from κ: the optical depth of material at a given frequency, τ_ν. This is expressed as:

$$\tau_\nu = \int_s^{s_0} \kappa_\nu ds,$$

where s and s_0 are the beginning and end points between which the radiation travels. The optical depth gives the absorption of the radiation through matter, independent of the amount of matter travelled through. The optically thick limit is defined when $\tau_\nu \geq 1$ and optically thin when $\tau_\nu \ll 1$. These cases are important when investigating abundance, ionic and isotopic ratios from emission lines. In carbon-rich AGB stars, many of the most abundant molecules often emit in optically thick transitions (e.g. CO and HCN).

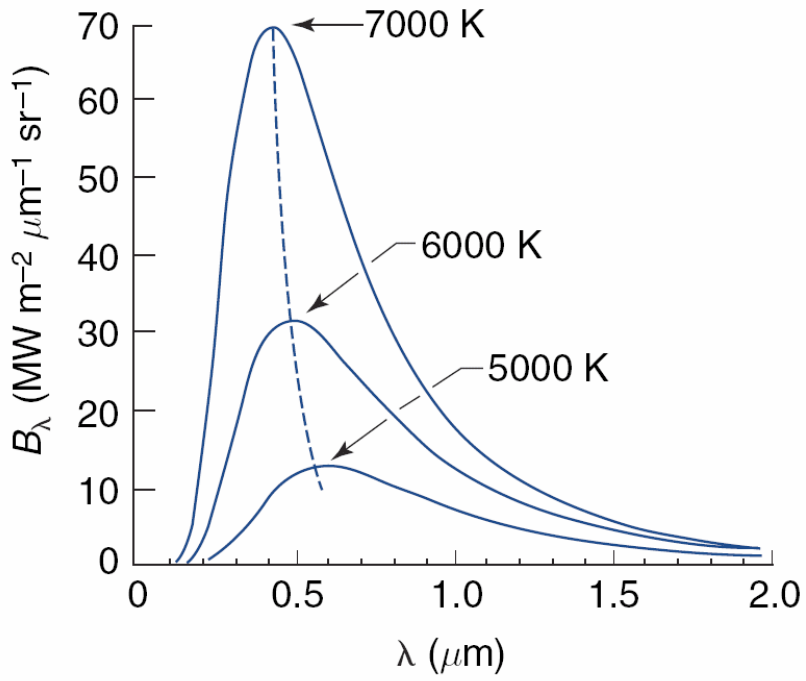

Figure 1.11: Examples of Planck spectra at various temperatures as a function of wavelength[a].

[a]Image credit:
http://www.geog.ucsb.edu/∼joel/g266_s10/lecture_notes/chapt04/oh10_4_1/oh10_4_1.html

1.4.4 Brightness temperature

Many astronomical objects are approximated as *black bodies* (a perfect absorber/emitter of radiation). Black bodies emit radiation according to the *Planck Law*:

$$B_\nu(T) = \frac{2\mathrm{h}\nu^3}{\mathrm{c}^2}\frac{1}{\exp(\mathrm{h}\nu/\mathrm{k}_B T) - 1}, \tag{1.4}$$

where $B_\nu(T)$ is the energy emitted at a frequency ν by a black body of temperature T and is known as the *Planck Function*. The Planck Law can also be written in terms of wavelength, see Rybicki & Lightman (2008) for further details. Examples of black body spectra at various temperatures are shown in Fig. 1.11.

Two important limiting cases to the Planck Law are often used. In the regime

where $h\nu \ll k_B T$, the Planck Law reduces to the Rayleigh-Jeans Law:

$$I_\nu^{RJ}(T) = \frac{2\nu^2}{c^2} k_B T. \tag{1.5}$$

In the case where $h\nu \gg k_B T$, the Wien Law is obtained:

$$I_\nu^{W}(T) = \frac{2h\nu^3}{c^2} \exp\left(-\frac{h\nu}{k_B T}\right). \tag{1.6}$$

Objects that do not behave as black bodies can be assigned a *brightness temperature*, which is the temperature that a black body would require to reproduce the observed intensity of radiation at a particular frequency.

Further details, including derivations, of the Planck, Rayleigh-Jean and Wien Laws may be found in Rybicki & Lightman (2008).

1.4.5 Transitions in two-level systems

There are a number of methods by which transitions may occur. Firstly, to be promoted up and down energy levels in the atom, ion or molecule (which shall henceforth be referred to as the particle), an excitation or de-excitation process must occur. A particle may be excited either radiatively, by absorbing a photon and being promoted to a higher energy state, or collisionally, by interaction with another particle. In order to be de-excited, the particle may undergo spontaneous emission, stimulated emission or collisional de-excitation. Stimulated (where emission is induced by an incident photon) and spontaneous emission are both radiative processes and result in the emission of a photon. These processes are shown schematically in Fig. 1.12.

A particle may also become ionised (or further ionised in the case of ions) as a result of the radiative and collisional interactions detailed above, if the energies involved are great enough. The reverse process, *recombination* can also occur. Emission lines resulting from the recombination of electrons and ions are visible in the highly ionised environments of planetary nebulae.

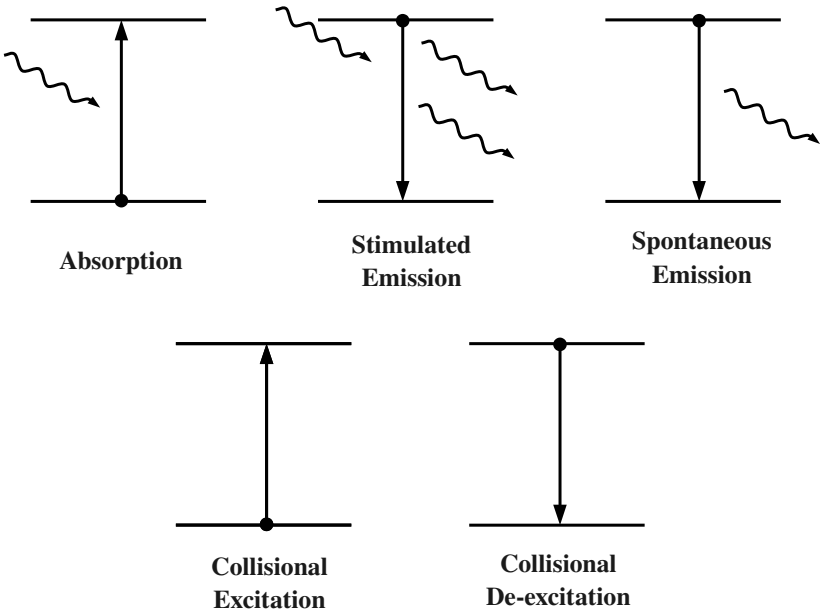

Figure 1.12: Radiative and collisional causes of transitions. Filled circles denote initial state occupied, photons are indicated by sinusoidal arrows and direction of energy level change is represented by the straight arrow.

The rates by which the bound-bound radiative processes occur are defined by a combination of Einstein's A and B coefficients, the intensity of the radiation field U_ν and the populations in each of the levels i and j. Level i is defined as the lower level and j the upper, giving the following relations:

- Rate of absorption = $U_\nu \mathrm{B_{ij}} n_i$,
- Rate of spontaneous emission = $\mathrm{A_{ji}} n_j$,
- Rate of stimulated emission = $U_\nu \mathrm{B_{ji}} n_j$,

where n_i and n_j are the populations of levels i and j respectively. The rates of collisional excitations and de-excitations are defined in a similar manner:

- Rate of collisional excitation = $n n_i q_{ij}$,
- Rate of collisional de-excitation = $n n_j q_{ji}$,

where q_{ij} is the collisional rate coefficient from level i to level j. Finally, the rates of radiative ionisation and recombination can be expressed:

- Rate of radiative recombination $= n_e n_j \alpha_{ij}$,
- Rate of radiative ionisation $= 4\pi n_i \int_{\nu_0}^{\infty} \frac{J(\nu)}{\mathrm{h}\nu} a_i(\nu) \mathrm{d}\nu$,

where α_{ij} is the radiative recombination coefficient, $a_i(\nu)$ is the photoionisation cross-section, $J(\nu)$ is the mean intensity of ionising photons and ν_0 is the minimum frequency for ionisation.

These formulae can be used in combination, depending upon the situation at hand, to identify rates of change of population with respect to time or, if equilibrium is assumed, the relevant formulae may be equated. For example, in an equilibrium system where both collisional and ionisation effects may be neglected, the bound-bound radiative rates may be equated:

$$U_\nu \mathrm{B_{ij}} n_i = \mathrm{A_{ji}} n_j + U_\nu \mathrm{B_{ji}} n_j.$$

1.4.6 Maser emission

Masers (Microwave Amplification of Stimulated Emission of Radiation) have a number of distinct features in their emission spectra: they often show an unusually narrow line profile and are often abnormally bright both with respect to lines of other species and to other lines in the masing species spectra. In non-masing systems, lower energy states of particles are more highly populated than those of the higher energy states. For a maser to be produced, a population inversion must be present: an over-population of a higher energy state with respect to a lower energy state. This inversion can lead to the production of an intense line from a single transition: the maser.

A population inversion is formed by a pumping mechanism, often a series of transitions leading to the masing transition, for which a canonical example

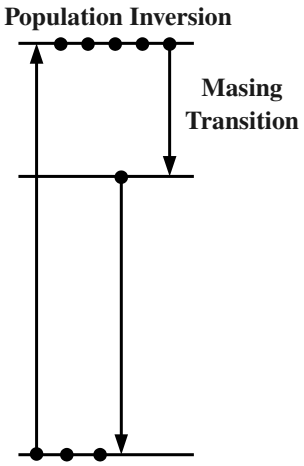

Figure 1.13: Schematic view of a canonical three-level maser. The levels increase in energy with height.

is shown in Fig. 1.13. If a population inversion is to be created in Fig. 1.13, and the levels are labelled as 1, 2 and 3 for the lower, middle and upper levels respectively, the rate of decay from level 3 to level 2, R_{32}, must be less than the rate of decay from level 2 to level 1, R_{21}. Additionally, R_{13}, the rate of promotion from level 1 to level 3 must be greater than R_{32}. If this is satisfied, then the 3-2 transition forms a bottleneck, resulting in a population inversion.

In reality, pumping mechanisms can be made up of many levels and may be dependent on outside incident radiation. In the case of multiple levels, the rates of promotion and decay to the upper masing level must be higher than the decay from the upper to the lower masing level. Additionally, any decays from the lower masing level to the ground state (or lowest level used in the pumping mechanism) must also be higher than the decay from the upper to the lower masing level.

1.5 Thesis outline

The following chapters describe four projects predominantly based on spectroscopic observations of evolved stars and planetary nebulae to better understand

these complex objects and how they affect Galactic chemical evolution. The first project, Chapter 2, presents an in-depth millimeter molecular line survey of a sample of five AGB stars and planetary nebulae. The second, Chapter 3, details a study into 89.087 GHz HCN maser emission in carbon-rich circumstellar envelopes and presents a new detection of the 89.087 GHz maser in IRAS 15082-4808. The third, Chapter 4, describes the detailed radiative transfer modelling of CO in the circumstellar envelope of II Lup, one of the sample stars in Chapter 2. The final project (Chapter 5) presents the results of a zinc abundance analysis of Galactic planetary nebulae. In Chapter 6, the results of each project are briefly summarised, the conclusions are set out and potential avenues for future work explored.

Chapter 2

A molecular line survey of a sample of AGB stars and planetary nebulae

2.1 Introduction

Asymptotic giant branch (AGB) stars and planetary nebulae (PNe) are rich sites of dust and molecule formation. As a result, their spectra are full of a variety of transitions. A vast quantity of molecular species present in these objects emit in the millimeter region of the spectrum. From these spectral lines, a host of information can be gleaned, including the abundances and temperatures of species present as well as their extent in the envelopes of the host stars. Thus millimeter molecular line surveys are an ideal method of identifying the chemical composition and thermodynamic properties of the regions in which these species exist.

J-type stars are a sub-set of carbon-rich AGB stars with an unusually low $^{12}C/^{13}C$ ratio (< 10). It is thought that these could be the origin of presolar A+B grains: silicon carbide (SiC) grains with pre-Solar System origins, found in

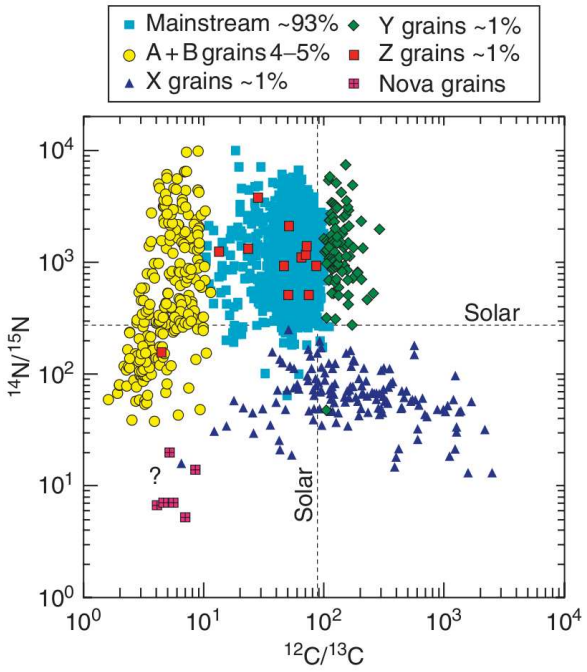

Figure 2.1: Plot from Zinner (2003) showing the different origins of presolar grains and their carbon and nitrogen isotopic abundances. Y and Z type grains originate in AGB stars, X grains from supernovae and nova grains from novae.

meteorites which do not have a confirmed origin (see Fig. 2.1 for further details about the SiC presolar grains). By identifying and subsequently studying J-type stars in detail, we can ascertain the isotopic characteristics of these stars and compare them to the measured isotopic abundances found in these mysterious A+B grains.

Isotopic abundance calculations often require transitions to be optically thin to measure the relative abundances of two isotopologues. However, often the method used to measure, for example, the optical depth of CO transitions, requires a knowledge of the carbon isotopic ratio. Transitions with hyperfine structure alleviate this requirement as the relative intensities of the different components vary with increasing optical depth of the overall transition. By fitting these hyperfine components, the optical depth may be constrained and thus accurate

isotopic ratios determined.

This chapter details a millimeter molecular line survey carried out over a sample of carbon-rich AGB stars and two oxygen-rich PNe. The aim of this survey is to use high velocity-resolution spectra to identify molecules present in the targets, resolve hyperfine structure where possible and ultimately determine reliable column densities and isotopic ratios for all sources observed. This line survey is intended to compliment those previously carried out (e.g. Woods et al. 2003; Edwards & Ziurys 2013; Ramstedt & Olofsson 2014) by fully resolving the lines and subsequently analysing both the line profiles and hyperfine structures of the transitions identified.

2.2 Observations

2.2.1 Targets

The sample comprises of five sources: three galactic carbon stars and two oxygen-rich planetary nebulae. These targets were selected due to their high brightness and their position. The brighter sources were more likely to be detected in multiple molecular transitions than the dimmer objects and their positions were such that they were observable at Mopra for long periods of time during the observing run. In the case of the AGB stars, their carbon-rich, mass-losing nature. Further details about the sources can be found in Table 2.1.

IRAS 15194-5115

IRAS 15194-5115, also known as II Lup, is the brightest carbon star in the southern hemisphere at 12 μm and the third brightest in both hemispheres at 12 μm, with only IRC+10216 and CIT 6 being brighter (Nyman et al. 1993). It has a pulsation period of 575 days (Feast, Whitelock & Marang 2003). The mass-loss rate for this star has been found from non-local thermodynamic equilibrium ra-

Table 2.1: Source and coordinate list

Source	Alternative Name	RA	Dec	Type
IRAS 15194-5115	II Lup	15 23 05.07	-51 25 58.7	C-AGB
IRAS 15082-4808	RAFGL 4211	15 11 41.89	-48 20 01.3	C-AGB
IRAS 07454-7112	AI Vol	07 45 02.80	-71 19 43.2	C-AGB
IRAS 14192-4355	IC 4406	14 22 26.278	-44 09 04.35	O-PN
IRAS 18021-1950	NGC 6537	18 05 13.104	-19 50 34.88	O-PN

diative transfer models to be 1×10^{-5} $M_{\odot}$ yr^{-1} (Ryde, Schöier & Olofsson 1999; Woods et al. 2003). Distance estimates in literature studies are between 600-1200 pc (Nyman & Olofsson 1995; Woods et al. 2003).

IRAS 15082-4808

IRAS 15082-4808, also known as RAFGL 4211, is also a mass losing, carbon-rich AGB star. Its mass loss rate has been derived from models to be approximately 1×10^{-5} $M_{\odot}$ yr^{-1} (Groenewegen et al. 2002). The distance to this star according to the literature ranges between 640 pc and 1500 pc with the general consensus between 640 and 850pc (Woods et al. 2003; Nyman & Olofsson 1995).

IRAS 07454-7112

IRAS 07454-7112 is a mass losing, carbon-rich Mira variable star (Menzies, Feast & Whitelock 2006). As a bright infrared star, this source has been part of several line surveys in the past as well as being studied in-depth by Nyman & Olofsson (1995) and Woods et al. (2003). The distance of this source varies in the literature from 710 pc to 850 pc (Woods et al. 2003; Menzies, Feast & Whitelock 2006), and its mass loss rate has been modelled as $\sim 10^{-5}$ $M_{\odot}$ yr^{-1} (Nyman & Olofsson 1995).

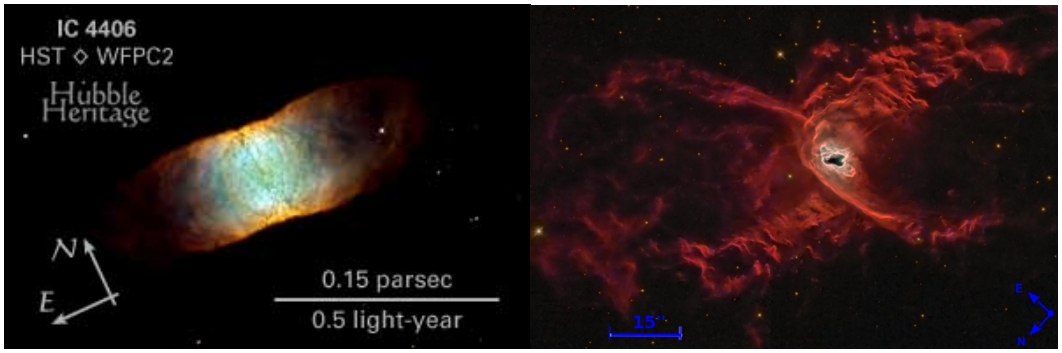

Figure 2.2: NASA Astronomy Picture of the Day *HST* images of IC 4406 (left) and NGC 6537 (right). Orientations and indications of scale are shown on the figures. Filters for IC 4406 image using the WFPC2 instrument: F502N ([O III]), F656N (H-alpha), F658N ([N II])[a]. NGC 6537 image: optical[b].

[a]http://heritage.stsci.edu/2002/14/fast_facts.html
[b]http://apod.nasa.gov/apod/ap121029.html

IC 4406

IC 4406 is an oxygen-rich, bi-polar planetary nebula with a molecular envelope. It has a collimated outflow parallel to the major axis of the nebula, and because of this outflow, there is a strong dependence of the shape of the line profile with changing position across the nebula, as shown by Sahai et al. (1991). The central star temperature has been found to be 8×10^4 K from three dimensional photoionisation modelling (Gruenwald, Viegas & Broguiere 1997). This nebula has been shown through both observation and modelling to have a cylindrical structure and extends over a region approximately 100″ by 30″ (Faes, Costa & Morisset 2011). A *Hubble Space Telescope* (*HST*) image of this nebula is shown in Fig. 2.2.

NGC 6537

NGC 6537, also known as the Red Spider Nebula, is a type I (rich in helium and nitrogen), bi-polar planetary nebula with outflows extending out to an angular size of 100″ in the direction NE-SW. The central star temperature is 2×10^5 K.

A small, opaque, dusty torus exists at 2-4″ from the centre with an asymmetric cavity, found by Matsuura et al. (2005) from *HST* Hα and Hβ maps. Sabin, Zijlstra & Greaves (2007) show, through maps taken with the Submillimetre Common-User Bolometer Array (SCUBA), that the central region of the nebula is approximately 20″ in diameter and appears to have a toroidal structure. A *HST* image of this nebula is shown in Fig. 2.2.

2.2.2 Telescope

The data were obtained using the 22 m Mopra telescope, situated approximately 450 km from Sydney, Australia. The 3 mm Monolithic Microwave Integrated Circuit (MMIC) receiver in June 2010 was used in conjunction with the Mopra Spectrometer (MOPS), in broadband mode for all observations. The MMIC receiver has a frequency range of 77-116 GHz and works in single-sideband mode[1].

The use of broadband mode with MOPS gives an observable frequency range of 8 GHz, split into 4 overlapping bands, each with 2048 channels over a 2.2 GHz frequency range, as shown schematically in Fig. 2.3. The band edges suffer from noise, but the overlap given in this set up compensates well for this so little data is lost. Three frequency set-ups were used to observe each source: 84.5–92.5 GHz, 90.5–98.5 GHz and 107.5–115.5 GHz, with the region between 98.5 GHz and 107.5 GHz unobserved.

The observations for this project (ID: M530) were taken over ten days: 18/06/2010 to 27/06/2010. The rms noise on a typical spectrum was 0.01 K. The efficiency of Mopra at this frequency is $\sim$0.5, the sensitivity is 22 Jy/K (converting from corrected antenna temperature) and the beam size at 90 GHz is 38″.

[1]Technical summary of the Mopra radio telescope: narrabri.atnf.csiro.au/mopra/mopragu.pdf

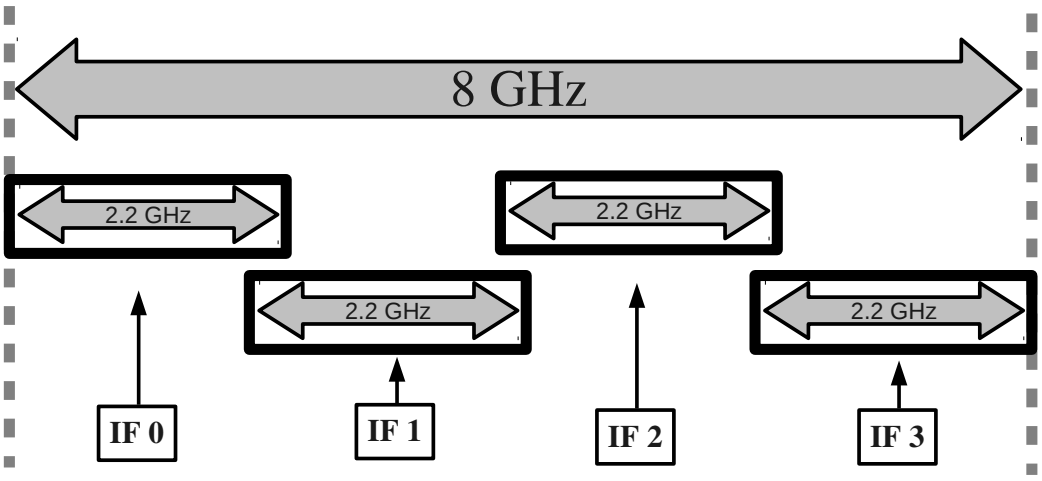

Figure 2.3: A schematic diagram of the IF set-up for MOPS in broadband mode.

2.2.3 Data reduction and line identification

The observations were made in position-switching mode, meaning that observations were taken in on/off source pairs. The on-off quotient[2] was created from these pairs and their corresponding T_{sys} (system temperature) and the resulting spectrum is the antenna temperature corrected for atmospheric and systematic effects, referred to henceforth as *corrected antenna temperature*. The main beam temperature is obtained by dividing the corrected antenna temperature by the efficiency of the telescope which varies with frequency. The main beam efficiency is documented as 0.49 at 78 GHz and 0.42 at 116 GHz[3]. Therefore, for this data, the efficiency was taken to be 0.49 between 84.5 GHz and 98.5 GHz and 0.42 between 107.5 GHz and 115.5 GHz.

The data were reduced using the ATNF Spectral Analysis Package (ASAP). The on/off observations were matched in time and the resultant spectrum formed. The polarisations of each set of observations were averaged, weighted by the system temperature. Multiple observations of each source in each frequency set-up were taken and thus needed to be coadded. However, some observations were

[2]The quotient is defined as: $T_a^* = \frac{ON-OFF}{OFF} T_{\rm sys}$.

[3]Technical summary of the Mopra radio telescope: narrabri.atnf.csiro.au/mopra/mopragu.pdf

taken during poor weather and/or suffered from severe baseline rippling. To remove the poor data prior to coadding, the spectrum of each individual observation had a 3rd degree polynomial baseline temporarily fitted and subtracted. Those observations that were badly affected were flagged and removed from all further analysis. The remaining spectra (taken before the polynomial baseline subtraction) were then averaged in time, weighted by the system temperature. A 3rd degree polynomial baseline was fitted to the averaged spectrum and subtracted to remove any remaining baseline rippling.

The spectra were inspected by eye for strong lines. These lines were then identified using the NIST and Splatalogue databases (Lovas 1992; Markwick-Kemper, Remijan & Fomalont 2006). All other transitions of those identified species that lay within the observed frequency range were searched for. In cases where it was unclear as to which species was the cause of a particular line, all observable transitions of each of the candidate species were examined for further detections. In most cases, this resulted in a clear identification of the line. However, if a major transition of a particular species was not detected, the corresponding minor transitions of the same species were not searched for (e.g. unusual vibrational transitions), unless the spectrum of the major transition suffered from a high level of noise. The same logic was applied to isotopologues: if transitions of the most common isotopologue were undetected, transitions of the rarer isotopologues were not searched for.

The final spectra are shown for each source in 0.3 GHz segments in Appendix A. These have been corrected for source local standard of rest (LSR) velocities, which have been taken as: -15.0 km/s (IRAS 15194-5115, De Beck et al. 2010), -0.76 km/s (IRAS 15082-4808, Smith, Zijlstra & Fuller 2014), -38.9 km/s (IRAS 07454-7112, Risacher & van der Tak 2009), -44.5 km/s (IC 4406, Sahai et al. 1991) and 10.0 km/s (NGC 6537, Edwards & Ziurys 2013).

2.3 Line profiles

The spectral lines observed from circumstellar envelopes (CSEs) have distinctive profiles that are affected greatly by both the optical depth of the emitting region and the size of the telescope beam with which it is observed. From these shapes we can ascertain the extent of the emitting region relative to the beam, the motion of the emitting molecules and the optical depth of the emitting species. In order to derive the profiles of the observed lines, a number of assumptions must be made:

1. The CSE is spherically symmetric;
2. Mass loss rate is constant with time;
3. The expansion velocity is constant with radius;
4. The local line width due to thermal motions and turbulence at any point in the envelope is much less than that created from Doppler broadening due to the expansion of the envelope;
5. The central star is negligible in size in comparison to the size of the envelope.

The assumption of constant expansion velocity with radius does not hold in the innermost regions of the CSE where the majority of the wind acceleration occurs. However, this region is extremely small when compared with the overall size of the envelope. Assumptions 1 and 2 have been examined in the literature and clumpy or anisotropic structures in CSEs have been reported. This should be kept in mind when comparing these theoretical curves to observations. Assumptions 4 and 5 are commonly found to be true in observations.

Using the above assumptions, it is possible to derive expressions for the line profiles as a function of observed velocity, first derived in Morris (1975) using the Sobolev (1960) approximation. What follows is a summary of this derivation; further details may be found in Morris (1975) and Sobolev (1960).

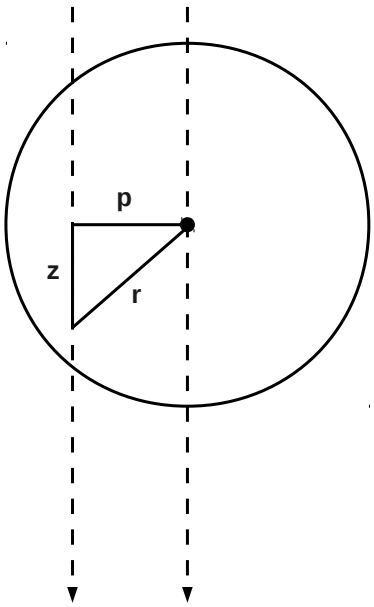

Figure 2.4: Schematic view of a line of sight passing through a CSE. The dashed lines represent line of sights to the observer (assumed at infinity) with the observation centred on the star.

Consider a line of sight passing through a region of a CSE, as depicted in Fig. 2.4 (left-most dashed line). The observed velocity of the line emitted by an infinitely small region of the CSE along the line of sight is given by:

$$v_{\rm o} = v_{\rm r}\frac{z}{r}, \tag{2.1}$$

where v_o and v_r are the observed velocity and radial expansion velocity respectively and z and r are defined in Fig. 2.4. The contribution to the brightness temperature, $T_{\rm b}$ of the transition observed from the CSE in this line of sight is:

$$\begin{aligned} T_{\rm b}(p, v_{\rm o}) &= \frac{{\rm c}^2}{2{\rm k_B}\nu_0^2}\left[B_{\nu 0}\left(T_{\rm ex}(r)\right) - B_{\nu 0}\left(T_{\rm bkgd}(r)\right)\right]\left(1 - {\rm e}^{-\tau({\rm p,v_o})}\right) \\ &= j(r)\left(1 - {\rm e}^{-\tau({\rm p,v_o})}\right), \end{aligned} \tag{2.2}$$

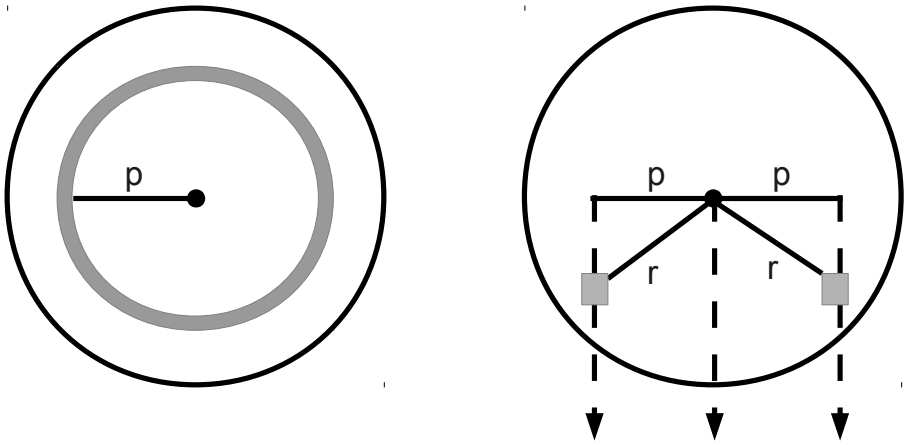

Figure 2.5: Pictorial representation of each annulus being integrated over in Equ. 2.3 for each given p. The left image has the line of sight coming out of the page and in the right, the orientation is the same as for Fig. 2.4. The grey regions represent the integration area for a given p at velocity $v_{\rm o}$. Once integrated over all possible p, this results in a cone-shaped region with uniform observed velocity.

where ν_0 is the rest frame frequency, $B_{\nu 0}$ is the Planck function at a temperature T which is dependent solely upon the distance, r, of the considered region of the envelope from the star and not the projected distance, p, given a particular line of sight. $\tau(p, v_{\rm o})$ is the optical depth of the region at a projected distance from the centre given a particular line of sight with the observed velocity v_o. $T_{\rm ex}$ and $T_{\rm bkgd}$ are the excitation temperatures of the transition and background respectively (e.g. the cosmic microwave background).

In reality, the telescope response must also be taken into account with the telescope response function, $G(p, R_{\rm beam})$, but for the case when the source is unresolved, this may be taken as constant, G, when integrated over the source. Integrating each annulus given by a particular p over all possible p for a given $v_{\rm o}$ (see Fig. 2.5 for a pictorial representation of the annuli being integrated) results in the following:

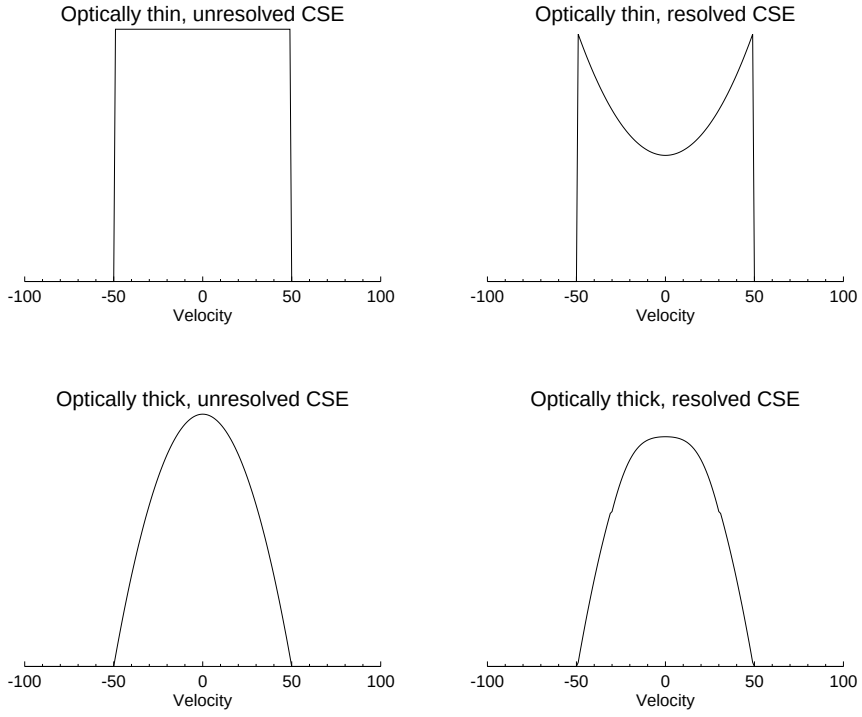

Figure 2.6: Line profiles emitted from an uniformly outwardly expanding, isotropic circumstellar envelope. Figure based upon Fig. 7.1 of Zuckerman (1987).

$$T_{\rm b}(v_{\rm o}) = G \int_0^{p=p_{\rm max}(v_{\rm o})} j(r) \left(1 - {\rm e}^{-\tau(p,v_{\rm o})}\right) 2\pi p {\rm d}p, \tag{2.3}$$

where $p_{\rm max}(v_{\rm o})$ is the maximum projected distance from the centre of the envelope whose line of sight contains the velocity component $v_{\rm o}$. $T_{\rm b}(v_{\rm o})$ is the intensity of the line in temperature units at $v_{\rm o}$.

2.3.1 Optically thin limit

In the optically thin regime, $\tau \ll 1$ and therefore $1 - {\rm e}^{-\tau} \rightarrow \tau$. As defined by Morris (1975),

$$\tau(p, v_{\rm o}) = \alpha(r) n(r) p \frac{\Delta v}{v_{\rm r}} \left(1 - \left(\frac{v_{\rm o}}{v_{\rm r}}\right)^2\right)^{-\frac{3}{2}}, \tag{2.4}$$

where $\alpha(r)$ is the absorption coefficient, $n(r)$ is the density of the emitting molecule and Δv is the local line width. Combining Equ. 2.3 and 2.4 in the optically thin limit, and utilising the relation $r^2\mathrm{d}r = (1-(v_\mathrm{o}/v_\mathrm{r})^2)^{-\frac{3}{2}}\, p^2\mathrm{d}p$ as derived from Equ. 2.1, leads to the following relation:

$$T_\mathrm{b}(v_\mathrm{o}) = 2\pi G \frac{\Delta v}{v_\mathrm{r}} \int_0^{r=\mathrm{R}} j(r)\alpha(r)n(r)r^2\mathrm{d}r, \tag{2.5}$$

which has no dependence upon v_o, save that $|v_\mathrm{o}| \leq v_\mathrm{r}$. Therefore in the optically thin limit, the line profile is a top-hat function. If the envelope is resolved, G cannot be taken as constant over the source and what results is a reduction in intensity in the central region of the profile, giving rise to the commonly-seen horned profile. These cases are shown in Fig. 2.6.

2.3.2 Optically thick limit

In the optically thick limit, $\tau \gg 1$ and therefore $1 - \mathrm{e}^{-\tau} \rightarrow 1$. Substituting for τ and following the methodology applied for the optically thin case, for $|v_\mathrm{o}| \leq v_\mathrm{r}$:

$$T_\mathrm{b}(v_\mathrm{o}) = 2\pi G \left(1 - \left(\frac{v_\mathrm{o}}{v_\mathrm{r}}\right)^2\right) \int_0^{r=\mathrm{R}} j(r)r\mathrm{d}r, \tag{2.6}$$

which again has an integral independent of v_o. T_b is dependent upon $-v_\mathrm{o}^2$, therefore the line profile in the unresolved, optically thick limit is a parabola. If the CSE were resolved, there would be a reduction in intensity in the central region, causing a flattening of the parabolic profile. These are also shown visually in Fig. 2.6. Both limits assume that the temperature is constant across the radius of the envelope.

Table 2.2: Details of all detected transitions. All molecular transitions relate to the ground vibrational state unless otherwise indicated. Transitions of the form $X_{y,z}$ are rotational transitions of asymmetric top molecules where X relates to the branch of energy levels, y and z are the K_{-1} and K_1 quantum numbers respectively. For further information on asymmetric top structure, see Cooke & Ohring (2012).

Molecule	Freq (GHz)	Transition
^{30}SiO	84.74617	J=2-1
HC_5N	85.20160	J=32-31
$C^{13}CH^b$	85.22933	N=1-0, J=3/2 - 1/2, F_1=2-1, F=5/2 - 3/2
$C^{13}CH^b$	85.23276	N=1-0, J=3/2 - 1/2, F_1=2-1, F=3/2 - 1/2
$C^{13}CH^b$	85.24771	N=1-0, J=3/2 - 1/2, F_1=1-0, F=1/2 - 1/2
$C^{13}CH^b$	85.25695	N=1-0, J=3/2 - 1/2, F_1=1-0, F=3/2 - 1/2
$C^{13}CH^b$	85.30397	N=1-0, J=1/2 - 1/2, F_1=1-1, F=1/2 - 3/2
$C^{13}CH^b$	85.30769	N=1-0, J=1/2 - 1/2, F_1=1-1, F=3/2 - 3/2
$C^{13}CH^b$	85.31438	N=1-0, J=1/2 - 1/2, F_1=0-1, F=1/2 - 1/2
c-C_3H_2	85.33891	$2_{1,2}$ - $1_{0,1}$
C_4H	85.63400	N=9-8, J=19/2 - 17/2
C_4H	85.67257	N=9-8, J=17/2 - 15/2
^{29}SiO	85.75920	J=2-1
$H^{13}CN$	86.34018	J=1-0
SiO	86.84700	J=2-1
$HN^{13}C$	87.09086	J=1-0
C_2H	87.28416	N=1-0, J=3/2 - 1/2, F=1-1
C_2H^b	87.31693	N=1-0, J=3/2 - 1/2, F=2-1
C_2H^b	87.32862	N=1-0, J=3/2 - 1/2, F=1-0
C_2H^b	87.40200	N=1-0, J=3/2 - 1/2, F=1-1
C_2H^b	87.40717	N=1-0, J=3/2 - 1/2, F=0-1
C_2H	87.44651	N=1-0, J=3/2 - 1/2, F=1-0
$H^{13}CCCN$	88.16683	J=10-9
HCN	88.63185	J=1-0
CCCN	89.04559	N=9-8, J=19/2 - 17/2
CCCN	89.06436	N=9-8, J=17/2 - 15/2
HCN	89.08791	J=1-0 F=2-1 v=(0,2,0)
HCO^+	89.18853	J=1-0
$HC^{13}CCN^b$	90.59306	J=10-9
$HCC^{13}CN^b$	90.60179	J=10-9
HNC	90.66356	J=1-0

^{b}: blended transitions

Table 2.2: – *continued.*

Molecule	Freq (GHz)	Transition
SiS	90.77156	J=5-4
HCCCN	90.97899	J=10-9
^{13}CS	92.49427	J=2-1
SiC_2	93.06364	$4_{0,4}$ - $3_{0,3}$
SiC_2	94.24539	$4_{2,3}$ - $3_{2,2}$
C_4H	95.15032	N=10-9, J=$^{21}/_2$ - $^{19}/_2$
C_4H	95.18894	N=10-9, J=$^{19}/_2$ - $^{17}/_2$
SiC_2	95.57938	$4_{2,2}$ - $3_{2,1}$
C^{34}S	96.41295	J=2-1
H^{13}CCCN	96.98300	J=11-10
CS	97.98095	J=2-1
Band Gap		
unidentified	107.973	...
^{13}CN	108.78020	N=1-0, J=$^3/_2$ - $^1/_2$, F_1=2-1, F=3-2
^{13}CN	108.78237	N=1-0, J=$^3/_2$ - $^1/_2$, F_1=2-1, F=2-1
^{13}CN	108.78698	N=1-0, J=$^3/_2$ - $^1/_2$, F_1=2-1, F=1-0
CCCN	108.83427	N=11-10, J=$^{23}/_2$ - $^{21}/_2$
CCCN	108.85302	N=11-10, J=$^{21}/_2$ - $^{19}/_2$
SiS	108.92430	J=6-5
HCCCN	109.17364	J=12-11
C^{18}O	109.78217	J=1-0
^{13}CO	110.20135	J=1-0
CN	113.14419	N=1-0, J=$^1/_2$ - $^1/_2$, F=$^1/_2$ - $^3/_2$
CN	113.17050	N=1-0, J=$^1/_2$ - $^1/_2$, F=$^3/_2$ - $^1/_2$
CN	113.19128	N=1-0, J=$^1/_2$ - $^1/_2$, F=$^3/_2$ - $^3/_2$
CN[b]	113.48812	N=1-0, J=$^3/_2$ - $^1/_2$, F=$^3/_2$ - $^1/_2$
CN[b]	113.49097	N=1-0, J=$^3/_2$ - $^1/_2$, F=$^5/_2$ - $^3/_2$
CN[b]	113.49964	N=1-0, J=$^3/_2$ - $^1/_2$, F=$^1/_2$-$^1/_2$
CN[b]	113.50891	N=1-0, J=$^3/_2$ - $^1/_2$, F=$^3/_2$ - $^3/_2$
CN[b]	113.52043	N=1-0, J=$^3/_2$ - $^1/_2$, F=$^1/_2$ - $^3/_2$
C_4H	114.18251	N=12-11, J=$^{25}/_2$ - $^{23}/_2$
C_4H	114.22104	N=12-11, J=$^{23}/_2$ - $^{21}/_2$
CO	115.27120	J=1-0
SiC_2	115.38239	$5_{0,5}$ - $4_{0,4}$

[b]: blended transitions

2.4 Results

Listed in Table 2.2 are details of all the transitions detected in the sample. A total of 64 transitions were detected across all sources, including some blended hyperfine transitions.

One of the transitions detected in IRAS 15194-5115 could not be identified. Its observed frequency is approximately 107.973 GHz, assuming no significant velocity offsets with respect to the systemic velocity of the envelope. A number of different candidate species were identified as potentially causing this transition: e.g. c-HCCCD, $(CH_3)_2CO$ and $CH_3O^{13}CHO$. However, these species have a large number of transitions within the observed frequency range and it would be expected that a number of other transitions would have also been detected. This is not the case. It is also possible that this transition could be an artefact of baseline ripple removal, although its strength and the stable baseline regions surrounding it make this option less likely. The line profile is unclear and thus constraints about the optical depth of this transition cannot be applied.

The peak intensities, integrated intensities and full line widths were measured for every transition in all five sources. For unblended transitions, the method was as follows. The spectra were smoothed, then a straight-line background was fitted to the data on either side of the line, usually using the regions offset from the line by $\pm$50-100 km/s, to correct for any systematic offset of the spectrum from zero. The limits of the line were identified manually, the peak intensity of the line was measured, and the integrated intensity calculated using the trapezium rule approximation for integration between the line of the spectrum and background. The line width was measured as the full width at the base of the profile. These parameters are noted for all transitions in all sources in Table 2.3 (AGB star sample) and Table 2.4 (PN sample).

The blended transitions fell into two categories: separable blended transitions and unseparable blended transitions. The unseparable transitions were those

that were blended to such an extent that the edges and thus the extent of the overlap of the individual lines were indeterminable. The integrated intensities, peak intensities and line widths for these blends were taken for the overall blended line and are indicated as such in Tables 2.3 and 2.4. Examples include the CN transitions at $\sim$ 113.49 GHz and the HC^{13}CCN and HCC^{13}CN transitions at $\sim$ 90.6 GHz.

The separable blended transitions are those that are on the limit of being blended, as for C_2H, or have clearly defined components, as in C^{13}CH. These transitions have been fitted to measure the integrated intensity emanating from each component and these integrated intensities are listed individually in Tables 2.3 and 2.4.

2.4.1 Line fitting

Pikaia

In order to fit the line profiles of the spectra to disentangle the hyperfine structure of transitions and to ascertain the optical depth, an optimization routine is required. The routine chosen for this task is the Genetic Algorithm (GA) PIKAIA, which is briefly described below. Further details on this routine may be found in Charbonneau (1995).

GAs are a class of optimization routine based upon the principle of "survival of the fittest" employed in nature to produce species that adapt to their environment. In nature, an individual in a population is more likely to survive and pass on its genetic material to offspring if it is well adapted to its environment, and those less well adapted are more likely to perish. In addition to this, genetic material may mutate between generations, producing either fitter or less fit individuals than the parents. Thus, a population slowly becomes more adapted to its surroundings by the elimination of environmentally-unsuitable genetic material. This process can be mimicked in computing to produce highly robust optimiza-

Table 2.3: Detected transitions in the AGB star sample. Frequencies are given in GHz, the line peak, T_{peak}, is given in K, the integrated intensity, $\int T dv$, is in K km/s and the full width of the line at the base of the line, Δv, is in km/s. All temperatures are given in corrected antenna temperatures. The efficiency of Mopra is 0.49 before the band gap and 0.42 after. The uncertainties on listed values are 5%, 15% and 17% for the line width, peak temperature and integrated intensity respectively.

Molecule	Frequency	IRAS 15194-5115			IRAS 15082-4808			IRAS 07454-7112		
	(GHz)	T_{peak}	$\int T dv$	Δv	T_{peak}	$\int T dv$	Δv	T_{peak}	$\int T dv$	Δv
^{30}SiO	84.74617	0.014	0.292	39.1	...	...	...	...	...	...
HC_5N	85.2016	0.018	0.534	48.4	...	...	...	...	...	...
$C^{13}CH^b$	85.22933	0.011	0.457	41.5	...	...	...	...	...	...
$C^{13}CH^b$	85.23276	0.007	0.291	41.5	...	...	...	...	...	...
$C^{13}CH^b$	85.24771	0.003	0.125	41.5	...	...	...	...	...	...
$C^{13}CH^b$	85.25695	0.007	0.291	41.5	...	...	...	...	...	...
$C^{13}CH^b$	85.30397	0.003	0.125	41.5	...	...	...	...	...	...
$C^{13}CH^b$	85.30769	0.006	0.249	41.5	...	...	...	...	...	...
$C^{13}CH^b$	85.31438	0.003	0.125	41.5	...	...	...	...	...	...
c-C_3H_2	85.33891	0.042	0.975	43.6	...	...	...	...	...	...
C_4H	85.634	0.043	1.420	43.4	...	...	...	...	...	...
C_4H	85.67257	0.045	1.520	41.5	...	...	...	...	...	...
^{29}SiO	85.75920	0.018	0.449	40.5	...	...	...	...	...	...
$H^{13}CN$	86.34018	0.522	17.410	55.2	0.068	1.820	41.2	0.062	1.360	34.6
SiO	86.847	0.174	5.250	46.5	0.082	1.790	37.3	0.039	0.708	27.9
$HN^{13}C$	87.09086	0.024	0.590	48.3	...	...	...	...	...	...
C_2H	87.28416	0.013	0.518	40.1	...	...	...	...	...	...
C_2H^b	87.31693	0.128	5.144	40.1	0.042	1.537	36.9	...	...	...

^{b}: blended transitions

Table 2.3: – *continued.*

Molecule	Frequency	IRAS 15194-5115			IRAS 15082-4808			IRAS 07454-7112		
	(GHz)	T_{peak}	$\int Tdv$	Δv	T_{peak}	$\int Tdv$	Δv	T_{peak}	$\int Tdv$	Δv
C_2H^b	87.32862	0.060	2.423	40.1	0.021	0.765	36.9	...	...	...
C_2H^b	87.402	0.077	3.072	40.1	0.021	0.769	36.9	...	...	...
C_2H^b	87.40717	0.028	1.132	40.1	0.009	0.310	36.9	...	...	...
C_2H	87.44651	0.014	0.543	40.1	...	...	...	...	...	...
$H^{13}CCCN$	88.16683	0.028	0.856	44.0	...	...	...	...	...	...
HCN	88.63185	0.506	14.800	56.5	0.437	10.360	43.8	0.141	2.750	35.6
CCCN	89.04559	0.022	0.691	44.0	0.024	0.375	37.8	...	...	...
CCCN	89.06436	0.023	0.667	42.6	0.024	0.603	38.7	...	...	...
HCN	89.08791	...	...	...	0.668	1.130	6.3	...	...	...
$HC^{13}CCN^b$	90.59306	0.043	1.784	74.0	...	...	...	...	...	...
$HCC^{13}CN^b$	90.60179									
HNC	90.66356	0.097	3.221	44.6	0.051	1.430	40.1	0.010	0.321	69.5
SiS	90.77156	0.060	2.050	44.5	0.052	1.640	45.4	0.023	0.457	36.5
HCCCN	90.97899	0.098	3.174	44.4	0.097	2.680	39.1	0.049	0.947	28.4
^{13}CS	92.49427	0.054	1.792	44.6	0.014	0.158	34.1	...	...	...
SiC_2	93.06364	0.066	1.870	42.5	0.045	0.870	38.2	0.024	0.407	31.3
SiC_2	94.24539	0.040	1.080	42.0	0.026	0.605	44.1	0.014	0.200	30.0

^{b}: blended transitions

Table 2.3: – *continued.*

Molecule	Frequency	IRAS 15194-5115			IRAS 15082-4808			IRAS 07454-7112		
	(GHz)	T_{peak}	$\int T dv$	Δv	T_{peak}	$\int T dv$	Δv	T_{peak}	$\int T dv$	Δv
C_4H	95.15032	0.045	1.500	45.0	0.025	0.465	41.6	...	...	...
C_4H	95.18894	0.047	1.570	43.3	0.026	0.540	41.6	...	...	...
SiC_2	95.57938	0.034	1.040	43.1	0.025	0.595	38.0	0.012	0.177	26.2
$C^{34}S$	96.41295	0.025	0.738	43.6	...	...	...	...	...	...
$H^{13}CCCN$	96.983	0.017	0.437	43.3	...	...	...	...	...	...
CS	97.98095	0.306	10.340	42.1	0.208	6.350	41.2	0.101	2.000	28.9
		Band Gap								
unidentified	107.973	0.023	0.342	38.2	...	...	...	...	...	...
$^{13}CN^b$	108.78020									
$^{13}CN^b$	108.78237	0.027	0.610	58.7	...	...	...	...	...	...
$^{13}CN^b$	108.78698									
CCCN	108.83427	0.018	0.510	48.3	0.032	0.528	37.9	...	...	...
CCCN	108.85302	0.026	0.754	47.5	0.027	0.707	36.4	...	...	...
SiS	108.9243	0.045	1.250	44.5	0.048	1.220	35.6	0.031	0.513	29.7
HCCCN	109.17364	0.057	1.920	44.4	0.089	2.480	40.7	0.057	1.120	31.8
^{13}CO	110.20135	0.272	8.540	46.2	0.061	1.360	40.3	0.078	1.620	29.3
CN	113.14419	0.012	0.782	31.4	0.062	1.108	38.5	0.022	0.275	32.9
CN	113.1705	0.052	1.110	43.6	0.055	0.906	39.3	0.044	0.617	28.6
CN	113.19128	0.057	0.743	30.0	0.069	0.906	32.9	0.048	0.642	30.7

^{b}: blended transitions

Table 2.3: – *continued.*

Molecule	Frequency (GHz)	IRAS 15194-5115			IRAS 15082-4808			IRAS 07454-7112		
		T_{peak}	$\int T dv$	Δv	T_{peak}	$\int T dv$	Δv	T_{peak}	$\int T dv$	Δv
CN[b]	113.48812									
CN[b]	113.49097									
CN[b]	113.49964	0.109	4.490	112.5	0.171	7.916	127.4	0.111	3.280	77.6
CN[b]	113.50891									
CN[b]	113.52043									
C_4H	114.18251	0.058	1.530	39.6	0.026	0.602	43.2	...	...	...
C_4H	114.22104	0.067	1.780	42.4	0.030	0.698	43.2	...	...	...
CO	115.2712	0.493	18.670	51.2	0.597	18.850	41.4	0.517	10.520	28.7
SiC_2	115.38239	0.044	1.020	49.0	0.031	0.583	37.8	0.027	0.315	25.9

[b]: blended transitions

Table 2.4: Detected transitions in the PNe sample. Frequencies are given in GHz, the line peak, T_{peak}, is given in K, the integrated intensity, $\int Tdv$, is in K km/s and the full width of the line at the base of the line, Δv, is in km/s. For the CO isotopologues in NGC 6357, the integrated intensity is that of the major peak only due to severe absorption being present in all these profiles. The linewidth of the CO isotopologues is across the whole profile, including the absorption region and secondary peak.

Molecule	Frequency	IC 4406			NGC 6357		
	(GHz)	T_{peak}	$\int Tdv$	Δv	T_{peak}	$\int Tdv$	Δv
$H^{13}CN$	86.34018	0.025	0.357	52.4	0.021	0.330	24.3
HCN	88.63185	0.042	0.900	57.4	0.075	0.872	20.1
HCO^+	89.18853	0.031	0.804	55.3	0.043	0.454	18.1
HNC	90.66356	0.030	0.437	46.3	0.059	0.432	14.3
^{13}CS	92.49427	...	...	...	0.020	0.183	17.5
$C^{34}S$	96.41295	...	...	...	0.027	0.254	17.6
CS	97.98095	...	...	...	0.051	0.522	18.1
	Band Gap						
$C^{18}O$	109.78217	...	...	...	0.066	0.352	49.3
^{13}CO	110.20135	0.030	0.448	53.5	0.396	2.252	45.5
CN[b]	113.14419	0.052	0.316	24.3	...	...	...
CN[b]	113.1705						
CN[b]	113.48812	0.071	2.055	101.8	...	...	...
CN[b]	113.49097						
CN[b]	113.49964						
CN[b]	113.50891						
CO	115.2712	0.162	3.246	51.9	0.501	1.302	52.6

[b]: blended transitions

tion routines that are able to cope with complex models and locate global rather than local minima.

When using PIKAIA, a user must define a fitness function that will be used by the routine to assess how fit the individuals in a population are. PIKAIA will always try to maximise this function. In this work, the fitness function was defined as $1/\chi^2$. A set of n individuals exist in a given population and the routine will run for m generations, where n and m are defined by the user.

In biological systems, the genetic material that makes up an individual is stored in chromosomes. Genes are a portion of a chromosome that control a certain aspect of the physical organism (e.g. hair colour) and an allele is a specific form of that gene (e.g. brown hair, Sivanandam & Deepa 2007). This is implemented in PIKAIA, so the parameters given to an individual in a population are coded into chromosome-like structures made up of 'genes'. For the initial population, the parameters are chosen using a random number generator over the entire X-dimensional parameter space. In subsequent generations, the parameters are constructed from the chromosomes and genes of the parents. The new parameters are formed using a crossover function which splits the chromosomes of the parents in two and substitutes one half of one chromosome from one parent for the corresponding half of another. A mutation may also occur on any given gene changing the parameters of the offspring further, the probability of which is defined by a mutation parameter set by the user. This results in two offspring solutions with a different combination of parameters to the parent solutions and the addition of the mutation inhibits the routine from converging to a local rather than global minima. The likelihood of a given individual solution being used as a parent for further solutions is proportional to its fitness, simulating the survival-of-the-fittest principle.

The reproduction plan chosen for this work was full generational replacement with elitism. This results in every member of the population being replaced every generation and the fittest individual saved with its parameters intact. This elite individual perpetuates through the generations until a fitter solution is created, at which point the elite individual is replaced with the superior individual.

GAs, in addition to their ability to reliably converge to global rather than local minima, have the benefit of being able to run over discontinuous functions as derivatives are not required.

C_2H

C_2H has six detected hyperfine components in IRAS 15194-5115 and four in IRAS 15082-4808. The hyperfine components may be used to constrain the optical depth without making an assumption about the $^{12}C/^{13}C$ isotopic ratio within the source (see Sect. 2.1).

The profiles of C_2H have an unusual appearance due to the lines being partially blended. The individual hyperfine components have square profiles, with the brightest in IRAS 15194-5115 showing a slight horned profile, indicating that C_2H is just resolved in the beam of the telescope and is optically thin. The two-level step profiles are caused by two hyperfine transitions on the verge of blending and the three-step profiles are caused by two square profile transitions with a significant overlap, resulting in excess emission in the central region of the profile.

The assumption about optical depth from the line profile shape can be confirmed using the method of Fuller & Myers (1993), but in contrast to this method's usage in that paper, the line profile is assumed to be a top-hat function rather than a Gaussian distribution.

The optical depth of the transition, τ, is now found using:

$$\tau(v) = \tau \sum a_i \phi_i(v), \tag{2.7}$$

where a_i is the relative intensity of hyperfine component i and ϕ_i is the line profile of hyperfine component i, given by:

$$\phi_i = \begin{cases} 1 & \text{if } (v_0 + v_i - \Delta v) < v < (v_0 + v_i + \Delta v) \\ 0 & \text{otherwise,} \end{cases}$$

where v_i is the offset velocity of component i with respect to the reference velocity, v_0, and Δv is the line half-width. The line may then be fitted using:

$$T(v) = A\left(1 - \mathrm{e}^{-\tau(\mathrm{v})}\right) + C, \tag{2.8}$$

where A is the amplitude and C is a constant to fit for any baseline offset from zero. It should, however, be noted that in the optically thin limit, this equation reduces to $T(v) = A\tau(v) + C$, thus the amplitude and optical depth cannot be separately calculated in this limit.

The hyperfine structure was fitted to Equ. 2.7 and 2.8 using PIKAIA. The results of the fitting are shown in Fig. 2.7. In both cases, the fitting suggests that the transition is optically thin. The resulting integrated intensities of each of the hyperfine components are listed in Table 2.3.

$C^{13}CH$

$C^{13}CH$ has seven hyperfine components which in the spectrum of IRAS 15194-5115, are blended into three line-regions. The same approach as outlined above was applied to the $C^{13}CH$ spectrum and again, the result was found to be optically thin. The results of the fitting are shown in Fig. 2.8. It should be noted, however, that these lines are subject to a low signal-to-noise ratio so the fits are less certain than those of C_2H. The resulting integrated intensities of each of the hyperfine components are listed in Table 2.3.

2.4.2 Detections in individual sources

IRAS 15194-5115

IRAS 15194-5115 had the largest number of detected transitions of all sources in the sample. CO and ^{13}CO both show a sharp peak on the blueshifted edge of the line profile. This is caused by contamination from an interstellar cloud that lies in the same line of sight as IRAS 15194-5115, further details of which can be found in Nyman et al. (1987) and Nyman et al. (1993). When measuring the peak and

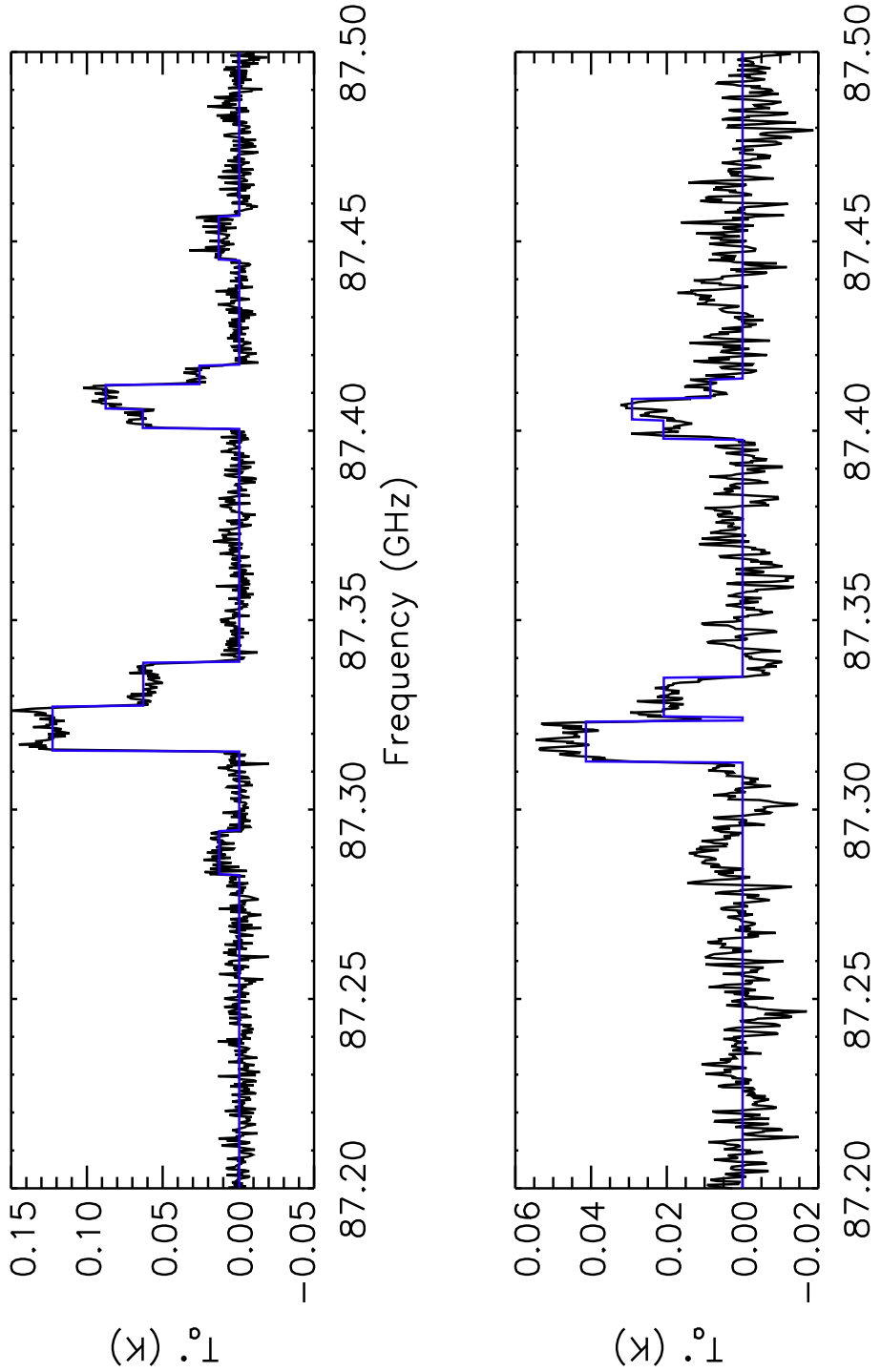

Figure 2.7: C_2H fitted for hyperfine structure. The upper spectrum is that of IRAS 15194-5115 and the lower is that of IRAS 15082-4808. The blue line indicates the best fit to the data.

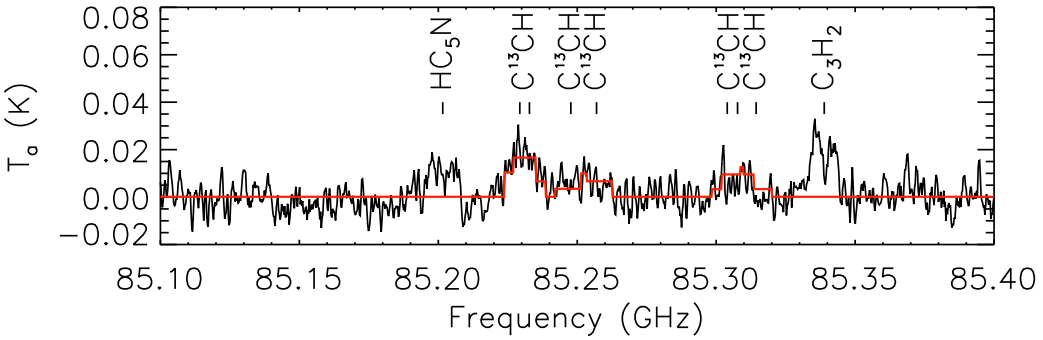

Figure 2.8: $C^{13}CH$ fitted for hyperfine structure in IRAS 15194-5115.

integrated intensities of these lines, the contaminant emission was removed and the line interpolated between the remaining points.

Transitions originating from silicon based molecules (e.g. SiO and SiC_2) have been detected, including the silicon isotopologues of SiO, allowing silicon isotopic ratios to be calculated.

Multiple ^{13}C species were detected in this source including, but not limited to, the ^{13}C isotopologues of HNC, CCH and HCCCN. Emission lines from molecules with a minor isotope of Si or S were also detected.

As explained in Sect. 2.3, the extent of emission and the optical depth of the transitions may be constrained by examining line profiles. CO, for example, has a flat topped parabolic profile with the ^{13}CO counterpart displaying a horned profile, implying optically thick and thin resolved emission respectively.

HCN displays a Gaussian line shape which, as shown in Chapt. 3, can be well modelled by a blend of the three hyperfine components, each having a Gaussian velocity distribution.

IRAS 15082-4808

IRAS 15082-4808 had the second highest number of transitions of the sample. The most unusual detection made is that of the vibrational (v_2=2) HCN maser emission at 89.087 GHz. Ten of these masers, including this detection, have been found to date (Smith, Zijlstra & Fuller 2014; Lucas et al. 1986; Guilloteau, Omont & Lucas 1987; Lucas, Omont & Guilloteau 1988; Lucas & Cernicharo 1989). An in-depth study of this maser can be found in Chapter 3 and in Smith, Zijlstra & Fuller (2014).

The CN line at 113.499 GHz shows interesting structure. The blue shifted part of the spectrum shows a significantly shallower drop than that on the red. This is probably due to a blend of hyperfine lines causing the appearance of a shallower drop. Similarly the HC_3N 109.173 GHz line has this feature, but on the red shifted region of the spectrum and is also likely to be caused by a hyperfine blend.

Isotopologues of a number of species were detected in this source, including the carbon isotopologues of CS, CO and HCN and the sulphur isotopologues of CS.

IRAS 07454-7112

IRAS 07454-7112 has the lowest number of detected transitions in the AGB star portion of the sample. The lines have significantly lower intensities than in the previous two AGB stars. Many of the detected transitions have parabolic shapes and the remainder have too low a signal-to-noise ratio to reliably ascertain the shape of the profile. Despite having similar T_{peak} for CO, HCN and CN lines to the aforementioned stars, neither C_2H nor C_4H were detected down to an RMS noise level of 0.01 K. However, three silicon bearing molecules were detected, including three transitions of SiC_2.

IC 4406

IC 4406 has the lowest number of detections of all of the sample, with transitions from seven species detected. This is to be expected as planetary nebulae are less molecule-rich than AGB stars due to the high levels of ionising radiation.

CO has a double-peaked appearance in this target; the blue-shifted peak is more intense than the red-shifted peak. The spherically symmetric model for line profiles does not hold for this nebula, thus it is difficult to infer information about optical depth and whether or not the nebula is resolved from the line profiles. The variation in line profiles of CO with position on the nebula were mapped by Sahai et al. (1991) and this shows the positional dependence on the profile shape, caused by the different gas and dust movements. The ^{13}CO line shows only the blue-shifted component, explained by its significantly less intense lines and the exact position of the telescope on the source. The integrated intensity of CO in Table 2.4 is the sum of the integrated intensities of the two components.

The remaining transitions also show the double-peaked appearance, although in the isotopologues of HCN and in HCO^+, the red-shifted component is more intense than the blue shifted peak.

NGC 6537

NGC 6537 has transitions from 10 detected species, the most unexpected being that of C^{18}O.

CO shows a significant amount of absorption, although a thin peak due to CO still remains. This is probably due to emission in the off position. Zhang, Sun & Ping (2000) detected CO in NGC 6537 and their observation also shows absorption. The same effect is seen in ^{13}CO and C^{18}O, however more of the line peak can be seen outside of the absorption in these two lines. These absorption features make it impossible to impose useful limits on the carbon and oxygen isotopic abundance ratios. The integrated intensities of these transitions have

been taken as the integrated intensity of the major peak and the line width has been taken as the width of the whole emission-absorption region. These are significantly wider than the other transitions seen in this source.

Two isotopologues of HCN were seen (HCN and $H^{13}CN$) along with HNC. Three isotopologues of CS were detected: CS, ^{13}CS and $C^{34}S$. HCO^+ was also detected.

2.5 Analysis

The analysis carried out on the data consists of the measurement of the rotational temperatures of different species using the population diagram method, the calculation of source-averaged column densities of each species and isotopic ratios from a number of sets of isotopologues. For the following analysis, the antenna temperature has been converted to main beam temperature, assuming an efficiency of 0.49 before the band-gap and 0.42 afterwards. All the constants used in the analysis are listed in Table B.1 and originate from the JPL and CDMS catalogues (Pickett et al. 1998; Müller et al. 2005).

2.5.1 Excitation temperatures: population diagram method

For those species where multiple transitions were detected (excluding hyperfine transitions), it was possible to use the population diagram method, as presented in Goldsmith & Langer (1999) and outlined below, to measure the rotational temperatures of different species. It has been assumed that the excitation temperature can be taken as the rotational temperature in the following analysis.

The population of the upper level of a transition, N_u, can be expressed, assuming local thermodynamic equilibrium (LTE), as:

$$N_u = \frac{N}{Q} g_u \exp\left(-\frac{E_u}{\mathrm{k_B} T_{\mathrm{ex}}}\right), \tag{2.9}$$

where N is the column density of the molecule, E_u is the energy of the upper level, g_u is the statistical weight of the upper level and $T_{\rm ex}$ is the excitation temperature. The partition function, Q is given by:

$$Q = \sum N_i = \sum g_i \exp\left(-\frac{E_{ui}}{\mathrm{k_B} T_{\rm ex}}\right), \tag{2.10}$$

where the sum is over all levels, i.

Thus, rearranging and taking logs of Equ. 2.9 leads to:

$$\ln\left(\frac{N_u}{g_u}\right) = -\frac{1}{T_{\rm ex}}\left(\frac{E_u}{\mathrm{k_B}}\right) + (\ln N - \ln Q), \tag{2.11}$$

which, when plotting $\ln\left(\frac{N_u}{g_u}\right)$ against $\left(\frac{E_u}{\mathrm{k_B}}\right)$, gives a straight line with gradient equal to $-\frac{1}{T_{\rm ex}}$ and y intercept equal to $(\ln N - \ln Q)$. The population of the upper level is given by:

$$N_u = \frac{8\pi \mathrm{k_B} \nu^2 W}{\mathrm{hc}^3 A_{ul}} \left(\frac{\Delta\Omega_a}{\Delta\Omega_s}\right)\left(\frac{\tau}{1-\mathrm{e}^{-\tau}}\right), \tag{2.12}$$

where W is the integrated intensity of the line in K m/s, A_{ul} is the Einstein A coefficient of transition u-l, τ is the optical depth of the transition and $\Delta\Omega_a$ and $\Delta\Omega_s$ are the antenna and source solid angles respectively.

Two assumptions are now made. First, it is assumed that the source fills the beam, thus $(\Delta\Omega_a/\Delta\Omega_s) = 1$. Second, the transition is assumed to be optically thin, meaning $(\tau/(1-\mathrm{e}^{-\tau})) = 1$. The robustness of these assumptions may be tested by studying the line profiles, either from their shapes or directly fitting the lines for optical depth, as described previously. This results in Equ. 2.12 reducing to:

$$N_u = \frac{8\pi \mathrm{k_B} \nu^2 W}{\mathrm{hc}^3 A_{ul}}, \tag{2.13}$$

which may be easily computed and used with Equ. 2.11 to measure the excitation temperature of the molecule.

For some species with hyperfine structure, the input parameters (e.g. A_{ul}) for the population diagram method are available for the overall N or J transition (e.g. HCCCN). In these cases, equation 2.13 may be directly applied, taking W as the total integrated intensity of all hyperfine transitions.

In many cases, the input parameters are only available for the individual hyperfine components. In this case, the method outlined above must be adapted. In this work, this has been carried out in several different ways.

Hyperfine structure: separable

If all hyperfine components of the overall N or J transition have been detected and they are either separated or separable (as is the case for C_2H in IRAS 15194-5115, see Sect. 2.4.1) so the integrated intensities of all individual hyperfine components are known, the population of the upper level can be taken as the sum over all levels:

$$N_u = \frac{8\pi \mathrm{k_B}}{\mathrm{hc}^3} \sum_i \frac{\nu_i^2 W_i}{A_i}, \tag{2.14}$$

where the summation is over all hyperfine levels, i.

If all components are not detected, but those that are detected are separated or separable, the method of calculating the population of the upper level must be adapted to compensate for those components not seen. Thus the upper level population becomes:

$$N_u = \frac{8\pi \mathrm{k_B}}{\mathrm{hc}^3} \frac{1}{\sum a_{i,\mathrm{obs}}} \sum_{i,\mathrm{obs}} \frac{\nu_{i,\mathrm{obs}}^2 W_{i,\mathrm{obs}}}{A_{i,\mathrm{obs}}}, \tag{2.15}$$

with the summations running over all observed hyperfine transitions (i, obs) and $a_{i,\mathrm{obs}}$ are the relative intensities of the observed hyperfine transitions. For this work, the relative intensities of the lines have been taken as the relative intrinsic line strengths, taken from the JPL or CDMS databases and normalised (Pickett

et al. 1998; Müller et al. 2005).

It is important to note that there is a distinct difference between the upper level, u, which is the unsplit upper energy level, and that of the individual hyperfine transitions, i. In cases where E_u, the energy of the unsplit upper level, is not known, the mean of the energies of the upper levels of the hyperfine transitions, $\frac{\sum E_{i,\mathrm{upper}}}{\sum i}$, is taken in its place.

Hyperfine structure: unseparable

For those transitions that are blended to the extent that they cannot be disentangled, yet the required input parameters for the population diagram method are only available for the individual components, a further adaptation is required. It has been assumed that the integrated intensities of the blended transitions are divided amongst their components according to the intrinsic line strength:

$$W_i = W_{\mathrm{blend}} \frac{a_i}{\sum_{j=0}^{n} a_j}, \tag{2.16}$$

where W_i is the integrated intensity of hyperfine component i, W_{blend} is the integrated intensity of the blend of n hyperfine transitions including hyperfine transition i and a_i is the relative intrinsic line strength of hyperfine component i. $\sum_{j=0}^{n} a_j$ is the sum of the intrinsic line strengths of all hyperfine components that make up the blend. The integrated intensities of the individual transitions may now be used in either Equ. 2.14 or 2.15 for those where all hyperfine components or some hyperfine components are detected, respectively.

Resulting excitation temperatures

The calculated excitation temperatures from the population diagram method are given in Table 2.5.

C_4H has been detected in two sources (IRAS 15194-5115 and IRAS 15082-

4808). The hyperfine structure lines are blended, with their relative intensities impossible to determine from the observed blended transition. Therefore the relative intensities were calculated according to Equ. 2.16. Only the major hyperfine components, which make up $\sim$ 99% of the transition intensity have been considered: for example, the N= 9-8, J=$^{19}/_{2}$ – $^{17}/_{2}$ fine line is considered to be split amongst the F=9-8 and F=10-9 components only.

The C_4H emission lines in IRAS 15194-5115 are square in profile, implying the assumption that the transitions are optically thin is valid. However, this also implies that the C_4H emission region is unresolved, although it is unlikely to be highly unresolved as numerous other species display resolved line profile shapes. In the spectra of IRAS 15082-4808, the C_4H lines have a low signal-to-noise ratio which makes it difficult to classify the line profiles. They appear to have noisy square profiles, but this not certain.

Two transitions of HC_3N have been detected in all three AGB stars in the sample: J=10-9 and J=12-11. These lines are each split into three hyperfine components, with a difference of up to 20 kHz in frequency. These are unresolved in all three AGB stars, however Einstein coefficients, upper level energies and statistical weights are available for the overall J=10-9 and J=12-11 transitions, thus alleviating the need to estimate the relative intensities of the unresolved hyperfine lines. In IRAS 15194-5115, the J=12-11 emission line has a square profile, suggesting optically thin, unresolved emission. The J=10-9 profile is less clearly defined, with straight edges but a more curved central region, suggesting this line could be bordering on optically thick and unresolved. Thus the assumptions made for the population diagram may be less robust for this object. The line profile of these HC_3N transitions in IRAS 15082-4808 and IRAS 07454-7112 are parabolic, implying that these lines are optically thick and unresolved. The assumptions previously discussed do not hold for these transitions, thus the derived values should be taken with caution. Additionally, as only two transitions of this molecule are observed, the reliability of this method is also significantly

Table 2.5: Calculated excitation temperatures for a variety of species in Kelvin.

Species	IRAS 15194-5115	IRAS 15082-4808	IRAS 07474-7112
C_4H	77	unphysical	...
HC_3N	14	35	240
$H^{13}CCCN$	5	...	...
SiS	7	10	55
SiC_2	24	62	15
C_3N	31	543	...

decreased. The calculated excitation temperatures are given in Table 2.5 and the column densities derived are given in Table 2.7.

Two transitions of SiS (J=5-4 and J=6-5) were detected in all three of the AGB stars in the sample. These lines have no fine or hyperfine splitting associated with them. The two lines have a relatively square profile shape in IRAS 15194-5115, although they show a degree of asymmetry, implying that these transitions are optically thin. In IRAS 15082-4808, the J=6-5 line has a square profile and the J=5-4 transition has a less clear line profile, with resemblance to both square and parabolic, implying these are likely to be optically thin. Both lines of SiS have parabolic profiles in IRAS 07454-7112, implying that both transitions are optically thick.

Up to four SiC_2 transition lines were detected in the spectra of each of the AGB stars in the sample. The lines in IRAS 15194-5115 and IRAS 15082-4808 appear to all be square, with only the $\sim$ 95 GHz transition in IRAS 15082-4808 potentially being parabolic. The lines in the spectra of IRAS 07454-7112 have too low a signal-to-noise ratio to be clearly classified.

C_3N was detected in two objects in the sample (IRAS 15194-5115 and IRAS 15082-4808) with two transitions. In both cases, the observed line profiles are square. As with C_4H, the lines are blends of unseparable hyperfine components with major components and essentially negligible minor components. Thus the same method for integrated intensity determination has been applied to C_3N as

was applied to C_4H.

2.5.2 Column densities

Two different methods of calculating the column densities of molecules have been applied. These both use the same assumptions: the source fills the beam, the emission is optically thin and LTE applies.

Column densities: population diagram method

Column densities can be calculated from the y-intercept, C, of the population diagram (Equ. 2.11):

$$C = (\ln N - \ln Q)\,, \tag{2.17}$$

where N is the source-averaged column density and Q is the partition function of the molecule. The partition functions have been taken from the Jet Propulsion Laboratory (JPL) database or the Cologne Database for Molecular Spectroscopy (CDMS) via Splatalogue (Remijan, Markwick-Kemper & ALMA Working Group on Spectral Line Frequencies 2007) and are calculated for a variety of excitation temperatures. The partition function evaluated at the closest temperature to that found from the population diagram analysis was adopted for each molecule.

The calculated column densities for all molecules that had population diagrams are shown in Table 2.6.

Column densities: single-line method

Population diagrams, as described above, could not be created for all molecules, thus the column densities were also calculated for all molecules by combining Equ. 2.9 and 2.13:

$$N = \frac{8\pi \mathrm{k_B} \nu^2 W}{\mathrm{hc^3 A}_{ul}} \frac{Q}{g_u} \exp\left(\frac{E_u}{\mathrm{k_B} T_{\mathrm{ex}}}\right), \tag{2.18}$$

Table 2.6: Column densities calculated using the population diagram method. Quoted values are in cm^{-2}. The partition function has been taken at the closest temperature to that found from the population diagram available in the CDMS catalogue.

Molecule	IRAS 15194-5115	IRAS 15082-4808	IRAS 07454-7112
C_4H	3.0×10^{15}	2.3×10^{14}	...
C_3N	1.8×10^{14}	8.1×10^{14}	...
HC_3N	$> 6.8 \times 10^{13}$	$> 2.5 \times 10^{13}$	$> 3.9 \times 10^{13}$
$H^{13}CCCN$	7.9×10^{12}	...	...
SiS	3.9×10^{13}	3.2×10^{13}	1.3×10^{13}
SiC_2	2.5×10^{13}	9.4×10^{13}	1.1×10^{13}

where all parameters are as defined in Sect. 2.5.1. For those molecules which had multiple transitions, the average calculated value was taken. Blended lines and hyperfine transitions were treated in the same fashion as Sect. 2.5.1. If the parameters are available for the overall transition, Equ. 2.18 becomes simply:

$$N = \frac{8\pi \mathrm{k_B}\nu^2}{\mathrm{hc^3 A}_{ul}} \frac{Q}{g_u} \exp\left(\frac{E_u}{\mathrm{k_B}T_{\mathrm{ex}}}\right) \sum_i W_i. \tag{2.19}$$

If parameters are only available for the individual hyperfine transitions, Equ. 2.18 becomes:

$$N = \frac{8\pi \mathrm{k_B}}{\mathrm{hc^3}} \frac{Q}{g_u} \exp\left(\frac{E_u}{\mathrm{k_B}T_{\mathrm{ex}}}\right) \sum_i \frac{\nu_i^2 W_i}{A_i}, \tag{2.20}$$

if all hyperfine components are observed, or

$$N = \frac{8\pi \mathrm{k_B}}{\mathrm{hc^3}} \frac{Q}{g_u} \exp\left(\frac{E_u}{\mathrm{k_B}T_{\mathrm{ex}}}\right) \frac{1}{\sum a_{i,\mathrm{obs}}} \sum_{i,\mathrm{obs}} \frac{\nu_{i,\mathrm{obs}}^2 W_{i,\mathrm{obs}}}{A_{i,\mathrm{obs}}}, \tag{2.21}$$

if only some hyperfine components are observed. The summations run over either all hyperfine transitions, i, or all *observed* hyperfine transitions i, obs.

For the molecules with calculated excitation temperatures from the population diagram, the partition function was taken at the closest temperature to that

calculated in Sect. 2.5.1, barring for C_4H in IRAS 15082-4808 for which a temperature of 37.5 K was assumed. For those without, an excitation temperature was assumed: 18.75 K for IRAS 15194-5115 and 37.5 K for all other sources. These were selected as closest to the mean of the calculated excitation temperatures for each of the AGB stars (excluding outliers) and were simply assumed for the PN as no excitation temperatures could be calculated.

The aforementioned excitation temperatures are given to a higher degree of precision than is realistic for our results from the population diagram analysis. The temperatures have been specified at that level of precision solely due to the fact that the partition functions, available from CDMS, have been calculated at these very specific temperatures. For the effect of the excitation temperature uncertainties on the isotopic ratios and column density calculations, see Sect. 2.6.7.

The results of these calculations are shown in Table 2.7. In general the results from the two methods agree to between 10 and 20%.

2.5.3 Isotopic ratios

Isotopic ratios are most directly measured using observations of optically thin lines. The optical depth can be somewhat constrained by examining the line profiles and making the assumptions described in Sect. 2.3.

The isotopic ratios have been calculated by comparing the source-averaged column densities, calculated using the single-line method in Sect. 2.5.2. The results are shown in Table 2.8.

Carbon isotopic ratios

A number of carbon-bearing species and their corresponding isotopologues were identified in these observations: CO, HCN, HNC, CS, HC_3N, CN and all of their corresponding ^{13}C isotopologues. Additionally, CCH and one of its carbon

Table 2.7: Column densities of all detected species in all sources. Quoted values are in cm^{-2}.

Species	IRAS 15194-5115	IRAS 15082-4808	IRAS 07454-7112	IC 4406	NGC 6357
CO	$> 5.1 \times 10^{16}$	$> 8.6 \times 10^{16}$	$> 4.8 \times 10^{16}$	1.5×10^{16}	...
^{13}CO	5.0×10^{16}	1.2×10^{16}	1.4×10^{16}	4.3×10^{15}	...
HCN	$> 2.2 \times 10^{14}$	$> 2.7 \times 10^{14}$	$> 7.1 \times 10^{13}$	2.3×10^{13}	2.3×10^{13}
H^{13}CN	$> 2.7 \times 10^{14}$	$> 5.0 \times 10^{13}$	3.7×10^{13}	9.8×10^{12}	9.0×10^{12}
HNC	1.5×10^{13}	1.1×10^{13}	2.6×10^{12}	3.5×10^{12}	3.4×10^{12}
HN^{13}C	3.7×10^{12}	...	...	...	...
C_2H	4.1×10^{15}	1.5×10^{15}	...	...	...
C^{13}CH	1.1×10^{15}	...	...	...	...
C_4H	2.9×10^{15}	7.7×10^{14}	...	...	...
C_3N	1.2×10^{14}	8.4×10^{14}	...	...	...
HC_3N	5.8×10^{13}	$> 2.3 \times 10^{13}$	$> 3.8 \times 10^{13}$	...	...
H^{13}CCCN	1.1×10^{13}	...	...	...	...
HC^{13}CCN	1.3×10^{13}	...	...	...	...
HCC^{13}CN	1.3×10^{13}	...	...	...	...
HC_5N	3.8×10^{13}	...	...	...	...
HCO^+	...	...	...	4.1×10^{12}	2.3×10^{12}
CN	1.2×10^{15}	2.9×10^{15}	1.4×10^{15}	6.3×10^{14}	...
^{13}CN	4.3×10^{14}	...	...	...	...

Table 2.7: – *continued*

Species	IRAS 15194-5115	IRAS 15082-4808	IRAS 07454-7112	IC 4406	NGC 6357
CS	$> 1.1 \times 10^{14}$	$> 1.1 \times 10^{14}$	$> 3.6 \times 10^{13}$	...	9.2×10^{12}
^{13}CS	4.2×10^{13}	6.2×10^{12}	...	...	$< 7.2 \times 10^{12}$
C^{34}S	7.9×10^{12}	5.1×10^{12}	...	...	4.6×10^{12}
C_3H_2	2.3×10^{13}	...	...	...	...
SiO	$> 2.8 \times 10^{13}$	$> 1.6 \times 10^{13}$	$> 6.2 \times 10^{12}$	...	...
^{29}SiO	2.4×10^{12}	...	...	...	...
^{30}SiO	1.6×10^{12}	...	...	...	...
SiS	4.2×10^{13}	3.7×10^{13}	$> 1.4 \times 10^{13}$	...	...
SiC_2	4.2×10^{13}	9.3×10^{13}	8.8×10^{12}	...	...

Table 2.8: Isotopic ratios derived from calculated column densities.

Ratio	Species	IRAS 15194-5115	IRAS 15082-4808	IRAS 07454-7112	IC 4406	NGC 6537
$^{12}C/^{13}C$	CO, ^{13}CO	> 1.1	> 7.2	> 3.4	3.5	...
	HCN, $H^{13}CN$	> 0.8	> 5.4	> 1.9	2.4	2.5
	HNC, $HN^{13}C$	4.0	...	...	...	...
	CS, ^{13}CS	>2.6	18.2	...	...	> 1.3
	C_2H, $C^{13}CH$	3.6	...	...	...	...
	HC_3N, H13CCCN	5.3	...	...	...	...
	HC_3N, HC13CCN	4.7	...	...	...	...
	HC_3N, HCC13CN	4.7	...	...	...	...
	CN, ^{13}CN	>2.8	...	...	...	...
$^{32}S/^{34}S$	$C^{34}S$, ^{13}CS	21.5^a	22.0^b	...	...	4^c
	CS, $C^{34}S$	14.2	22.1	...	...	2
$^{28}Si/^{29}Si$	SiO, ^{29}SiO	> 11.5	...	...	...	...
$^{28}Si/^{30}Si$	SiO, ^{30}SiO	> 17.2	...	...	...	...
$^{29}Si/^{30}Si$	^{29}SiO, ^{30}SiO	1.5	...	...	...	...

^{a}: $^{12}C/^{13}C = 4.0$, ^{b}: $^{12}C/^{13}C = 18.2$, ^{c}: $^{12}C/^{13}C$ =2.5

isotopologues, $C^{13}CH$ was identified. The transitions of the second isotopologue, ^{13}CCH, are outside the frequency range of these observations.

For those species with a single isotopologue, such as CO and CS, the isotopic ratio is found by comparing the column densities of the two isotopologues. For those with multiple isotopologues, the isotopic ratio can be determined from each pair and should be equal, assuming there is no formation bias towards one isotopologue. For example, HC_3N has three isotopologues ($H^{13}CCCN$, $HC^{13}CCN$ and $HCC^{13}CN$) and the isotopic ratio may be found by dividing the column density of the ^{12}C-containing isotopologue by each of the column densities of the ^{13}C-containing isotopologues resulting in three $^{12}C/^{13}C$ isotopic ratios.

CO and HCN appear to be optically thick in all the AGB stars in the sample, thus the ratios found from these molecules are lower limits only and, as expected, give the lowest calculated ratios. HNC, HC_3N and C_2H are optically thin in IRAS 15194-5115 and their ratios agree well with one another. ^{12}CS in some cases appeared to be on the borderline between optically thick and optically thin. In IRAS 15194-5115, the measured isotopic ratio is lower from CS than from HNC and C_2H, which would be expected if CS were somewhat optically thick. The hyperfine transitions of CN were, in general, blended making it difficult to identify whether the transitions were optically thick or thin. The calculated carbon isotopic ratio is lower than the ratios found from HNC and C_2H, implying that it is optically thick.

The ratios calculated here are lower than those found by directly evaluating the integrated intensities of the lines, without compensating for the transitions' different Einstein coefficients. For IRAS 15194-5115, for example, the integrated intensity ratios of isotopologues HNC and CS are 5.5 and 5.8 respectively.

Sulphur isotopic ratios

Three isotopologues of CS were detected in multiple sources: $^{12}C^{32}S$, $^{12}C^{34}S$ and $^{13}C^{32}S$. A further two isotopologues were not detected in any of the sample stars:

$^{12}C^{33}S$ and $^{12}C^{36}S$.

Deriving $^{32}S/^{34}S$ can be done in two ways with the detected transitions: by comparing the integrated intensities of the $^{12}C^{32}S$ and $^{12}C^{34}S$ lines or by dividing the integrated intensity of $^{13}C^{32}S$ with that of $^{12}C^{34}S$ and multiplying by the carbon isotopic ratio of the source.

$^{12}C^{34}S$, where detected, has an optically thin profile. $^{12}C^{32}S$, however, showed a borderline optically thick/thin profile. In IRAS 15082-4808, both methods give consistent ratios of approximately 22 for $^{32}S/^{34}S$. In IRAS 15194-5115, the ratios differ by a factor of ~ 1.5, suggesting that CS is indeed optically thick in this star.

All three CS isotopologues were detected in NGC 6537. $^{32}S/^{34}S$ was measured to be 2 and 4 from the two aforementioned methods, which is significantly lower than those of the AGB stars. However, the minor isotopologues had low signal-to-noise ratios and therefore these values should be taken with caution.

Silicon isotopic ratios

^{28}SiO, ^{29}SiO and ^{30}SiO have been detected in IRAS 15194-5115. ^{28}SiO has a clear parabolic profile, meaning only lower limits can be derived for ^{28}Si ratios. ^{29}SiO and ^{30}SiO showed square profiles and are thus optically thin. The measured $^{29}Si/^{30}Si$ ratio (1.5) is consistent with the Solar value.

Oxygen isotopic ratio

Although $C^{18}O$ was detected in NGC 6537, oxygen isotopic ratios cannot be calculated due to the strong absorption features present in the spectrum that almost entirely block the emission from the nebula.

2.6 Discussion

2.6.1 Emission extent

From the observed line profiles, limits can be placed on the extent of the emitting regions. For example, the line profile of CO in IRAS 15194-5115 has a flattened parabolic profile (neglecting the contaminant emission) and ^{13}CO has a double-peaked profile, both of which imply resolved emission. Assuming a distance of 1 kpc to IRAS 15194-5115, the beam (33″) resolves an area with radius 3.0×10^{17}cm, putting a lower limit on the CO emission region. The limit is dependent on the distance to the source used. Assuming a distance of 600 pc, the radius of the area subtended by the beam reduces to 1.6×10^{17}cm and if a distance of 1.2 kpc is assumed, this radius increases to 3.2×10^{17} cm. González Delgado et al. (2003) report the CO photodissociation radii for a sample of 12 M-type AGB stars to vary between 1.7×10^{16} and 2.4×10^{17} cm which agrees well with our calculated values, despite IRAS 15194-5115 being a C-type AGB star.

A number of other molecules, including HC_3N, SiO and their isotopologues, show unresolved profiles, implying that their emission region is smaller than that of CO. The upper level energies of the resolved transitions (molecules: CO, ^{13}CO, C_2H and likely CN and CS) are less than 5 K, whereas the upper level energies of the unresolved emission lines are, as expected, higher.

2.6.2 Excitation temperatures

Rotation temperatures were determined for up to six molecules in the AGB star portion of the sample. IRAS 15194-5115 has six measured rotation temperatures. These range from 5 K for H^{13}CCCN to 77 K for C_4H. Woods et al. (2003) determine rotation temperatures for this source as part of their molecular line survey using data obtained on the Swedish-ESO Submillimeter Telescope (SEST) and the Onsala Space Observatory (OSO) 20 m telescope. Of the eight molecules

that they were able to measure rotation temperatures for, three also appear in our results: $H^{13}CCCN$, HC_3N and SiS. Our results agree to better than 3 K for HC_3N and agree to within 1 K for SiS and $\sim$2 K for $H^{13}CCCN$. Our calculated temperature for SiC_2 agrees well with the average result obtained for their AGB star sample (24.4 K). The determined temperature of C_3N (31 K) has reasonable agreement with SiC_2. C_4H, however, is a little higher at 77 K.

Woods et al. (2003) have also measured rotation temperatures in the remaining two sources of our AGB sample. Our obtained value for the rotation temperature of SiS agrees to within 5 K in IRAS 15082-4808, however our calculated value for IRAS 07454-7112 is a factor of 10 higher than that measured in Woods et al. (2003). Additionally, our measured value of SiC_2 is $\sim$25 K higher in IRAS 15082-4808 than that measured by Woods et al. (2003). These differences could be caused by the different methods used to obtain the rotation temperatures or could be an effect of the different beam sizes of the telescopes used to obtain the data: Mopra has a beam size of $36''\pm3$ at 86 GHz while SEST and OSO 20 m had $57''$ and $44''$ respectively at the time of observation.

HC_3N in IRAS 15082-4808 and both HC_3N and SiS in IRAS 07454-7112 appear to be optically thick. This results in the underestimation of the upper level populations and will also have an effect on the rotation temperature derived if the optical depth of the transitions varies with upper level energy.

The calculated excitation temperature of C_4H is unphysical (negative) in IRAS 15082-4808. This temperature has therefore not been used in subsequent analyses.

2.6.3 Source-averaged column densities

Source-averaged column densities have been calculated in each source for up to 27 different molecules. Two methods were used: the population diagram method and a direct calculation. The results were consistent with one another for those molecules that could have both methods applied. The AGB stars in the sample

have higher numbers of molecular species detected on average than those of the planetary nebulae in the sample. This is typical for PNe in comparison to AGB stars due to the high levels of ionising radiation which dissociate many molecular species in the nebulae.

In the work of Ali (2006), a number of molecular column densities are predicted from gas phase models of IRAS 15194-5115. Our calculated abundances for CN, HNC, SiC_2, C_3H_2 and HC_5N agree to within a factor of two of those predicted by the models of Ali (2006). The abundance limits of molecules such as CS and HCN, whose transitions are optically thick, agree as far as is possible to discern, to the models of Ali (2006). Our measured abundance of SiS is two orders of magnitude lower than the predicted value. The abundance of HC_3N is a factor of 100 higher than the predictions of Ali (2006), but more in-line with the measured column densities of HC_3N in IRC+10216 by Woods et al. (2003).

In general, the column densities of the AGB star sample are broadly similar, with differences of up to a factor of 3 between sources. Notably, IRAS 07454-7112 had no detections of C_2H, C_4H and C_3N, despite the column densities of the detected species being very similar to those of IRAS 15082-4808 and IRAS 15194-5115.

Edwards & Ziurys (2013) have studied NGC 6537 in-depth in similar frequency ranges to those observed here and use the non-LTE RADEX code to analyse the data. Our column densities for HNC agree to within 20% of that found by Edwards & Ziurys (2013). However, our HCN and $H^{13}CN$ are higher than their calculated column densities by a factor of 4, although the ratio of the two agrees to within 4%. As the CO isotopologue regions of the spectra included contaminant absorption, it was impossible to calculate column densities for these molecules. The work of Edwards & Ziurys (2013) does not mention suffering from contamination, although the data in this region is not shown.

Cox et al. (1992) have studied abundances of IC 4406 relative to HCN. Assuming all species are present over the same region, we can compare our source-

averaged column densities to those abundances reported in Cox et al. (1992). Our relative abundance of HNC to HCN is approximately consistent with that found in Cox et al. (1992). However the relative abundances of CO, CN and HCO^+ differ from those measured by Cox et al. (1992) by factors of 2, 1.5 and 3 respectively. This may be due to the different extents of the emission regions or due to the observations having been taken from a different region of the nebula as the strength and profile of the lines has been shown to vary across the nebula.

Despite the carbon-rich molecular species and the lack of oxygen-rich molecular species detected in both planetary nebulae in the sample, the ionised regions have both been reported as being oxygen-rich, with C/O ratios of 0.79 (IC 4406, Delgado-Inglada & Rodríguez 2014) and 0.95 (NGC 6537, Pottasch, Beintema & Feibelman 2000).

2.6.4 Isotopic Ratios

A number of isotopic ratios have been calculated for the sample, assuming each of the molecular isotopologue column density ratios is equal to the overall elemental isotopic ratio. Only lower limits could be applied to IRAS 07454-7112 due to the lack of detected ^{13}C species, suggesting that this source has the highest $^{12}C/^{13}C$ of the sample. IRAS 15082-4808, however, has been found to have a $^{12}C/^{13}C$ ratio of 18.2 from CS, and significantly lower limits from HCN and CO isotopologues. This puts this carbon-rich AGB star above the threshold for a J-type star.

Both of the observed planetary nebulae are oxygen-rich. Their $^{12}C/^{13}C$ have been measured in this work at 2.4 and 2.5 from HCN isotopologues in IC 4406 and NGC 6537 respectively. The value for NGC 6537 agrees to within 4% of that reported by Edwards & Ziurys (2013). These isotopic ratios are lower than those of other planetary nebulae (e.g. Balser, McMullin & Wilson 2002) as well as those of the oxygen-rich AGB stars reported by Milam, Woolf & Ziurys (2009). As these values are below the equilibrium value of the CNO cycle (3-4), it is likely

that they are lower limits.

IRAS 15194-5115 had the largest number of isotopologues detected and thus had the largest number of isotopic ratios calculated. The $^{12}C/^{13}C$ ratios are consistent across HNC, C_2H and CS at 3-4. The value derived from HC_3N and its isotopologues is approximately 5, which is higher, but not drastically dissimilar. The limits ascertained for CO and HCN are lower than these values, thus are also consistent. The $^{12}C/^{13}C$ as derived from CN isotopologues, however, is only 2.8. The transitions of CN used are blended, with the contributions from the individual hyperfine components impossible to ascertain, thus neither the line profiles nor the hyperfine structure ratios could be examined to constrain the optical depth. It is plausible this low ratio is due to the CN transitions being optically thick or due to the assumptions made whilst disentangling the hyperfine structure not being sufficiently robust. Due to the clarity of the line profiles and robustness of the optically thin assumption, the HNC and C_2H ratios are the most reliable indicators of $^{12}C/^{13}C$ in IRAS 15194-5115.

In addition to carbon isotopic ratios in IRAS 15194-5115, silicon and sulphur isotopic ratios were determined. Due to the high optical depth of ^{28}SiO, only limits could be placed on the $^{28}Si/^{29}Si$ and $^{28}Si/^{30}Si$. However, both ^{29}SiO and ^{30}SiO appear to be optically thin. The resulting $^{29}Si/^{30}Si$ of 1.5 is exactly in agreement with Solar. Peng et al. (2013) measures the $^{29}Si/^{30}Si$ in 15 oxygen-rich AGB stars and finds the sample have values that are either ~ 1.5 or lower. Few carbon-rich $^{29}Si/^{30}Si$ ratios are reported in the literature, due to the low intensity of the ^{29}SiO and ^{30}SiO emission lines. The $^{29}Si/^{30}Si$ has been reported by Cernicharo, Guélin & Kahane (2000) to be 1.45 ± 0.13 and by He et al. (2008) to be 1.46 ± 0.11 in IRAS 15194-5115. It is currently uncertain as to whether Si isotopic ratios are affected throughout the life of an AGB star. Discussions on this topic can be found in Zinner et al. (2006) and Decin et al. (2010).

$^{32}S/^{34}S$ ratios were calculated for both IRAS 15194-5115 and IRAS 15082-4808 using two methods: directly from CS and $C^{34}S$ and indirectly using the $^{12}C/^{13}C$

already calculated along with ^{13}CS and C^{34}S. In IRAS 15082-4808, both methods yield a value of 22, the Solar value. The results from IRAS 15194-5115 from the indirect method are almost 50% greater than that found using the direct method. This suggests that the CS line is optically thick - which is also suggested by the line profile. As both ^{32}S and ^{34}S are primarily produced by high mass stars in supernovae and the ^{32}S/^{34}S has remained approximately constant at the Solar ratio for the last 7 Gyr (Hughes et al. 2008), this almost-Solar ratio in both AGB stars is expected.

2.6.5 Evidence for mixing processes

Karakas (2010) has published updated stellar yields from evolutionary models. The results include the average mass fractions of various species in the stellar wind which, as is reported, are suitable for comparison with planetary nebula abundances. These models use metallicities of Z=0.02 (Milky Way metallicity), Z=0.008 (Large Magellanic Cloud metallicity), Z=0.004 (Small Magellanic Cloud metallicity) and Z=0.0001. The ^{12}C/^{13}C ratio varies between 4 and 23000 depending upon initial mass and metallicity. At Solar metallicity, ^{12}C/^{13}C ratios of less than ten are only found in the higher mass progenitors: $M_{star} \geq 5$ $M_{\odot}$.

NGC 6537 has been reported in the literature as having a core mass of 0.7-0.9 $M_{\odot}$ and a probable progenitor mass of 3-7 $M_{\odot}$ (Matsuura et al. 2005). Its C/O ratio has been found to be 0.95 (Pottasch, Beintema & Feibelman 2000). The 5 $M_{\odot}$ model of Karakas (2010) with Z=0.02 is oxygen rich (C/O = 0.7) and has a ^{12}C/^{13}C ratio of 6. The final mass of the star is 0.879 $M_{\odot}$. These parameters have reasonable agreement with the measured values of NGC 6537, both in this work and the literature (e.g. Edwards & Ziurys 2013). This model includes hot bottom burning (HBB) but no partial mixing zone (PMZ). This suggests that in NGC 6537, hot bottom burning was present, in agreement with the findings of Edwards & Ziurys (2013).

The carbon isotopic ratios of IC 4406 are less reliable than that of NGC 6537 due to the low signal-to-noise ratio of the ^{13}C species transitions; Josselin & Bachiller (2003) report ^{12}C/^{13}C=23. The post-AGB mass has been estimated by Sahai et al. (1991) to be between 0.6 and 0.76 $M_{\odot}$, requiring a lower mass progenitor than for NGC 6537. The low-mass progenitor models (1.5-2 $M_{\odot}$) of Karakas (2010) at Z=0.02 result in ^{12}C/^{13}C of 22 with no HBB or PMZ present and a final mass of 0.6-0.64 $M_{\odot}$. This implies our carbon isotopic ratio is likely a lower limit and that the star did not undergo HBB.

2.6.6 J-type stars and A+B grains

J type stars, those characterised by ^{12}C/^{13}C < 10, have been suggested as a potential origin of the SiC presolar A+B grains (Zinner et al. 2006). The A+B grains have low ^{12}C/^{13}C, a trend between the Si isotopes (known as the Si MS line on a plot of δ^{29}Si against δ^{30}Si[4], with equation: $\delta^{29}\text{Si} = -20 + 1.37 \times \delta^{30}\text{Si}$, Hoppe et al. 2010) and more varied S isotopic ratios, but still centred on Solar. The silicon isotopic ratio plot from Zinner (2003) can be found in Fig. 2.9.

IRAS 15194-5115 has been measured to have a low carbon isotopic ratio, of ~ 4 from column densities of HNC and C_2H, in line with the values obtained from A+B grains. The silicon ratios are difficult to assess due to the ^{28}SiO transition being optically thick. The ^{32}S/^{34}S ratio is also in line with that found in A+B grains (Hoppe et al. 2010; Zinner et al. 2006). This evidence suggests that this probable J-type star could be an example of the class of object from which the A+B grains originate. SiC has been detected in the *ISO* spectra of a number of carbon stars (Yang, Chen & He 2004) and the presence of SiC dust in this star's *ISO* spectra will be discussed further in Chapt. 4.

[4] $\delta^{i}\text{Si} = 1000 \left(\frac{^{i}\text{Si}/^{28}\text{Si}}{^{i}\text{Si}_{\odot}/^{28}\text{Si}_{\odot}} \right)$ (Decin et al. 2010)

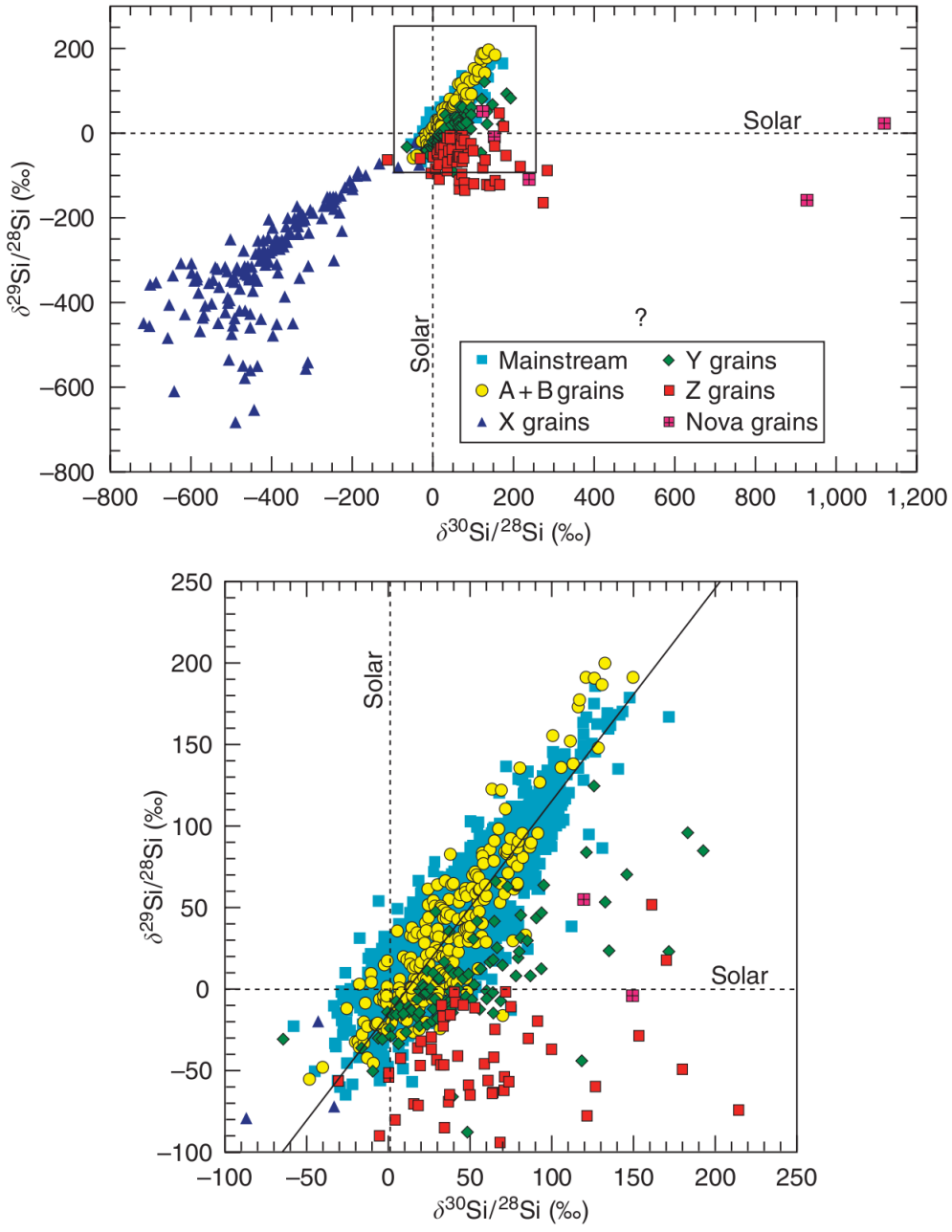

Figure 2.9: Silicon isotopic ratios in SiC presolar grains from Zinner (2003). Grain origins are the same as in Fig. 2.1.

2.6.7 Uncertainty considerations

A number of assumptions have been made in the analysis within this chapter and these assumptions dominate the uncertainties of the results. Some of these may be quantified, others may not. The first is the assumption of optical depth. This has been tested by examining the shape of the line profiles or, when sufficiently resolved hyperfine structure exists, the lines have been fitted to accurately constrain this. Any value obtained from a transition deemed likely to be optically thick is listed as a lower limit to the column density.

The assumption that the source fills the beam can also be tested by examining the line profiles. Some lines show resolved profiles and others show unresolved profiles, indicating that the emission regions in each case should not deviate too far from a beam filling factor of 1. Therefore the assumption that the beam filling factor is unity should not contribute significantly to the uncertainties on the calculated column densities.

Excitation temperatures have been assumed for the majority of the molecular species. In some cases these were taken as the closest temperature for which a published partition function exists to the temperature resulting from the population diagram analyses. These temperatures are uncertain as many are obtained from only two or three transitions. Looking at the rotation temperatures as a whole, two outliers exists (543 K and 240 K) and the remainder lie within the range 5-77 K. Taking CO as an example: the calculated column density deviates from the value at 37.5 K by factors of 2.5 and 3.5 when the temperature is changed to 5 K and 150 K respectively. Across all molecules, the uncertainty due to the temperature can generally be taken as a factor of 3.

The remaining assumptions are difficult to quantify, but we estimate that overall the column densities are accurate to a factor of 6. As the isotopic ratios are dependent upon the column densities, we expect the uncertainties of the isotopic ratios to be similar to those of the column densities.

2.7 Conclusions

Presented here are the results of a molecular line survey, covering the frequency range 80.5-115.5 GHz, carried out over a sample of five targets: three carbon-rich AGB stars and two oxygen-rich planetary nebulae. The data was obtained from the Mopra Telescope, Australia.

68 individual transitions were identified in the data, emanating from 27 different molecular species. The hyperfine structures of C_2H and $C^{13}CH$ were fitted according to the model of Fuller & Myers (1993) to measure the optical depth and the contribution to the integrated intensity of the blended lines from the individual hyperfine components. Rotation temperatures were calculated for those species with multiple detected transitions using the population diagram method (Goldsmith & Langer 1999). Source-averaged column densities were calculated using both the population diagram method and a direct calculation using a single transition. We have also detailed the method used to calculate the column densities of species with resolvable and unresolvable hyperfine structure.

From the calculated column densities, carbon, silicon and sulphur isotopic ratios have been determined, where detections allow, for the sample. This includes $^{32}S/^{34}S$ and $^{29}Si/^{30}Si$ ratios of the probable J-type star, IRAS 15194-5115. This probable J-type star has been shown to exhibit isotopic ratios in-line with those expected for the source of the A+B presolar grains.

Chapter 3

A new HCN maser in IRAS 15082−4808

The work in this chapter has been published in Smith, Zijlstra & Fuller (2014).

3.1 Introduction

Masers are found in a wide variety of astrophysical environments, both Galactic and extra-Galactic, and are a unique tool in the investigation of the dynamics, composition and structures found within these regions. OH and H_2O masers, for example, are found in active galactic nuclei (AGN) and luminous infrared galaxies tracing accretion disks, radio jets and winds of an AGN (e.g. Lo 2005 and references therein). In star formation regions, masers can be used to probe outflows and disks as well as shocked regions of gas (Caswell, Vaile & Forster 1995; Fish 2007).

Masers can also be used to study the circumstellar envelopes of evolved stars and planetary nebulae, with the chemistry and composition of the source dictating the observable species of maser. For instance, there are three types of maser often found in the circumstellar envelopes of oxygen-rich asymptotic giant branch (AGB) stars, namely SiO, H_2O and OH molecular transitions. In contrast, only

one species of maser is commonly found in carbon-rich AGB stars. CO has been found to mase rarely, despite its high abundance in circumstellar envelopes. HCN, on the other hand, has been observed to mase in many different transitions (Guilloteau, Omont & Lucas 1987; Schilke & Menten 2003; Shinnaga et al. 2009).

These masers allow us to probe very specific regions of the circumstellar envelopes of the AGB stars in which they reside. SiO masers trace regions close to the star that are under the influence of stellar pulsational shocks and magnetic fields (Assaf et al. 2013; Pérez-Sánchez & Vlemmings 2013), whereas H_2O masers (at 22 GHz) are found outside the dust formation zone and OH masers are found further still from the host star (Cotton, Perrin & Lopez 2008). The 89.087 GHz HCN maser is thought to be formed in a small region close to the inner boundary of the circumstellar envelope of the host star, similar to the SiO masing region, due to the J=1-0 F=2-1 v=2 level lying 2050 K above the ground state and the maser spectral profiles' blue-shifted nature (Goldsmith et al. 1988; Pérez-Sánchez & Vlemmings 2013). The HCN J=1-0 F=2-1 v_2=2 (one of the hyperfine transitions of the J=1-0 transition of the second overtone of the doubly degenerate bending mode) 89.087 GHz maser therefore traces the region of the envelope which is currently undergoing acceleration. Having such a tracer is a useful tool in assisting in the understanding of envelope dynamics and wind acceleration.

To date, nine HCN 89.087 GHz masers have been detected in carbon-rich AGB stars (Lucas et al. 1986; Guilloteau, Omont & Lucas 1987; Lucas, Omont & Guilloteau 1988; Lucas & Cernicharo 1989). A number of these have been shown to vary on month-long time-scales, with some masers being completely undetected in subsequent observations and others having a change in line profile or intensity (Lucas, Omont & Guilloteau 1988).

In this chapter, we present a new detection of the 89.087 GHz HCN maser in IRAS 15082−4808, along with an investigation of maser intensity variation with stellar pulsational period.

IRAS 15082−4808, also known as AFGL 4211, is a mass losing, carbon-rich AGB star. This source has been part of a number of line surveys (e.g. Nyman & Olofsson 1995; Woods et al. 2003). Its mass loss rate has been measured at approximately 1×10^{-5} $M_{\odot}$ yr^{-1}(Groenewegen et al. 2002). The literature values for the distance to this star vary between 640 pc and 1500 pc. However the general consensus is between 640 pc and 850 pc (Woods et al. 2003; Nyman & Olofsson 1995).

3.2 Observations

3.2.1 Mopra 2010

The observations of IRAS 15082−4808 were taken using the 22 m Australia Telescope National Facility (ATNF) Mopra telescope, 450 km from Sydney, Australia, between the 18th June 2010 and the 27th June 2010 as part of the molecular line survey detailed in Chapt. 2.

The 3 mm Monolithic Microwave Integrated Circuit receiver (MMIC) coupled with the Mopra Spectrometer (MOPS) in broadband mode were used, and covered the frequency range 84.5 to 92.5 GHz over four overlapping 2.2 GHz intermediate frequency bands (IFs). The IF of interest covered the range 88.5-90.5 GHz, putting this maser, at 89.087 GHz, more than 500 MHz from the edge of the band. The beam size at 90 GHz is 38″ and the antenna efficiency is ~ 0.5. The sensitivity of Mopra at 86 GHz is 22 Jy/K[1].

The observations were reduced using the ATNF Spectral Analysis Package (ASAP). Observations that were affected by poor observing conditions were identified and subsequently removed. The remaining sets of observations were averaged (weighted by the system temperature, $T_{\rm sys}$) and a polynomial baseline was fitted. The total integration time was 3 hours and the velocity resolution was

[1] *Technical summary of the Mopra radiotelescope* (2005), www.narrabri.atnf.csiro.au/mopra/mopragu.pdf

0.91 km/s. The rms noise of the resulting spectrum was 0.015 K in units of corrected antenna temperature and the $T_{\rm sys}$ was 189 K. The spectra were inspected and lines identified using the Splatalogue and National Institute of Standards and Technology (NIST) databases (Lovas 1992; Markwick-Kemper, Remijan & Fomalont 2006).

3.2.2 Literature and archive data

Following the identification of the HCN maser emission line in the Mopra 2010 data, the literature and archives were searched for additional sets of observations of IRAS 15082−4808 in the required frequency range. Two sets of observations were found. The first were observations taken in August 1993 as part of the molecular line survey by Woods et al. (2003) using the Swedish-ESO Submillimeter Telescope (SEST, Booth et al. 1989) with an rms noise level 0.014 K (main beam temperature units) and a spectral resolution of 2.4 km/s. The sensitivity of SEST at 86 GHz is 25 Jy/K[2]. The second were observed in June 2011 and are publicly available data from the Mopra archive.

The reduction of the SEST data is described in Woods et al. (2003). The Mopra archive data was unpublished at the time of this investigation, so the raw data files were taken from the Australian Telescope Online Archive and reduced in an identical manner to the Mopra 2010 data. The total integration time was 2.4 hours. The rms noise of the Mopra 2011 spectrum is 0.006 K in units of corrected antenna temperature, $T_{\rm sys}$ is 157 K and the velocity resolution is 0.91 km/s.

The maser was detected in the Mopra observations from 2010 and 2011 but was not detected in the SEST observations from 1993. All resulting spectra are shown offset in Fig. 3.1. The maser line profile has varied significantly over the course of a single year, as is common for masers, going from an intense peak

[2] *SEST parameters* (1990), www.apex-telescope.org/sest /html/telescope-instruments/telescope/index.html

with a secondary component in 2010 to a significantly less intense peak with only a single detected component. Lucas, Omont & Guilloteau (1988) discuss the variability of this maser transition and indicate that it could be related to the pulsational period of the star as is the case with SiO masers (Alcolea et al. 1999).

3.3 Analysis

3.3.1 Velocity

The maser in IRAS 15082−4808 is non-Gaussian in profile, with the Mopra 2010 observation having two distinct components. The HCN J=1-0 v=2 line is split into three hyperfine components: F=1-1 at 89.086 GHz, F=2-1 at 89.087 GHz and F=0-1 at 89.090 GHz. In order to identify whether the two components of the maser line are as a result of kinematic effects or multiple hyperfine components being observed, the velocities of the two peaks were compared with the theoretical separation of the hyperfine components of the J=1-0 v=2 transition. The velocities of the two observed components in the profile are taken at their respective peak values without fitting due to the maser line being unresolved. The major and minor components are separated by 2.7±1.2 km/s which is significantly smaller than the separation between the hyperfine components of the HCN J=1-0 v=2 line which lie at separations of 5.02 km/s (between F=1-1 and F=2-1) and 7.46 km/s (between F=2-1 and F=0-1). Therefore, the double-peaked line profile is unlikely to be caused by a second masing hyperfine component, and it is more likely that it is caused by intrinsic motion of the masing molecules within the circumstellar envelope.

The HCN 89.087 GHz maser has been observed in nine other sources to date, which are listed in Table 3.1 along with this new source, IRAS 15082-4808. The 89.087 GHz maser is blue-shifted by up to 5 km/s with respect to the host star in all nine previously known sources (Guilloteau, Omont & Lucas 1987; Lucas,

Table 3.1: Known HCN 89.087 GHz maser sources with CO expansion velocities from Groenewegen et al. (2002) and maser velocity parameters taken from Lucas, Omont & Guilloteau (1988) and Guilloteau, Omont & Lucas (1987). Mass-loss rates are taken from the reference listed in column 7. Velocity offset is defined as the difference between the velocity of the maser and the velocity of the shell with a negative value indicating a blue-shifted maser. In cases where the maser has multiple components, the velocity of the major component has been used. The number of detections is the number of observations of the maser, excluding null detections. The period of pulsation is that derived from fitting the photometric data, as described in Section 3.3.3.

Source	V_{exp} (km/s)	Velocity offset (km/s)	No. detections	Period (days)	$\dot{M}$ ($M_\odot$/yr)	Reference
CIT 6	17.5	−5	7	637	6.5×10^{-6}	1
IRC +10216	15.4	−3	4	647	3.3×10^{-5}	1
S Cep	22.5	−3.1	2	484	2.9×10^{-6}	1
FX Ser	28.4	−1.1	2	531	3.1×10^{-5}	1
IRC +50096	15.9	−0.2	1	544	5.9×10^{-6}	1
AFGL 2513	25.6	−3.6	1	592	2.05×10^{-5}	2
AFGL 2047[a]	17.1	−4.6	1	631	8.6×10^{-6}	3
IRC +30374	24.4	−0.8	1	587	1.0×10^{-5}	4
T Dra	16.8	−0.7	1	424	8.2×10^{-6}	1
IRAS 15082−4808	20.4	−2.0	2	647	1.0×10^{-5}	5

[a] Shell velocity taken as the mean of the central velocities of the CO(1-0) and HCN(1-0) lines from Nguyen-Q-Rieu et al. (1987).

References: 1. Bergeat & Chevallier (2005), 2. Guandalini et al. (2006), 3. Loup et al. (1993), 4. Schöier, Olofsson & Lundgren (2006), 5. Woods et al. (2003).

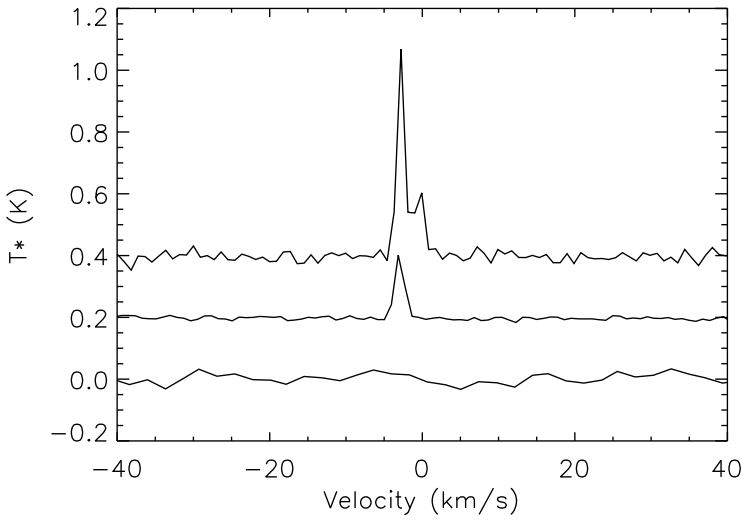

Figure 3.1: HCN 89.087 GHz maser observations at three epochs. Velocity denotes the offset from LSR velocity in the frequency frame of the HCN maser. The upper spectrum shows the observation made in 2010 with Mopra, the middle spectrum shows the observation made in 2011 with Mopra and the lower spectrum shows the observation made in 1993 using SEST and is in units of main beam temperature. The Mopra observations are in units of corrected antenna temperature and the efficiency of Mopra at this frequency is ∼0.5. The sensitivities of Mopra and SEST at 86 GHz are 22 Jy/K[1] and 25 Jy/K[2] respectively.

Omont & Guilloteau 1988; Lucas & Cernicharo 1989).

To compare the velocity shift of the maser in IRAS 15082−4808 to those observed in the other nine sources, we have taken the ground state, non-masing HCN 88.631 GHz (J=1-0, F=2-1) emission line, also observed as part of the larger observing programme mentioned in section 3.2.1, as reflecting the systemic velocity of the envelope as done by Lucas, Omont & Guilloteau (1988). However, the line observed at this frequency at Mopra in the configuration described previously, is a blend of the hyperfine components of HCN: F=2-1, F=1-1 and F=0-1. These components must therefore be fitted in order to derive an accurate systemic velocity.

Using the methodology of Fuller & Myers (1993), we assume that the velocity profile is well-described by a Gaussian distribution, and thus the optical depth

as a function of velocity, $\tau(v)$, of the J=1-0 transition can be expressed as:

$$\tau(v) = \tau \sum_{i=1}^{3} \mathrm{a}_i \exp\left(-\frac{(v - v_0 + v_i)^2}{2\sigma^2}\right), \tag{3.1}$$

where τ is the total optical depth of the transition, a_i is the relative intensity of transition i, σ is the dispersion and v_i is the offset velocity of transition i with respect to a reference velocity, v_0, taken as the velocity of the central hyperfine component. The line profile can then be determined from:

$$T(v) = A(1 - \mathrm{e}^{-\tau(v)}) + C, \tag{3.2}$$

where $T(v)$ is the temperature as a function of velocity, A is the amplitude and C is a constant to fit for any baseline offset that may exist.

The above function was fitted to the data using a hybrid method, based upon the use of the genetic algorithm PIKAIA (Charbonneau 1995) followed by the non-linear least squares fitting routine, MPFIT (Markwardt 2009). The uncertainties on the fitted parameters were calculated by the latter from the covariance matrix. The result of the fitting is shown in Fig. 3.2 and gives the velocity of the central hyperfine component with respect to LSR velocity to be -0.76 ± 0.06 km/s.

The velocity of the major observed component of the maser is offset with respect to the systemic velocity by -2.0 ± 0.9 km/s (blue-shifted) and the minor component is offset with respect to the systemic velocity by $+0.7 \pm 0.9$ km/s (red-shifted).

3.3.2 Maser pumping

The velocity by which the maser line in IRAS 15082−4808 is blue-shifted is significantly less than the expansion velocity of the envelope (20.4 km/s, Groenewegen et al. 2002). This suggests that the maser is formed in a distinct region of gas below the wind acceleration zone. The red-shifted component of the maser in IRAS

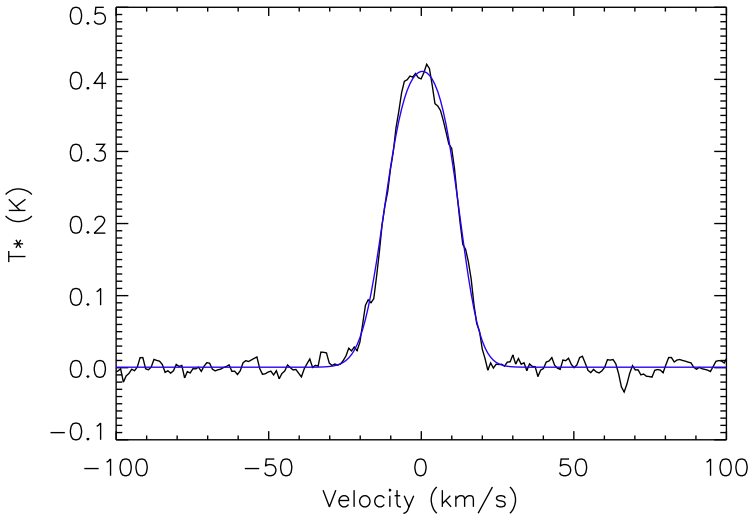

Figure 3.2: HCN 88.631 GHz line as a blend of the F=2-1, F=1-1 and F=0-1 hyperfine components and the best-fit to the data is shown in blue. Velocity denotes the offset from LSR velocity in the frequency frame of the HCN 88.631 GHz line. T* is the corrected antenna temperature and the efficiency of Mopra at this frequency is ∼0.5. The sensitivities of Mopra and SEST at 86 GHz are 22 Jy/K and 25 Jy/K respectively.

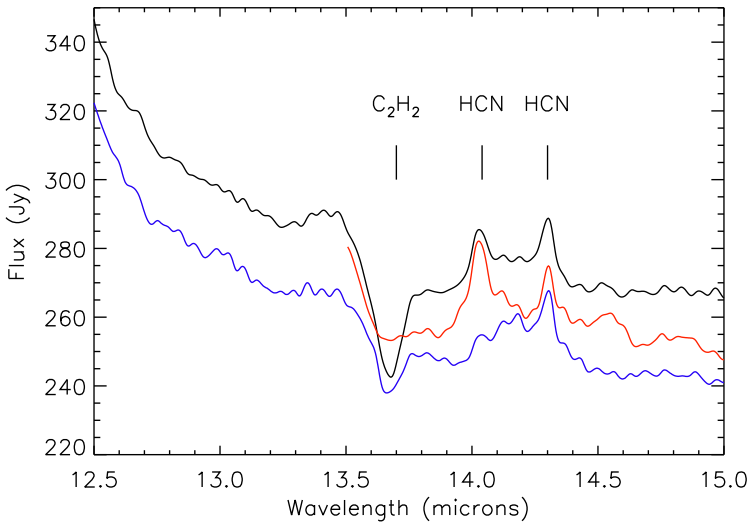

Figure 3.3: SWS spectra from Sloan et al. (2003) showing the HCN and C_2H_2 features around 14 μm. IRC +50096 is shown in black, T Dra (multiplied by a factor of 3) is shown in blue and the partial spectrum of S Cep is shown in red.

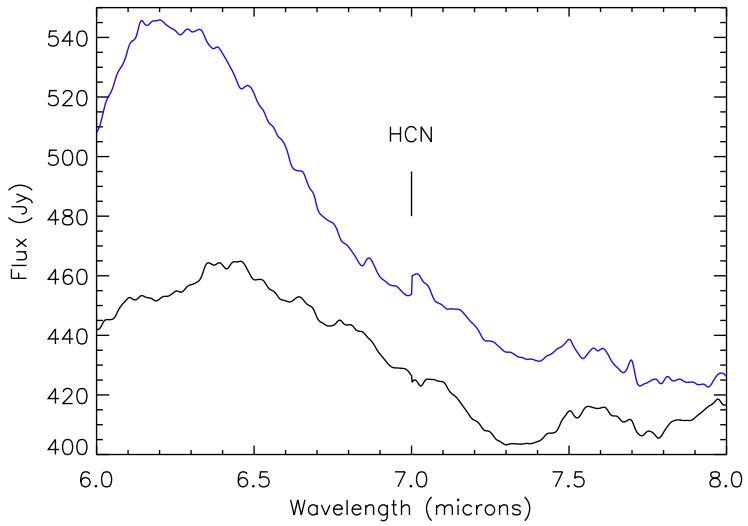

Figure 3.4: SWS spectra from Sloan et al. (2003) showing the region of the 7 μm feature. IRC +50096 is shown in black and T Dra (multiplied by a factor of 2.7) is shown in blue.

15082−4808 has a velocity that is within uncertainties of the systemic velocity of the envelope. The lack of an observed definite red-shifted component suggests that either the maser is formed close enough to the star that the red-shifted component is obscured by the host star itself or that the maser amplifies photons emanating directly from the photosphere. These would both be in agreement with the interferometric observations of CIT 6 and IRC +10216 by Carlstrom et al. (1990) and Lucas & Guilloteau (1992) which suggest that the maser is located within five stellar radii.

As shown by Bujarrabal & Nguyen-Q-Rieu (1981) and Lockett & Elitzur (1992), SiO masers are formed close to the photosphere of the star but are amplified tangentially to the surface rather than radially. As shown by Gray et al. (2009) using a dynamic atmosphere and maser propagation model of SiO, in many cases the SiO emission is red-shifted with respect to the systemic velocity of the envelope (see their Fig. 11-13). The degree of redshift can, depending upon the model, increase with increasing phase. In contrast, the blue-shifted central

velocity of the 89.087 GHz maser with respect to the systemic velocity of the envelope suggests that the HCN maser is amplified radially. OH masers are also amplified radially, albeit significantly further from the stellar surface than is the case for this HCN maser. This difference in amplification direction between SiO masers and HCN masers means that the latter can be used to study the outflow velocities, whereas SiO masers cannot.

Ziurys & Turner (1986) show that it is possible for this maser to be pumped by the ∼14 μm and/or the 7 μm infra-red photons emitted by the star from the v_2 bands of HCN. The features at 14.0 μm originate from the $2v_2^2 - 1v_2^1$ and $2v_2^0 - 1v_2^1$ transitions of HCN, the 14.3 μm feature from the $1v_2^1 - 0v_2^0$ transition and the 7 μm feature from the $2v_2^0 - 0v_2^0$ transition (for further details see Aoki, Tsuji & Ohnaka 1999). *Infrared Space Observatory* (*ISO*) Short Wavelength Spectrometer (SWS) spectra from Sloan et al. (2003) were available for three of the previously known HCN maser sources from Table 3.1 (IRC +50096, T Dra and S Cep). All three sources exhibit some degree of 14.0 μm and 14.3 μm emission and their spectra in this region are shown in Fig. 3.3. Emission in this band is suggested by Aoki, Tsuji & Ohnaka (1999) as being fairly common in carbon stars, and as shown by Cernicharo et al. (1999), it is possible for the 14.3 μm emission peak to be pumped radiatively from the ground state to the v_2 state. Fig. 3.4 indicates that there was little-to-no 7 μm emission in either T Dra or IRC +50096 when the *ISO* observations were made, which supports the 14 μm pumping mechanism. S Cep has no spectrum available at this wavelength.

The collisional rate coefficients of HCN $v_2 = 2$ are not yet published and therefore collisional excitation mechanisms cannot yet be ruled out. This should be addressed by modelling once these parameters are available.

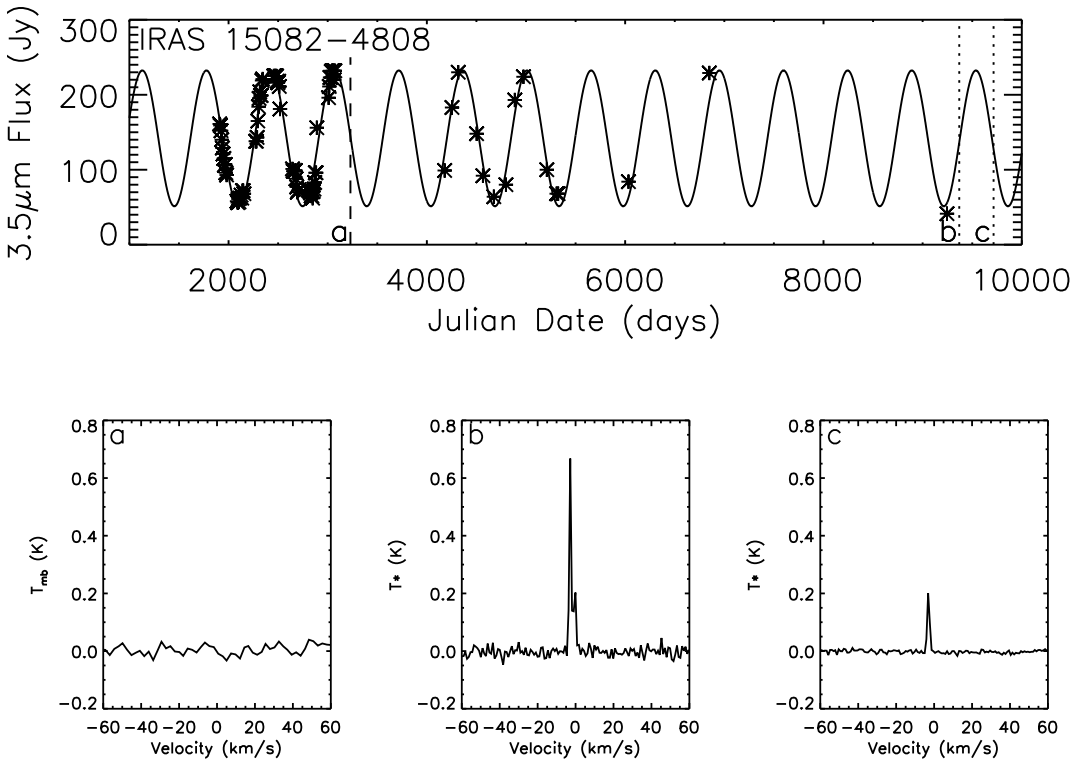

Figure 3.5: Pulsational cycle shown using 3.5 micron photometry. Photometric data taken from Cutri et al. (2012), Whitelock et al. (2006) and Cutri et al. (2003a). The vertical dashed lines indicate the dates when the spectral observations were taken, and below are the spectra at each date. The spectrum labelled 'a' is taken from Woods et al. (2003). The abscissa shows (Julian Date - 2446000) days.

3.3.3 Relation to variability

To determine the relation between variability and maser emission in IRAS 15082−4808, the pulsational cycle was investigated using literature photometry (Cutri et al. 2012; Price et al. 2010; Whitelock et al. 2006; Cutri et al. 2003a). 3.5 μm photometry was collected and a sinusoidal curve fitted using the genetic algorithm PIKAIA (Charbonneau 1995, see Chapt. 2 for further details). The resulting variability curve is shown in Fig. 3.5.

The 1993 observation was taken mid-way between a maximum and minimum brightness of the star. The 2011 observation was taken at a very similar point

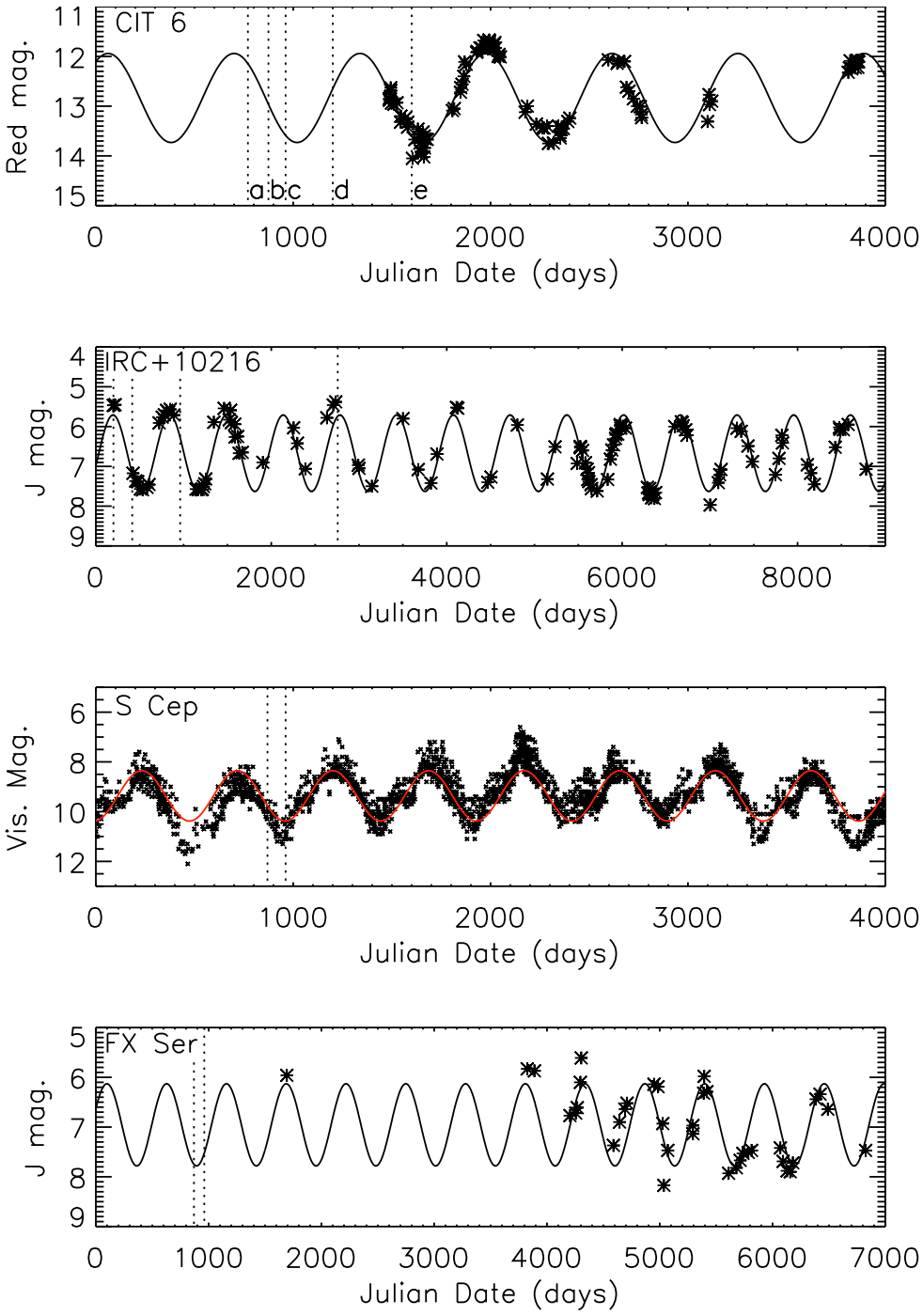

Figure 3.6: Photometry data as a function of (Julian Date - 2446000) days. Dotted lines indicate positive detections and dashed lines indicate null detections of the 89.087 GHz HCN maser. A further detection of the maser in CIT 6 was made by Nguyen-Quang-Rieu et al. (1988) but the date of observation and the spectrum obtained were unavailable in the literature, thus this has not been included on the figure. The letters appearing on the CIT 6 figure refer to the observations in Fig. 3.7. The three photometric data sets of IRC +10216 were offset from one-another in intensity; in order to fit a single sine curve to the data, offsets were applied to two of the data sets. This was not applied to any other source.

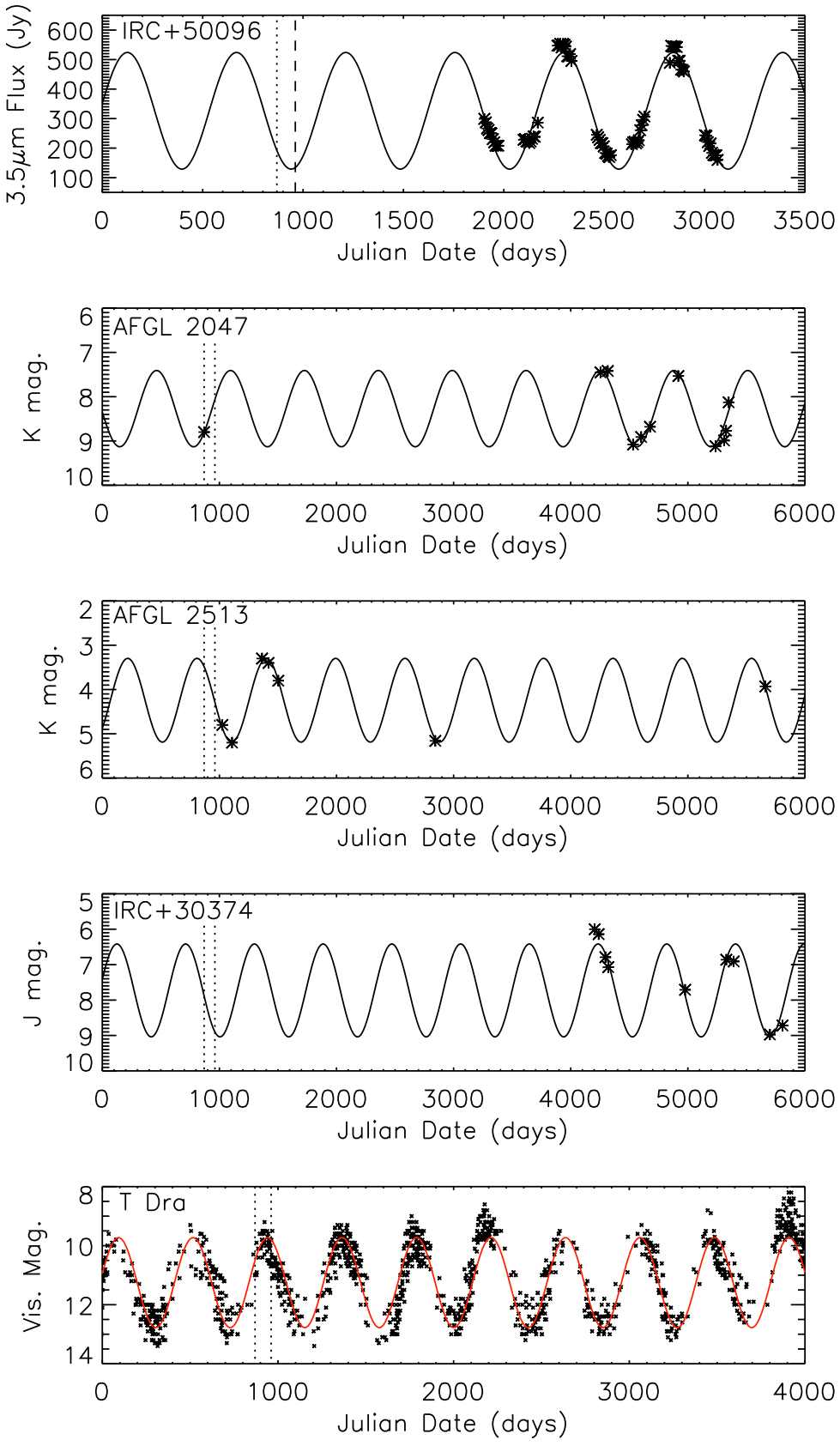

Figure 3.6: – *continued.*

in the pulse phase, although there was little photometry taken around the time of this observation. However, if the pulsational period was the only cause of the maser variability and the pulsational cycle of IRAS 15082−4808 had not changed significantly, then it would be expected that these two observations would have very similar intensities. This is not the case: the 2011 observation clearly detects the maser and the 1993 observation is a null detection.

Variability curves were also created, following the same method as above, for each of the nine sources (Fig. 3.6). Dotted lines indicate positive detections and dashed lines indicate null detections. AFGL 2047, AFGL 2513, T Dra and IRC +30374 were observed either in March or June 1987 with no indication as to which. Therefore both these dates are indicated on their respective variability curves.

The photometric data was taken from: Alksnis (1995); Le Bertre (1992); Cutri et al. (2003a); Whitelock et al. (2006); Shenavrin, Taranova & Nadzhip (2011); Henden (2013); Fouque et al. (1992); DENIS Consortium (2005); Kerschbaum, Groenewegen & Lazaro (2006); Price et al. (2010); Helou & Walker (1988); Jones et al. (1990); Epchtein, Le Bertre & Lepine (1990). The maser spectroscopic data was taken from: Lucas et al. (1986); Guilloteau, Omont & Lucas (1987); Goldsmith et al. (1988); Lucas, Omont & Guilloteau (1988); Lis, Goldsmith & Predmore (1989); Carlstrom et al. (1990); Lucas & Guilloteau (1992).

The variability curves show that the HCN maser has been detected at a variety of phases in the stars' pulsational period, although some of the stellar curves have been extrapolated further than is reliable owing to the lack of available photometry data. Most of the sources have only one published maser spectrum, despite there being multiple detections reported in the literature. Therefore it is impossible to determine whether the maser intensity or profile varies with period in these sources.

CIT 6, however, has seven detections of the maser noted in the literature. Five of these have published spectra which are shown together in Fig. 3.7. There

is a small change in central velocity and width of the line over the different observations, although these were made by a variety of telescopes at a variety of resolutions which could contribute to this. The intensity of the line has varied significantly over these observations: four show similar peak intensities of approximately 40 Jy and the other approximately 75 Jy.

To examine this variation with phase more closely, the integrated intensities of the CIT 6 lines were measured and plotted against phase, as derived from the sinusoidal fitting. The results are shown in Fig. 3.8, along with all other sources with multiple detections. The intensities were normalised to the maximum observed intensity of the maser in each source to allow comparisons between sources to be made. Where null detections were made, an intensity of zero is plotted. A phase of 0.0 or 1.0 indicates maximum intensity and a phase of 0.5 indicates minimum intensity.

The maser in CIT 6 was shown to be most intense close to stellar maximum and at lower intensities close to stellar minimum. This is somewhat in agreement with IRC +50096 whose maser was detected at a phase of 0.37 and then not detected at a phase of 0.54. IRC +10216 was observed to have similar intensities and profiles at all epochs of observation (Lucas et al. 1986; Guilloteau, Omont & Lucas 1987; Lucas, Omont & Guilloteau 1988; Lucas & Guilloteau 1992). IRAS 15082−4808 as previously discussed, shows the intensity increasing between the phases of 0.2-0.7.

Smith, Price & Moffett (2006) show that there are lags between the infrared and optical light curves emitted by Mira variable stars from AAVSO (optical) and DIRBE (infrared) data. They find that the infrared generally lags behind the optical by 0.1-0.2 of a phase. As some of our data is optical and some infrared, a shift was applied to the relevent data to see if correlation was improved. No improvement was found, thus the data in Fig. 3.8 is the original unshifted data.

The 89.087 GHz maser in CIT 6 has been shown by Goldsmith et al. (1988) to exhibit linear polarisation of 20%. The observations were taken by a variety

of instruments at a variety of elevations, so this polarisation will have an effect on the observed intensity of the maser. For all other sources, polarisation has not been measured. The cause of this polarisation is currently unknown and further measurements are required in order to ascertain the cause (Goldsmith et al. 1988; Pérez-Sánchez & Vlemmings 2013). Due to this, it is difficult to draw firm conclusions about variability with pulsation phase. In order to examine this more closely, a long-term measurement of maser intensity and polarisation in collaboration with photometric monitoring would need to be carried out over at least one pulsational period. From such a study, the effect of stellar variability on the intensity of the maser, the correlation between the two and, if mapped, the position of this maser with respect to the host star could be firmly established. This has been carried out successfully for SiO masers by Reid & Menten (2007), who used the VLA at 43 GHz to measure the radio continuum and resolve SiO masers to simultaneously measure the positions of the radio photosphere and the masing regions. They found that SiO maser emission is found in partial ring-like structures at 2-3 stellar radii from the radio photosphere.

3.3.4 Applications to AGB winds

Richards et al. (2012) have examined water masers in oxygen-rich AGB envelopes. As part of their investigation, they studied the expansion velocities of the maser shells with respect to distance from the host star: Fig. 44 of Richards et al. (2012).

The expansion velocities obtained for the inner water maser shells at less than 20 AU from the star are consistent with the central velocity of the HCN masers with respect to the systemic velocities of their envelopes. A distance from the star of less than 20 AU is also consistent with current thoughts about the formation distance of the HCN masers: Carlstrom et al. (1990) report an upper limit of 180 AU on the size of the masing region in CIT 6 and interferometric

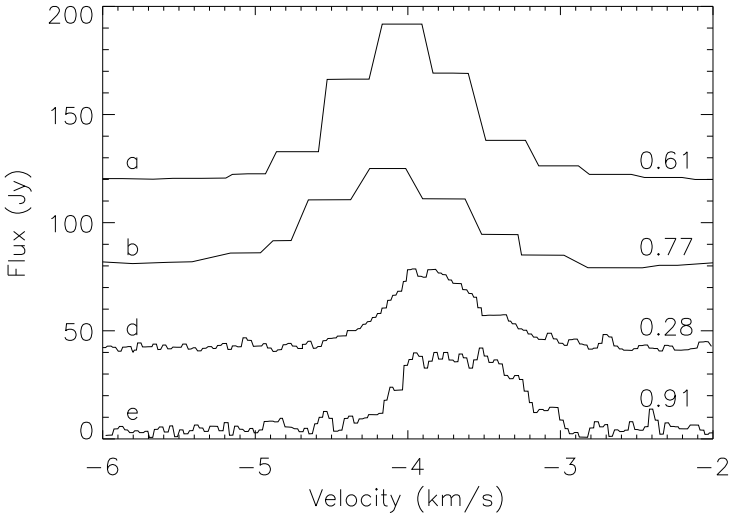

Figure 3.7: CIT 6 spectra overlaid. *a*, *b*, *d* and *e* correspond to the dates indicated on the upper plot of Fig. 3.6. Each spectrum is labelled on the right hand side of the figure with the stellar phase at the time of observation. A phase of 0.0 or 1.0 corresponds to stellar maximum and a phase of 0.5 corresponds to stellar minimum. Spectral data taken from Guilloteau, Omont & Lucas (1987); Goldsmith et al. (1988); Lucas, Omont & Guilloteau (1988); Lis, Goldsmith & Predmore (1989); Carlstrom et al. (1990). There is only a partial spectrum published for the observations made at date 'c' and is therefore not included in this figure.

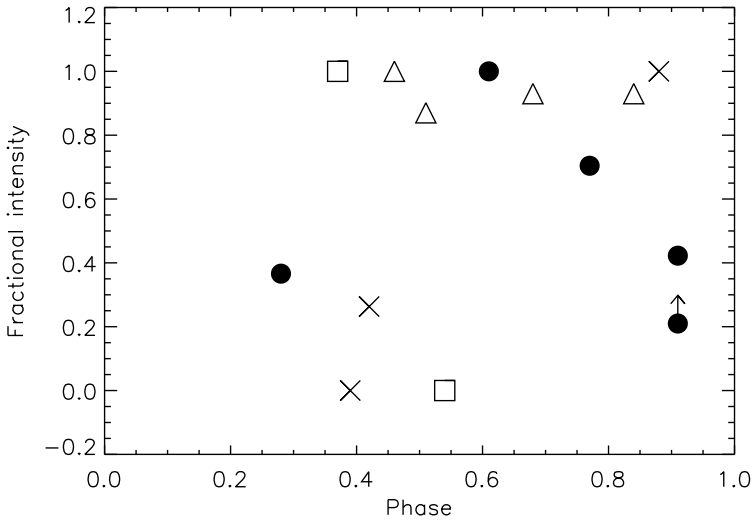

Figure 3.8: Plot showing integrated intensity as a fraction of the strongest maser in each source against stellar pulse phase as calculated from the variability curves shown in Fig. 3.5 and Fig. 3.6. Filled circles: CIT 6, crosses: IRAS 15082−4808, triangles: IRC +10216, squares: IRC +50096.

observations by Lucas & Guilloteau (1992) suggest that the maser in IRC +10216 is located within five stellar radii. These imply that the HCN masers are tracing the expansion velocity of the region of the envelope in which they reside.

The region in which HCN $v_2 = 2$ masers are thought to be formed in is very distinct. Thus the expansion velocity of a specific region inside the acceleration zone is represented by the velocity of the maser. Cernicharo et al. (2011) report detections of more than 60 vibrational transitions of HCN in IRC +10216, including the masing 89.087 GHz transition. That work showed that there is a correlation between the excitation energy of the upper level (E_u and the observed line widths and suggests that this is due to the different transitions emanating from different regions of the circumstellar envelope. This places the HCN $v_2 = 2$ maser in IRC +10216 within the 2-5 R* region of the envelope, which is consistent with the works of Carlstrom et al. (1990) and Lucas & Guilloteau (1992).

Fig. 3.9 shows the expansion velocities, taken as half of the measured linewidth, of the transitions reported in Cernicharo et al. (2011) against the energy of each upper state. Overplotted in red are the offset velocities of all ten detected HCN masers and these are found to be less than the velocities suggested by the velocity-E_u correlation of Cernicharo et al. (2011). This suggests that the pumping mechanism for this maser may contain one of the high energy states found in zone 1.

3.3.5 Insights into AGB atmospheres

Masers can provide insight into the winds of AGB stars through comparison of observed parameters with model extended atmospheres. The 89.087 GHz maser provides two significant constraints. First, there is very little velocity variability with pulsation phase, and no evidence for infall. This places the maser in a region of stable outflow. Second, the maser velocity is very low compared to the expansion velocity shown by CO. This locates the maser in a region where little acceleration has occurred.

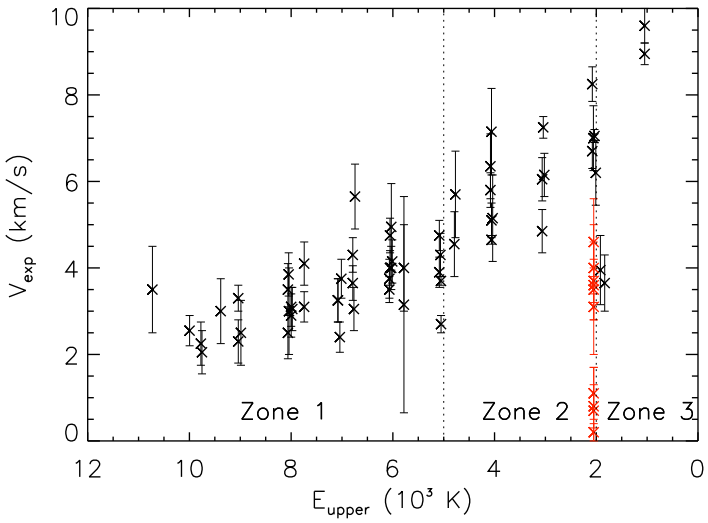

Figure 3.9: Expansion velocity against the energy of the upper state (K) of a number of vibrational transitions of HCN in IRC+10216. Expansion velocity is defined as $0.5\Delta V$ for the data taken from Cernicharo et al. (2011) (black points) and as the offset velocity with respect to the systemic velocity of the envelope for the ten HCN masers (red points). The zones are as calculated by Cernicharo et al. (2011): zone 1 represents a region $\sim$ 1.5 R*, zone 2 $\sim$ 5 R* and zone 3 $\sim$ 29 R*.

The dynamic model atmospheres published in Höfner et al. (2003a), simulate time-dependent pulsations of the star for both mass-losing and non-mass-losing stars. Two models are discussed in detail in their Fig. 2 to 5, consisting of a star with parameters: 7000 $L_\odot$, 1.0 $M_\odot$, 355 $R_\odot$, a stellar temperature of 2800 K and a C/O of 1.4. One of these models is a mass-losing AGB star with a mass loss rate of 2.4×10^{-6} $M_\odot$/yr, the other is non-mass-losing. The pulsation period in both models, at 390 days, is significantly lower than that of any of the known maser sources. The parameters used for the two models differ only by the magnitude of the piston velocity amplitude and have values of 2 km/s and 4 km/s. A 2 km/s piston velocity amplitude is insufficient to cause mass-loss whilst a 4 km/s piston velocity allows dust production and subsequently mass-loss to occur. When these two models are compared with the parameters determined from the HCN 89.087 GHz masers, a number of insights can be made.

From the aforementioned mass-losing model of Höfner et al. (2003a), it is

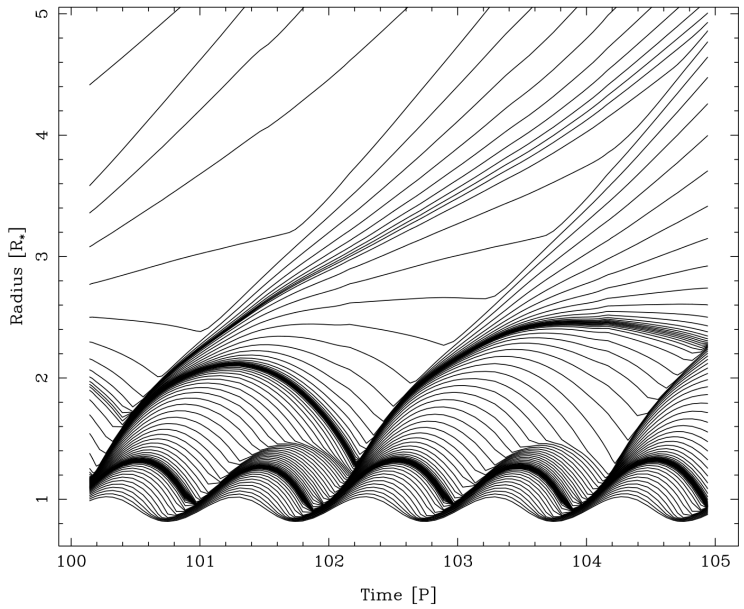

Figure 3.10: Positions of selected shells as a function of time in pulsation periods (P) for the mass-losing model 170t28c14u4, reproduced from Fig. 2 of Höfner et al. (2003a), A&A, 399, 589 by kind permission of S. Höfner and ESO ©.

clear that there are regions of the envelope undergoing regular expansion and contraction, clearly shown in Fig. 3.10 (reproduced from Höfner et al. 2003a with kind permission from S Höfner and ESO ©). Given the lack of correlation of maser intensity variability with pulse phase, it is unlikely that the maser would originate from one of these regions. The lack of an observed in-fall velocity suggests that the maser exists at the point that mass-loss begins. In model 170t28c14u4 of Höfner et al. (2003a), these requirements are satisfied at roughly 2 stellar radii from the host star, as can be seen in Fig. 3.10, coinciding with shocked regions of the envelope and in keeping with the expected distance of less than five stellar radii from Carlstrom et al. (1990) and Lucas & Guilloteau (1992).

The lack of an observed substantial increase (more than a few km/s) in central velocity of the HCN maser lines indicates that this maser should not exist for long within a particular region of gas as it moves outwards. The implication is that the maser may cease operating as the region outwardly expands from the central

star.

The upper level of the HCN 89.087 GHz maser lies at 2050 K above the ground state. The gas temperature in model 170t28c14u4 drops below this at roughly 1.5 stellar radii. The region of the model AGB atmosphere between 1 and 2 stellar radii has a highly variable flow velocity, changing with pulse phase (−13 km/s to +10 km/s). If the maser is radiatively pumped by photospheric photons, the maser will exist further from the host star than that dictated by the gas temperature. In the aforesaid model, at 2.5 to 3.5 stellar radii, the velocity is more stable with pulse phase, and with flow velocities of 0 km/s to +8 km/s, more closely reflects the offset velocities of HCN masers. The gas temperature in this region is approximately 1000 K.

The non-mass-losing model, 170t28c14u2, has flow velocities of between +1 and +4 km/s in the region of 1.1 to 1.2 stellar radii for two of four pulse phases and between −11 and −13 km/s for the remaining phases. In this region, the gas temperature is roughly 2000 K. At 1.2 to 1.4 stellar radii, the temperature drops to approximately 1000 K and the flow velocities range from −10 km/s to +10 km/s. The 89.087 GHz HCN masers are only observed in mass-losing carbon rich AGB stars, thus this model is not a suitable representation for these stars.

Neither of these models perfectly reproduce the conditions required for this maser to exist, but these models are not tailored to the individual sources and several model parameters vary significantly from those of the known host stars (e.g. pulse period). However, it is promising that the formation regions suggested from the mass-losing model agree with the regions predicted in Carlstrom et al. (1990) and Lucas & Guilloteau (1992).

3.4 Conclusions

We have identified a new 89.087 GHz HCN maser in the AGB star IRAS 15082 − 4808. This maser was first detected in this source in June 2010 using the Mopra

telescope in Australia, and was detected once again in June 2011 at Mopra. It was, however, undetected in a molecular line survey by Woods et al. (2003) based upon observations taken at SEST in 1993.

The observation in 2010 has two components to the maser, and that of 2011 has only a single component at the same velocity shift as the major component in 2010. It is highly unlikely that the two-component profile is due to a second hyperfine component being observed. It is more likely that the observed profile is due to motions of the masing molecule within the stellar envelope.

The major component of the maser in IRAS 15082−4808 as observed in 2011 is offset by -2.0 ± 0.9 km/s (blue-shifted) with respect to the systemic velocity as derived from the HCN 88.631 GHz emission line and the minor component by $+0.7 \pm 0.9$ km/s (red-shifted). The offset velocity of the major component is in-keeping with the -0.3 to -5 km/s offset of all previous detections of this maser in other sources (Guilloteau, Omont & Lucas 1987; Lucas, Omont & Guilloteau 1988; Lucas & Cernicharo 1989).

The variability of the maser in all ten sources in which it has been detected to date has been investigated, although firm conclusions could not be drawn due to lack of observations and polarisation effects. Long term monitoring of intensity and maser polarisation in conjunction with regular photometric measurements would allow the variation of maser intensity with stellar pulsation to be properly assessed.

Finally, comparisons of the derived maser parameters from all known host stars have been made to published models of AGB atmospheres. The comparison suggests that the masers are formed between 2 and 4 stellar radii from the host star and at the point that mass-loss begins. This region also contains shocked gas. Despite the gas temperature within this region being lower than that of the upper maser level, radiative pumping from photospheric photons would allow the existence of this maser within this region. The outflow velocities of the gas within this region are matched well by the offset velocities of the known masers. This

region also agrees with the measurements and predictions of Carlstrom et al. (1990) and Lucas & Guilloteau (1992), which place the maser within 5 stellar radii. High spatial resolution interferometry would be required to be able to identify for certain the exact region of the envelope in which this maser is formed.

Chapter 4

Modelling CO in the circumstellar envelope of II Lup

4.1 Introduction

CO plays an important role in shaping the chemistry that occurs in an AGB star's circumstellar envelope. Due to its high binding energy, CO preferentially forms over other molecules. This gives rise to the 'locking up' of carbon in oxygen-rich AGB stars and conversely oxygen in carbon-rich AGB stars. In oxygen-rich AGB stars, this allows the formation of water molecules, other oxides and oxygen-rich silicates such as pyroxene and olivine, whereas in carbon-rich AGB stars, a multitude of carbon-containing molecules and dust are free to form.

II Lup, also known as IRAS 15194-5115, is one of the stars from the Mopra molecular line survey in Chapt. 2. It is a mass-losing, carbon-rich AGB star with a pulsation period of 575 days and is the brightest carbon star in the Southern Hemisphere sky at 12 μm (after IRC+10216 and CIT 6). It has also been shown to be a probable J-type star (e.g. Chapt. 2 and references therein). J-type stars may be an example of the class of object from which the pre-solar SiC A+B grains form.

Modelling AGB stars in CO and ^{13}CO allows thorough investigations of the thermodynamic structure and chemistry of circumstellar envelopes to be carried out. By modelling II Lup in a variety of CO transitions, we can improve our understanding of J-type stars and the behaviour of their envelopes.

4.2 The code

The modelling in this chapter has been carried out using a combination of the radiative transfer codes MCMax (Min et al. 2009) and GASTRoNOoM (Decin et al. 2006, 2010), using the interface code ComboCode (Lombaert 2013; Lombaert et al. 2013). MCMax models the continuum emission of dust whilst making assumptions about the gas temperature and velocity structure. GASTRoNOoM models the gas velocity and temperature structure, level populations and emission line profiles whilst making assumptions about the density structure of the region. As the behaviour of the dust has an impact on the thermodynamics of the gas and vice versa, it is important to understand and model the two components consistently. As described in Lombaert (2013), Lombaert et al. (2013) and in further detail below, ComboCode iterates over the two codes, using the output of one as a partial input to the other, improving the results over using either code in a stand-alone capacity.

4.2.1 MCMax

MCMax is a 2D Monte Carlo radiative transfer code which models the continuum emission of dust and was written by Min et al. (2009). It uses the Monte Carlo method of 'continuous absorption and re-emission' by Bjorkman & Wood (2001). Discrete photon packages are emitted by the central star and subsequently traced through the surrounding medium whilst undergoing scattering, absorption and re-emission by the dust. The medium has a disk structure with variations allowed in both the radial and vertical directions. As implemented by Lombaert et al.

(2013), this code is used in a one-dimensional capacity, assuming variations are allowed only in the radial direction.

MCMax uses two approximations to the Monte Carlo method in order to reduce statistical noise in low photon-count regions and increase the speed of the calculations in high optical depth regions. The partial diffusion approximation (PDA) improves the statistical noise in low-photon count regions (see the 'diffusion approximation', as described by Rosseland 1924 and Wehrse, Baschek & von Waldenfels 2000). The modified random walk (MRW) reduces the computation time in high optical depth regions where photons can get 'lost' in a very high number of interactions with dust particles, dominating the computing time. By allowing a photon to interact multiple times for a single calculation using the radiative diffusion equation in defined regions of constant temperature and density, the MRW procedure reduces the number of computations that are required. For further details on the MRW approximation, see Fleck & Canfield (1984) and Min et al. (2009).

Within MCMax, stellar input parameters such as temperature, mass and radius (calculated within ComboCode) must be defined. In addition, the fractional composition of the dust must be specified, including their opacities. This allows the user to alter the proportions of contributing grains as well as their shapes. For example, either continuous distribution of ellipsoids (CDE) or distribution of hollow spheres (DHS) may be used (determined by their opacities) for amorphous carbon. The dust species, optical constants and stellar parameters all have a significant impact on the resulting spectral energy distribution (SED) and dust thermodynamic properties, which will be explored further in Sect. 4.5.1.

4.2.2 GASTRoNOoM

GASTRoNOoM, developed by Decin et al. (2006, 2010), is a spherically symmetric, non-local thermodynamic equilibrium (LTE) radiative transfer code. It is

used to model the thermodynamic structure of gas, including temperature and velocity profiles (gas velocity and drift velocity), level populations and line profiles. The code has three distinct parts: Cooling, Mline and Sphinx. Cooling is responsible for calculating the temperature and velocity structure of the gas, Mline calculates the level populations of each molecule and Sphinx calculates the line profiles from the data outputted from a combination of Cooling, Mline and a telescope specification file (if desired).

The self-consistent calculations for the gas temperature profile, carried out in Cooling, take into account a number of different heating and cooling processes: gas-grain collisional heating, photoelectric heating from dust grains, dust-gas heat exchange, cooling via rotational excitation of H_2O and CO and cooling by the vibrational excitation of H_2. Each of these mechanisms is described in further detail in Decin et al. (2006). However, it is also possible to define a gas temperature profile manually in the form of a power law with up to 3 components, valid in different regions of the envelope:

$$T(r) \propto r^{-\varepsilon}, \tag{4.1}$$

where $T(r)$ is the temperature profile as a function of radius, r, and ε is a constant defined by the user.

Mline carries out the non-LTE line radiative transfer calculations, which are subsequently ray-traced using Sphinx to result in line profiles. Sphinx also allows the convolution of the line profiles with a specified telescope beam profile so that comparisons with observations can be easily made.

Both constant and variable gas mass loss may be simulated by GASTRoNOoM. The central star may be taken as either a black body or as one of several stellar atmosphere models (see Decin et al. 2010). For this work, the central star is assumed to be a black body and mass loss is assumed to be constant with radius, unless otherwise stated.

GASTRoNOoM assumes an oxygen-rich dust composition with a grain size distribution equal to that found in the interstellar medium. As discussed in Decin et al. (2006), the grain size distribution found in AGB star circumstellar envelopes may not reflect that found in the ISM. GASTRoNOoM also assumes a power law profile for the dust temperature.

4.2.3 ComboCode

ComboCode, written by Lombaert et al. (2013), acts as an interface between GASTRoNOoM and MCMax. ComboCode iterates over each radiative transfer code twice, using the outputs from the previous step as input for the next. This is shown diagrammatically in Fig. 4.1.

By iterating over the two codes, a number of improvements can be made over using either one alone. The results from MCMax are improved by using the drift velocity profile calculated from GASTRoNOoM rather than assuming a constant drift velocity. The results from GASTRoNOoM are improved by using the dust parameters outputted by MCMax. As mentioned above, GASTRoNOoM assumes that the dust is composed of oxygen-rich dust and the dust temperature is in the form of a power law. MCMax allows a variety of dust species to be used, outputting the required opacities, temperature profile and defining the inner dust radius from its calculations, all of which are given as input to GASTRoNOoM via ComboCode, superseding the aforementioned assumptions.

In addition to using ComboCode to iterate over the two radiative transfer codes, ComboCode also gives the user the option of running either code individually. This feature is exploited in the SED modelling method, detailed in Sect. 4.4.1.

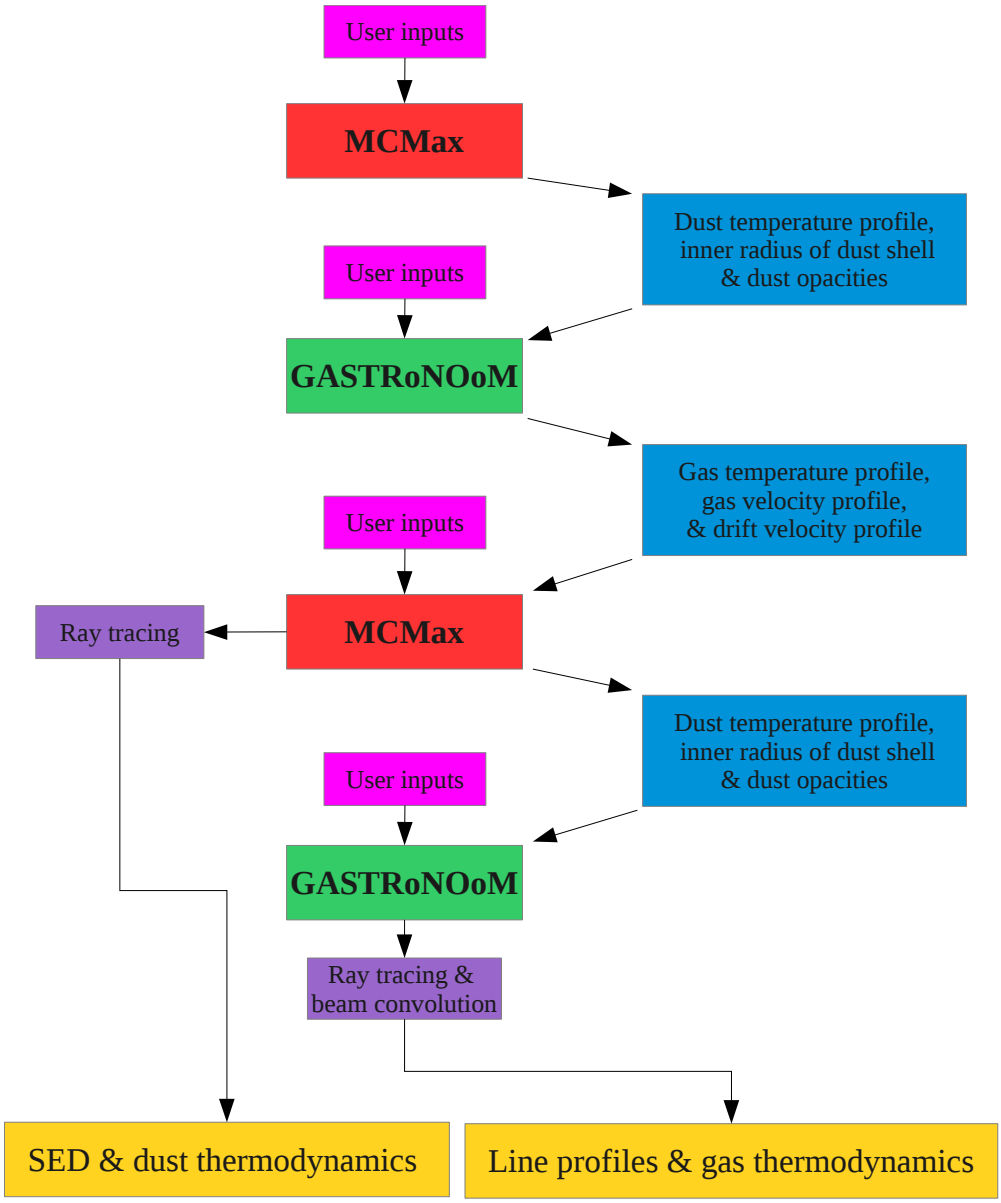

Figure 4.1: Structure of ComboCode, adapted from Lombaert (2013).

4.3 The data

The data used to evaluate the models come from a variety of sources and fall into two categories. The first data set is that forming an SED of the source. These data may be of low spectral resolution and are used to model the continuum emission. Higher resolution data are required to evaluate the model emission line

Table 4.1: SED data.

Instrument	Wavelength range (μm)	Origin of data
ISO SWS	2.359 - 45.198	Sloan et al. (2003)
ISO LWS	43.046 - 196.827	*ISO* archive
Herschel PACS	55.403 - 192.516	Lombaert et al. (in prep.)

Table 4.2: CO line profile data. Although all covered transitions were detected in the APEX and Mopra data, there were many non-detections within the PACS data.

Instrument	Transition	Transition frequencies (GHz)
Mopra	^{13}CO J=1-0	110.201
Mopra	CO J=1-0	115.271
JCMT	CO J=2-1	230.538
APEX	CO J=3-2	345.796
APEX	^{13}CO J=4-3	440.765
APEX	CO J=4-3	461.041
APEX	CO J=7-6	806.652
Herschel PACS	CO, ^{13}CO J=13-12 to J=52-51	1483.280 - 5891.322

profiles and must clearly show the individual CO lines. The data is discussed in more detail below and summarised in Tables 4.1 (SED data) and 4.2 (CO line data).

4.3.1 SED data

The data used to construct an SED are from three different sources. The first are *ISO* SWS (henceforth known as SWS) data from the catalogue of uniformly reduced *ISO* data by Sloan et al. (2003). These data cover the wavelengths 2.359 to 45.198 μm and form the majority of the SED. The second are *Herschel* PACS data (henceforth simply PACS), reduced using HIPE, from Lombaert et al. (in prep.). This covers the region 55.403 - 192.516 μm. The third are *ISO* LWS data (henceforth LWS), taken as post-pipeline reduced data from the *ISO* archive[1],

[1]http://www.ipac.caltech.edu/iso/iso_archive/archive_instruct.html

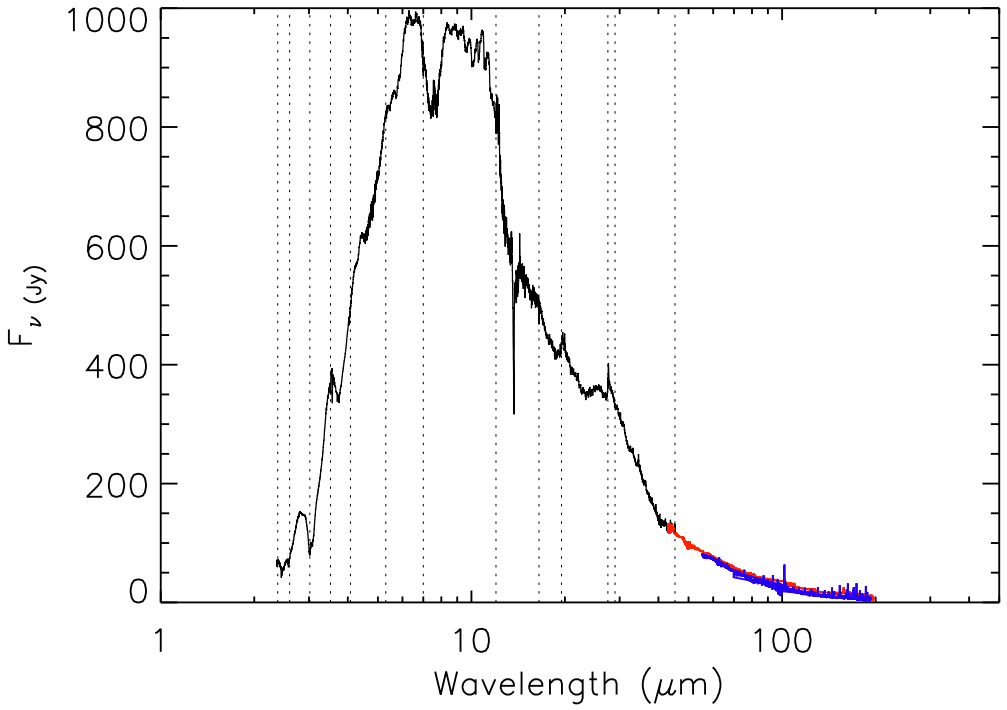

Figure 4.2: Plot of the observed SED constructed from SWS, LWS and PACS data. The SWS data is shown in black, the LWS data in red and the PACS data in blue. The SWS band edges are shown by the vertical dotted lines.

covering the wavelength range 43.046 - 196.827 µm. Each of the datasets were taken at different times and thus different pulsation phases. The LWS data is offset with respect to the other two datasets: it has a higher intensity than both SWS and PACS. We therefore scaled the LWS data to both the PACS and SWS data using a constant scaling factor of 0.55. The SED data is shown in its entirety in Fig. 4.2. Overlaid on Fig. 4.2 are the SWS band edges.

4.3.2 Spectral line data

The spectral line data, containing CO and ^{13}CO lines, are from four telescopes: the Photoconductor Array Camera and Spectrometer (PACS) onboard *Herschel*, the Atacama Pathfinder Experiment (APEX), the James Clark Maxwell Tele-

scope (JCMT) and the Mopra Radio Telescope. The PACS data, discussed above, cover the J=13-12 to J=52-51 transitions (inclusive). The data were reduced using HIPE by R. Lombaert and full details of the PACS data reduction will be found in Lombaert et al. (in prep.). A number of the transitions are undetected due to their low signal-to-noise ratio, but upper limits may be placed upon their intensities and thus limits on the model may be applied. The integrated intensities were measured by P. Royer and R. Lombaert by fitting a Gaussian profile on top of a continuum (Lombaert 2013). A complete discussion on the treatment of the model fitting to the PACS data may be found in Sect. 4.4.3.

CO transitions J=7-6, J=4-3 and J=3-2 were taken from APEX data of II Lup from Decin et al. (2008) and used by kind permission of L. Decin. One transition of ^{13}CO, J=3-2, was also taken from the same APEX dataset.

The JCMT data were provided by, and used with kind permission of, S. Alharbi. The beam efficiency of JCMT was taken as 0.59.

The molecular line survey data, discussed in detail in Chapt. 2, taken using the Mopra Telescope, Australia, contained the J=1-0 transitions of CO and ^{13}CO.

4.4 Modelling

The method used to model II Lup using ComboCode occurs in several stages:

1. Using MCMax only, the SED is initially modelled using an extensive grid of models.

2. The best-fit SED model is then re-run with GASTRoNOoM (Cooling and Mline only) and a smaller, finer grid of models run to refine the initial SED best-fit model.

3. Sphinx is included to model the individual lines.

These steps and the results of each are discussed in the following sections. The first two stages are not particularly computationally intensive, however the

last step can be very computationally intensive. The stellar mass has been kept constant at 1 $M_{\odot}$. The distance to II Lup has been reported in the literature to be between 500 and 1200 pc. In the following analysis, we assume a distance of 600 pc.

4.4.1 SED modelling

The model SED is affected by a number of different input parameters defined by the user and passed to MCMax. These are primarily the stellar temperature and luminosity, the dust mass-loss rate, the dust composition, the outer dust radius, whether or not there is thermal contact between the dust species and whether or not the high temperature dust is destroyed.

An initial coarse grid of more than 1000 models was run using MCMax alone. This grid covered a wide range of parameter space, centered around parameters identified within the literature. The models were initially evaluated on their goodness-of-fit using a χ^2 function. The data were evaluated against the SWS and PACS data where possible but in the region between the two datasets, the models were compared with the LWS data. The PACS and SWS data were favoured due to the scaling applied to the LWS data.

The parameter space around the best-fit models was explored with consistently finer grids until an acceptable model was identified. Although a χ^2 function was used to identify the 'best fit' model in the large grids, the final model was fine-tuned by eye. This is due to the presence of strong absorption features within the observed data, caused by molecules that are unsupported in the MCMax model, meaning the best fit according to the χ^2 function was not the model that most accurately represented the data.

GASTRoNOoM was then switched on and a grid surrounding the best-fit MCMax-only model calculated. Only small changes in dust mass-loss rate were required to bring the MCMax + GASTRoNOoM model in line with the initial

Table 4.3: Input parameters for the best SED using MCMax and GASTRoNOoM in combination.

Parameter	Value
Central star temperature	2300 K
Stellar luminosity	7600 $L_\odot$
Dust composition (mass fraction):	5% SiC
	20% MgS
	75% Amorphous C[1]
Dust mass-loss rate	1.1×10^{-8} $M_\odot$ yr^{-1}
Outer dust radius	8500 R^*
Thermal contact between dust particles	True
Destruction of high temperature dust	False

[1]: Amorphous carbon as a distribution of hollow spheres, size=0.01 μm, opacities taken from Acke et al. (2013).

MCMax model.

The best fit SED model using MCMax + GASTRoNOoM in combination is shown in Fig. 4.3, along with the spectrum obtained from using MCMax alone with identical initial parameters. The model parameters are listed in Table 4.3.

4.4.2 SiC feature

The presence of the SiC feature is important in the study of pre-solar grains (see Chapt. 2). The origin of the A+B grains, thought to be J-type stars, must have SiC dust present. II Lup is a J-type star, thus the SiC feature has been examined in detail to ascertain the level of confidence of its presence.

Fig. 4.4 shows the best-fitting model in the region of the SiC feature (5 % SiC by mass). Overlaid is the best fitting model without SiC present in the dust composition. All parameters are identical save for the composition and mass loss rate, which had to be decreased from 1.10×10^{-8} $M_\odot$ yr^{-1} to 1.05×10^{-8} $M_\odot$ yr^{-1} to get the best fit with the different composition. The χ^2 measured within the 5-15 μm region is marginally better (0.5 %) for the SiC composition than without

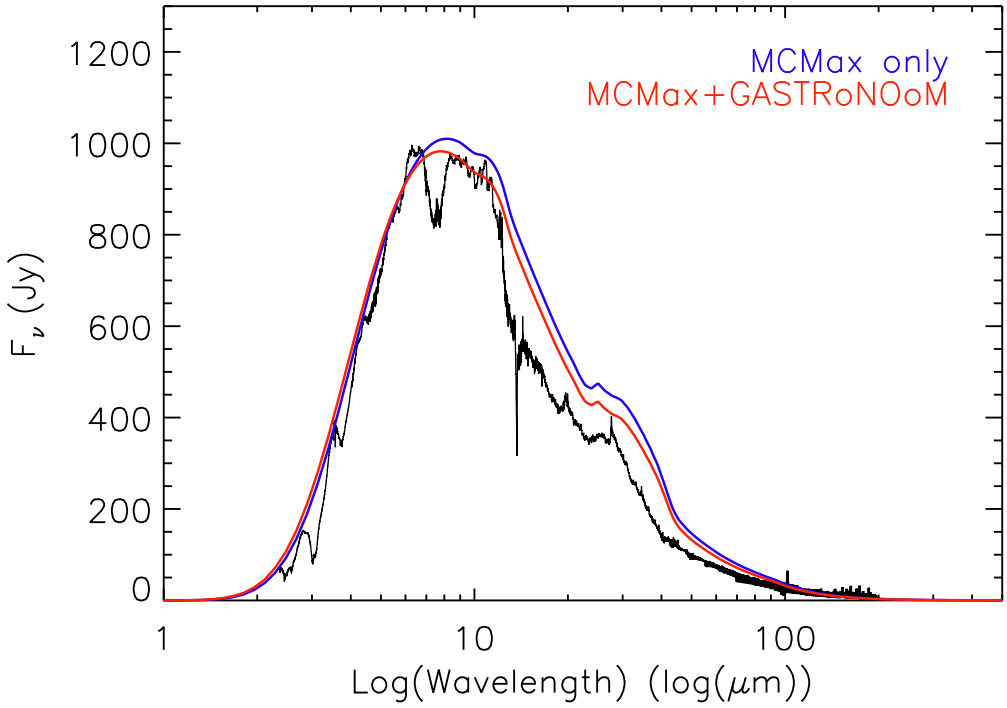

Figure 4.3: Best SED model using MCMax and GASTRoNOoM iteratively. Also shown is the initial MCMax-only model.

SiC. As the improvement is so small, the presence of SiC cannot be confidently confirmed.

For all further models, the dust composition has been assumed to contain 5% by mass of SiC.

4.4.3 Spectral Line Modelling

The line radiative transfer calculations uses energy levels of up to J_u=60 for CO in the ground and first vibrational states. The energy levels, transition frequencies and Einstein A coefficients were taken from Goorvitch & Chackerian (1994) and further details can be found in Appendix A of Decin et al. (2010) (R. Lombaert, priv. comm.). As described in Decin et al. (2006), the equations of radiative transfer are those of Schoenberg & Hempe (1986) and include CO-H_2 collisions

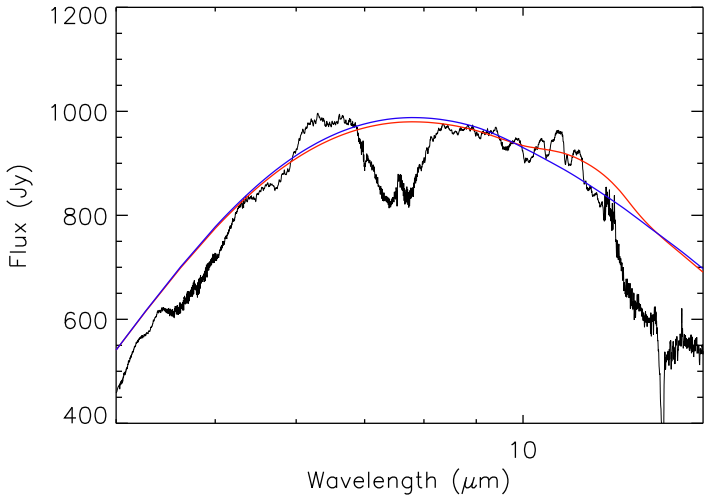

Figure 4.4: Examination of the 5-15 μm region of the SWS spectrum. The two models shown have a fractional composition (by mass) of 0.2 MgS, 0.05 SiC and 0.75 amorphous C (red) and 0.2 MgS and 0.8 amorphous C (blue). The dust mass-loss rates are 1.1×10^{-8} $M_{\odot}$ yr^{-1} (red) and 1.05×10^{-8} $M_{\odot}$ yr^{-1} (blue). All other model input parameters are identical and are the same as those listed for the best-fit SED model in Table 4.3.

and scattering by photons from the stellar photosphere, dust and the CMB. The collision rates for CO-H_2 were also taken from Larsson, Liseau & Men'shchikov (2002) (R. Lombaert, priv. comm.). The temperature and velocity equations are solved simultaneously to give the temperature and velocity structure of the CSE, further details of which can be found in Decin et al. (2006). The velocity at the inner boundary of the CSE is taken as the local sound speed (Decin et al. 2006). The turbulent velocity was assumed to be constant at 1.5 km/s. The central star is assumed to be a black body, with temperature and luminosity as user-input parameters. The gas mass-loss rate is also a user-input parameter. The effect of varying these parameters on the emergent line profiles is discussed in Sect. 4.5.2.

Following the aforementioned modelling method, after a satisfactory SED fit had been found using both MCMax and GASTRoNOoM, Sphinx was included.

The initial model using the parameters defined by the SED model had excel-

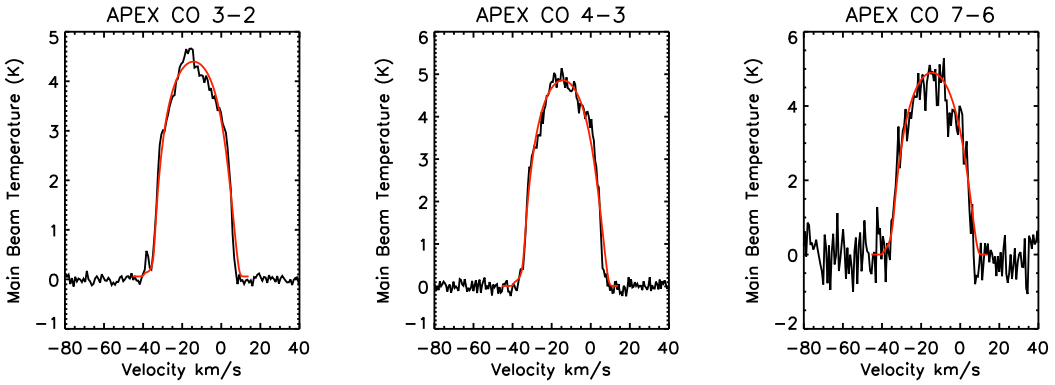

Figure 4.5: ^{12}CO APEX model-data comparison for the APEX cooling model. The data is shown in black and the model in red.

lent agreement with the APEX data, and the model-data comparison is shown in Fig. 4.5. A grid of models was run centered around these parameters in order to identify if any improvements could be made to the APEX lines and none were found. This model is henceforth referred to as the "APEX cooling model" (AC model). However, the AC model had poor agreement with the PACS data; the entire model-data comparison can be found in Fig. C.1 and a sample of the data is shown in Fig. 4.6. Fig. 4.7 shows the fractional difference between the integrated intensities as measured from the model lines and from Gaussian fits to the data for each transition. The model fits were carried out and kindly provided by Pierre Royer and Robin Lombaert. As is shown, the model underestimates the intensities of all the longer wavelength lines and overestimates the shorter wavelength emission lines.

Progressively larger and coarser grids were run to locate a good fit to the PACS data whilst still assuming a constant mass loss rate. A satisfactory fit was eventually found by using the power law gas temperature profile (see Sect. 4.2.2). When identifying the best model to fit the PACS data, lines with wavelengths less than 90 μm were neglected because they form in the innermost regions of the envelope where there are very few theoretical constraints, PACS has a less-reliable

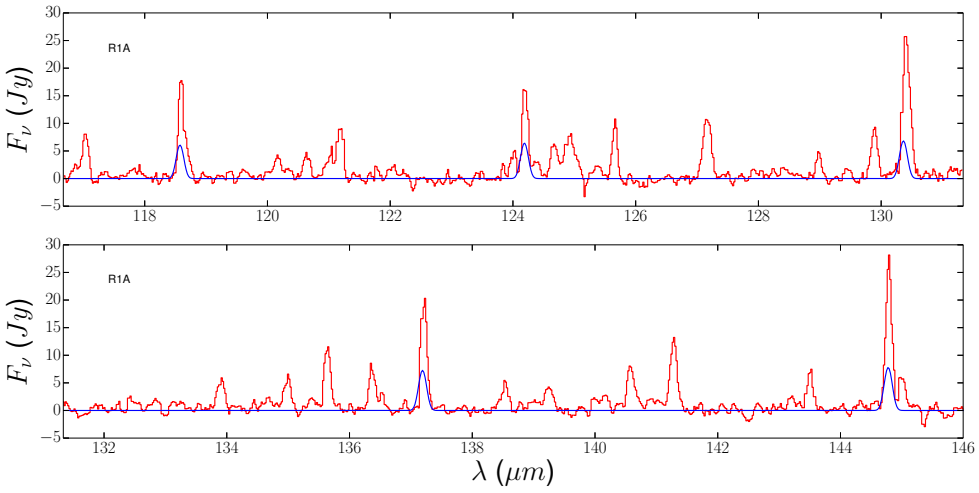

Figure 4.6: Partial PACS model-data comparison for the APEX cooling model. Data is shown in red and the model in blue. The full spectrum can be found in Fig. C.1.

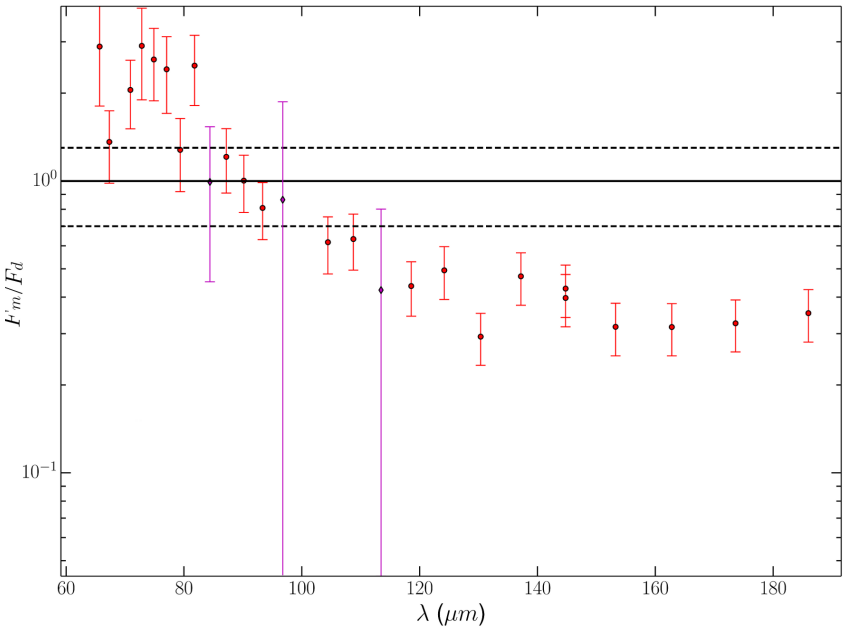

Figure 4.7: ^{12}CO fractional integrated intensity ratio of model lines compared to Gaussian fits to the data for the APEX cooling model. Purple error bars indicate blended lines. Note the log scale on the ordinate axis.

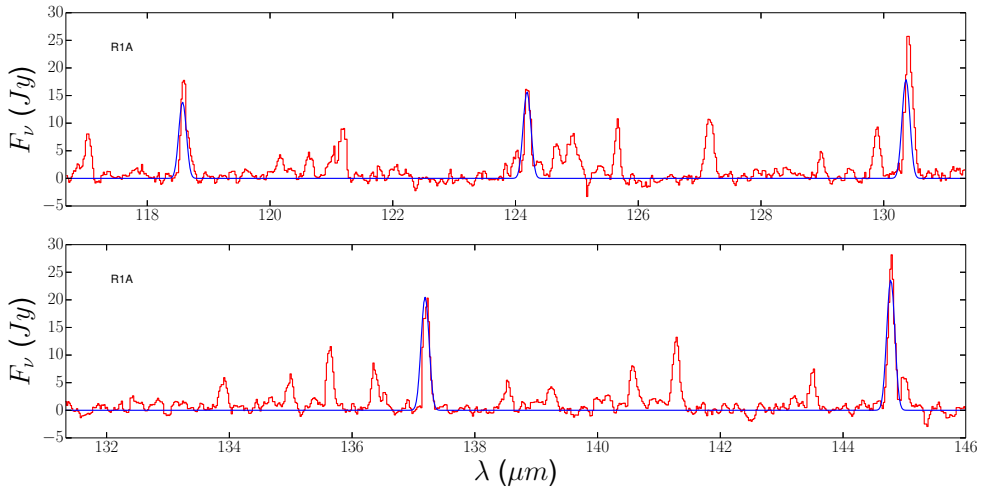

Figure 4.8: Partial PACS model-data comparison for the Pacs Epsilon model. Data is shown in red and the model in blue. The full spectrum can be found in Fig. C.2.

flux calibration at these wavelengths and the signal-to-noise ratios of these lines is low. Khouri et al. (2014) in their analysis of CO in W Hya only use PACS observations of lines up to J= $24-23$ (~ 108 μm) for these reasons.

A sample of the model-data comparison for this model is shown in Fig. 4.8. The fractional difference between the integrated intensities as measured from the model lines and from Gaussian fits to the PACS data for each transition are shown in Fig. 4.9. A comparison between the APEX and model data can be found in Fig. 4.10. This model is henceforth referred to as the "PACS epsilon model" (PE model). As can be seen, it generally has good agreement with the PACS data except in the innermost region of the envelope, where the model assumptions are likely to be invalid. However, this model has poor agreement with the APEX data, overestimating all lines by a factor of three or more. Improvements in the agreement between the PACS data and model were accompanied by a decline in the agreement between the APEX model and data and vice versa.

The two models differ only on the basis of temperature profile through the envelope. Each spectral line is formed from a slightly different region of the envelope, some of which overlap with one another. The higher level transitions

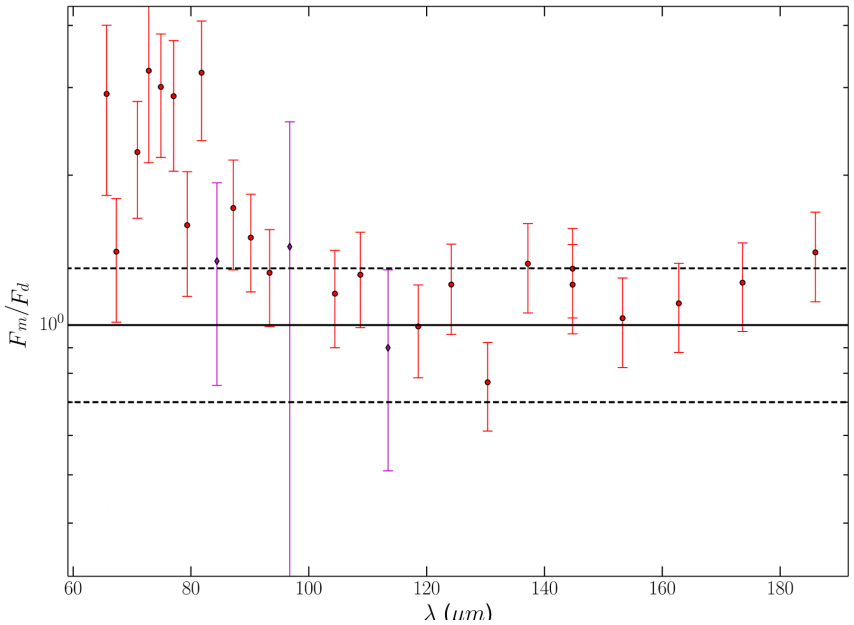

Figure 4.9: ^{12}CO fractional integrated intensity ratio of model lines compared to Gaussian fits to the data for the Pacs Epsilon model. Purple error bars indicate blended lines. Note the log scale on the ordinate axis.

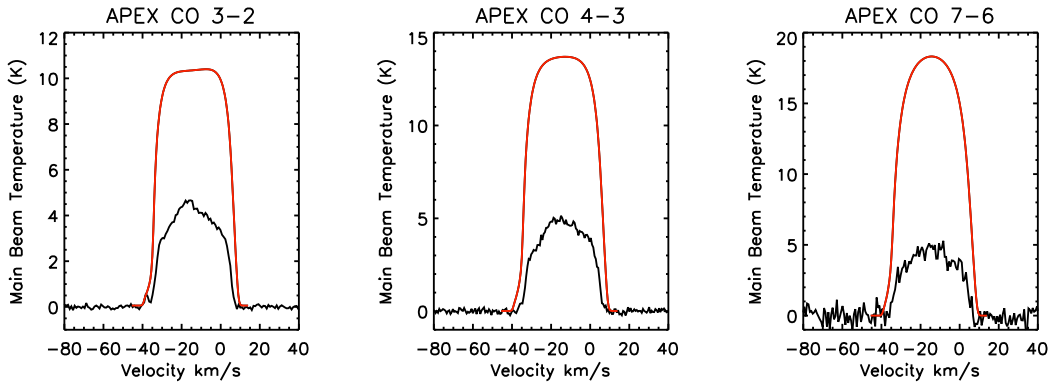

Figure 4.10: ^{12}CO APEX model-data comparison for the Pacs Epsilon model. The data is shown in black and the model in red.

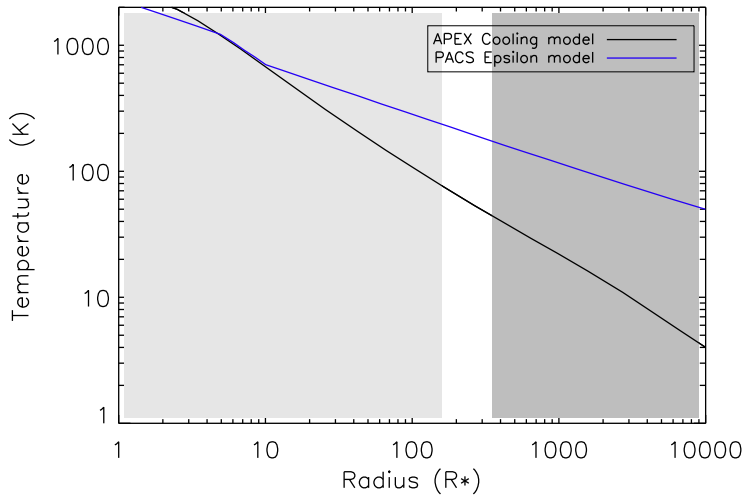

Figure 4.11: APEX cooling (AC) and PACS Epsilon (PE) model temperature profiles. The AC model is shown in black and the PE model in blue. The light grey area indicates the region which dominates the PACS line emission and the dark grey indicates the region dominating the APEX line emission.

originate in regions of the envelope closer to the star than the lower lying transitions. The temperature profile through the envelope for both the PE model and the AC model are shown in Fig. 4.11. Overlaid are the regions of the envelope that dominate the PACS lines and the APEX lines.

As can be seen in Fig. 4.11, the PE model has a significantly higher temperature in the APEX line emission region of the envelope than the AC model and the AC model has a lower temperature in the PACS dominated region than the PE model. As the line intensities are sensitive to the gas temperature in the region of formation, this explains the discrepancy between the fits of the two models. This difference between the two regions suggests that either there is a temperature discontinuity in the envelope or one of the assumptions in the model does not hold for this star. If the latter, it is likely that the assumption of constant mass loss does not apply, as the intensities of the gas lines correlate strongly with gas mass loss rate (see Sect. 4.5.2).

To examine the possibility of a discontinuous temperature profile, the tem-

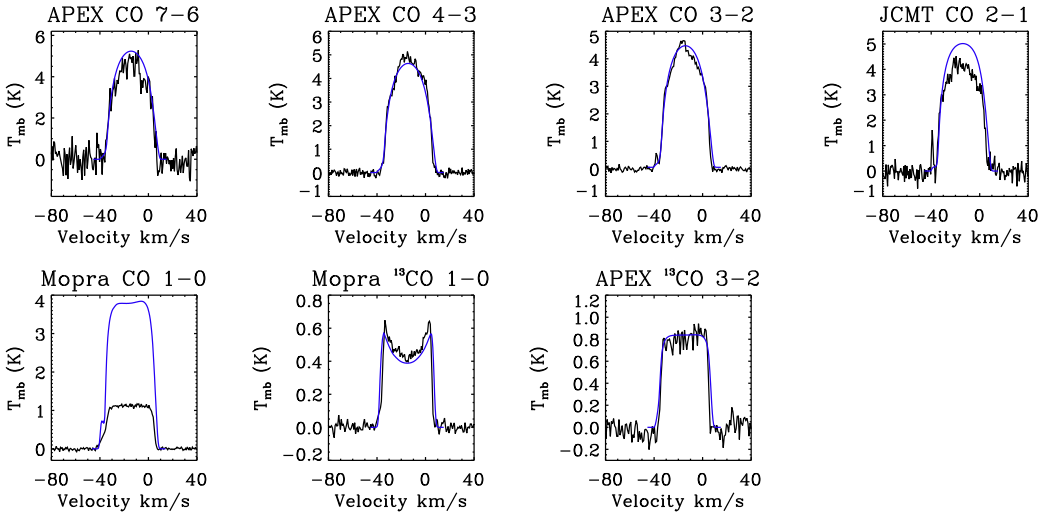

Figure 4.12: ^{12}CO APEX, Mopra and JCMT model-data comparison for the DT model. The data is shown in black and the model in red.

perature profile power-law was broken into three parts: the first following the PE model temperature profile, the third following the AC model and the second part introduced a temperature drop in the region between the two profiles. This led to the model henceforth known as the "discontinuous temperature model" (DT model), whose details are shown in Fig. 4.12 to 4.14.

The alternative explanation is that the assumption of a constant mass-loss does not apply to II Lup. ComboCode allows the user to define different mass-loss rates in different regions of the envelope. The AC model was taken as the base model. The gas mass-loss rate was 1.4×10^{-5} $M_{\odot}$ and the temperature profile was calculated using the Cooling code. The PACS lines in the AC model are too intense in the 60-80 μm region of the spectrum and are too weak in the 100-190 μm region. Decreasing the mass-loss rate leads to an decrease in the intensity of the model emission lines. Therefore the mass loss rate in the innermost region of the envelope, from which the 60-80 μm emission lines originate, needed to be decreased. The mass-loss rate in the more central region of the envelope had to be increased in comparison to the base model gas mass loss

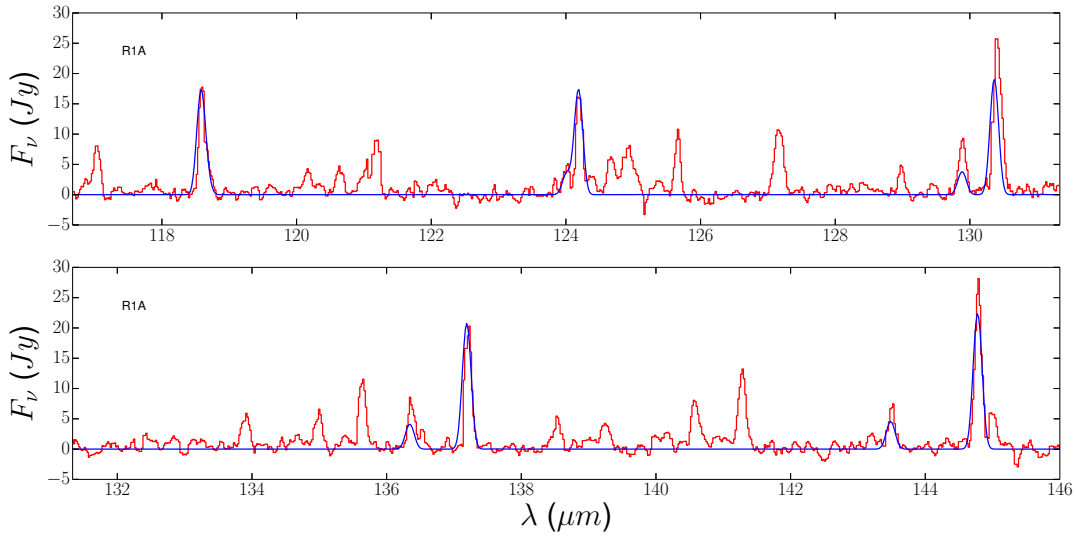

Figure 4.13: Partial PACS model-data comparison for the DT model. Data is shown in red and the model in blue. The full spectrum can be found in Fig. C.3. Figure shows both ^{12}CO and ^{13}CO lines.

rate. The outer region ($R > 300$ R*), in which the APEX lines form, required no change in mass-loss rate.

The optimum changes in mass loss rates were obtained by gridding over 4 orders of magnitude, initially as a coarse grid which was then followed by consistently finer grids as the mass-loss rates were refined. The radial points where the mass-loss changes were required were obtained in a similar fashion. The model resulting from these grids is henceforth known as the "variable mass loss model" (VM model) and had 3 different mass-loss rate regions. The innermost region (2-75 R*) had a mass-loss rate of 0.8×10^{-6} M$_\odot$ yr^{-1}, the central region (75-190 R*) had a massloss rate of 1.4×10^{-4} M$_\odot$ yr^{-1}, and the outer region (>190 R*) had a mass-loss rate of 1.1×10^{-5} M$_\odot$ yr^{-1}. The lines in the inner region (wavelengths < 90 μm) were significantly affected by the changing mass-loss rate, but this was compensated for by the inclusion of the low mass-loss rate in the inner-most region of the CSE. However, as previously mentioned, this region is not well-constrained theoretically (e.g. shocks may play an important role) thus this low mass-loss rate should be taken with caution.

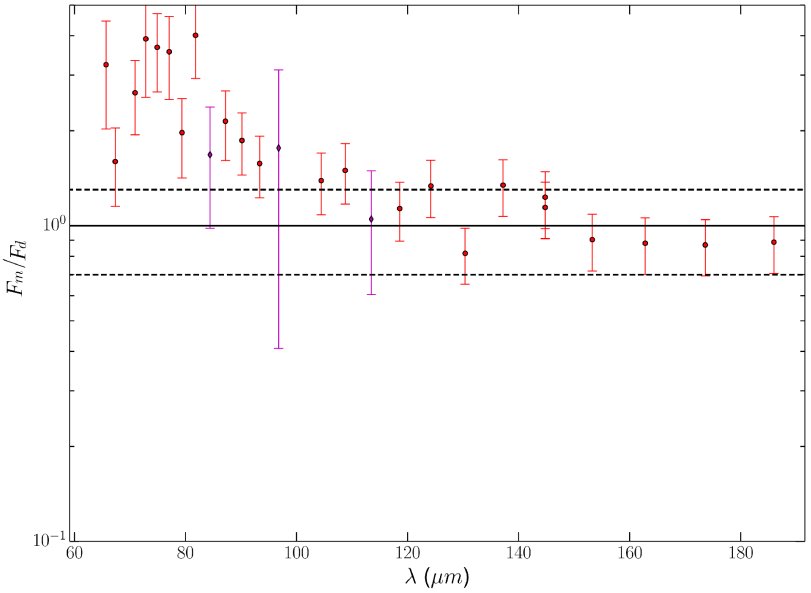

(a) ^{12}CO

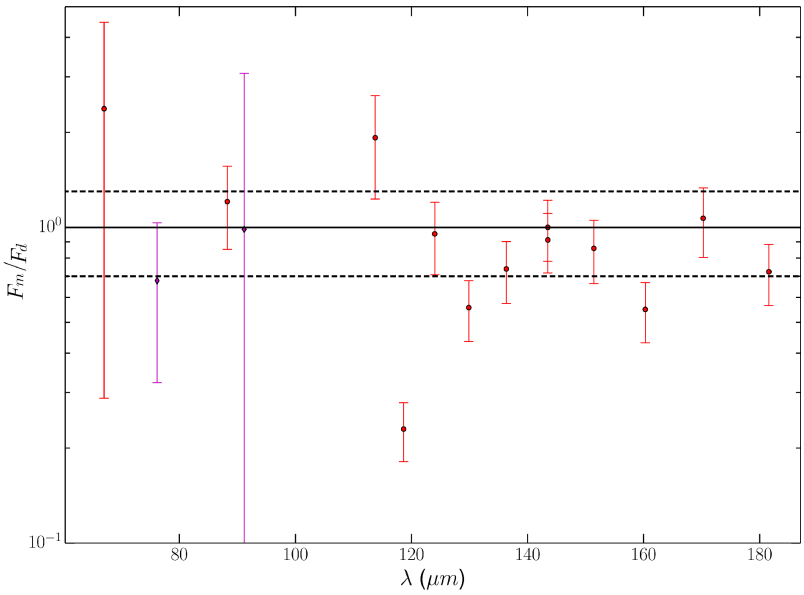

(b) ^{13}CO

Figure 4.14: ^{12}CO and ^{13}CO fractional integrated intensity ratio of the DT model lines compared to Gaussian fits to the data. Purple error bars indicate blended lines. Note the log scale on the ordinate axis.

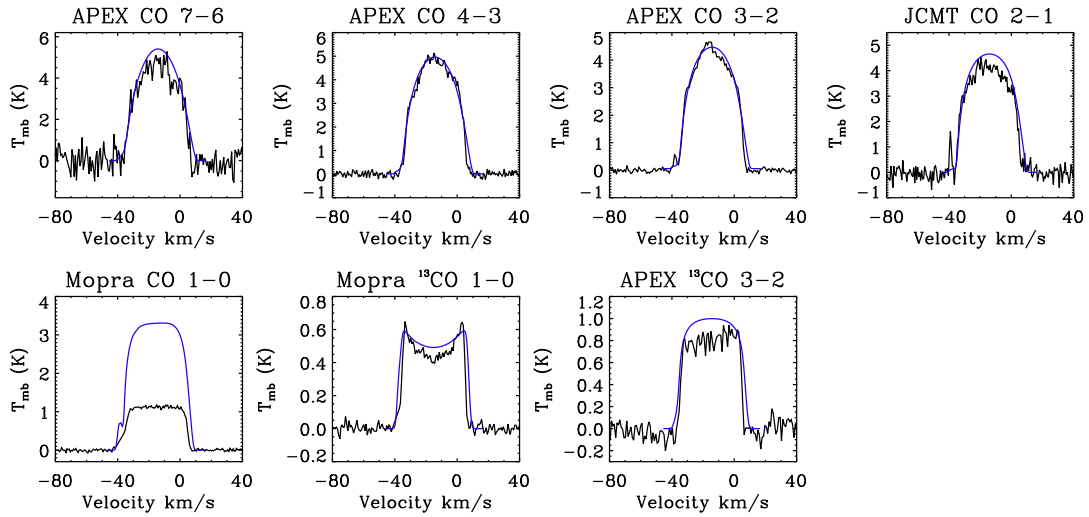

Figure 4.15: ^{12}CO APEX, Mopra and JCMT model-data comparison for the VM model. The data is shown in black and the model in blue.

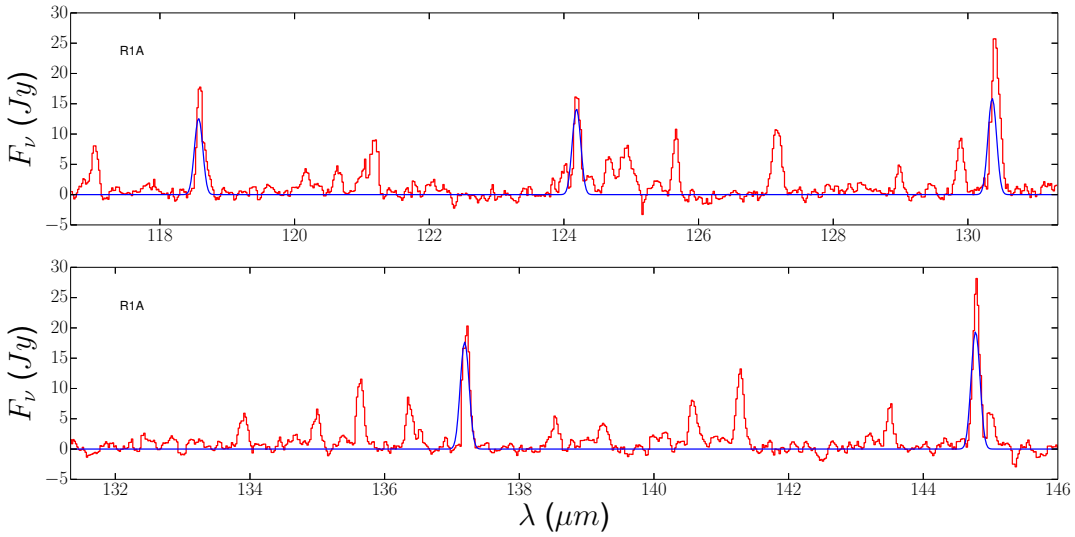

Figure 4.16: Partial PACS model-data comparison for the VM model. Data is shown in red and the model in blue. The full spectrum can be found in Fig. C.4.

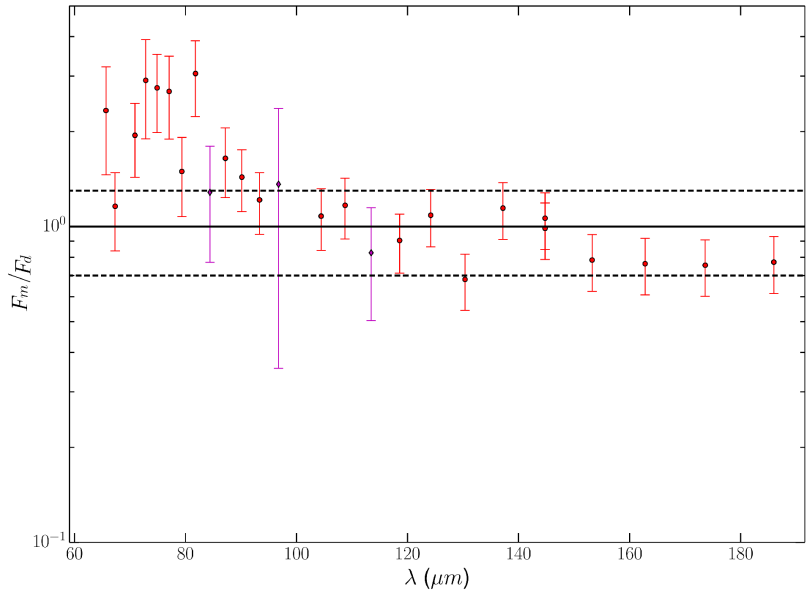

(a) ^{12}CO

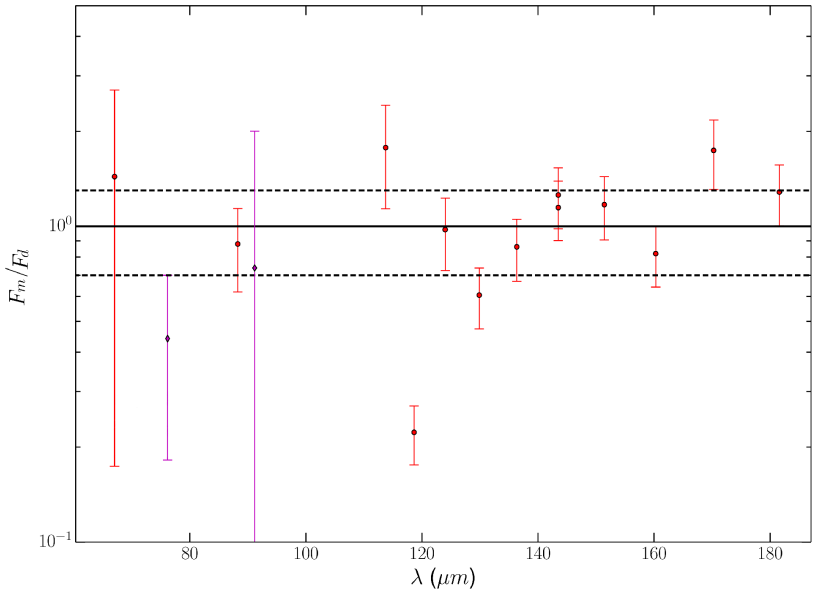

(b) ^{13}CO

Figure 4.17: ^{12}CO and ^{13}CO fractional integrated intensity ratios of the VM model lines compared to Gaussian fits to the data. Purple error bars indicate blended lines. Note the log scale on the ordinate axis.

Having obtained two models that satisfactorily fit the PACS and APEX data (VM model and DT model), the final datasets were included. These consisted of the Mopra CO and ^{13}CO J=1-0 lines, the APEX ^{13}CO J=3-2 line and a JCMT J=2-1 line. The ^{12}C/^{13}C ratio was adjusted until an optimal fit was obtained. The ^{13}CO lines are matched by both models to within 10%-15% which is within the calibrated uncertainty of the data.

The parameters for the VM model and the DT model are detailed in Table 4.4.

4.5 Model sensitivity to input parameters

4.5.1 Dust model

A number of different parameters affect the shape of the model SED. These are primarily related to the physical parameters of the dust.

The composition, shape and size distribution of the dust grains has a large effect on the appearance of the SED. Some components, such as SiC and MgS, have characteristic features (e.g. SiC at $\sim$11 μm and MgS between approximately 25 and 50 μm) which would otherwise not exist in the spectra, whilst others affect the overall shape of the SED. For example, changing the fraction of dust from amorphous carbon in a continuous distribution of ellipsoids to amorphous carbon as a distribution of hollow spheres increases the peak intensity and shifts it towards the longer wavelength region of the spectrum whilst reducing emission at the shorter wavelengths.

A variety of compositions were modelled in the initial grid and it was found that a composition of 75% amorphous carbon (distribution of hollow spheres) with 20% MgS and 5% SiC best recreated the observed SED. A number of species that cause significant absorption features, such as HCN and C_2H, are not possible to include in MCMax, hence why these features are not seen in the model spectrum.

The resulting SED has a strong dependence upon the dust mass-loss rate.

Table 4.4: Parameters of each of the models discussed in detail within this chapter. The temperature structure is listed either as COOLING or as the input parameters for the epsilon temperature scheme: $T(r) \propto r^{-\varepsilon}$. In cases where the outer radius is listed as Mamon, the limit of the envelope was defined as the CO photodissociation radius from the formula of Mamon, Glassgold & Huggins (1988).

Parameter	DT Model	VM model	AC model	PE model
$\dot{M}_{gas}$ ($M_\odot$ yr^{-1})	1.4×10^{-5}	0.8×10^{-6} (2-75 R*)	1.4×10^{-5}	1.4×10^{-5}
		1.4×10^{-4} (75-190 R*)		
		1.1×10^{-5} (>190 R*)		
Temp. Structure	ε_1: 0.45 (< 75 R*)	COOLING	COOLING	ε_1: 0.4 (< 5 R*)
	ε_2: 2.0 (75-200 R*)			ε_2: 0.8 (5-10 R*)
	ε_3: 0.55 (>200 R*)			ε_3: 0.4 (>10 R*)
$^{12}C/^{13}C$	8	9	...	...
Terminal velocity (km/s)	21.5	18.5	21.5	21.5
Gas outer radius	8500 R*	8500 R*	Mamon	Mamon

Changing the dust mass-loss rate alters the position and height of the peak, with higher mass-loss rates moving the peak of the profile towards longer wavelengths. When the dust mass loss rate is too high, the model has an excess of emission at wavelengths longer than approximately 7 μm and has a deficit at shorter wavelengths.

Changing the central star black body temperature has a small effect on the model SED. Increasing the central star black body temperature decreases the peak intensity and shifts the distribution to the shorter wavelength end of the spectrum. The SED is more sensitive to changes in luminosity than temperature, with increases to the luminosity causing increases in all regions of the spectrum.

Decreasing the outer radius decreases the intensity of the emission in the longer wavelength tail of the SED - the region made up of the PACS and LWS data sets.

Two switches in MCMax affect the model SED. One is whether or not there should be thermal contact between the dust particles and the other is whether high temperature dust should be destroyed. Turning off the thermal contact results in decreased emission in the SiC and MgS spectral feature regions of the SED. Turning off high temperature dust destruction reduces the emission in the shorter wavelength regions whilst increasing the emission at the higher wavelength region - a surprising result as one would expect the shorter wavelength emission to increase if dust is allowed to form closer to the stellar surface than the model would otherwise allow. This reduction in low-wavelength intensity may be caused by an increase in obscuration of the star by the dust when high temperature dust destruction is turned off. Our best fit model was found by turning off the high temperature dust destruction and keeping thermal contact on.

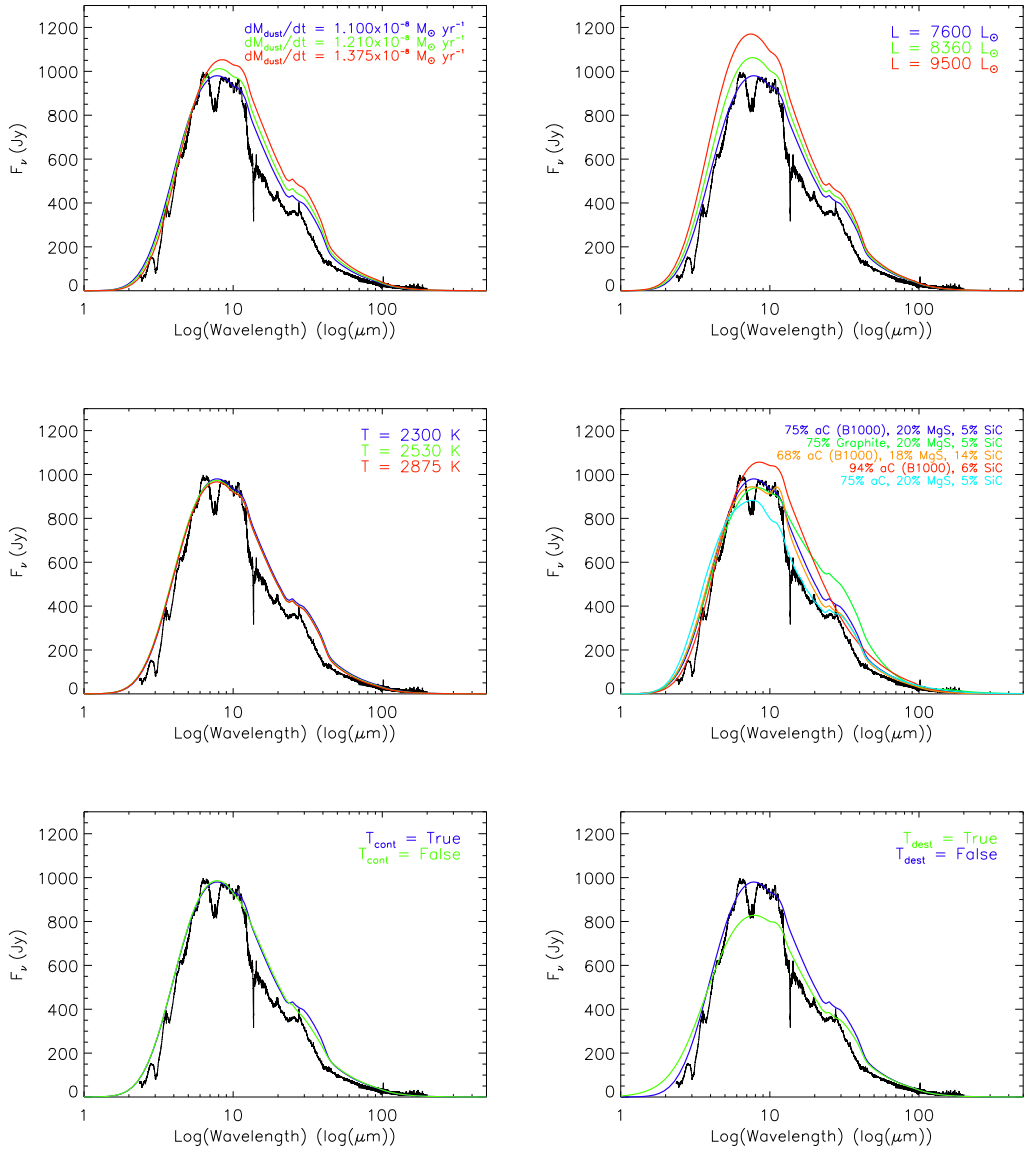

Figure 4.18: The effect of varying different model parameters on the model SED. Parameters are the same in all models, except for the single parameter being varied. These are, top to bottom, left to right: dust mass-loss rate, luminosity of the central star, effective temperature of the central star, dust composition, thermal contact between dust (true or false), destruction of high temperature dust (true or false) and outer dust radius.

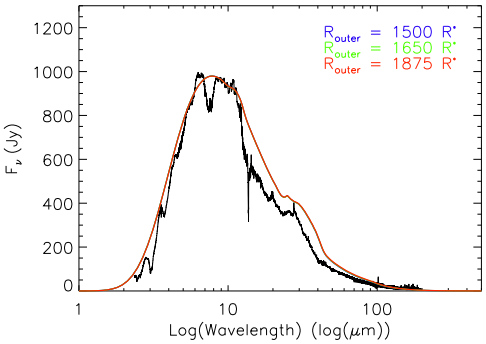

Figure 4.18: – *continued.*

4.5.2 Line profile sensitivity

A number of parameters affect the intensities and shapes of the emission lines. Shown in Fig. 4.19 are the effects of various parameters on the J=1-0, J=3-2 and J=7-6 lines of ^{12}CO. The lines shown in each plot are the base value (blue), the base value +10% (green) and the base value +25% (red). The base values are listed in the figure caption and are the parameters for the best APEX model for II Lup, barring the outer radius which was set to 8500 R* rather than that of Mamon, Glassgold & Huggins (1988). In the figure showing changes to the outer radius, the colours indicate: 8500 R* (blue), 5000 R* (green) and 1500 R* (red). This is so the changes to line profile can be seen.

As is shown in Fig. 4.19, increasing the luminosity increases the peak intensity of all the emission lines. There is no discernible change in line profile with increasing intensity. As the SED is very sensitive to changes in luminosity, this parameter was left unchanged in the line modelling and was instead set by the SED models.

Changing the gas mass-loss rate has a smaller effect on the spectral lines than altering the luminosity. However, in contrast to the luminosity, the gas mass-loss rate has a negligible effect on the SED, allowing this parameter to be varied significantly. Increasing and decreasing the gas mass-loss rate at various

points in the envelope leads to different lines increasing or decreasing in intensity respectively.

The size of the gas outer radius has a significant effect on the intensity of the J=1-0 line; the effect becomes progressively weaker as the transitions increase in energy. The low-J lines originate predominantly from the outer region of the envelope whilst the higher energy transitions form from regions in closer proximity to the star, causing the aforementioned effect that varies with transition. As the outer radius is decreased, the J=1-0 line decreases in intensity and the profile gradually changes from a flat-topped parabola (indicating optically thick emission) to a horned profile (indicating optically thin emission).

Increasing the black-body temperature of the central star, whilst having a negligible effect on the SED, decreases the intensity of the emission lines. The effect is, again, related to the energy of the transition: it is greatest on the lowest level lines with the higher level lines least affected. However, the J=3-2 line is more susceptible to changes in the black body temperature than to changes in the outer radius, allowing the temperature to be well-constrained independently.

Finally, the terminal velocity has the same effect on all the emission lines: increasing the terminal velocity leads to a broadening of the line and a reduction in intensity. The terminal velocity has been constrained solely by the width of the lines as many other parameters affect the intensities.

4.6 Understanding the envelope of II Lup

4.6.1 Physical interpretation of the models

It is apparent that a 'standard' smooth model does not fit the CO emission of II Lup. The APEX emission lines were well represented by a model of constant mass loss and temperature calculated self-consistently with the Cooling code. However, this was not the case for the PACS emission lines. With constant mass

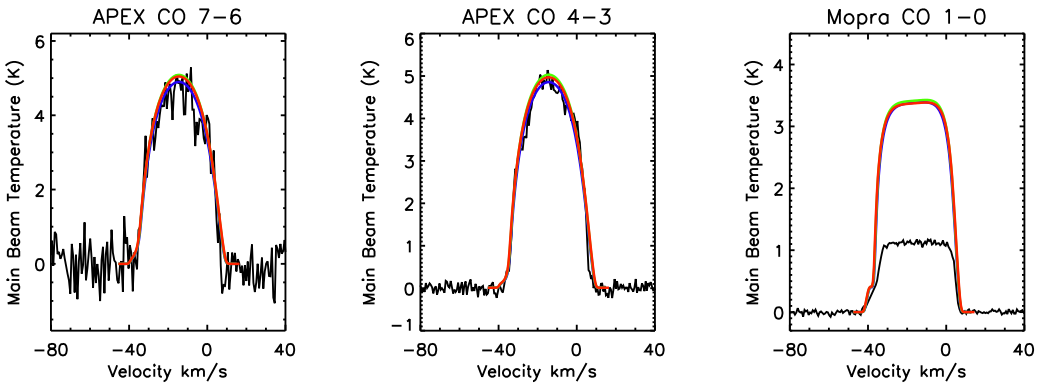

(a) Changing luminosity.

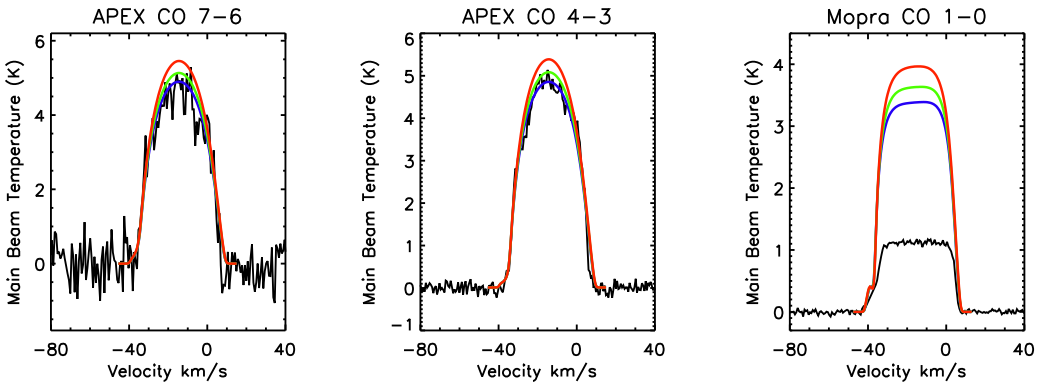

(b) Changing gas mass-loss rate

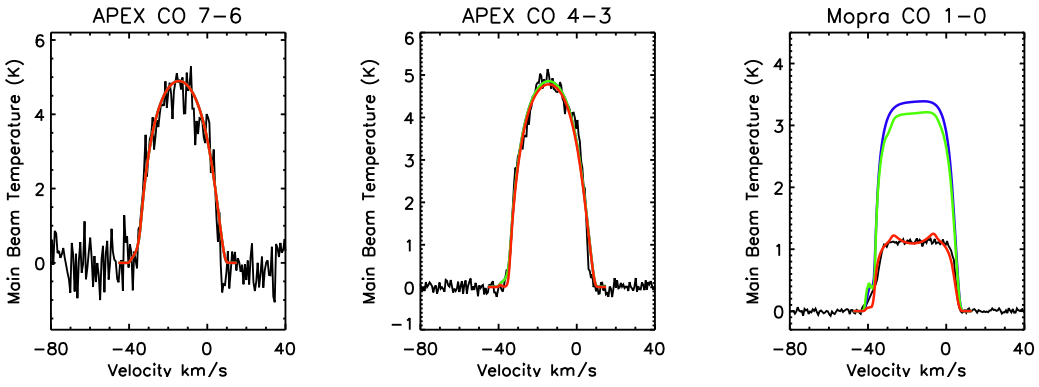

(c) Changing gas outer radius.

Figure 4.19: The effect of varying different model parameters on the model profiles. Parameters are the same in all models, except for the single parameter being varied. Blue line indicates original value, green indicates original value + 10% and red indicates original value + 25%, barring for the outer radius change where the colours indicate: 8500 R* (blue), 5000 R* (green) and 1500 R* (red). In the plot varying the terminal velocity, the velocity base value was taken as 18.5 km/s rather than the 21.5 km/s that was taken for the others.

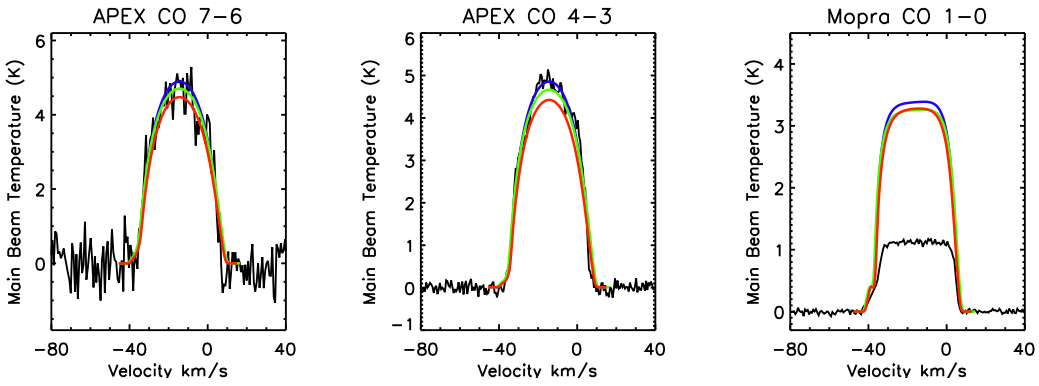

(d) Changing central star BB temperature.

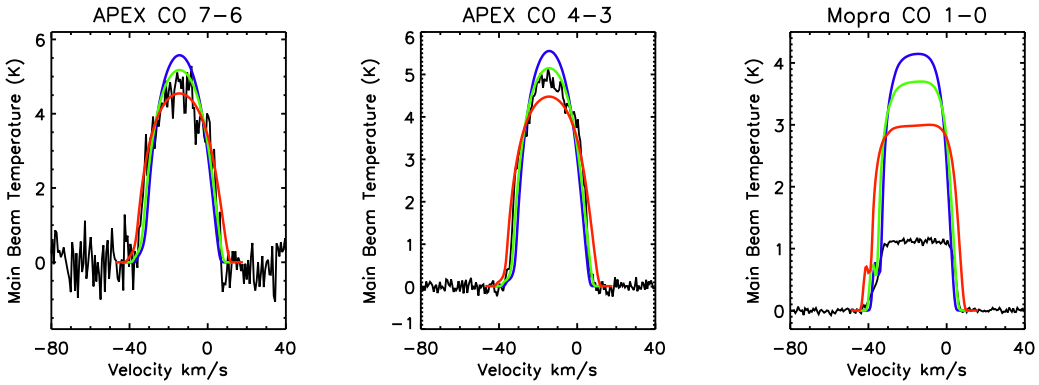

(e) Changing terminal velocity.

Figure 4.19: – *continued.*

loss and a COOLING temperature profile, the integrated intensities of the lines emanating from the innermost region of the envelope were overestimated and those in the central region underestimated. Two different approaches to solving these discrepancies were explored: a model with a variable mass loss rate through the envelope and a model with a region of heavy cooling. Neither model can be ruled out on the current data, although due to the atypical nature of some of the physical properties resulting from the variable mass-loss rate (described in further detail in Sect. 4.6.2), the DT model is considered to be more likely. Outlined below are the physical interpretation of both models and what would be required to distinguish between the two cases.

Variable mass loss

A model using a variable mass loss through the envelope satisfactorily fits the combination of PACS and APEX lines simultaneously. The mass loss has been found to be at its lowest in the region R <75 R*, with a mass loss rate of 0.8×10^{-6} $M_{\odot}$ yr^{-1}. The central region, 75 R*< R <190 R*, has a mass loss of 1.4×10^{-4} $M_{\odot}$ yr^{-1} and the outer region, R> 190 R*, has a mass loss rate of 1.1×10^{-5} $M_{\odot}$ yr^{-1}. The mass-loss rate in the inner region should be taken with some degree of caution as many of the assumptions made in the model do not apply in this region.

The model structure can be interpreted as evidence of the existence of a CO shell in the envelope of II Lup, potentially as the result of a thermal pulse. Similar shells have been reported in the literature (e.g. Maercker et al. 2012, Olofsson et al. 2010) from observations of CO. The shells of R Scl and U Cam in particular show similar traits to the theoretical shell structure required in this model. The thickness of our high-mass-loss shell ($\sim$ 125 R* in width, equivalent to 4.8×10^{15} cm) is in very good agreement with the widths of the shells of R Scl and U Cam at 5×10^{15} cm and 4×10^{15} cm respectively (Olofsson et al. 2010). Using the gas terminal velocity of 21.5 km/s, the duration of our theoretical shell is 70 years, which is in good agreement of those of R Scl (100 years) and U Cam (50 years). The major difference between our shell and the literature shells is its distance from the star. Taking the radius as the centre of the shell to the centre of the star, our shell exists at 140 R*, which is equivalent to a distance of 5.3×10^{15} cm: an order of magnitude less than the radii of the shells of R Scl and U Cam (Olofsson et al. 2010). This indicates that the shell of II Lup would have to be substantially younger than those of R Scl and U Cam: 80 years in comparison to 1700 and 700 years for R Scl and U Cam respectively (Olofsson et al. 2010).

Feast, Whitelock & Marang (2003) carried out photometric monitoring of II Lup over 18 years and from this have found evidence for asymmetries in the

circumstellar envelope. They attribute this to the formation and destruction of "quasi-spherical dust shells" in the line of sight which can cause significant changes in the observed luminosity in the J-band. Although this work is based upon dust structure and these shells are closer to the star than the one we identify, given asymmetries exist in the dust distribution, it is likely that asymmetries also exist in the gas.

The most effective way to test this model would be to obtain high resolution imaging of the CO emission, as has been done for R Scl. If a high mass-loss rate region exists, this would be seen as a ring or similar structure in the envelope when mapped in CO. If this region were not seen in the imaging, then this model could be ruled out with certainty.

Intense cooling

The alternative model of II Lup retains a constant mass loss rate throughout the envelope but requires a significant reduction in the gas temperature in the region $75 < R < 200$ R*. This would require the presence of an efficient cooling molecule in the envelope (e.g. HCN) which is less abundant or less efficient at cooling in the inner region and outer region than in the central region (R. Lombaert, priv. comm.).

The HCN absorption bands are strong in the II Lup SWS spectrum, indicating relatively high abundances of HCN are present. From the line profile analysis of the molecular line survey in Chapt. 2, the HCN 1-0 emission region appears to be less extended than the CO 1-0 emission region in II Lup, although the magnitude of the difference is unclear. HCN therefore has a different radial abundance profile and it is plausible that its cooling effects may be more noticeable in the central regions of the envelope.

The most effective way to test this model would be to carry out a full radiative transfer analysis of HCN and include HCN cooling in the model of II Lup. The former is beyond the scope of this work, but is an avenue of future work.

Alternative explanations

There are a number of other potential explanations for the difference in intensities between the central and outer regions of the envelope. As reported by Teyssier et al. (2014), variable infrared fluxes in the central region can cause significant changes in the intensities of a number of emission lines. Teyssier et al. (2014) studied the time variability of emission lines in IRC+10216 using PACS, HIFI and Spire onboard *Herschel*. They found variations in the intensities of the high J ($J_u > 15$, $\lambda < 174\,\mu m$) lines of many molecules including CO due to the changing infrared flux in the envelope caused by stellar pulsations. The low J lines of CO and ^{13}CO were unaffected. Infrared pumping is not supported in GASTRoNOoM and we have data from only a single epoch, therefore this avenue could not be explored further.

It is possible that the abundance of CO may be higher in the central region of the envelope as a result of, for example gas-grain interactions (Millar, priv. comm.). This effect has been somewhat mimicked by the introduction of a higher gas mass-loss rate. This would result in a higher than expected emission from the high abundance region.

The presence of a torus may also explain the discrepancy between the inner and outer regions of the envelope. A torus, such as that found in V Hya (Lykou 2013; Hirano et al. 2004) could explain the extra cooling required in the DT model. The presence of a torus would cause higher opacities and increased cooling than would be observed in a standard smooth model. However, as the radiative transfer codes used in this investigation assume spherical symmetry, this could not be explored further. High spatial resolution imaging would be required to determine if a torus is present.

The effect of the beam sizes of the APEX data and PACS data were also examined. The smallest beam size is that of the APEX 7-6 line observation[2], with

[2]http://www.apex-telescope.org/telescope/efficiency/

a beam size of approximately 7.7″. The PACS beam sizes[3] vary with wavelength from 9.3″ to 13″. As the CO emission at the PACS wavelengths is originating from a smaller area than the 7-6 emission, which has the smallest beam size of all, and the APEX 7-6 emission appears unresolved (parabolic profile), it is unlikely that the beam size is causing the problem with the CO line intensities.

Mopra CO 1-0 line

In all models, the intensity of the CO 1-0 line in the Mopra data could not be well recreated. The intensity was only able to be recreated by setting the gas outer radius to approximately 1500 R*, which is approximately an order of magnitude smaller than the CO dissociation radius predicted by Mamon, Glassgold & Huggins (1988). Additionally, the model line profile takes a horned appearance at 1500 R*, implying the emission in this case is optically thin. Reducing the radius to 1500 R* also had a detrimental effect on the J=2-1 line fit.

The peak intensity of the Mopra CO 1-0 line (1.17 K) is approximately 10% lower than that reported in Nyman et al. (1993), Ryde, Schöier & Olofsson (1999) and Woods et al. (2003), which were all taken using the Swedish ESO Submillimeter Telescope (SEST). SEST has a diameter of 15m, whereas Mopra has a diameter of 22m. Assuming that the source is resolved in both beams, the Mopra observation would be expected to have a higher intensity ($T_{mb} \sim 3$ K) which would bring the observation in line with the model prediction. The ^{13}CO line in Mopra has a peak intensity approximately 1.5 times that of the ^{13}CO line in Ryde, Schöier & Olofsson (1999). Therefore there may be a problem with the calibration of the Mopra CO 1-0 line and this requires further investigation.

[3]http://herschel.esac.esa.int/Docs/PACS/html/ch04s06.html

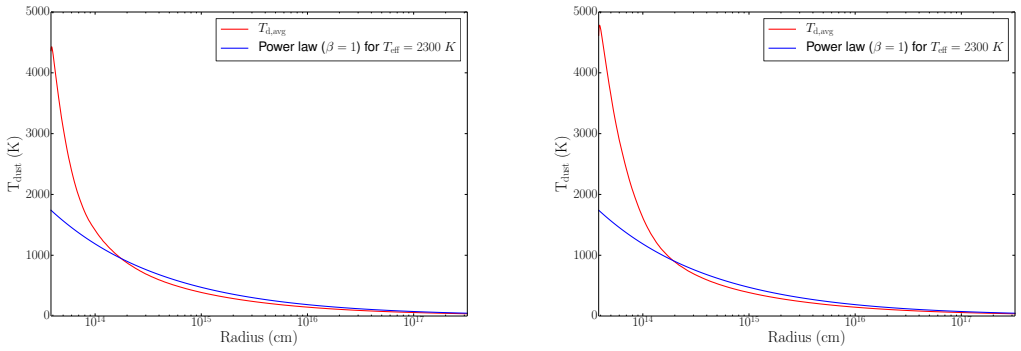

(a) DT model dust temperature profile.

(b) VM model dust temperature profile.

Figure 4.20: Dust temperature profiles for both the DT and VM models. The power law, which would be the assumed dust temperature profile of GASTRoNOoM if MCMax were not used, is shown in blue on both plots.

4.6.2 Insights into the composition and thermodynamics

In addition to the aforementioned insights into the overall structure of the envelope of II Lup, more specific information can be gleaned from the two final models. Below these are discussed in further detail.

Dust properties

Further to the discussion of the dust composition in Sect. 4.4.1, the models also allow us to examine the temperature distribution of the dust and the opacities of the individual species. Shown in Fig. 4.20 are the dust temperature profiles through the envelope. As the dust in both models was set to be in thermal contact, all species are assumed to have the same temperature.

There is little difference between the dust temperature profiles of the two models. The initial temperature of the VM model is ∼500 K higher than that of the DT model. Both temperature profiles are initially higher than a standard power law for 2300 K (the assumed dust temperature profile of GASTRoNOoM if MCMax were not used, shown in blue on both plots) and at $\sim 1 \times 10^{14}$ cm, the dust temperature profiles drop below the power law. The power law is of the

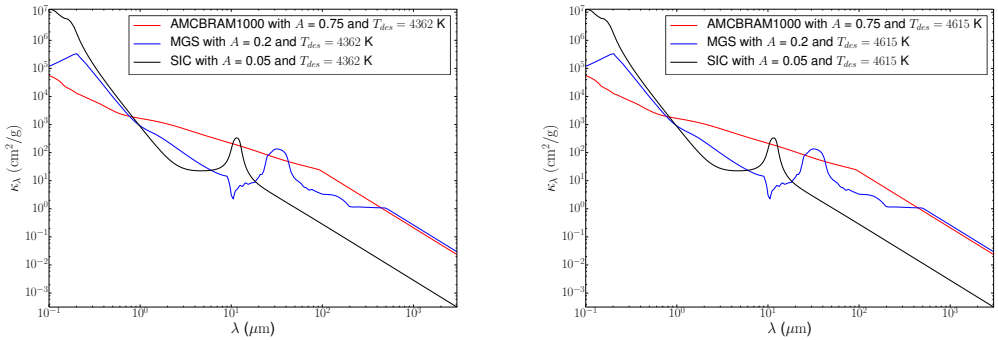

(a) DT model opacities for all dust species. (b) VM model opacities for all dust species.

Figure 4.21: Dust opacity profiles for all species in the DT and VM models.

form:

$$T_{\rm d}(r) = T_* \left(\frac{R_*}{2r}\right)^{\frac{2}{4+\beta}}, \tag{4.2}$$

where $T_{\rm d}(r)$ is the dust temperature as a function of radius, r, T_* and R_* are the stellar temperature and radius respectively and β has been taken as 1 (Decin et al. 2006; Habing & Olofsson 2012).

The opacities of the different dust species as a function of wavelength from the MCMax models are shown in Fig. 4.21. The opacities, as expected, do not differ greatly between the two models. SiC and MgS have their characteristic peaks at ∼10 µm and ∼30 µm and the amorphous carbon shows a general trend of decreasing in opacity with increasing wavelength.

Temperature structure

The gas temperature structure varies significantly between the two models. The VM model uses the self-consistent cooling calculations included in the Cooling code, whereas the DT model has a three-step power law function including a drop in the central region of the envelope. These profiles are shown in Fig. 4.22. The irregular section of the VM model plot is due to the high mass-loss rate

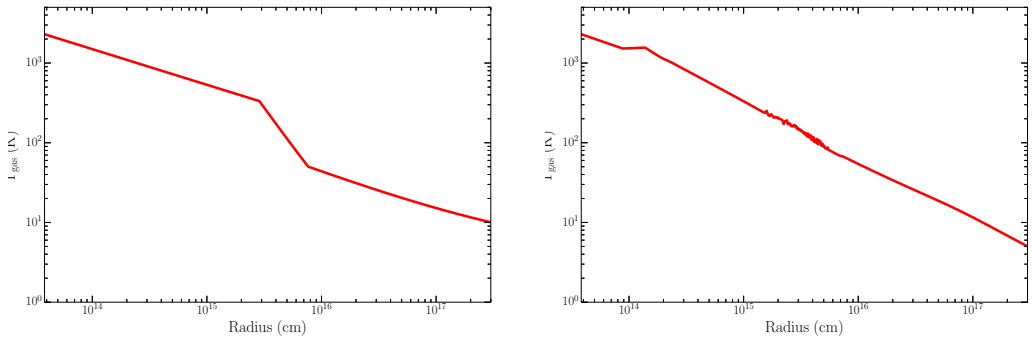

(a) DT model gas temperature profile. (b) VM model gas temperature profile.

Figure 4.22: Gas temperature profiles for the DT and VM models.

within that region, but should not significantly affect the line profiles presented in previous sections (R. Lombaert, priv. comm.).

Velocity structure

The gas velocity structures differ between the DT and VM models. As is shown in Fig. 4.23, the DT model has a smoother profile with a steep initial increase followed by a flattening at larger radii. In contrast, the increase in the VM model occurs at a larger radius with the initial velocity being significantly lower than that of the DT model. This reduction in velocity would most likely be accompanied by a reduction in line width of the highest J-lines in comparison to those of the DT model. This would have been observed as a reduction of the high-J model line integrated intensity in comparison to the observed data in this model.

Abundances and abundance distribution

The abundance distributions of CO and ^{13}CO show the greatest difference between the two models - predominantly due to the variation in mass loss through the envelope in the VM model. The abundance of CO has a smooth, mostly flat profile in log-log space, with a drop in the outer region in the DT model. This

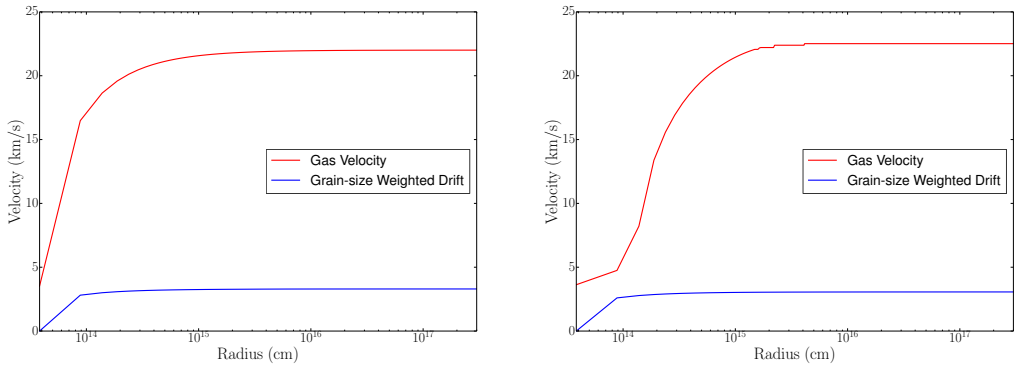

(a) DT model velocity profiles. (b) VM model velocity profiles.

Figure 4.23: Gas velocity profiles for the DT and VM models. 1 R* = 3.83×10^{13} cm.

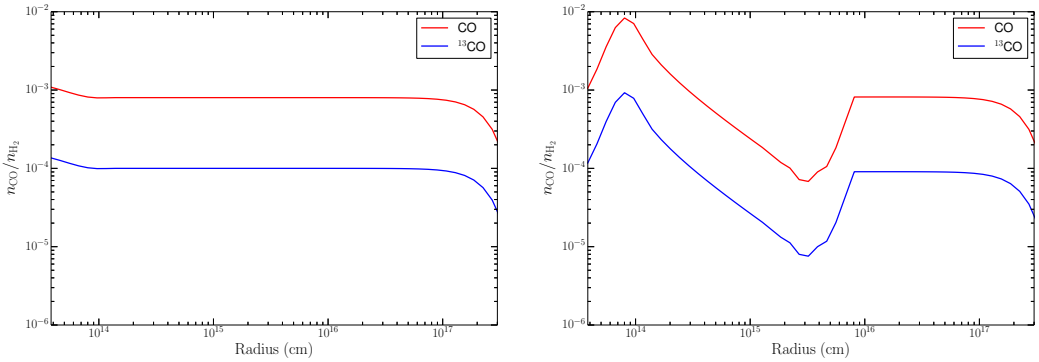

(a) DT model abundance profiles. (b) VM model abundance profiles.

Figure 4.24: CO and ^{13}CO abundance profiles for the DT and VM models.

is the profile expected for this type of object. However, the abundance of CO and ^{13}CO in the VM model show an intense peak followed by a drop where the fractional composition with respect to hydrogen changes by 3 magnitudes. The CO and ^{13}CO distributions have similar, but offset, profiles when each model is considered individually. These atypical profiles are likely due to the constant dust mass-loss rate used in combination with a variable gas mass-loss rate.

The ^{12}C/^{13}C ratio has been found to be 8 and 9 from the DT and VM models respectively. Both of these values place II Lup in the J-type star category. These values are a factor of 2 higher than that obtained in Chapt. 2, which is within

the calculated uncertainties of the value calculated in Chapt. 2.

4.6.3 Comparison with literature models

Ryde, Schöier & Olofsson (1999) model eleven rotational transitions of CO and ^{13}CO lines in II Lup (J=1-0, J=2-1 and J=15-14 to J=22-21, ground vibrational state only). Their dataset comprises of *ISO* LWS data taken in 1997 combined with SEST data from Nyman et al. (1993). Their model assumes spherical symmetry and a constant mass-loss rate of $1.0 \pm 0.2 \times 10^{-5}$ M$_\odot$ yr^{-1} and they measure a ^{12}CO/^{13}CO ratio of 5.5 ± 1. These are in reasonable agreement with our findings both in this chapter and in Chapt. 2, considering uncertainties associated with all values. Ryde et al. (1999), however, do state that the large uncertainties on the LWS data mean that changes of up to a factor of three in mass loss rate would still agree well with their model. Ryde et al. (1999) find their LWS lines are formed from the region of the envelope within 10 R*, which is somewhat closer than our model predicts. Their low-J emission lines were found to be formed at distances larger than 1000 R*, which is further from the star than our model finds. Their models find that there have been no significant changes to the stellar wind over the last 5000 years, which is in opposition to the VM model but in agreement with the DT model.

Schöier, Ryde & Olofsson (2002) also model II Lup *ISO* LWS data after having modelled the SED from IRAS photometry, using DUSTY. Their mass-loss rates were calculated as $1.2 \pm 0.5 \times 10^{-5}$ M$_\odot$ yr^{-1} (gas model) and 3.5×10^{-6} M$_\odot$ yr^{-1} (total mass-loss rate obtained from dust mass-loss rate and dust-to-gas ratio from CO radiative transfer modelling). The former is in good agreement with our results. This difference in dust mass-loss rate is likely due to the different data used in the SED modelling which is dependent on pulse phase at the time of observation (De Beck et al. 2012).

Ramstedt & Olofsson (2014), as part of a larger survey, examine lower level

rotational transitions of CO and ^{13}CO in II Lup. Their data consists of J=1-0 to J=3-2 inclusive for both CO and ^{13}CO. Their work assumes a spherical symmetry, constant mass loss rate and constant expansion velocity. As with our work, Ramstedt & Olofsson (2014) utilise two different codes to model the dust and gas components: DUSTY (dust component) and the non-LTE code of Schöier & Olofsson (2001). Their model for II Lup has a higher luminosity and temperature (8900 $L_\odot$ and 2800 K respectively) than our model (7600 $L_\odot$ and 2300 K), and a lower distance is used (500 pc as opposed to 600pc). The difference in temperature and luminosity could be due to the different dust species used in the modelling or due to the dust continuum data being taken at a different phase than our SED data. Their gas mass-loss rate, at 1.5×10^{-5} $M_\odot$ yr^{-1}, is in good agreement with our value (1.4×10^{-5} $M_\odot$ yr^{-1}).

Schöier et al. (2013) use similar data to model CO and HCN emission from II Lup. Their derived mass loss rate (6×10^{-6} $M_\odot$ yr^{-1}) is more than a factor of two lower than our value, but their stellar temperature is more in line with our value than that of Ramstedt & Olofsson (2014), at 2400 K. They do not calculate ^{12}C/^{13}C so this cannot be compared.

Woods et al. (2003) use the non-LTE radiative code of Schöier & Olofsson (2001) to model the CO emission lines detected in their molecular line survey from SEST observations. Their models assume spherical symmetry, constant mass-loss rate, constant expansion velocity and a distance of 600 pc. The stellar temperature and luminosity used are lower and higher than ours respectively at 930 K and 8800 $L_\odot$. Their derived mass-loss rate (1.5×10^{-5} $M_\odot$ yr^{-1}) and ^{12}CO/^{13}CO ratio (6) are in reasonable agreement with our results.

4.7 Conclusions

In this chapter, we have presented the results of in-depth radiative transfer modelling of CO in the envelope of the mass-losing carbon-rich AGB star II Lup

(IRAS 15194-5115). Initially the SED, constructed from *ISO* SWS and LWS data in combination with *Herschel* PACS data, was modelled using MCMax - a 2D Monte Carlo radiative transfer program (used in a 1D capacity). Subsequently, the spectral lines were modelled using GASTRoNOoM - a 1D non-LTE radiative transfer code, capable of calculating gas thermodynamics, level populations and spectral line profiles.

The resulting models have shown that a 'standard' model does not fit the inner regions of II Lup. The lines originating in the innermost regions of the envelope were under-estimated by the model. The spectral lines formed in the central region of the envelope were over-estimated by the model. This lack of correlation was solved in two ways: by invoking a 3-term power law, including a strong reduction in temperature between 75 and 200 R* and by using a variable mass-loss rate through the envelope, including an intense mass-loss rate region between 75 and 190 R*. Whilst neither model may be ruled out on current data alone, based upon the characteristics of the velocity profiles and the fits to the low-level J-lines of CO, the intense cooling model appears to better represent II Lup.

Neither model has successfully reproduced the CO J=1-0 line, over-estimating it by a factor of 3, whilst satisfactorily reproducing the ^{13}CO J=1-0. The intensity of the J=1-0 line in the data presented here is well-matched by literature observations (e.g. Woods et al. 2003; Nyman et al. 1993). It is possible that the CO J=1-0 line is sufficiently optically thick to have entirely obscured the CMB. By adding 2.7 K to the observed line intensities, the model and data are brought into reasonable agreement.

Chapter 5

Zinc abundances of planetary nebulae

Part of the work in this chapter has been published in Smith, Zijlstra & Dinerstein (2014).

5.1 Introduction

Iron has been shown to be heavily depleted from the gaseous form in ionised media through both optical (Delgado Inglada et al. 2009; Shields 1975) and infrared observations (Likkel et al. 2006). In planetary nebulae it can be depleted by more than 90% (Delgado Inglada et al. 2009). As shown in Sterling et al. (2005), depletion may be not be uniform throughout a planetary nebula. Iron depletion is also seen in many environments in the interstellar medium (ISM) (McDonald et al. 2010; Savage & Sembach 1996). Therefore deriving iron abundances of planetary nebulae through direct observations of iron lines will not result in an accurate elemental abundance for the precursor star.

Zinc, of which there are five different natural isotopes, exists most abundantly as ^{64}Zn and is predominantly created in two processes: the alpha rich freeze-out of supernovae and the s-process (Clayton 2003; Woosley & Weaver 1995). The

condensation temperature of zinc is 684 K which is significantly lower than that of the other iron-peak elements which range from 1170 K for Cu to 1600 K for Ti, with iron itself having a condensation temperature of 1337 K (Lodders & Fegley 1998). This low condensation temperature means it is significantly less likely for zinc to condense into solids in the progenitor star's envelope than it is for iron.

Zinc abundances and depletion in the interstellar medium have been widely studied over the past several decades (e.g. Morton 1975). In warm, low-density regions of the interstellar medium, zinc has been shown to be depleted by 0.0-0.2 dex (Savage & Sembach 1996; Welty et al. 1999).

The abundance of zinc over a wide range of metallicities within the Milky Way was studied by Sneden, Gratton & Crocker (1991) by examining a large sample of field and globular cluster stars. The Zn/M abundance was shown to be constant over a wide range of M/H, where M/H is defined as the average metallicity of the star derived from observations of Fe and Ni. There have been some recent studies which find some discrepancies between Zn and Fe abundances in Galactic stars: Prochaska et al. (2000), for example, find a mean enhancement of [Zn/Fe] to be 0.093 ± 0.025 from a sample of ten thick disk stars and Chen, Nissen & Zhao (2004) find [Zn/Fe] to be unenhanced in a sample of five alpha-poor halo stars but enhanced by 0.15 dex in a sample of ten thick disk stars. However, these are based upon much smaller samples than that studied by Sneden, Gratton & Crocker (1991). Saito et al. (2009), report measurements of [Zn/Fe] of a sample of 35 stars to be Solar to within uncertainties over the range $-2 < \mathrm{[Fe/H]} < 0$. Saito et al. (2009) also combine their measurements with that of 399 literature stars with the resulting sample covering the range $-4.5 < \mathrm{[Fe/H]} < 0.5$. [Zn/Fe] was found to be consistent with Solar in the ranges $-2 < \mathrm{[Fe/H]} < +0.5$ to within the measured standard deviation.

In planetary nebulae, the 3.625 μm [Zn IV] line is well suited to abundance derivation as it lies between two hydrogen Humphreys series emission lines (3.646 μm and 3.607 μm) and less than 0.125 μm away from the much stronger

Pfund series emission line at 3.741 μm. Zn^{3+}, in contrast to most of the abundant Fe ions in nebulae, has a sparse energy level structure in its ground configuration, making the 3.625 μm line relatively strong. The 3.625 μm line is the only emission line of zinc observed in the infrared in planetary nebulae.

The 3.625 μm [Zn IV] line was first identified by Dinerstein & Geballe (2001) in spectra taken using CGS4 on the UK Infrared Telescope (UKIRT) of NGC 7027 and IC 5117. They find the central wavelength, after corrections for the Earth's orbital motion, to be within uncertainties of that predicted for the Zn^{3+} $^2D_{3/2} -^2 D_{5/2}$ transition. They consider alternative identities of the line from nearby transitions of H_2 or Cu^{4+}. In the case of H_2, this is ruled out on the basis of the observed wavelength of the line. The $^4F_{5/2} -^4 F_{9/2}$ Cu^{4+} transition was deemed less likely than the $^2D_{3/2} -^2 D_{5/2}$ transition of Zn^{3+} due to the lower elemental abundance, stronger depletion and higher ionisation state of the former species.

Dinerstein & Geballe (2001) presented the procedure for deriving Zn^{3+}/H^+ from their measurements. However, since the collision strength of the Zn transition was not known at the time, their abundance estimates were necessarily expressed in terms of the value of this parameter (their Equ. 4). After correcting for the presence of other ions of zinc, elemental Zn/H can be determined. Dinerstein & Gaballe suggested that such Zn/H values are excellent tracers of the total Fe/H abundances and that [Zn/H] can be used as a surrogate for [Fe/H], in view of the minimal depletion of Zn and the fact that Zn closely tracks Fe over a wide range in metallicity.

Small contributions of the elemental abundance of zinc are expected from nucleosynthesis in AGB stars. The models of Karakas et al. (2009) show that this enhancement of Zn over the course of a star's time on the AGB is small: only the very low metallicity models show [Zn/Fe] > 0.1, and the majority of the remaining models show [Zn/Fe] < 0.05. Thus the measured abundance of Zn in planetary nebulae will, in general, reflect the abundance of Zn of the progenitor

star.

The ability to determine meaningful Fe/H values in nebulae is important because Fe/H is the most widely used index of metallicity in stars; therefore by determining undepleted Fe/H ratios, reliable metallicities of the precursor stars of the planetary nebulae can be determined. By examining the O/Zn ratio as a proxy for O/Fe, α-element enhancement in these objects can be assessed.

The remainder of this chapter will detail measurements of zinc abundances of a sample of planetary nebulae using the 3.625 μm emission line, and the extrapolated iron abundances.

5.2 Observations and data reduction

A sample of 23 planetary nebulae, the majority of which are Galactic bulge nebulae, were observed using ISAAC (Infra-red Spectrometer And Array Camera, Moorwood et al. 1998) on UT3 at ESO Paranal, Chile, either between 28/05/2012 and 30/05/2012 (sample 1) or between 21/07/2013 and 30/07/2013 (sample 2). These nebulae were selected from the Catalogue of Galactic Planetary Nebulae (Acker et al. 1992) and were chosen based upon their presence in the Galactic bulge, size of the nebula ($< 5''$ in diameter), brightness (log(Hβ flux) > -13 log[mW m^{-}2]) and the high intensities of the [O III] 4363 and 5007 Åand He II 4686 Ålines (indicating sufficient ionisation for the detection of the [Zn IV] line).

Our program was designed to target planetary nebulae belonging to the Galactic bulge. However, in sample 1, four nebulae not belonging to the bulge, namely PNG $019.7 + 03.2$, PNG $040.4 - 03.1$, PNG $023.0 + 04.3$ and PNG $049.3 + 88.1$ were observed as back-up targets when high winds caused pointing restrictions during part of the run. The last two objects yielded no detections or useful limits, and are not discussed further. Of the nine nebulae observed in sample 1, seven were detected in the 3.625 μm line including five bulge sources.

In sample 2, a total of 14 targets were observed. Four of these were observed

Table 5.1: Basic information and literature parameters for each source. Angular diameters are in arc seconds, where $^{\rm opt}$ indicates values derived from optical observations and $^{\rm rad}$ denotes values derived from radio observations (Acker et al. 1992). The first seven nebulae are those that make up sample 1, the following six are from sample 2 and the remaining two nebulae are from Dinerstein & Geballe (2001). References for optical spectra and central star effective temperatures are listed in column 11.

PNG	Name	RA	Dec	Ang. dia. (arcsec)	$T_{\rm star}$ (10^4 K)	T_e(O III) (10^4 K)	N_e(S II) (10^3 cm^{-3})	O/H (10^{-4})	O^{++}/O	Ref.
$004.0-03.0$	M 2-29	18 06 41	-26 54 56	$3.6^{\rm opt}$	7.6	1.9 ± 0.3	3 ± 3	$0.3^{+0.1}_{-0.2}$	$0.9^{+0.5}_{-0.8}$	1,2
$006.1+08.3$	M 1-20	17 28 58	-19 15 54	$1.9^{\rm rad}$	7.9	1.01 ± 0.02	6^{+3}_{-1}	3.4 ± 0.3	0.93 ± 0.13	3,2
$006.4+02.0$	M 1-31	17 52 41	-22 21 57	$7.0^{\rm rad}$	5.8	0.76 ± 0.04	8^{+4}_{-1}	7.7 ± 1.6	0.94 ± 0.28	4,2
$006.8+04.1$	M 3-15	17 45 32	-20 58 02	$4.2^{\rm opt}$	7.9	0.85 ± 0.02	5^{+3}_{-1}	6.0 ± 0.7	0.96 ± 0.16	4,2
$019.7+03.2$	M 3-25	18 15 17	-10 10 09	$3.9^{\rm opt}$	5.2	$1.09 \pm 0.03^{\rm b}$	14 ± 1	3.9 ± 0.4	0.82 ± 0.11	5,6
$040.4-03.1$	K 3-30	19 16 28	$+05$ 13 19	$3.3^{\rm rad}$	...	$1.0^{\rm a}$	$10.0^{\rm a}$	$3.9^{\rm a}$	$0.80^{\rm a}$	-
$355.4-02.4$	M 3-14	17 44 21	-34 06 41	$2.8^{\rm rad}$	7.9	0.87 ± 0.04	3.4 ± 0.2	6.5 ± 0.1	0.73 ± 0.03	7,2
$003.6+03.1$	M 2-14	17 41 57	-24 11 16	$2.2^{\rm rad}$	4.4	$0.79^{+0.07}_{-0.09}$	11 ± 1	$4.0^{+1.8}_{-1.0}$	$0.5^{+0.4}_{-0.2}$	5,2
$011.0+05.8$	NGC 6439	17 48 20	-16 28 44	$5.0^{\rm opt}$	...	1.01 ± 0.01	3.7 ± 0.1	$5.0^{+0.3}_{-0.1}$	$0.84^{+0.06}_{-0.03}$	5, -
$352.1+05.1$	M 2-8	17 05 31	-32 32 08	$4.2^{\rm opt}$	12.8	0.94 ± 0.01	3.2 ± 0.1	$4.8^{+0.3}_{-0.2}$	$0.77^{+0.05}_{-0.06}$	5,2
$354.5+03.3$	Th 3-4	17 18 52	-31 39 07	$0.0^{\rm opt}$	...	$1.6 \pm 0.4^{\rm b}$	17^{+1}_{-2}	$1.4^{+1.4}_{-0.6}$	$0.88^{+1.1}_{-0.7}$	5,2
$355.9+03.6$	H 1-9	17 21 32	-30 20 49	$0.7^{\rm rad}$	3.8	1.1 ± 0.1	100^{+0}_{-73}	$2.0^{+1.2}_{-0.4}$	$0.8^{\rm a}$	2,4
$358.2+03.6$	M 3-10	17 27 20	-28 27 51	$3.2^{\rm opt}$	9.3	1.08 ± 0.03	$7.5^{+2.0}_{-1.4}$	$5.0^{+0.3}_{-0.4}$	$0.82^{+0.08}_{-0.14}$	5,2
$084.9-03.4$	NGC 7027	21 07 02	$+42$ 14 10	$14.0^{\rm opt}$	18.0	1.25 ± 0.04	13^{+10}_{-3}	3.9 ± 0.5	0.67 ± 0.01	8,9
$089.8-05.1$	IC 5117	21 32 31	$+44$ 35 48	$1.5^{\rm rad}$	12.0	1.25 ± 0.04	16^{+11}_{-4}	2.7 ± 0.3	0.94 ± 0.13	10,10

1: Exter, Barlow & Walton (2004); 2: Gesicki & Zijlstra (2007); 3: Wang & Liu (2007); 4: Górny et al. (2009); 5: Górny et al. (2004); 6: Kondratyeva (2003); 7: Cuisinier et al. (2000) ; 8: Zhang et al. (2005); 9: Pottasch & Bernard-Salas (2010); 10: Hyung et al. (2001).

a: adopted value; b: T_e(NII) used.

outside the requested observational constraints and, although the planetary nebulae had at least borderline detections of hydrogen, the spectra suffered from very poor signal-to-noise ratios and thus did not yield meaningful limits. A further four nebulae (PNG $006.3+04.4$, PNG $009.6-10.6$, PNG $351.9-01.9$ and PNG $353.5-04.9$) resulted in null detections within the requested observational constraints and are not discussed further. Of the remaining six nebulae, five were detected in the 3.625 μm line and the final source had a high signal to noise ratio spectra with no detected [Zn IV] line, allowing upper limits to be placed on the Zn abundance within this nebula.

The observations used the Long Wavelength Spectrometer using the jiggle-nod method, with on-source exposure times of 30-60 minutes. The slit length was $120''$, the slit width used was $1''$ for sample 1 and $1.5''$ for sample 2. The wavelength coverage was 3.55-3.80 μm and the resulting resolution was $R = 2000$ for sample 1 and $R = 1500$ for sample 2. Nodding was done along the slit, with nods of $15''$ to $30''$ depending upon the source being observed. This results in the source being in the field of view at all times during the observation, reducing the required observing time whilst still allowing an effective background subtraction. The slit was aligned through the brightest portion of the nebulae and in most cases included more than 50% of the object due to their small angular size.

The detector spectral coverage in this wavelength domain and at this resolution is 0.255 μm, allowing the [Zn IV] emission line to be observed concurrently with five lines from the Humphreys series of hydrogen (n=21-6 to n=17-6) and one Pfund series hydrogen emission line (n=8-5, henceforth H_{8-5}).

The data were reduced using the jiggle-nod recipes provided by the ESO common pipeline library, including flat fielding. The wavelength calibrations were done using arc lamp lines rather than sky lines, as recommended in the ISAAC user manual, due to there being no usable sky emission lines within this wavelength range.

Relative flux calibration of the data was carried out using the telluric standard

Table 5.2: Telluric standards for each source, including their spectral type and effective temperatures, taken from the Hipparcos Catalogue.

PNG	Telluric Standard	Spectral Type	T_{eff} (K)
$004.0 - 03.0$	HIP088012	B3II/III	17,000
$006.1 + 08.3$	HIP076243	B6IV	14,000
$006.1 + 08.3$	HIP085442	B9.5IV	9,790
$006.4 + 02.0$	HIP085442	B9.5IV	9,790
$006.8 + 04.1$	HIP085355	K3Iab	4,420
$019.7 + 03.2$	HIP085355	K3Iab	4,420
$040.4 - 03.1$	HIP095732	B6III	14,100
$355.4 - 02.4$	HIP089439	B0/1Ia/ab	26,000
$003.6 + 03.1$	HIP094378	B5V	15,200
$011.0 + 05.8$	HIP091014	B2III/IV	20,300
$352.1 + 05.1$	HIP085885	B2II	20,000
$354.5 + 03.3$	HIP103571	G0V	5,940
$355.9 + 03.6$	HIP087164	B2II	20,000
$358.2 + 03.6$	HR7236	B9Vn	10,500

stars observed with each planetary nebula observation. These telluric standard stars are almost exclusively B-type stars taken from the Hipparcos Catalogue[1], and are listed in Table 5.2. Their stellar types are well documented and, from these types, an effective temperature of each star could be estimated. In this spectral region, these stars are well described by blackbody distributions calculated from their effective temperatures. The correction function to apply across the spectrum was calculated by dividing the blackbody function of each of the standard stars by the observed telluric stellar spectrum, after the removal of stellar spectral features, and normalising. The observed planetary nebulae data were then multiplied by the normalised functions to produce relative flux calibrated data. One nebula was observed twice and its two resulting relative flux calibrated spectra were averaged. There was no significant difference in the intensities of the two spectra. We estimate the relative flux calibrations to be accurate to 5-10%.

[1]ESA, 1997, The Hipparcos and Tycho Catalogues, ESA SP-1200

Absolute flux calibrations are not required for the analysis done here because both the hydrogen and zinc lines are contained within the same spectrum and only the ratio of the two is required to derive the zinc-to-hydrogen abundance.

The resulting spectra of samples 1 and 2 are shown in Fig. 5.1. Two spectral ranges are shown for each source so that the intensity of both the H_{8-5} and [Zn IV] lines can be clearly seen.

In order to measure the integrated line intensities for abundance calculations, the spectra were first smoothed, then a straight-line background level was fitted and the integrated intensities of lines measured, after correcting for obvious noise spikes. The abundance calculations were then carried out as described in Sect. 5.3.

5.2.1 Literature data

The [Zn IV] 3.625 μm emission line was first identified by Dinerstein & Geballe (2001) through observations of NGC 7027 and IC 5117. We include these observations, using the newly calculated values of the energy averaged collision strength, in order to compare the results from the new sample of nebulae to that of results obtained from well-studied nebulae, calculated using the same method as for the new sample.

The observations of Dinerstein & Geballe (2001) contained the 3.625 μm emission line as well as two lines of hydrogen from the Humphreys series (n=20-6, 3.607 μm and n=19-6, 3.646 μm, hereafter H_{20-6} and H_{19-6}). The observations did not include the stronger H_{8-5} line that we use for the new sample due to its higher intensity.

The *ISO* archive was also searched for further observations covering the 3.625 μm wavelength range. NGC 7027 is the only planetary nebula observed at sufficient resolution to identify the [Zn IV] emission line: Target Dedicated Time (TDT) number = 02401183 taken from Sloan et al. (2003), shown in Fig.

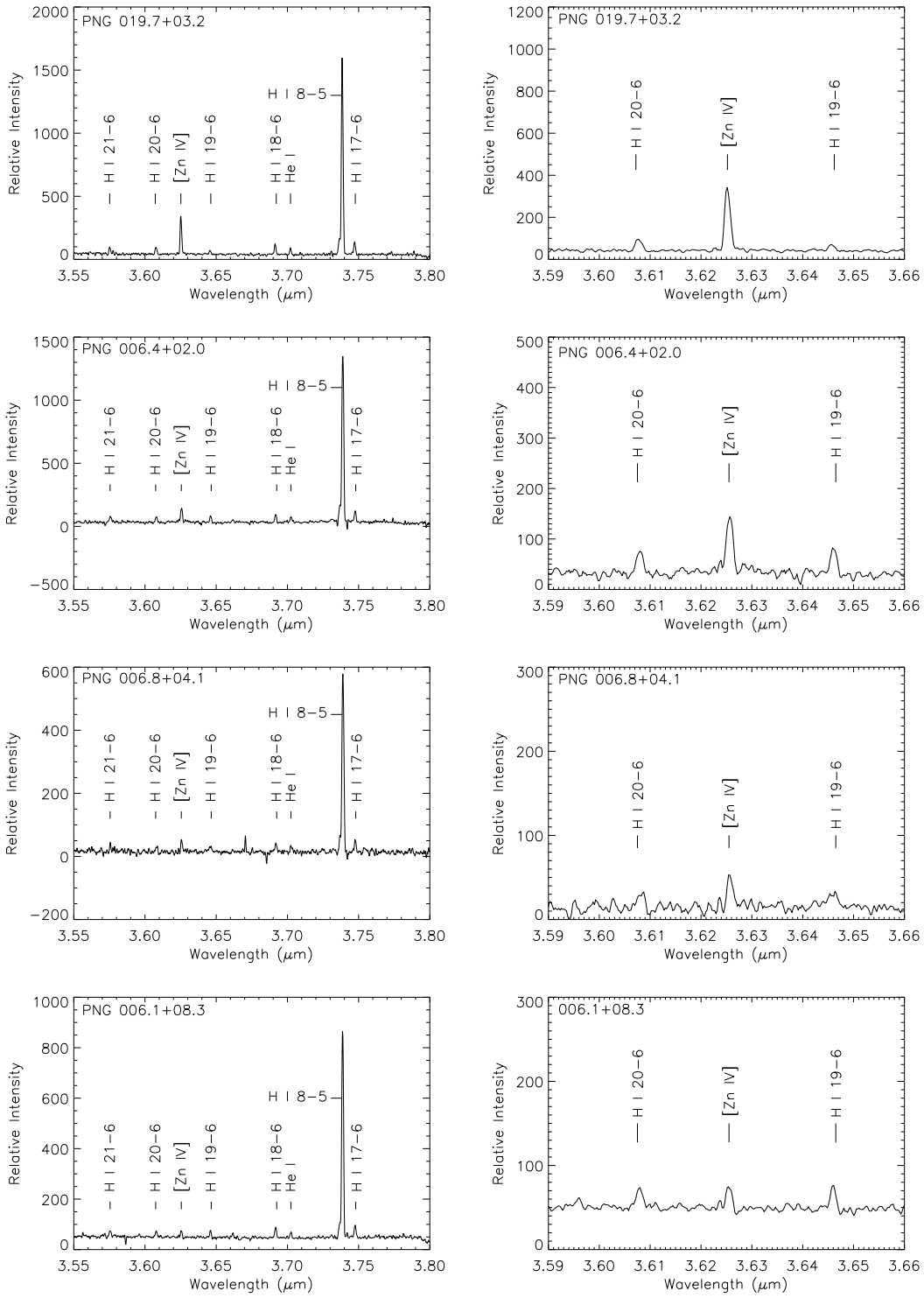

Figure 5.1: Spectra of all sources with detections of the [Zn IV] line. The spectra have been background subtracted and subsequently smoothed, except that of PNG $355.4-02.4$ which had a noise spike in close proximity to the [Zn IV] emission line and thus was not smoothed.

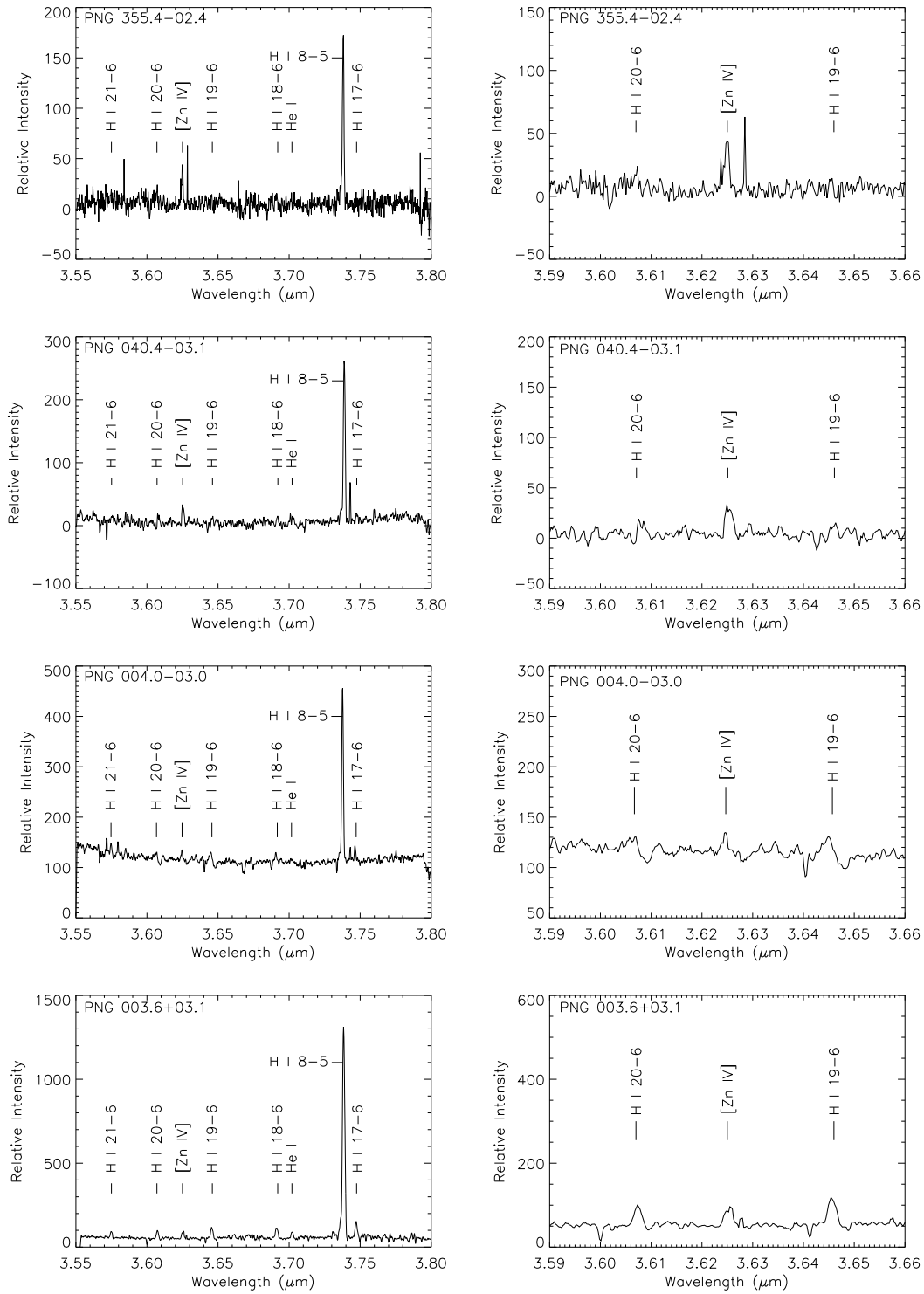

Figure 5.1: – *continued.*

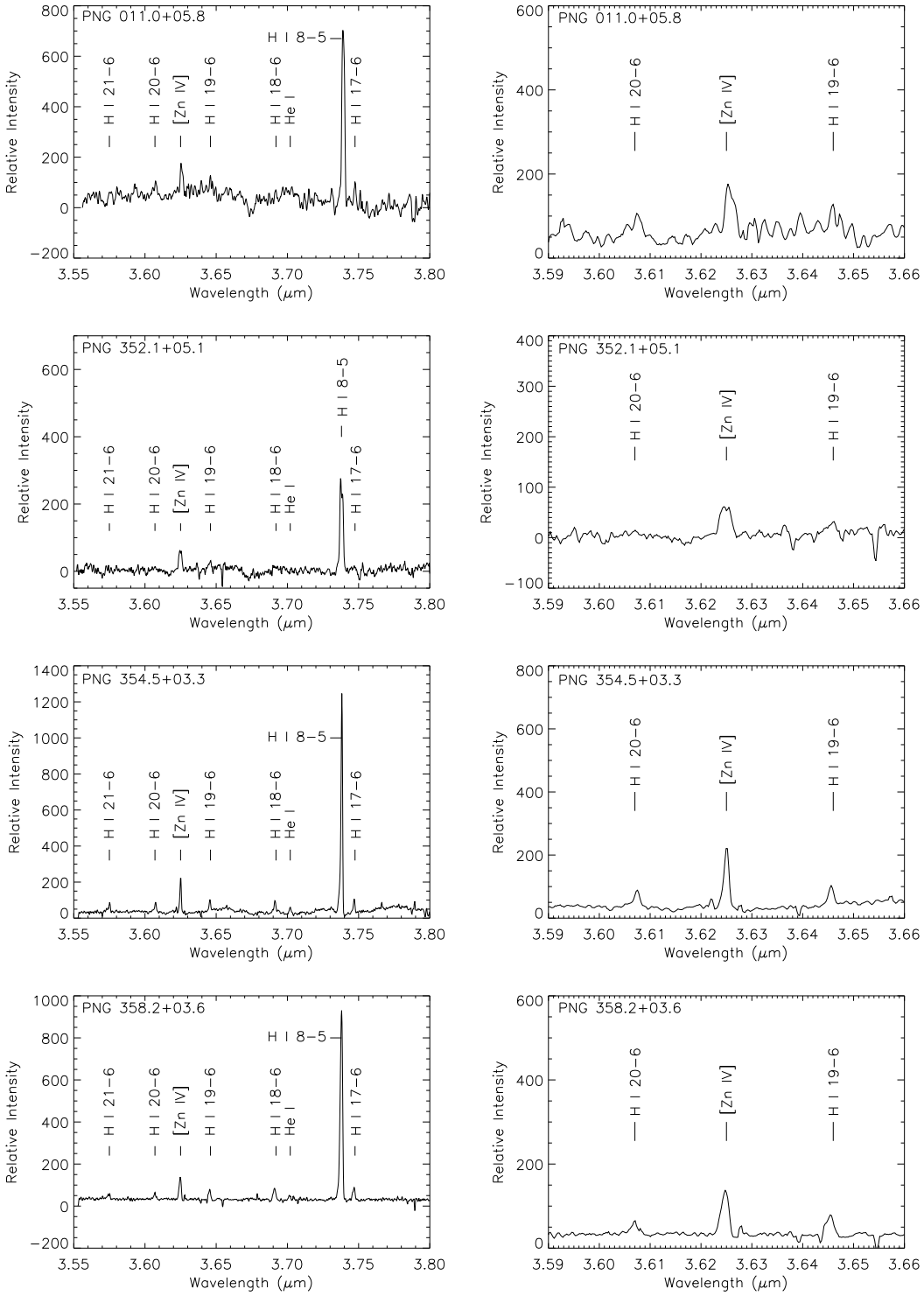

Figure 5.1: – *continued.*

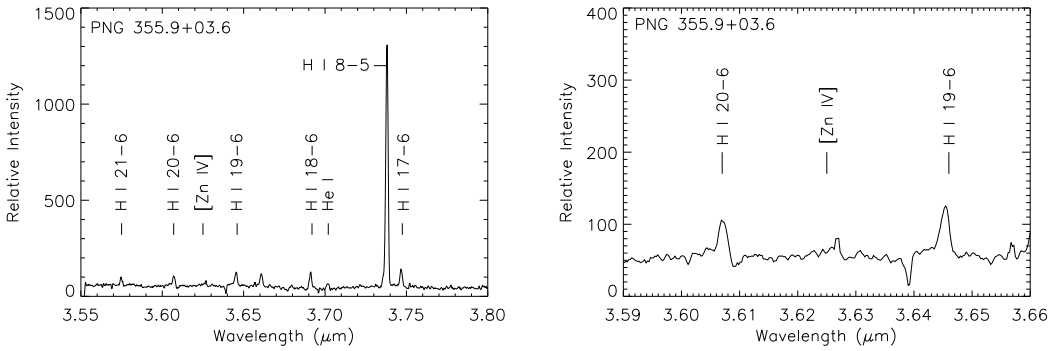

Figure 5.1: – *continued.*

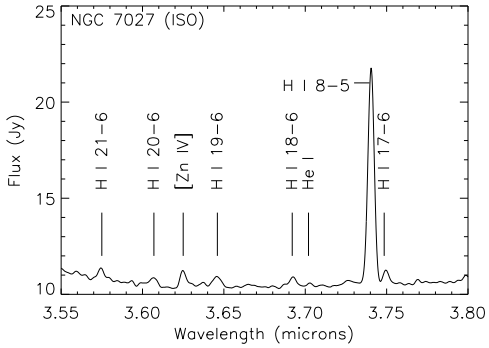

Figure 5.2: *ISO* spectrum of NGC 7027, TDT: 02401183, taken from Sloan et al. (2003).

5.2. Both the [Zn IV] and H_{8-5} lines are visible, although at much lower resolution than the spectra in Dinerstein & Geballe (2001). There were no new detections of [Zn IV] in other planetary nebulae found within the *ISO* archive.

5.3 Abundance derivation

In order to calculate zinc abundances from observed line intensity ratios, a number of calculations must be carried out. First, the emissivities of the lines must be calculated, then the ionic abundances may be derived. The unobserved ions must be accounted for using a suitable ionisation correction factor before the elemental abundances can be calculated.

5.3.1 Determination of physical parameters

Basic information about each new source detected in zinc is shown in Table 5.1 as well as for the two nebulae previously observed by Dinerstein & Geballe (2001). $T_{\rm star}$ was quoted from the second reference in column 11 and the angular diameters are taken from Acker et al. (1992). For sample 1, $T_{\rm e}$(O III), $N_{\rm e}$(S II), O/H and O^{++}/O were calculated from the optical spectra published in the first reference in column 11 using the Nebular Empirical Analysis Tool (NEAT, Wesson, Stock & Scicluna 2012). NEAT uses the Kingsburgh & Barlow (1994) ionisation correction factor scheme. Further technical details of the code, including error propagation and sources of atomic data, may be found in Wesson, Stock & Scicluna (2012). The number of lines used as input varied from source to source, depending upon the available literature spectra. NGC 7027 had the largest input line list (227 lines in the wavelength range 3327.1–8727.2 Å) and PNG 019.7+03.2 had the smallest input line list (14 lines in the wavelength range 4340.4–7330.2 Å). All lines published in the listed reference that are recognised by NEAT were used, and a full list of lines is available in each source's corresponding reference (column 11).

The literature optical spectra for sample 2 were more limited than those of sample 1 and did not provide a sufficient number of lines for the NEAT package to be applied or the results, when it was possible to apply the package, had very large uncertainties. Thus for sample 2, the nebular parameters were taken directly from the first reference in column 11.

There was not a sufficiently complete set of emission line fluxes for PNG 019.7 + 03.2 (sample 1) in the literature to successfully apply the NEAT package, nor to derive $T_{\rm e}$(O III) directly, so the value listed in Column 7 of Table 5.1 is $T_{\rm e}$(N II). Using a published sample of 51 planetary nebulae from Górny et al. (2009) with derived $T_{\rm e}$(N II) and $T_{\rm e}$(O III), it is possible to extrapolate a $T_{\rm e}$(O III) from the available $T_{\rm e}$(N II) value using a straight-line fit to their data.

This would predict $T_{\rm e}$(O III)=1.05×10^4 K for a $T_{\rm e}$(N II)=1.09×10^4 K. As these values are so similar, the effect on the emissivities is negligible, therefore $T_{\rm e}$(N II) is used for the remainder of the paper. Similarly, $T_{\rm e}$(O III) could not be determined for PNG 354.5 + 03.3, thus the quoted temperature is that of $T_{\rm e}$(N II) for this nebula.

PNG 040.4−03.1 did not have sufficient optical data available in the literature to derive the required parameters. Therefore typical nebular parameters of 10^4 K and 10^4 cm^{-3} were adopted for $T_{\rm e}$(O III) and $N_{\rm e}$(S II) respectively, and typical values of O/H and O^{++}/O for our disk nebula sample were assigned.

PNG 355.9 + 03.6 does not have a published value for the abundance of O^{++}. Literature optical spectra were processed using NEAT and also did not result in an O^{++} abundance. Thus, we have adopted a 'typical' value of 0.8 for the O^{++}/O ratio.

5.3.2 Line emissivities

By definition, j_{ul}, the emission coefficient of the spontaneous cooling from an upper state u to a lower state l, is given by:

$$j_{ul} = \frac{{\rm h}\nu_{ul}{\rm A}_{ul}n_u}{4\pi},$$

where ${\rm A}_{ul}$ is the Einstein coefficient for the transition and n_u is the population of the upper state. From this, the 'density normalised emissivity' can be written:

$$\varepsilon_{ul} = \frac{4\pi j_{ul}}{n_{\rm e}n_{\rm tot}} = \frac{{\rm A}_{ul}{\rm h}\nu_{ul}n_u}{n_e n_{\rm tot}}, \tag{5.1}$$

where n_{tot} is the total number density of ions.

Hydrogen emissivities are available as an extensive data list with an interpolation program from Storey & Hummer (1995). The H_{8-5} at 3.741 μm is the strongest hydrogen line in our observed wavelength range, and is therefore the most appropriate line to use in the calculations. Using $T_{\rm e}$(O III) and $N_{\rm e}$(S II)

listed in Table 5.1, the interpolation code was used to give more accurate H_{8-5} emissivities. For NGC 7027 and IC 5117, the H_{20-6} and H_{19-6} lines were used and their emissivities determined in the same manner as for H_{8-5}.

[Zn IV] line emissivities are not available in the literature and must be calculated. Using the methodology described in Dinerstein & Geballe (2001), the emissivity of the [Zn IV] line, ε(Zn IV), was calculated in the low-density limit and using new collision strengths, Υ, integrated over the electron energy distribution at temperature $T_{\rm e}$ (Keith Butler, priv. comm.). For this case,

$$\frac{n_u}{n_{\rm tot}} \sim \frac{n_u}{n_l} = \frac{g_u}{g_l} \exp\left(-\frac{\Delta E_{ul}}{{\rm k}T}\right) \frac{n_e q_{ul}}{{\rm A}_{ul}}, \tag{5.2}$$

where g_i is the statistical weight of level i and ΔE_{ul} is the energy of the transition $u-l$. q_{ul} is the collision rate coefficient of the transition, and is given by:

$$q_{ul} = \frac{\beta \Upsilon_{ul}}{\sqrt{T} g_u}, \tag{5.3}$$

where β is defined as $\sqrt{(2\pi\hbar^4)/(m_e^3 {\rm k})} = 8.629 \times 10^{-6}$ (cgs units).

Combining equations 5.1, 5.2 and 5.3 leads to the following formula, used to calculate the emissivity of the [Zn IV] line:

$$\varepsilon({\rm Zn\ IV}) = \exp\left(-\frac{\Delta E_{ul}}{{\rm k}T_{\rm e}}\right) \frac{{\rm h}\nu_{ul} \beta \Upsilon}{g_l \sqrt{T_{\rm e}}}, \tag{5.4}$$

with all values in cgs units.

The energy-averaged collision strengths were calculated over a grid of electron temperatures ranging from 5000 K to 25000 K (Keith Butler, priv. comm.). The energy-averaged collision strengths were interpolated to the electron temperatures of each source using a power law.

5.3.3 Ionic abundances

After measuring the integrated line intensity ratios of [Zn IV] and H_{8-5}, calculating the ionic abundance ratios is carried out using:

$$\frac{Zn^{3+}}{H^{+}} = \frac{F([\text{Zn IV}])}{F(H_{8-5})} \frac{\varepsilon(H_{8-5})}{\varepsilon(\text{Zn IV})},$$

where $F(i)$ is the flux of transition i, given in Table 5.3. Extinction effects are negligible in this wavelength range, so need not be considered.

5.3.4 Ionisation correction factors

To convert the ionic abundances into elemental abundances, it is necessary to correct for those ions of that species that are not seen. For hydrogen, it is assumed that all H is present as H^+, however this is not the case for Zn.

In order to examine the ionisation correction factor required for zinc, as well as the dominance of the Zn^{3+} ion, we have run a grid of CLOUDY (v 13.01) photoionisation models (Ferland et al. 2013). The grid of models were given Solar abundances and spherical geometry. Luminosity, initial radius and hydrogen density were set as $\log(L_{\text{tot}}[\text{erg/s}])$=38, $\log(R_{\text{initial}}[\text{cm}])$=17 and $\log(n_{\text{H}}[\text{cm}^{-3}]) = 4$. The central star's radiation field was assumed to be a blackbody with temperatures ranging from 2×10^4 K to 4×10^5 K.

At central star temperatures between 6×10^4 K and 1×10^5 K, $Zn^{3+}/Zn > 0.9$ at most depths, where depth is defined as the distance from the illuminated face of the nebular cloud. When the depth into the cloud is small, the fraction of zinc in other ions becomes significant, as shown in Fig. 5.3. The dominance of Zn^{3+} also does not hold when examined at temperatures smaller than 6×10^4 K and greater than 1×10^5 K.

These models also show that over the range of central star temperatures 5×10^4 K to 1.5×10^5 K, the fraction of zinc in the Zn^{3+} ion is closely mapped by the fraction of oxygen present as O^{++}, which is the dominant oxygen ion over

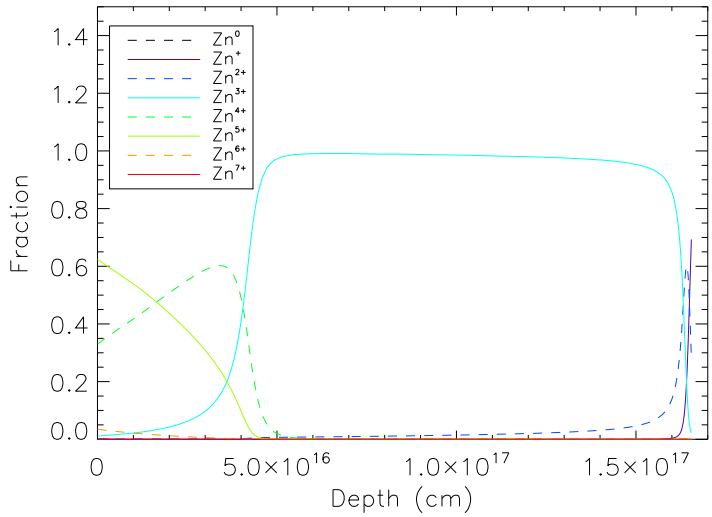

Figure 5.3: Fractional ionisation abundance of zinc from CLOUDY models. This model: $T_{\rm star} = 10^5$K.

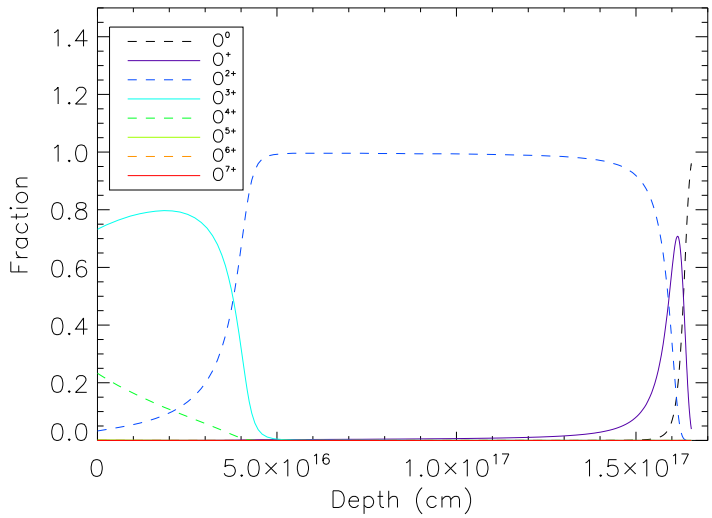

Figure 5.4: Fractional ionisation abundance of oxygen from CLOUDY models. This model: $T_{\rm star} = 10^5$K.

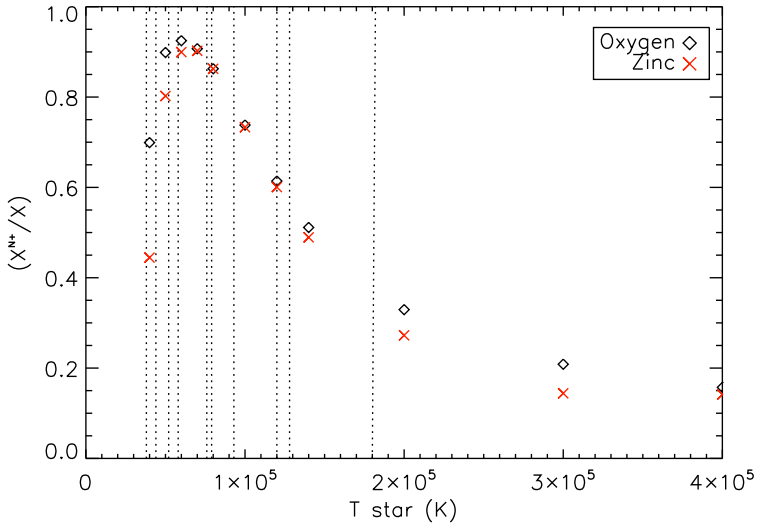

Figure 5.5: Fractional abundances of O^{++} and Zn^{3+} over the central star temperature range 4×10^4 K to 4×10^5 K. Dotted vertical lines indicate the central star temperatures of the sample nebulae.

the same temperature range, as shown in Fig. 5.4 and 5.5. O^{++}/O has been determined for the majority of our sample from optical observations and most central stars of the sample of planetary nebulae lie within this temperature range. Therefore, the ionisation correction factor for Zn^{3+} can be taken as $(O^{++}/O)^{-1}$ and the values are listed in Table 5.1 for each nebula.

Dinerstein & Geballe (2001) use Ar/Ar^{3+} as the ionisation correction factor rather than O/O^{++}. Our CLOUDY models show that O^{++}/O follows Zn^{3+}/Zn more closely than Ar^{3+}/Ar does, hence our choice of species. Additionally, over the temperature range 6×10^4 K to 1.2×10^5 K, the models show that Zn^{3+}/Zn is most closely mapped by O^{++}/O in comparison to all other species included in the model nebula. This is shown in Fig. 5.6.

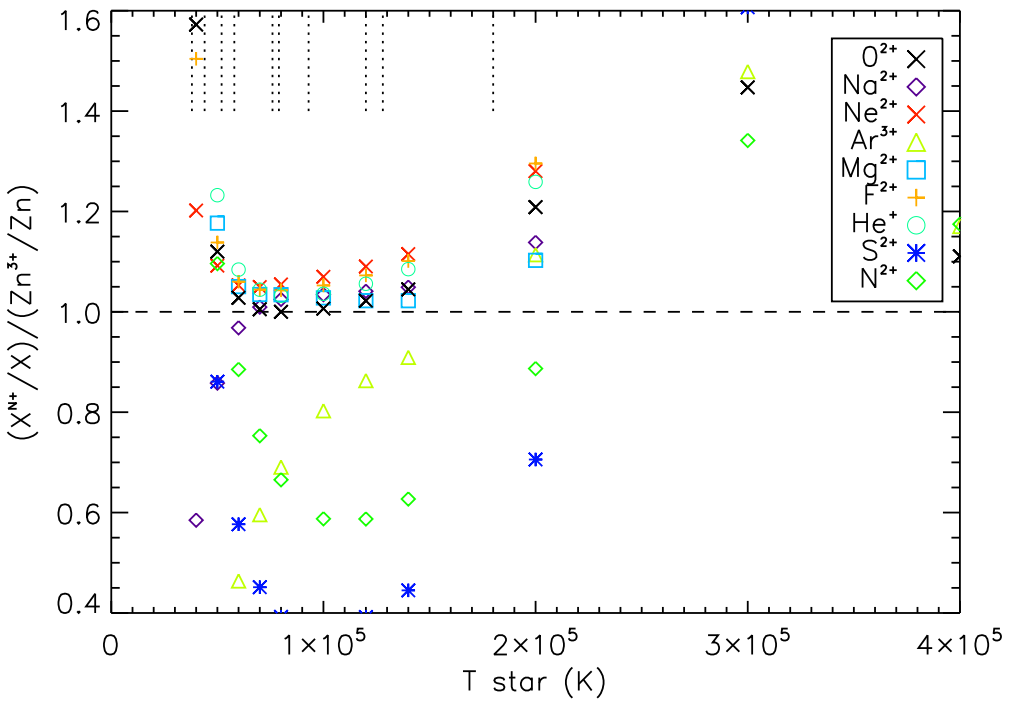

Figure 5.6: Fractional abundances of a variety of species in comparison to the fractional abundance of Zn^{3+} over the central star temperature range 4×10^4 K to 4×10^5 K. The species included are those that most closely follow the fractional abundance of Zn^{3+}, except Fe ions. The dotted vertical lines indicate the central star temperatures of the sample nebulae.

5.3.5 Elemental abundances

From the calculated ionic abundances and using O^{++}/O to correct for the unobserved ions of zinc, the Zn elemental abundance is simply:

$$\frac{Zn}{H} = \frac{Zn^{3+}}{H^+}\frac{O}{O^{++}}, \tag{5.5}$$

Outside of the temperature range 5×10^4 K to 1.5×10^5 K, applying this correction will lead to inaccurate results where the abundance of Zn will be underestimated. Zn/H may be converted to Zn/O using the O/H values shown in Table 5.1. As discussed earlier, the value of Zn/Fe has essentially the Solar value for stars for

[Fe/H] > -2 (Saito et al. 2009; Umeda & Nomoto 2002; Sneden, Gratton & Crocker 1991), which includes all of our targets. Thus, it is possible to convert from [Zn/H] and [Zn/O] to [Fe/H] and [Fe/O] using the Solar ratio of Zn/Fe.

5.4 Results

The results are shown in Table 5.3 in both logarithmic and linear forms. The former uses the standard definition:

$$\left[\frac{\mathrm{X}}{\mathrm{Y}}\right] = \log_{10}\left(\frac{\mathrm{X}}{\mathrm{Y}}\right) - \log_{10}\left(\frac{\mathrm{X}}{\mathrm{Y}}\right)_{\odot}.$$

The Solar elemental abundances are taken from Asplund et al. (2009). The results from the *ISO* observations are not displayed in Table 5.3 as they are within errors of those determined from the observations in Dinerstein & Geballe (2001), but due to their lower resolution had significantly larger uncertainties.

5.4.1 Uncertainty considerations

All uncertainties associated with the physical conditions and chemical composition of the sample nebulae are shown in Table 5.1. The uncertainties on the measured flux ratio are given in Table 5.3. These errors have all been combined according to standard error propagation to give the uncertainties on the final abundances.

For PNG 040.4−03.1, we have adopted values of ± 0.2 and ± 0.3 dex for [Zn/H] and [O/Zn] ratios respectively.

There are also further uncertainties associated with the use of ionisation correction factors. The ionisation correction factor $\mathrm{O/O^{++}}$ agrees to within 2% with the value of $\mathrm{Zn/Zn^{+3}}$ predicted by the photoionisation models for the majority of the sample. NGC 7027, PNG 019.7 + 03.2 and PNG 003.6 + 03.1 have uncertainties introduced by the ionisation correction of about 10% due to the very

Table 5.3: Abundances of zinc and iron with respect to hydrogen and oxygen for the new sample and the literature sample. Iron abundances may be calculated from the zinc abundances using the Solar ratio of Zn/Fe. Flux ratios are listed in column 3 and are given as the flux of the [Zn IV] line with respect to to the flux of the H line used, H_{8-5} unless otherwise indicated. Emissivities are quoted in erg s^{-1} cm^{-3}.

PNG	ε([Zn IV]) ($\times10^{-21}$)	$F_{[Zn\ IV]}/F_H$ ($\times10^{-2}$)	Zn^{3+}/H^+ ($\times10^{-8}$)	Zn/H ($\times10^{-8}$)	Zn/O ($\times10^{-5}$)	[Zn/H]	[O/Zn]
$004.0-03.0$	7.6 ± 1.8	4.4 ± 1.5	$0.35^{+0.16}_{-0.15}$	$0.39^{+0.28}_{-0.38}$	13^{+10}_{-13}	$-1.0^{+0.2}_{-0.3}$	$-0.2^{+0.2}_{-0.3}$
$006.1+08.3$	7.1 ± 1.4	2.6 ± 0.4	0.5 ± 0.1	0.5 ± 0.1	1.5 ± 0.4	-0.9 ± 0.1	0.70 ± 0.1
$006.4+02.0$	6.6 ± 1.3	8.1 ± 1.1	2.2 ± 0.6	2.3 ± 0.9	3 ± 1	-0.2 ± 0.1	0.4 ± 0.2
$006.8+04.1$	6.8 ± 1.3	5.6 ± 0.8	1.3 ± 0.3	1.3 ± 0.3	2.2 ± 0.7	-0.4 ± 0.1	0.5 ± 0.1
$019.7+03.2$	7.2 ± 1.4	17.4 ± 2.5	2.8 ± 0.7	3.5 ± 0.9	9 ± 3	-0.02 ± 0.10	-0.08 ± 0.10
$040.4-03.1^a$	7.2 ± 1.6	10.0 ± 1.4	1.8 ± 0.8	2 ± 1	6 ± 5	-0.2 ± 0.2	0.1 ± 0.3
$355.4-02.4$	6.9 ± 1.4	24.4 ± 3.5	5.5 ± 1.4	7.5 ± 1.9	12 ± 3	0.3 ± 0.1	-0.2 ± 0.1
$003.6+03.1$	6.7 ± 1.3	3.1 ± 0.4	$0.79^{+0.23}_{-0.21}$	$1.6^{+1.3}_{-0.8}$	4^{+4}_{-2}	$-0.4^{+0.3}_{-0.2}$	$0.3^{+0.3}_{-0.2}$
$011.0+05.8$	7.1 ± 1.4	14.4 ± 2.0	2.5 ± 0.6	3.0 ± 0.8	6 ± 2	-0.1 ± 0.1	0.1 ± 0.1
$352.1+05.1$	7.0 ± 1.4	18.8 ± 2.7	3.8 ± 0.9	4.9 ± 1.3	10 ± 3	0.1 ± 0.1	-0.1 ± 0.1
$354.5+03.3$	7.5 ± 1.8	14.4 ± 2.0	$1.4^{+0.6}_{-0.5}$	$1.6^{+2.1}_{-1.3}$	11^{+19}_{-10}	$-0.4^{+0.4}_{-0.3}$	$-0.2^{+0.4}_{-0.3}$
$355.9+03.6$	7.2 ± 1.5	<0.005	<0.08	<0.01	<0.5	<-1.5	>1.2
$358.2+03.6$	7.2 ± 1.4	9.9 ± 1.4	1.6 ± 0.4	2.0 ± 0.6	4 ± 1	-0.3 ± 0.1	0.3 ± 0.1
NGC 7027	7.4 ± 1.5	149 ± 7^b	0.88 ± 0.18	1.3 ± 0.3	3.4 ± 0.8	-0.44 ± 0.08	0.34 ± 0.09
IC 5117	7.4 ± 1.5	260 ± 50^b	1.7 ± 0.4	1.8 ± 0.5	7 ± 2	-0.31 ± 0.10	0.06 ± 0.12

a: values are an estimate using average values for oxygen ratios in calculations where literature values were unavailable
b: flux are given for the H_{19-6} transitions and abundances are the mean of those derived from the H_{19-6} and H_{20-6} transitions, taken from Dinerstein & Geballe (2001).

high, in the case of the former, and low, in the case of the latter two, central star temperatures respectively.

PNG $355.9 + 03.6$ has a significantly lower central star temperature than any of the other sample nebulae, introducing an uncertainty due to the ionisation correction factor of $\sim$20%. As this nebula has no measured value for the abundance of O^{++}, we have adopted the same uncertainties as for PNG $040.4 - 03.1$.

The calculated collision strength for [Zn IV] is estimated to be accurate to 20% (Keith Butler, priv. comm.), and the line emissivity should have a similar uncertainty. The uncertainties in the emissivities of the optical oxygen lines are likely to be greater due to their strong temperature dependences.

The sensitivity of the results on the derived physical input parameters can be examined by comparing the results of sample 1 as derived using the parameters calculated by the NEAT code with those calculated from literature parameters. In general, the results of [Zn/H] agree to less than 0.08 dex, which is within the calculated uncertainties of the results. The only nebula with a difference in [Zn/H] greater than 0.08 dex is NGC 7027, with a difference of 0.14 dex. The results of [O/Zn] agree to within 0.09 dex for all nebulae except PNG $006.4+02.0$ which has a discrepancy of 0.3 dex. This difference is primarily caused by an increase in the value of O^{++}/O as derived through NEAT in comparison to that value derived in the literature. In general, the results are consistent to within calculated uncertainties.

The H_{8-5} line is asymmetrical in profile, potentially caused by a blend with a significantly weaker He I emission line. This is more obvious in the spectra of sample 1 than sample 2 due to the differing resolutions. In order to assess the effect this has on the calculated abundances, we have calculated abundance ratios for the four highest signal-to-noise spectra from sample 1 (namely PNG $006.1 + 08.3$, PNG $006.4 + 02.0$, PNG $006.8 + 04.1$ and PNG $019.7 + 03.2$) from both the peak intensities of the H_{8-5} and [Zn IV] line and also using the integrated intensities of the H_{18-6} lines. The results are not significantly different

from those derived using the integrated intensities of the H_{8-5} line. In general, [Zn/H] is reduced by 0.1 dex, but the abundance ratios of some nebulae are entirely unaffected (e.g. PNG 019.7+03.2). The abundances derived for NGC 7027 and IC 5117 are unaffected due to the H_{19-6} and H_{20-6} lines being used in their calculations.

5.5 Discussion

All calculated ionic and elemental abundance ratios are shown in Table 5.3. Our results show a general trend of sub-Solar Zn/H, with the lowest being 10% that of Solar.

We have derived [Zn/H] and [O/Zn] in order to calculate the metallicities of the precursor stars of the planetary nebulae in our sample and to determine whether α elements such as oxygen are enriched relative to Solar. A range of O/Zn is shown, with six of the sample nebulae showing enhancement of O/Zn in comparison to Solar values and one showing sub-Solar O/Zn.

PNG 004.0 − 03.0 shows sub-Solar [O/Zn], however the uncertainties associated with this nebula are large, putting the Solar value well within one sigma. [Zn/H] for this nebula is the most sub-Solar at −1.0, five sigma away from Solar. Additionally, as discussed in Gesicki et al. (2010), this nebula contains a high density inner region which is likely an opaque disk. This may be the cause of the unusually low calculated values.

PNG 355.4 − 02.4 showed a very intense [Zn IV] emission line and has the highest F([Zn IV])/F(H_{8-5}) of all the sample, leading to the highest [Zn/H] in the sample, suggesting that this nebula may simply be more metal-rich than the Sun. In addition to the high F([Zn IV])/F(H_{8-5}) ratio, no Humphreys emission lines were detected in PNG 355.4 − 02.4. It is possible that this nebula could be hydrogen-poor rather than zinc-rich, although the low signal-to-noise ratio in this spectrum may be the cause of the non-detections of the Humphreys emission lines.

The 3.625 μm line has several noise spikes in close proximity, and it is possible a noise spike could be overlaid on the emission line, significantly increasing the measured zinc abundance which would also account for the high value of [Zn/H].

PNG 006.1 + 08.3, PNG 006.4 + 02.0 and PNG 006.8 + 04.1 show α enhancement, with oxygen being enhanced over zinc by factors of 5, 2.5 and 3 respectively. PNG 006.4+02.0 and PNG 006.8+04.1 both have significantly sub-Solar [Zn/H]. PNG 006.1 + 08.3, on the other hand, shows a [Zn/H] ratio that is more in line with Solar. PNG 003.6+03.1 and PNG 358.2+03.6 both show slightly sub-Solar [Zn/H] and slightly above-Solar values for [O/Zn]. These results imply that these five nebulae are, to varying degrees, enhanced in α-elements over zinc.

PNG 019.7 + 03.2, a disk nebula, is consistent with Solar for both Zn/H and O/Zn. Additionally, the bulge nebulae PNG 011.0 + 05.8, PNG 352.1 + 05.1 and PNG 354.5+03.3 are also consistent with Solar for both Zn/H and O/Zn, although the ratios in the latter nebulae are subject to large uncertainties stemming from the oxygen abundance ratios.

Due to the lack of optical spectroscopy for the probable disk planetary nebula PNG 040.4 − 03.1, it was necessary to assume values for its electron temperature, electron density, and ionic and elemental oxygen abundances. Its Zn/H and O/Zn values are consistent with Solar, within estimated errors, however the results should be recalculated if optical spectra for this nebula become available.

The [Zn IV] 3.625 μm line was not detected in PNG 355.9+03.6, thus only limits could be placed by measuring the integrated intensity of the region where the [Zn IV] line should have been observed and comparing this to measured hydrogen integrated intensity. This gives an upper limit on the values of [Zn/H] and [O/Zn] to be −1.5 and 1.2 respectively. All hydrogen lines from the Humphreys and Pfund series within this wavelength range were detected. This nebula has a very low central star temperature of 3.8×10^4 K, and it is at this temperature that [Zn IV] loses its dominance according to our CLOUDY models. Thus, this nebula may not be as metal-poor as these limits suggest. Taking Zn^{3+}/Zn to be 0.45

(the result obtained from CLOUDY at this central star temperature), the limits on [Zn/H] and [O/Zn] reduce to −1.3 and 0.9 respectively. These values suggest that this nebula may have a significantly lower abundance of zinc in comparison to the Sun.

The well-studied disk nebula NGC 7027 displays Zn/H at approximately 1/3 that of the Solar value, whilst being enhanced in O/Zn by a factor of 2. This deviation from Solar may be explained in part by its high temperature (1.8×10^5 K) and in part by its large size of 14 arcseconds. The zinc observations and optical observations were taken with different slit widths at different orientations, and therefore will not trace the same regions of gas. In such a large nebula, this effect could be significant and could cause the zinc abundance to be underestimated due to the slit losses being different for different elements. For the majority of the other nebulae, the slit and nebulae have similar sizes meaning that this is less likely to cause discrepancies.

IC 5117 has a lower Zn/H ratio than Solar by a factor of two, whilst being consistent with Solar for O/Zn.

Two of the sample nebulae, PNG 006.1 + 08.3 and PNG 006.8 + 04.1, show significant enhancements in [O/Zn] such that when errors are taken into account, they still lie at values greater than 0.2 over Solar. Both nebulae have central star temperatures of 7.9×10^4 K, putting them within the temperature range where O^{++}/O maps Zn^{3+}/Zn in model nebulae to within approximately 2%.

5.5.1 Metallicity as a function of Galactocentric distance

The planetary nebulae in this sample are at a variety of Heliocentric distances and Galactic latitude and longitudes. Transforming these parameters into a Galactocentric distance can be simply executed via geometry:

$$R_G = \sqrt{\mathrm{R}_0^2 - 2\mathrm{R}_0 R\cos(b)\cos(l) + R^2}, \tag{5.6}$$

Table 5.4: Heliocentric (R) and calculated Galactocentric distances (R_G) and l and b coordinates for all sources. Heliocentric distances and calculated Galactocentric distances are accurate to 20%.

PNG	R (kpc)	l (deg)	b (deg)	R_G (kpc)
$004.0-03.0$	8.4	4.087	−3.005	0.79
$006.1+08.3$	8.0	6.188	+8.362	1.6
$006.4+02.0$	5.2	6.455	+2.015	3.4
$006.8+04.1$	6.8	6.805	+4.160	2.0
$019.7+03.2$	5.8	19.752	+3.273	3.6
$040.4-03.1$	9.5	40.441	−3.157	6.0
$355.4-02.4$	5.8	355.444	−2.467	2.8
$003.6+03.1$	2.3	3.618	+3.185	6.2
$011.0+05.8$	6.4	11.012	+5.894	2.1
$352.1+05.1$	9.4	352.188	+5.125	1.8
$354.5+03.3$	3.2	354.569	+3.353	5.3
$355.9+03.6$	10.1	355.969	+3.626	2.1
$358.2+03.6$	5.4	358.241	+3.634	3.1
NGC 7027	1.1	84.930	−3.496	8.5
IC 5117	8.2	89.873	−5.134	12

where R_G is the distance from the source to the Galactic centre, R is distance between the source and the Sun, l and b are the source's Galactic longitude and latitude respectively and R_0 is the distance between the Sun and the Galactic centre which has been taken to be 8.5 kpc. The distance between the Sun and the Galactic centre has been taken to be 8.5 kpc.

The l and b coordinates for all sources have been taken from Cutri et al. (2003b) and the Heliocentric distances from Stanghellini & Haywood (2010), and are shown, along with their calculated Galactocentric distances (R_G), in Table 5.4.

Fig. 5.7 and 5.8 show [Zn/H] and [O/Zn] as a function of the Galactocentric distances of the observed sources.

Abundance gradients throughout the Milky Way have been previously stud-

ied. For example, Rich (1998) shows a decline in [Fe/H] from ~ 0 to ~ -0.4 over 1000 pc in the Galactic bulge. Results derived specifically from planetary nebulae generally focus on the gradients of O and Ne through the galaxy. Pottasch & Bernard-Salas (2006), for example, find that the abundance of oxygen decreases over the range 3-11 kpc at a rate of -0.085 dex/kpc. Gutenkunst et al. (2008) derive abundance gradients for a sample of Galactic Bulge and Galactic Disk nebulae for Ne, S, Ar and O. They report negative gradients for the abundance trends of Galactic disk nebulae of between -0.08 and -0.14 dex/kpc. For Galactic bulge planetary nebulae, the results are less clear, with fits to the abundances having very large uncertainties. It is clear that the bulge and disk do not share an abundance trend with Galactocentric distance.

As shown in Fig. 5.7, from our sample, [Zn/H] appears to increase with increasing R_G until ~ 4 kpc, in contrast to Rich (1998) but more in agreement with the results of Gutenkunst et al. (2008). After this point, [Zn/H] appears to settle at a value below Solar and perhaps decreases with increasing distance, in agreement with the results from Pottasch & Bernard-Salas (2006) and Gutenkunst et al. (2008). However, due to the small sample size and large uncertainties involved, this must be taken with caution.

Fig. 5.8 shows that around half of our sample lie within one sigma of Solar [O/Zn], one nebula shows sub-Solar [O/Zn] and the remaining nebulae show enhancement in oxygen. No trend of [O/Zn] with Galactocentric distance is discernible.

5.6 Conclusions

We have derived [Zn/H] and [O/Zn] for a sample of fifteen planetary nebulae: thirteen newly observed nebulae (eleven from the Galactic bulge and two from the Galactic disk) and two which were previously observed by Dinerstein & Geballe (2001).

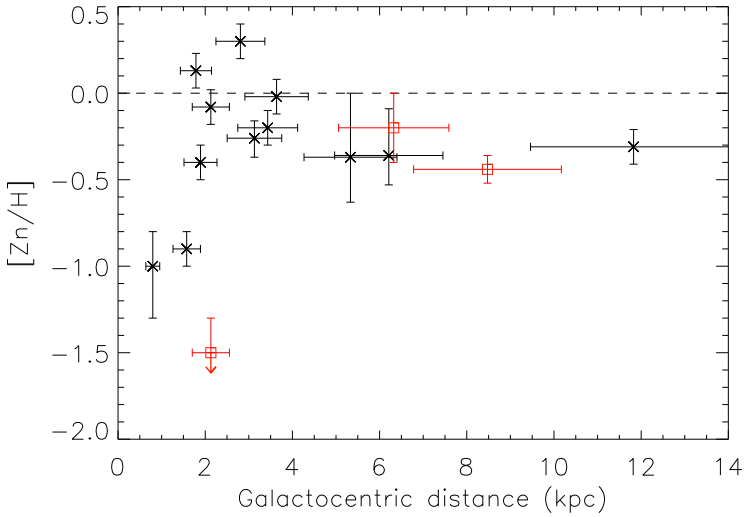

Figure 5.7: [Zn/H] against Galactocentric distance of sources. Red points indicate those sources with assumed parameters or those that lie outside the temperature range where O/O^{++} is a reliable ionisation correction factor.

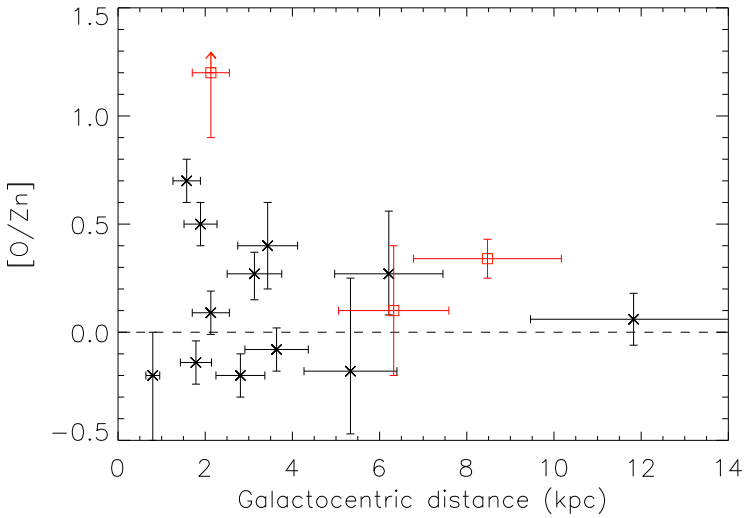

Figure 5.8: [O/Zn] against Galactocentric distance of sources. Red points indicate those sources with assumed parameters or those that lie outside the temperature range where O/O^{++} is a reliable ionisation correction factor.

Ten out of eleven of those nebulae present in the Galactic bulge show sub-Solar [Zn/H] and elevated [O/Zn]. The remaining bulge nebula shows an unusually high [Zn/H] and low [O/Zn]. One of the bulge nebulae, PNG 355.9 + 03.6, only has upper limits placed on the abundance of zinc, but these are very sub-Solar, thus this nebula appears to be metal-poor in comparison to the Sun.

One of the Galactic disk nebulae, PNG 019.7 + 03.2, shows Solar abundances for both [Zn/H] and [O/Zn], whereas the other, PNG 040.4−03.1, shows sub-Solar [Zn/H] and elevated [O/Zn]. The latter, however, should be taken with caution as values for ionic abundances and nebular temperatures and densities could not be computed as sufficient optical spectra were not available in the literature.

The two nebulae, NGC 7027 and IC 5117, as observed by Dinerstein & Geballe (2001) show [Zn/H] lower than Solar by more than a factor of 2. NGC 7027 also exhibits an enhanced [O/Zn] ratio in comparison to Solar, whereas IC 5117 displays [O/Zn] which is in line with Solar. The distinct difference from Solar values in NGC 7027 may be attributable to the large size of the nebula (14 arcseconds) resulting in a significant difference between the slit losses of the optical observations, from which the nebular temperature, densities and oxygen abundances were derived, and of the infra-red observations, from which the zinc abundances were derived. NGC 7027 also has a very high central star temperature of 1.8×10^5 K, which places this nebula outside the range of temperatures where O^{++} is a reliable ionisation correction factor for Zn^{3+}.

Overall, we have found the majority of this sample to exhibit sub-Solar [Zn/H], with the lowest measured at 10% of Solar. Half of the sample show [O/Zn] in line with the Solar value whilst the remaining half show enhancement in [O/Zn].

Chapter 6

Conclusions and further work

In this chapter, the research in this thesis is briefly summarised and the findings of each study are highlighted. Possible avenues of further work in these or related areas are then outlined.

6.1 Conclusions

Chapter 2: Molecular line survey

The chemistry of an AGB star is often very rich, containing many molecular and dust species. The chemical composition of an AGB star's circumstellar envelope is determined by the chemical composition of the stellar surface at the time of ejection. This composition is affected by a number of different mixing and nuclear processes that occur throughout the stellar lifetime.

Line surveys are an excellent method of examining the chemical composition of these diverse objects. A broadband molecular line survey has been carried out on five targets (3 C-rich AGB stars, 2 PNe) over the frequency range 84.5-115.5 GHz using the Mopra telescope, Australia. This survey has resulted in the detection and identification of up to 68 different transitions in each source.

The hyperfine structure of C_2H and $C^{13}CH$ have been fitted to derive their

optical depths. For those transitions without hyperfine structure, the emission line profiles have been used to constrain their optical depths. Rotational temperatures have been determined for all species which were detected in multiple transitions. Source-averaged column densities have been calculated for all detected species using both the direct calculation and population diagram method, where possible. From the column densities, isotopic ratios have been determined for a number of elements, including isotopologues of carbon, silicon and sulphur.

These results support the carbon-rich AGB star, IRAS 15194-5115 also known as II Lup, as being a J-type star whilst ruling out the remaining two AGB stars in the sample as J-types. Only carbon isotopic ratios could be determined for the planetary nebulae in the sample. These nebulae have abnormally low $^{12}C/^{13}C$ which, in the case of NGC 6537, is evidence for HBB having occurred.

Chapter 3: A new HCN maser in IRAS 15082-4808

Masers are a unique probe of astrophysical environments. In circumstellar envelopes of AGB stars, different maser species trace different regions of the envelope. In oxygen-rich stars, SiO, H_2O and OH masers are often found, with SiO tracing the inner-most region, below the dust formation zone and OH masers tracing the outer-most regions. In carbon-rich stars, only HCN masers are commonly found.

From the aforementioned Mopra dataset, we have identified a new source of the 89.087 GHz $v_2 = 2$ HCN maser. The offset velocity of the maser with respect to the systemic velocity of the envelope (taken as the velocity of the HCN J=1-0 non-masing line from the same dataset) was measured and found to be -2.0 ± 0.9 km/s. This agrees well with the nine other known maser sources, whose maser offset velocities vary between 0 and -5 km/s.

Drawing on all published detections of this maser in all sources, an investigation into the relationship between stellar phase and maser variability has been performed. This investigation utilised literature photometric data published over

more than 20 years and a genetic optimisation algorithm to fit sinusoidal light curves to the data. The results have shown no correlation of maser intensity with pulse phase, although maser observations have been sparse, so a study using coordinated photometric and spectroscopic observations would be desirable.

Comparing the known maser parameters with the works of Richards et al. (2012) and Cernicharo et al. (2011) constrains the maser formation to within 5 stellar radii, with a pumping mechanism that likely includes high energy states. Comparing the velocities of the masers with the models of Höfner et al. (2003b) results in a formation region around 2 stellar radii. Both these studies show that this maser forms below the dust formation zone in a region that is currently undergoing acceleration, providing an important tool in studying this inner region.

Chapter 4: Modelling CO in the circumstellar envelope of II Lup

Carbon monoxide plays a vital role in determining the chemistry of an AGB star. Its high binding energy means that it forms preferentially over other molecules. This results in the least abundant element being 'locked-up', leaving the more abundant element free to form other molecules. In oxygen-rich AGB stars, this results in the chemistry being dominated by silicates. In carbon-rich stars, a variety of carbon-containing molecules form.

Using a combination of radiative transfer codes (MCMax Min et al. 2009, GASTRoNOoM Decin et al. 2006, 2010 via the interface code ComboCode Lombaert 2013) we have modelled the carbon-rich AGB star II Lup (IRAS 15194-5115). Initially the SED was modelled, based upon *ISO* SWS and LWS data in combination with *Herschel* PACS data. CO and ^{13}CO were then modelled over a wide range of transitions (J=1-0 to J=52-51).

The resulting models suggest that II Lup cannot be represented by a 'standard' model. In order to recreate the observed line integrated intensities seen in the PACS data, either a variable mass-loss rate or a discontinuous temperature profile had to be invoked. The discontinuous temperature profile could be explained by

the presence of a cooling molecule (such as HCN) and the variable mass-loss rate would require a high mass-loss rate shell to be present. Neither model may be ruled out, but upon examination of the physical characteristics, the discontinuous temperature model appears to be the more likely representative model of this source.

Chapter 5: Zinc abundances of planetary nebulae

Determining the metallicity of planetary nebulae can be problematic. Fe/H is often taken as an indicator of the general metallicity of a star. However, iron emission lines in planetary nebulae are faint and iron can be depleted by up to 90% in ionised media. This results in iron abundances calculated directly from iron lines will only measure the gaseous abundance of iron rather than the overall iron abundance in the nebulae.

Zinc has a low condensation temperature which makes it significantly less likely to be depleted in the ionised environments of planetary nebulae. The Galactic Zn/Fe ratio is roughly constant at the Solar value over the range -3 < [Fe/H] < 0.5, making Zn an excellent surrogate element for measuring iron abundances. Finally, the 3.625 μm emission line, identified by Dinerstein & Geballe (2001), is detectable in planetary nebulae and represents the most abundant ion of zinc.

Building on the work of Dinerstein & Geballe (2001), infrared spectra of two samples of Galactic planetary nebulae have been obtained using ESO's Very Large Telescope (VLT). The total sample contains 23 nebulae, of which 13 yielded sufficiently high signal-to-noise spectra to detect or put meaningful upper limits on the [Zn IV] 3.625 μm line. The sample were selected on the basis of size, brightness, excitation and position in the Galaxy. The majority of the nebulae belong to the Galactic Bulge, with some nebulae (back-up targets, observed due to pointing restrictions during the observing runs) belonging to the Galactic Disk.

A grid of CLOUDY models, spanning a wide range of temperatures and den-

sities, has shown that the abundance of Zn^{3+} is most closely mapped by that of O^{++}, allowing the use of O/O^{++} as an ionisation correction factor for Zn^{3+}. Using literature optical spectra and the Nebular Empirical Analysis Tool (NEAT, Wesson, Stock & Scicluna 2012), a variety of physical parameters, including oxygen elemental and ionic abundances, have been calculated for these nebulae. Using these parameters, [Zn/H] and [O/Zn] have been successfully calculated for the sample.

[Zn/H] is generally sub-solar for the sample. [O/Zn] is, in general, either within uncertainties of Solar or slightly enriched in comparison to Solar. Abundances of [Zn/H] and [O/Zn] have been examined as a function of Galactocentric distance and a trend could not be determined in either case.

6.2 Further Work

Extending the model of II Lup

The model of II Lup could be extended by the inclusion of further molecules, such HCN, SiS or SiO. Modelling these additional molecules would follow the same method followed for CO, as detailed in Chapter 4. These molecules would form in different regions of the envelope and thus would allow the thermodynamic structure of different regions to be examined in detail. Further, by including silicon and sulphur-based molecules, silicon and sulphur isotopic ratios could be measured throughout the envelope of a J-type star. These modelled ratios could be compared with the properties of the A+B grains to further constrain their origin.

Further maser studies

With regards to the maser study carried out in Chapter 3, two areas of further work present themselves. The first is radiative transfer modelling of the masers

to determine the pumping mechanism, to further constrain their formation regions and to further examine their variability. This requires the collisional rate coefficients of the vibrationally excited lines to be available and, at the time of writing, these constants were not yet in the public domain.

Since the first discovery of the 89.087 GHz HCN masers, there has been only one published attempt at mapping the masing region of a circumstellar envelope. Carlstrom et al. (1990) report an upper limit on the size of the region as 0.45 arcseconds, which is approximately 180 AU using the distance estimates for CIT 6 available at the time. However, the region was not resolved and this distance is greater than that predicted by earlier works. Since this work was undertaken, improvements in telescope technology and a new generation of telescope provide the opportunity to observe at sufficiently high spatial resolution to successfully resolve this region (e.g. Global VLBI at 3 mm), thus this forms the second area of potential further work.

High resolution maps of this region would reveal the exact positioning of the maser in the circumstellar envelope, testing the previous assumptions about its proximity to its host star. From the sizes, shapes and intensities of the emission regions, information can be inferred about the mechanism and environment required for this maser to form. This will also provide invaluable data which can be used within models to examine the pumping mechanism once reliable rate coefficients become available.

Further planetary nebula investigations

Taking the zinc abundances calculated in Chapter 5 as the inherent metallicity of those nebulae, a follow-up investigation based upon examining s-process abundances as a function of metallicity, could be carried out.

The abundances of s-process elements, such as Kr, Xe and Br, in TP-AGB stars has been shown to correlate with the length of time the star has spent in this phase of evolution, with a longer time resulting in a higher abundance. Plan-

etary nebulae have completed this phase of evolution and therefore the measured abundances of s-process elements reflect the final abundances after all enrichment processes have occurred. Planetary nebulae are also the brightest phase of low-mass stellar evolution with a variety of observable forbidden transitions of a multitude of elements at a range of ionisation states available.

If high spectral-resolution optical data could be obtained for the nebulae in the sample of Chapter 5, the abundances of a number of S-process elements (in particular Xe and Kr as these noble gases do not condense out of the ionised medium) could be calculated using a nebular diagnostic code, such as NEAT (see Chapt. 5 for further details of this code).

In addition to examining any trend of s-process abundance with metallicity, the s-process abundances can also be used to constrain the population and thus formation theories of the Galactic Bulge. If s-process elemental abundances in the Galactic bulge were found to be enhanced with respect to Solar, this would provide evidence of the existence of a younger stellar population within the bulge.

Appendix A

Mopra spectra

The following sections show the final obtained spectra of each source, displayed in 0.3 GHz segements. These spectra have been corrected for source LSR velocities, which have been taken as: -15.0 km/s (IRAS 15194-5115, De Beck et al. 2010), -0.76 (IRAS 15082-4808, Smith, Zijlstra & Fuller 2014), -38.9 km/s (IRAS 07454-7112, Risacher & van der Tak 2009), -44.5 km/s (IC 4406, Sahai et al. 1991) and 10.0 km/s (NGC 6537, Edwards & Ziurys 2013).

A.1 IRAS 15194-5115

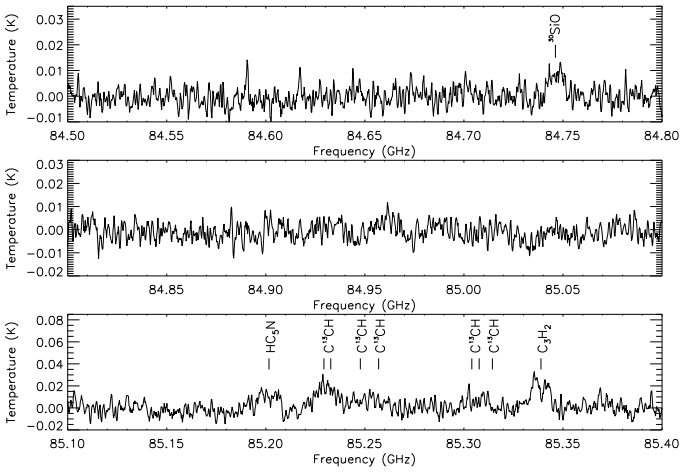

Figure A.1: Mopra spectrum of IRAS 15194-5115.

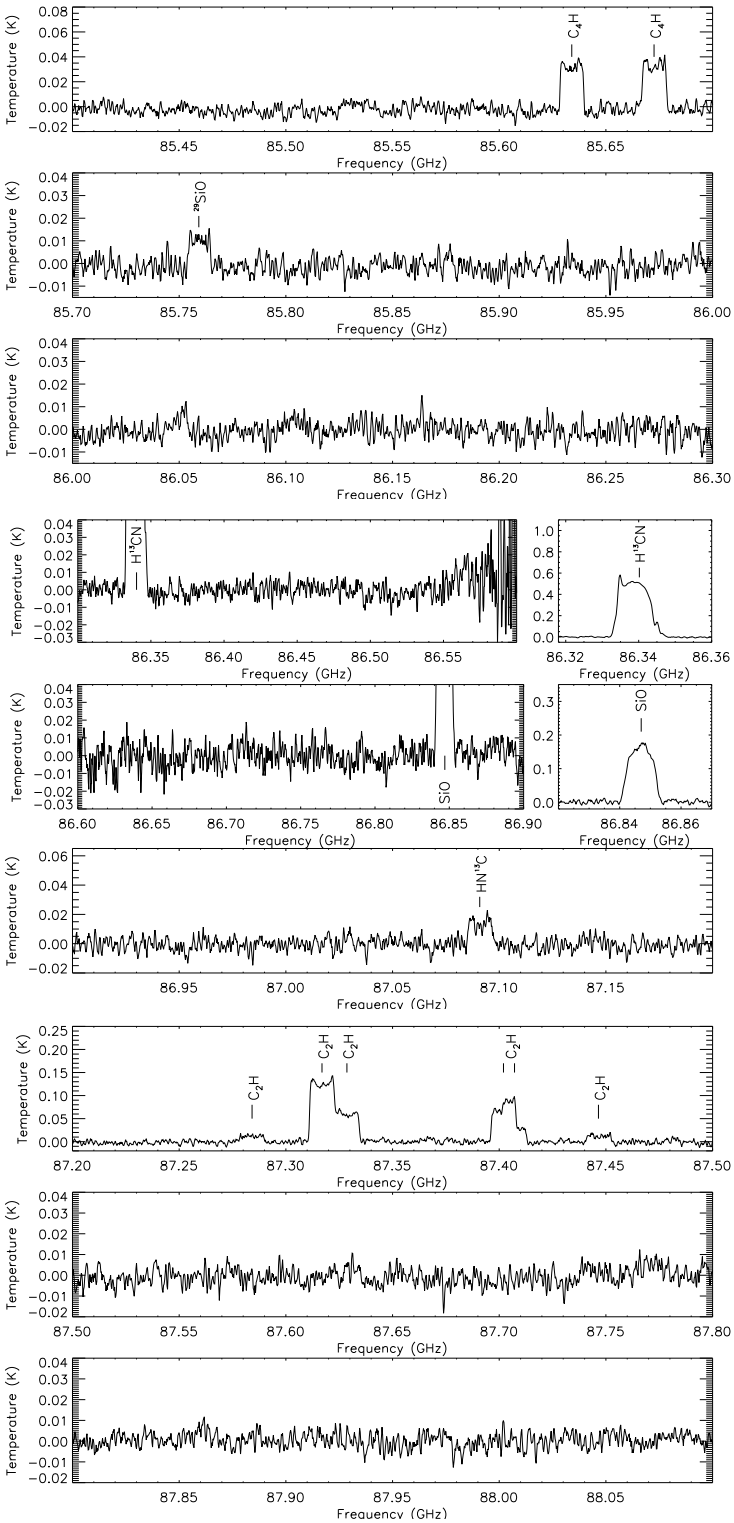

Figure A.1: – *continued.*

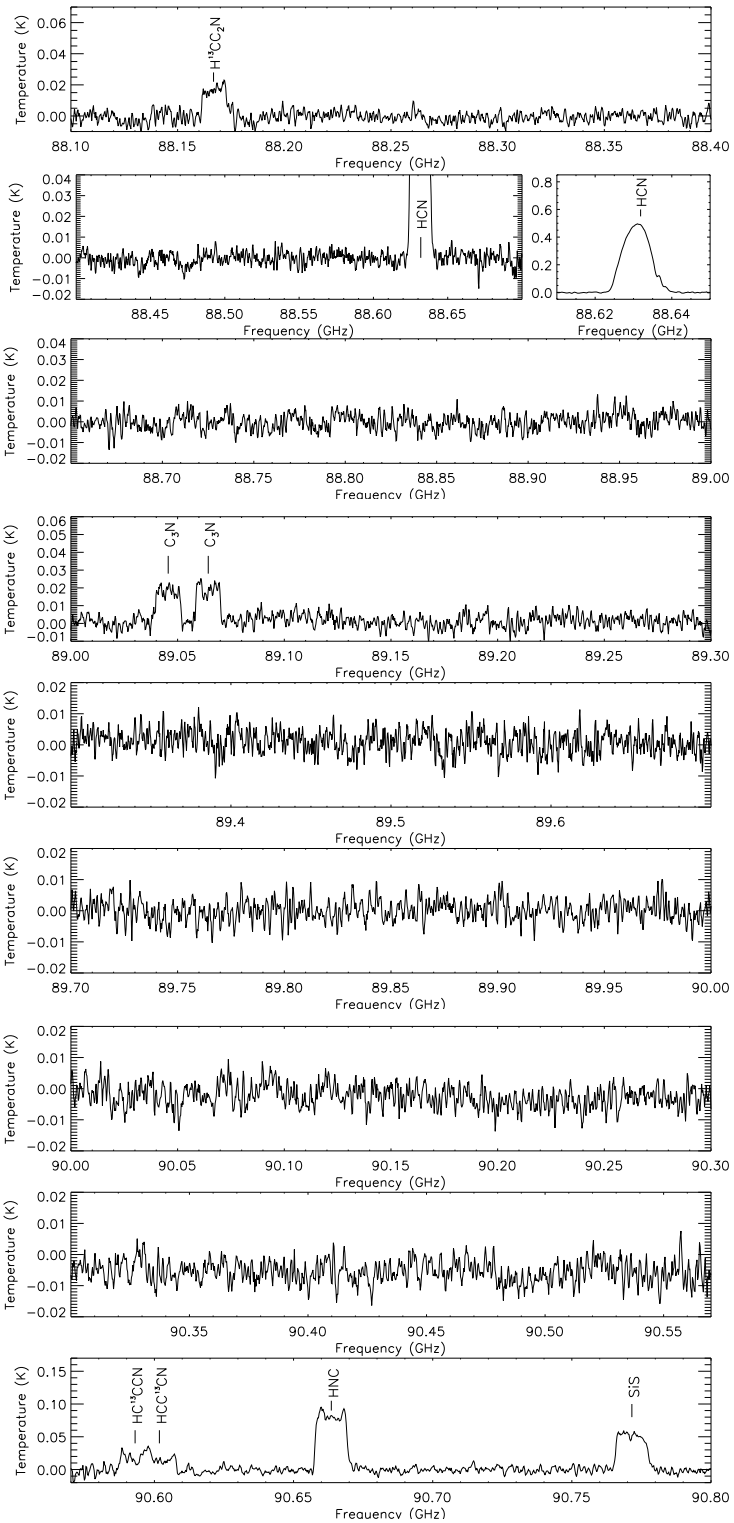

Figure A.1: – *continued.*

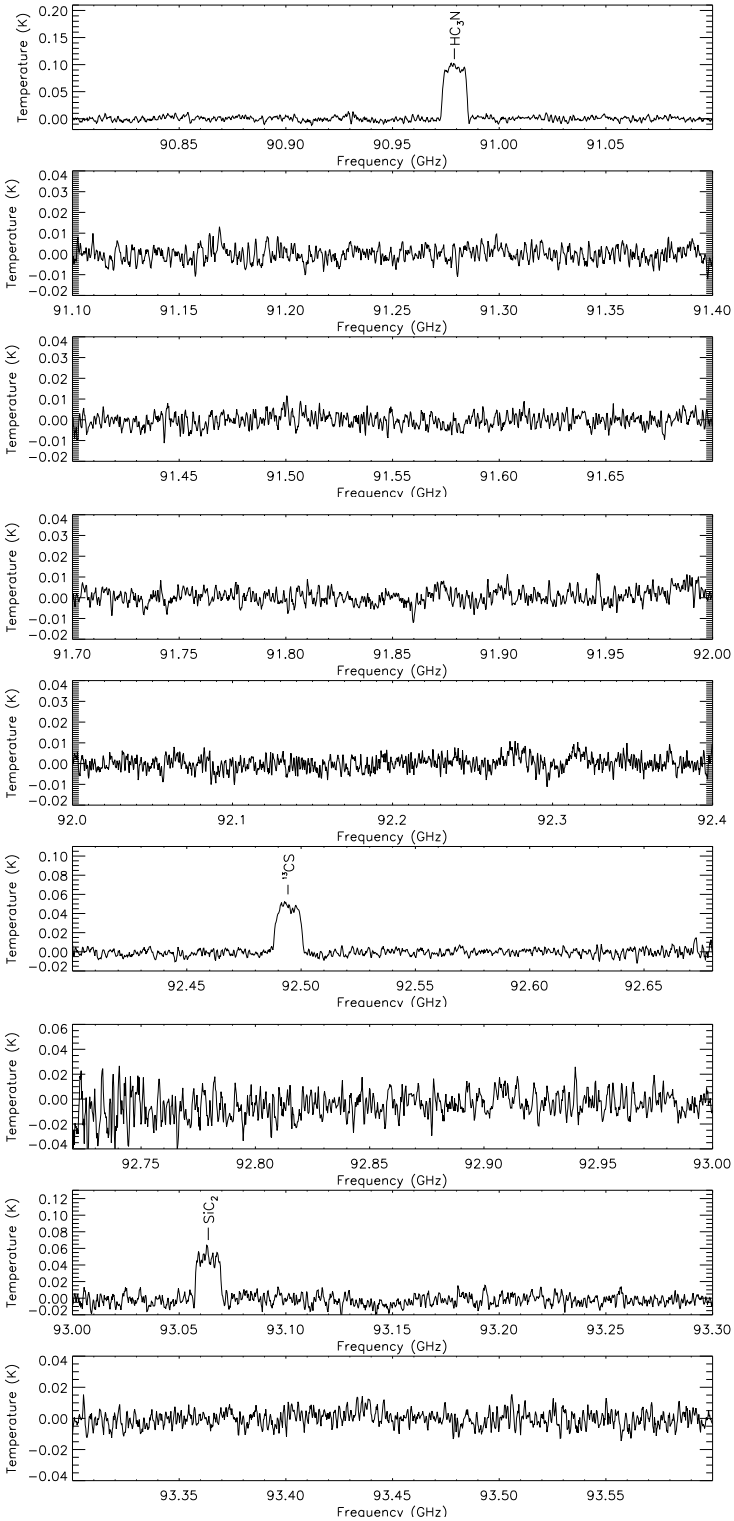

Figure A.1: – *continued.*

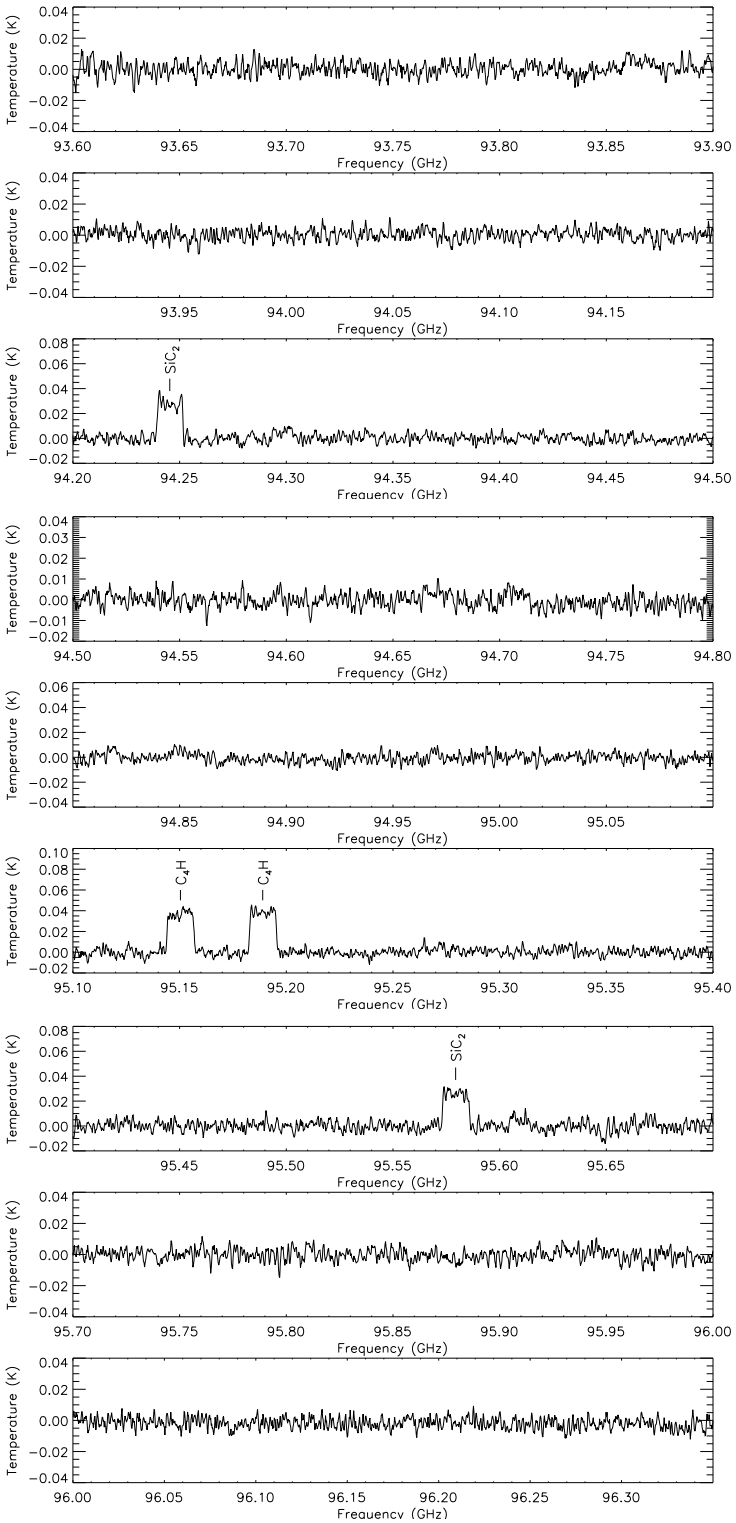

Figure A.1: – *continued.*

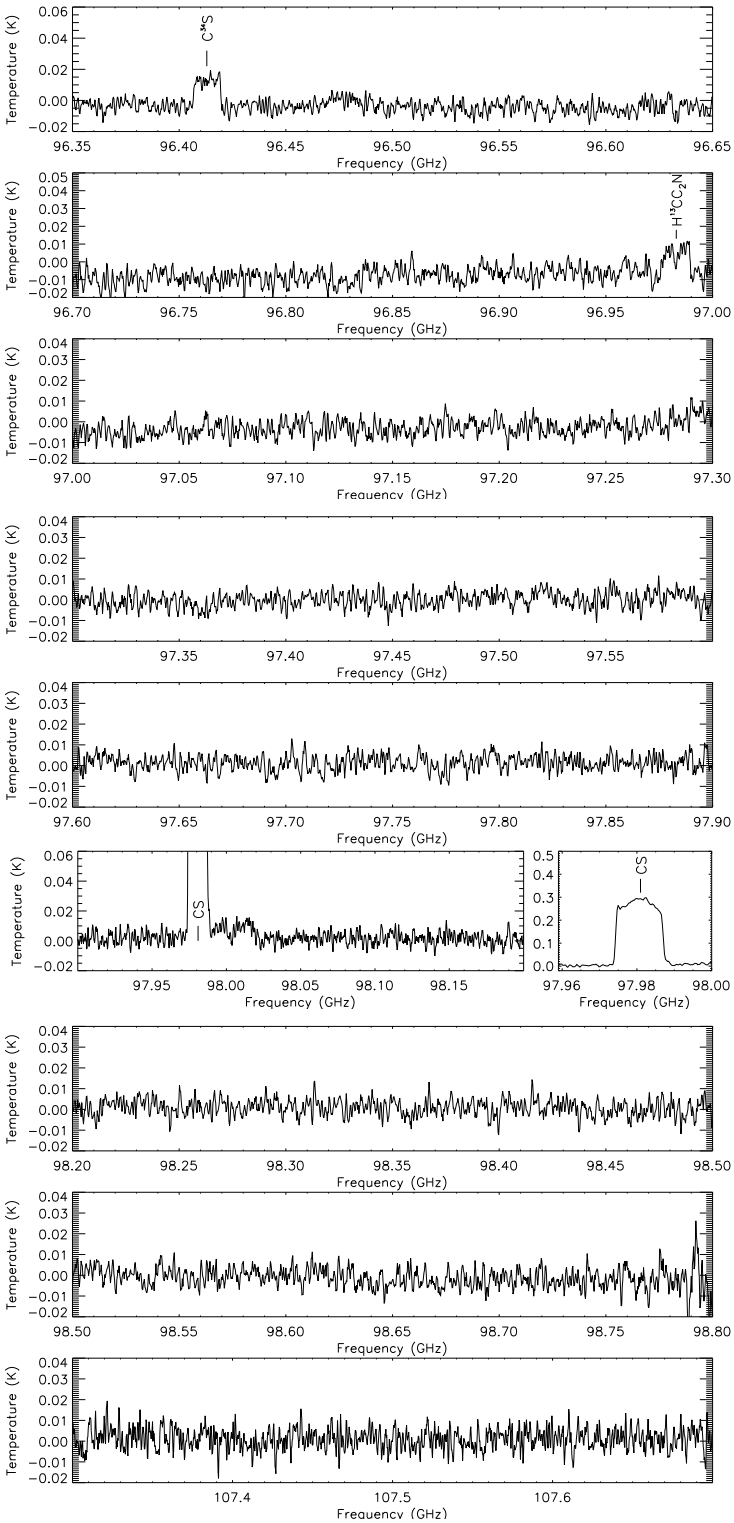

Figure A.1: – *continued.*

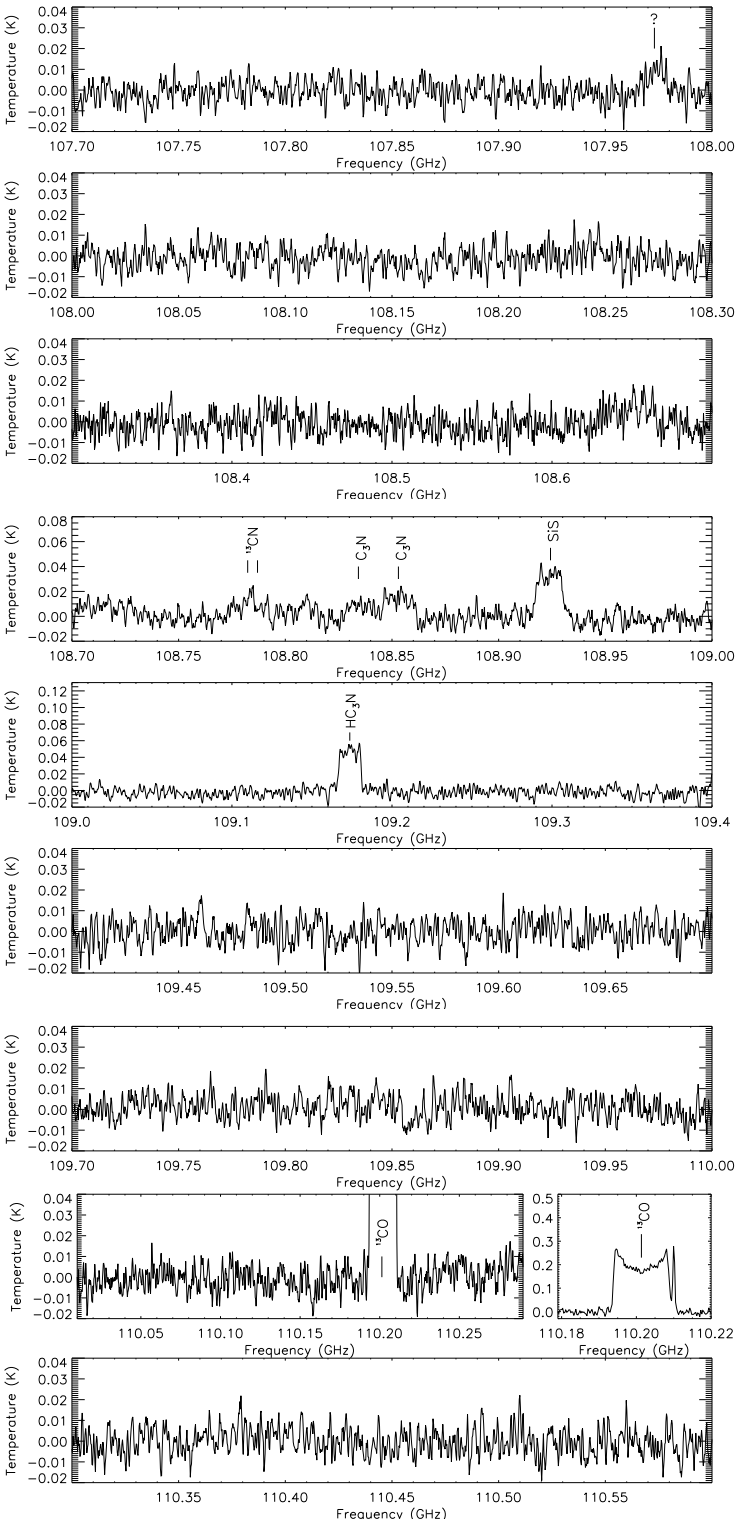

Figure A.1: – *continued.*

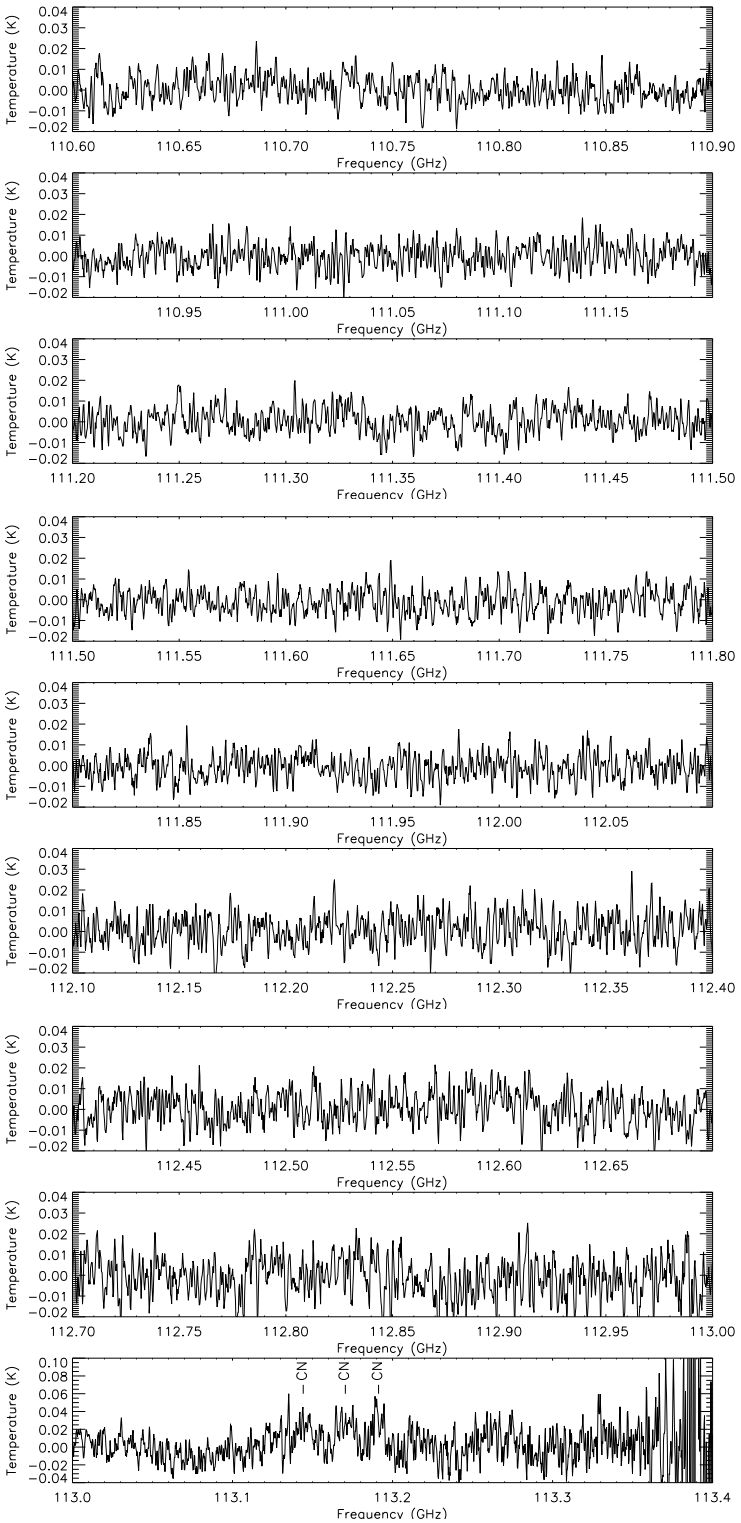

Figure A.1: – *continued.*

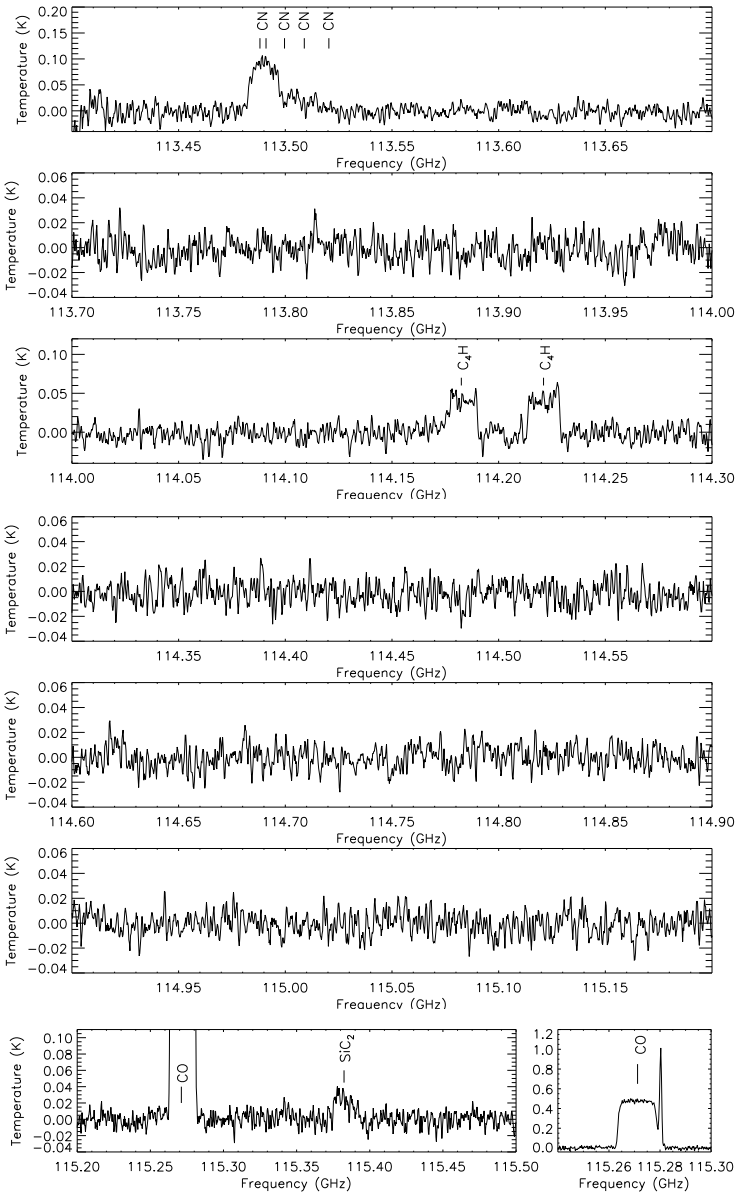

Figure A.1: – *continued.*

A.2 IRAS 15082-4808

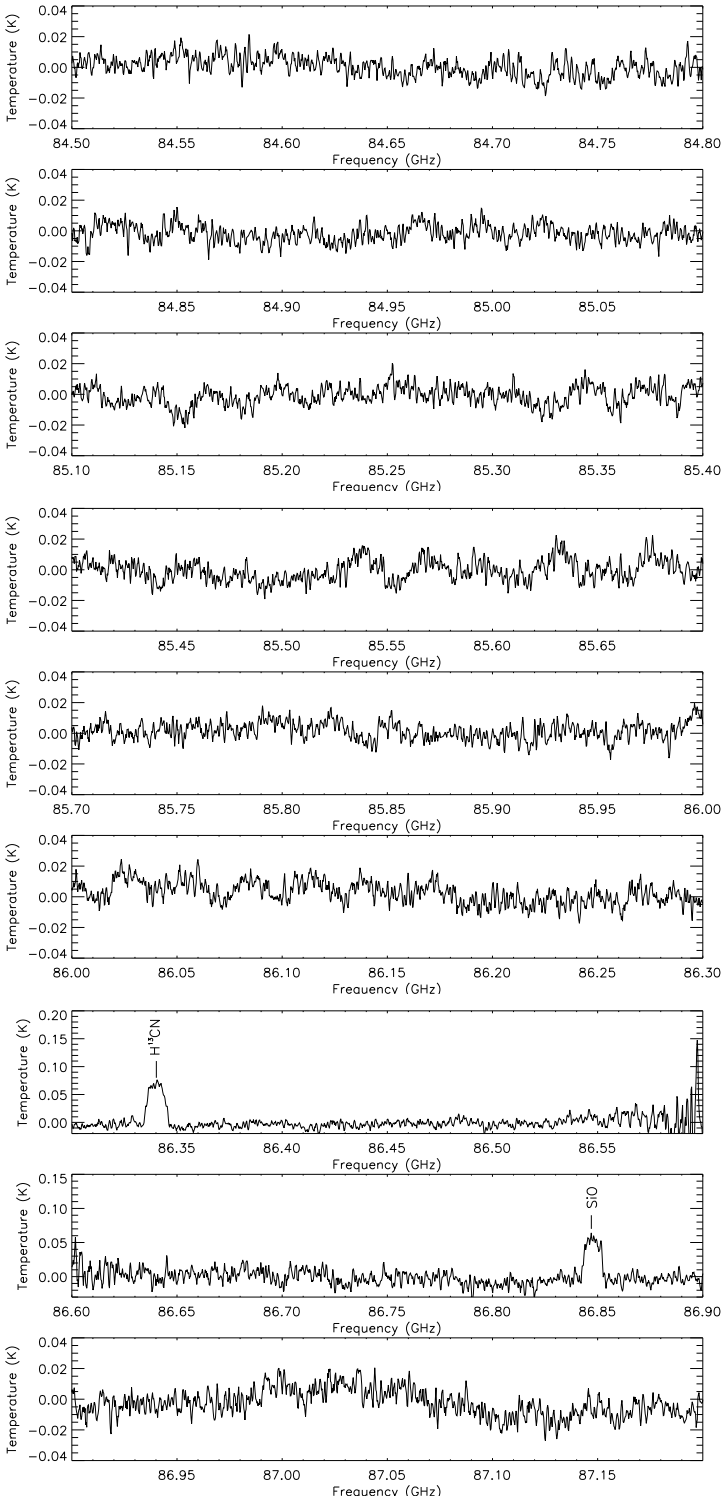

Figure A.2: Mopra spectrum of IRAS 15082-4808.

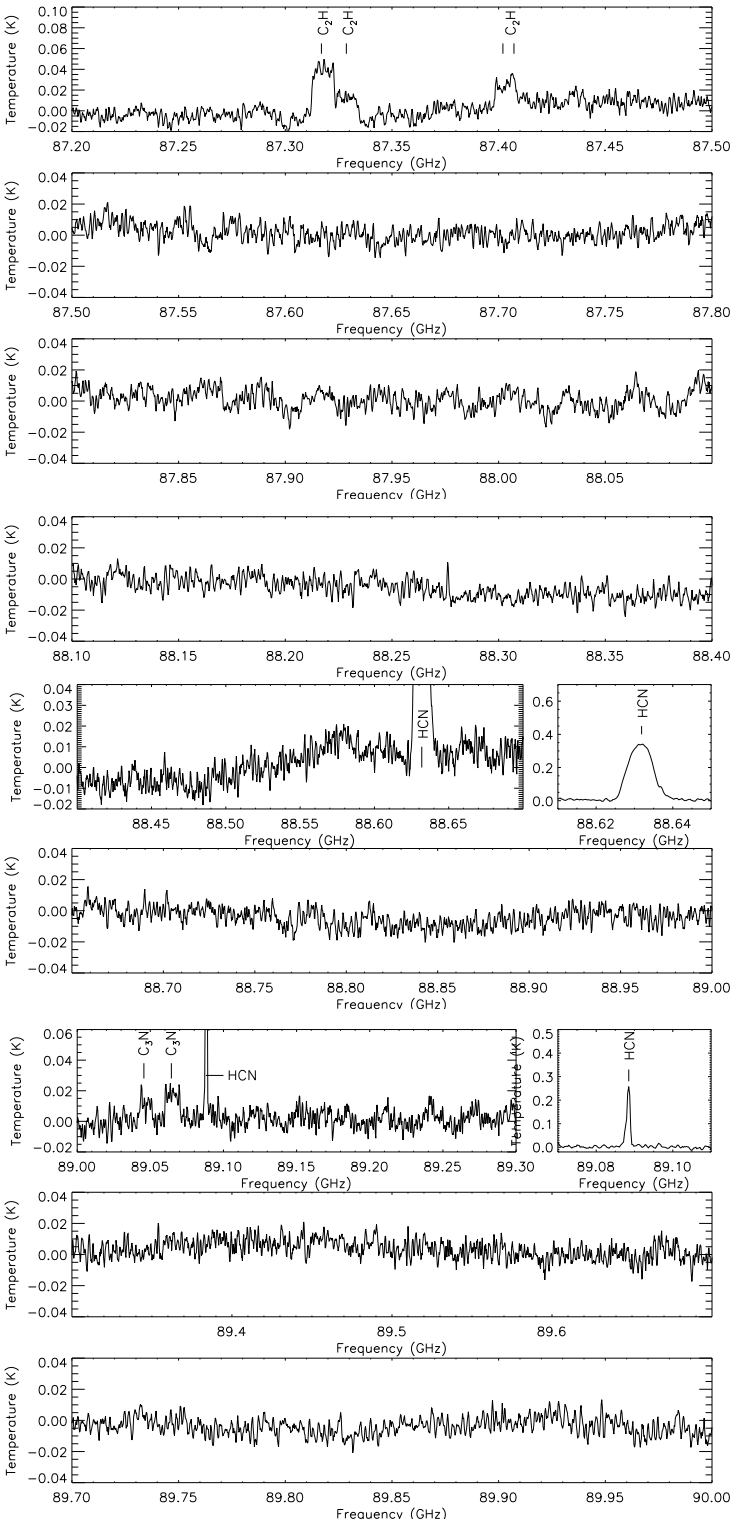

Figure A.2: – *continued.*

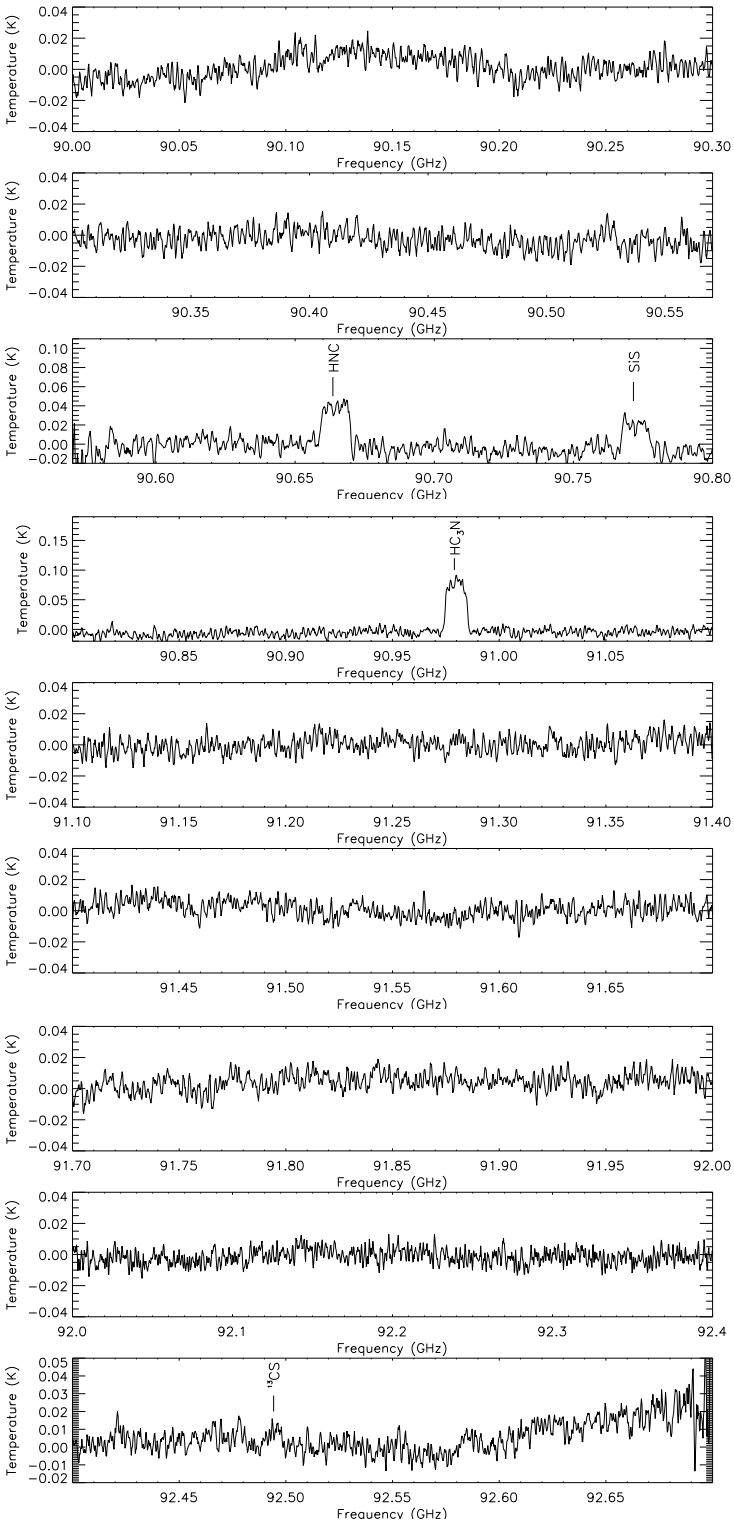

Figure A.2: – *continued.*

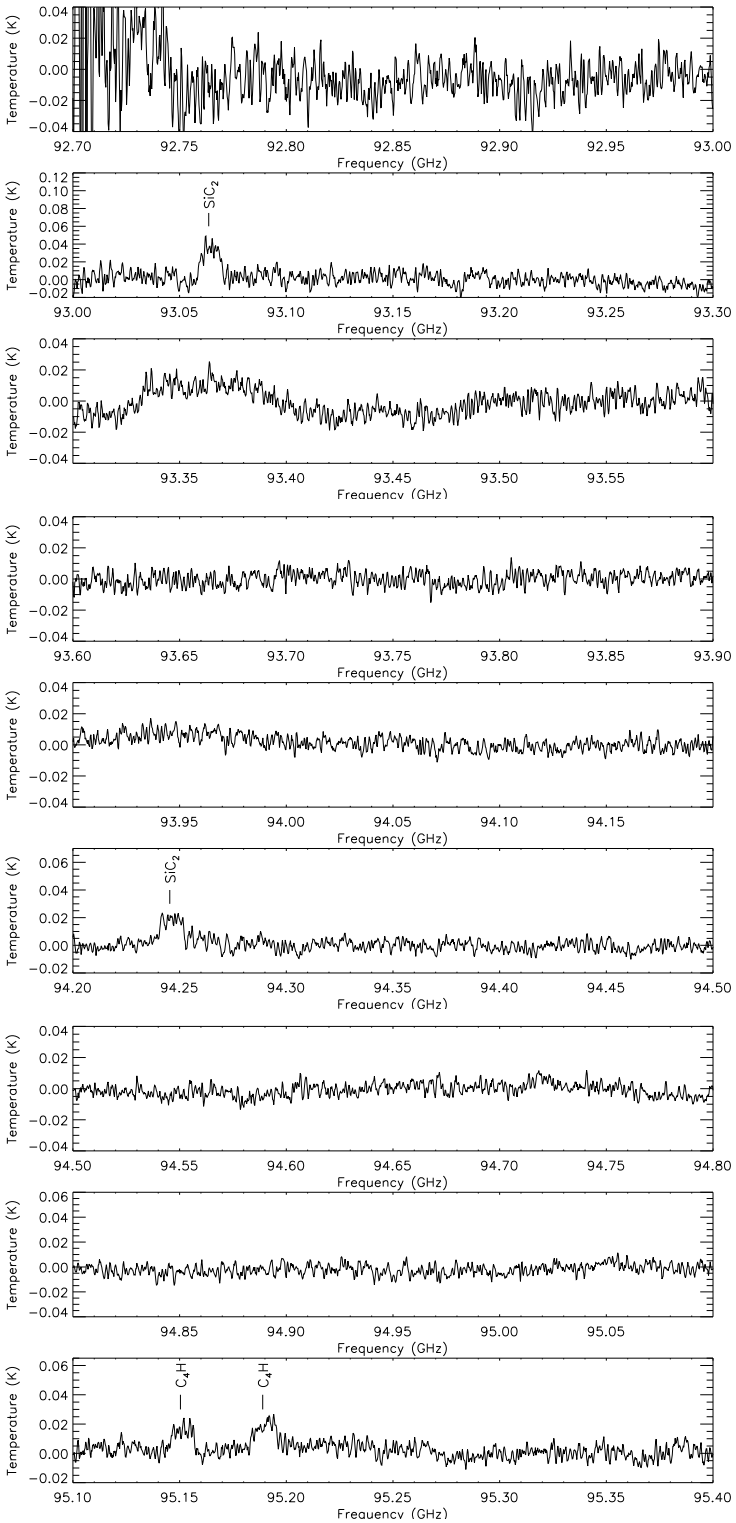

Figure A.2: – *continued.*

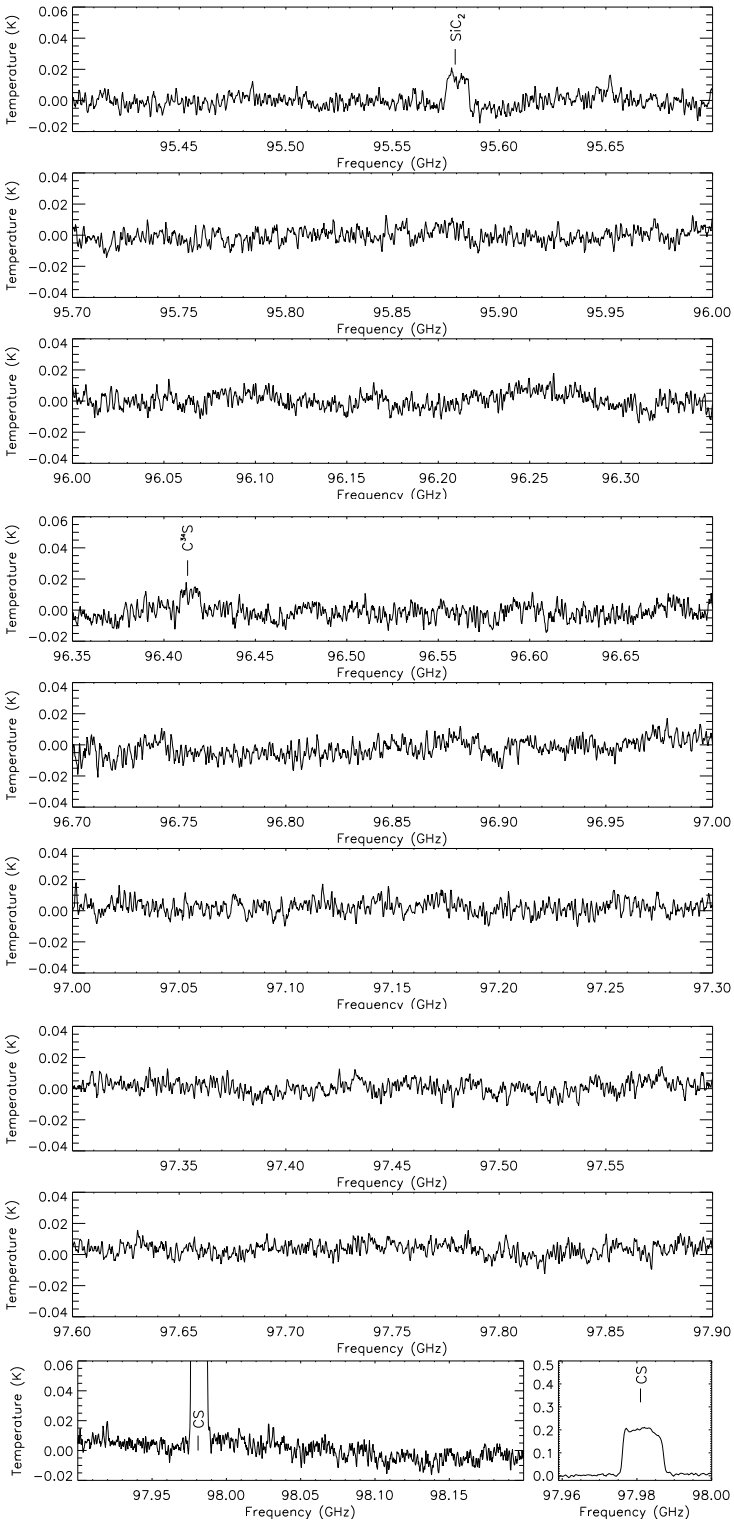

Figure A.2: – *continued.*

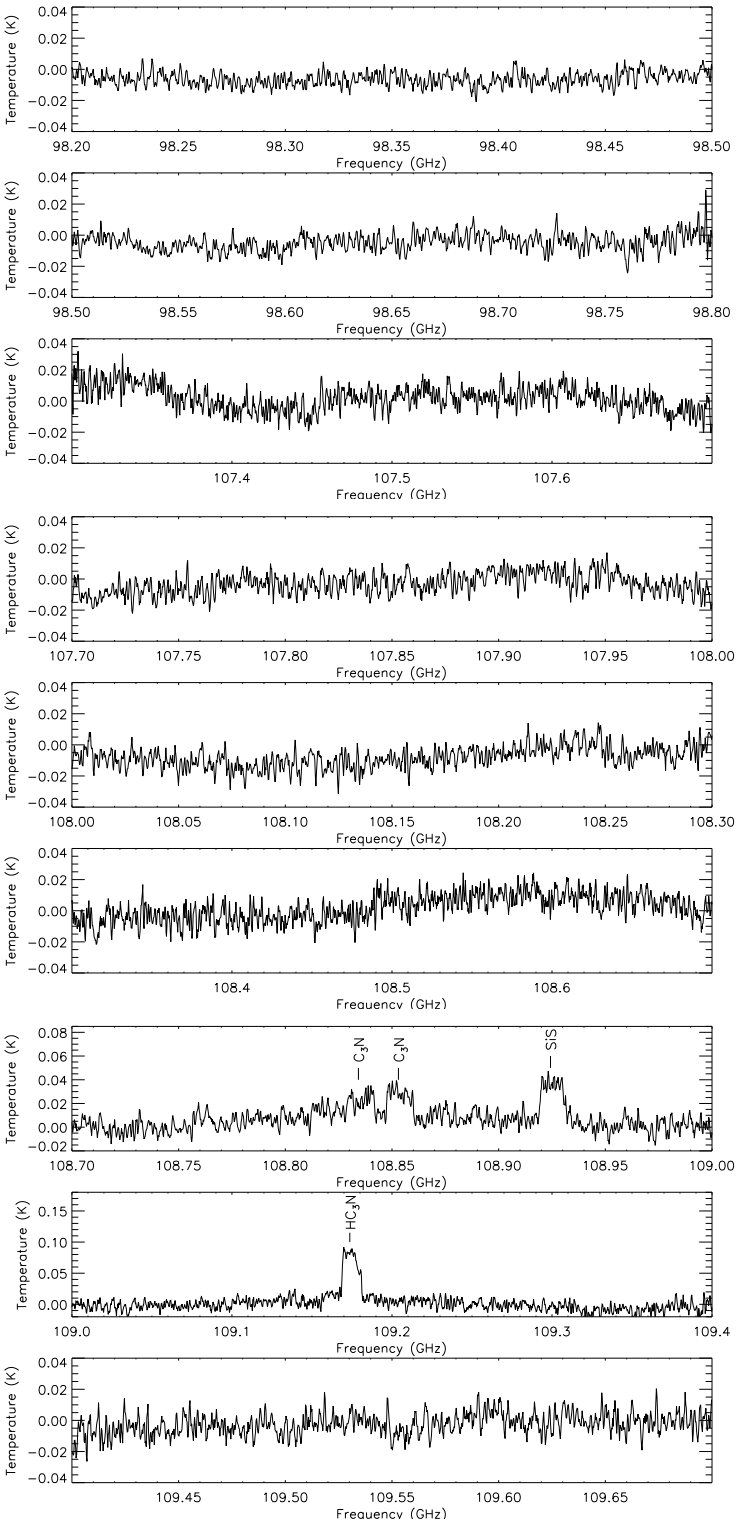

Figure A.2: – *continued.*

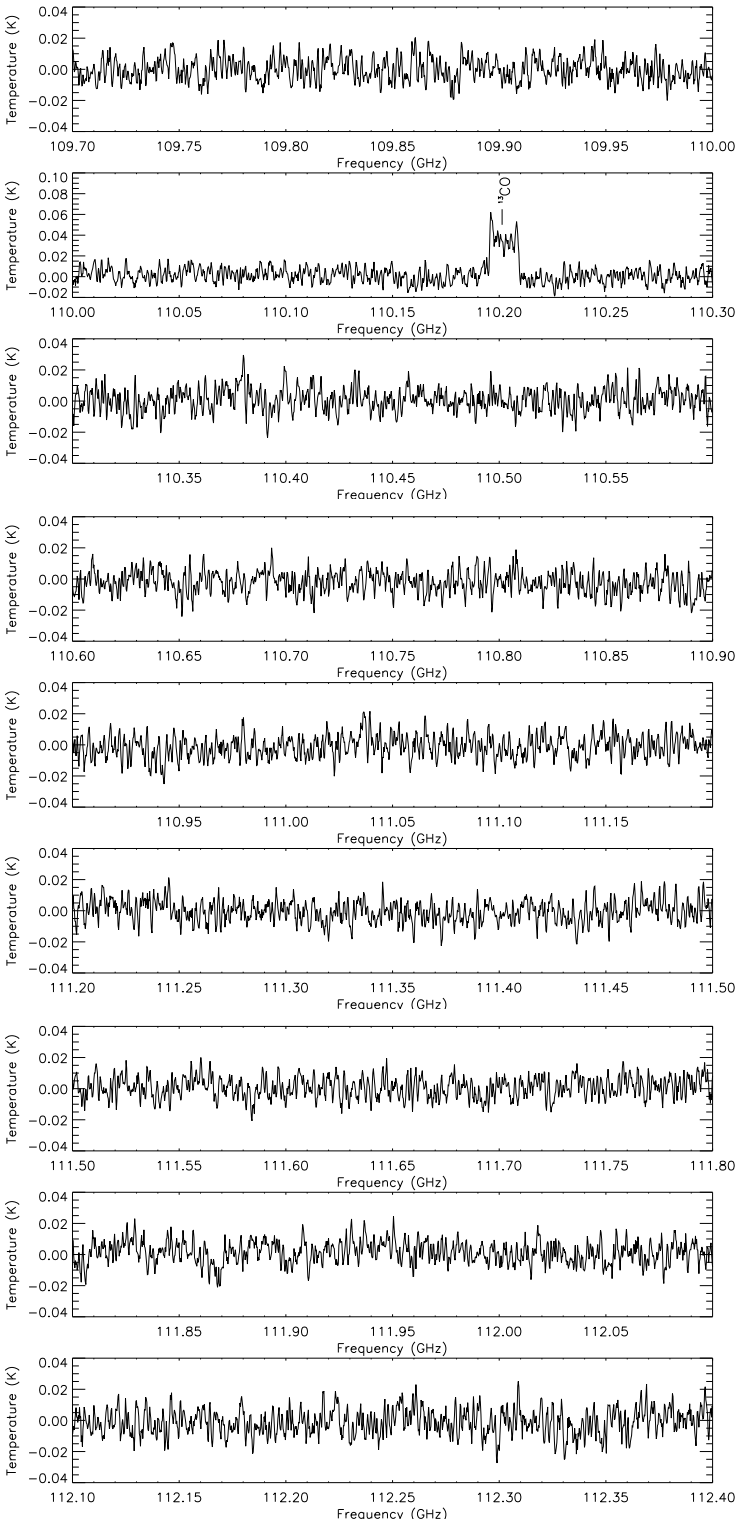

Figure A.2: – *continued.*

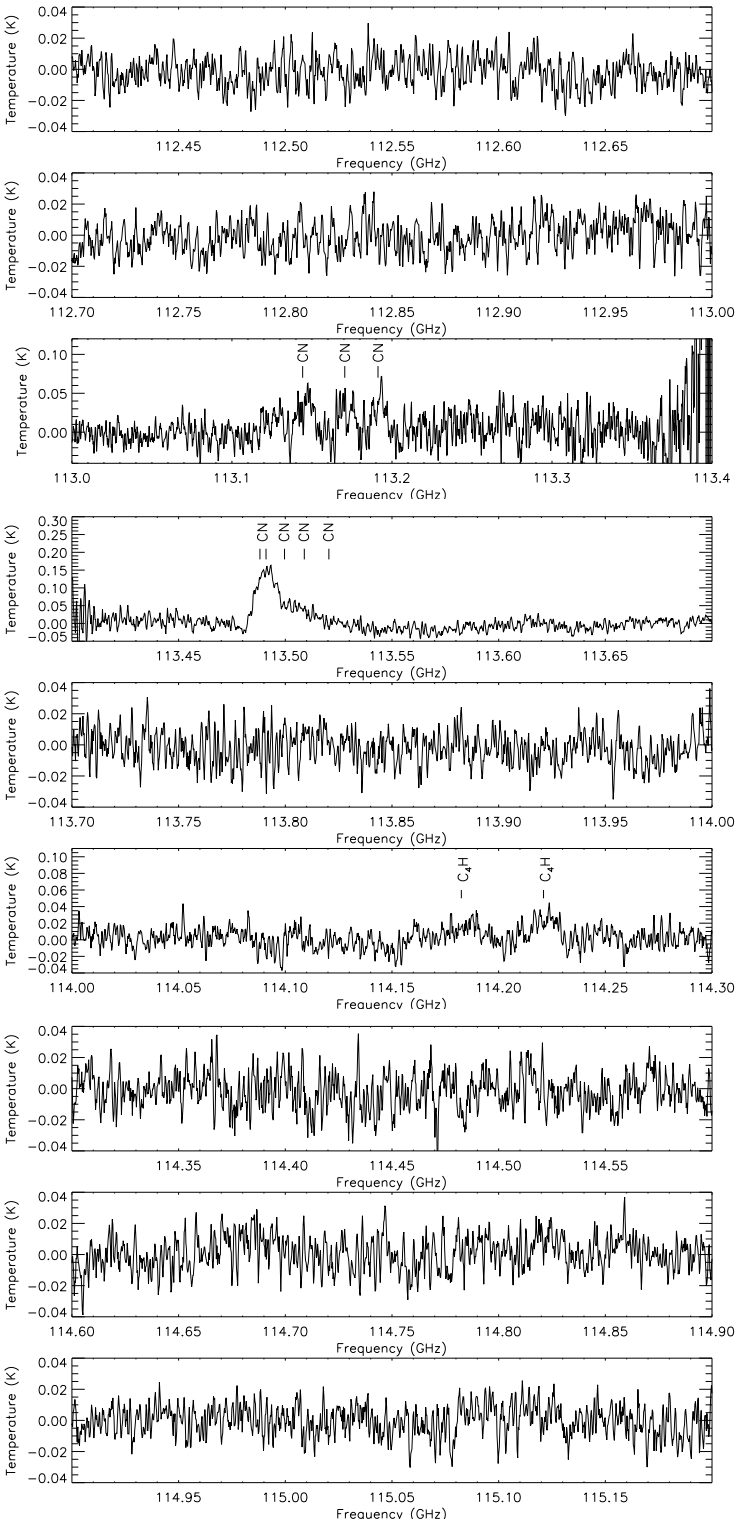

Figure A.2: – *continued.*

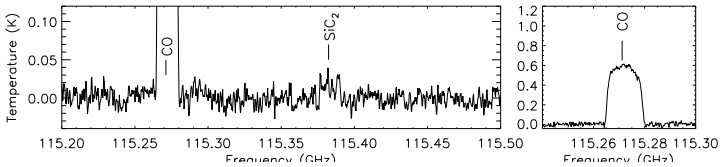

Figure A.2: – *continued.*

A.3 IRAS 07454-7112

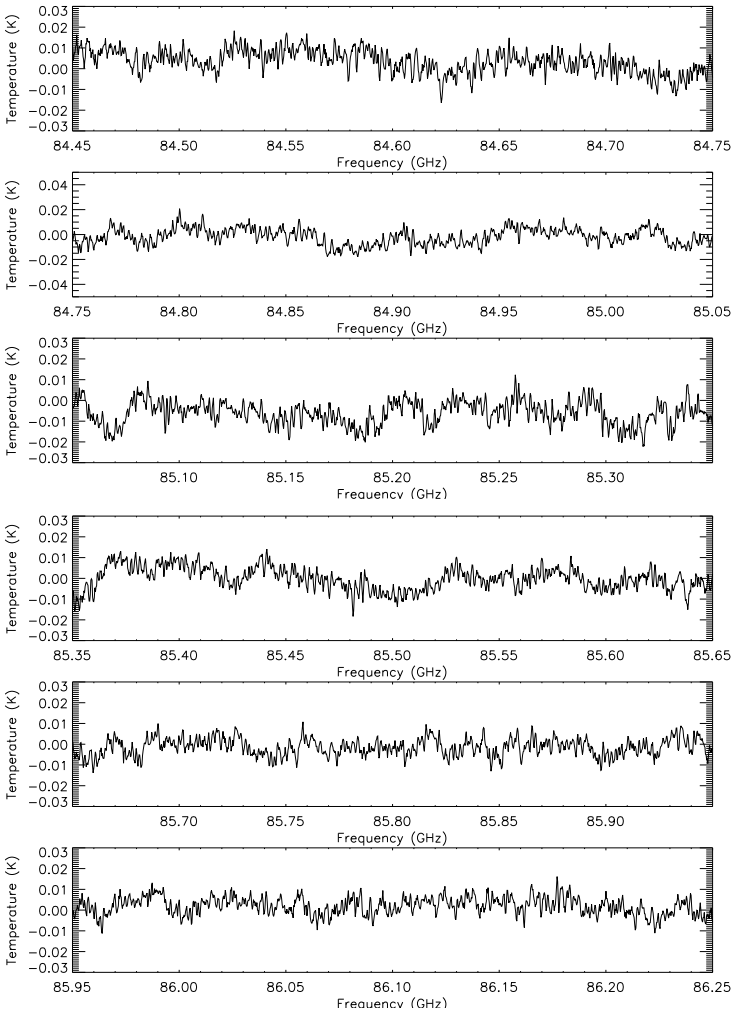

Figure A.3: Mopra spectrum of IRAS 07454-7112.

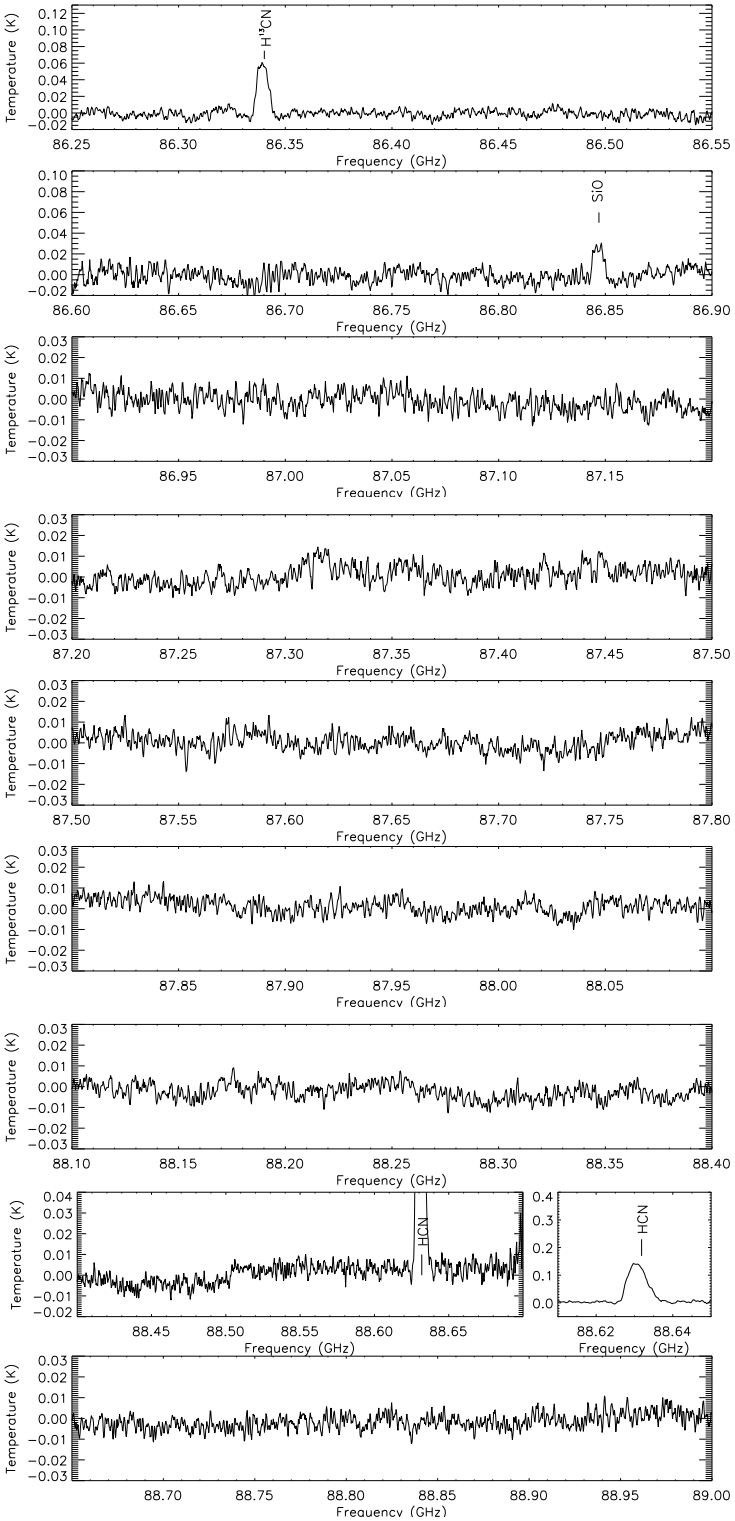

Figure A.3: – *continued.*

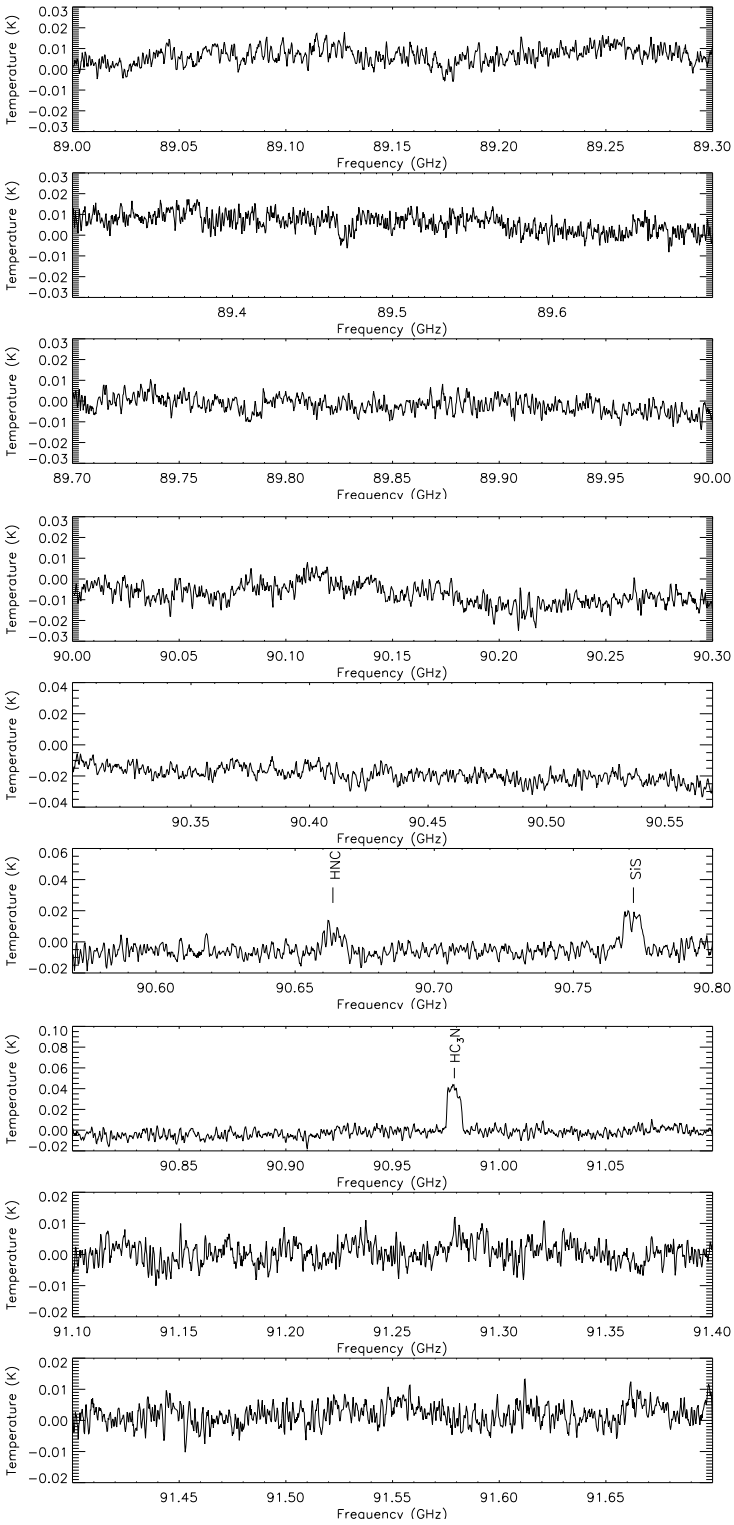

Figure A.3: – *continued.*

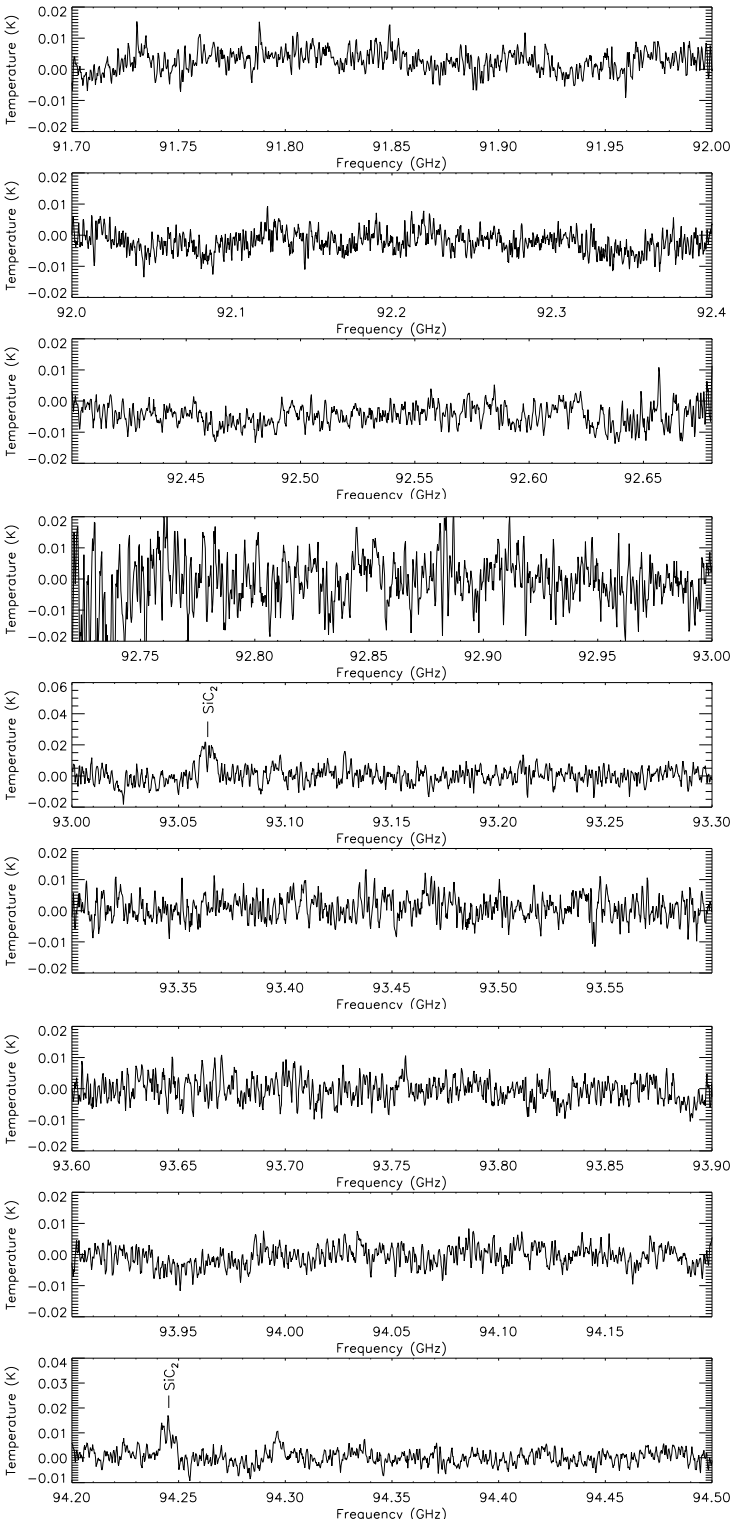

Figure A.3: – *continued.*

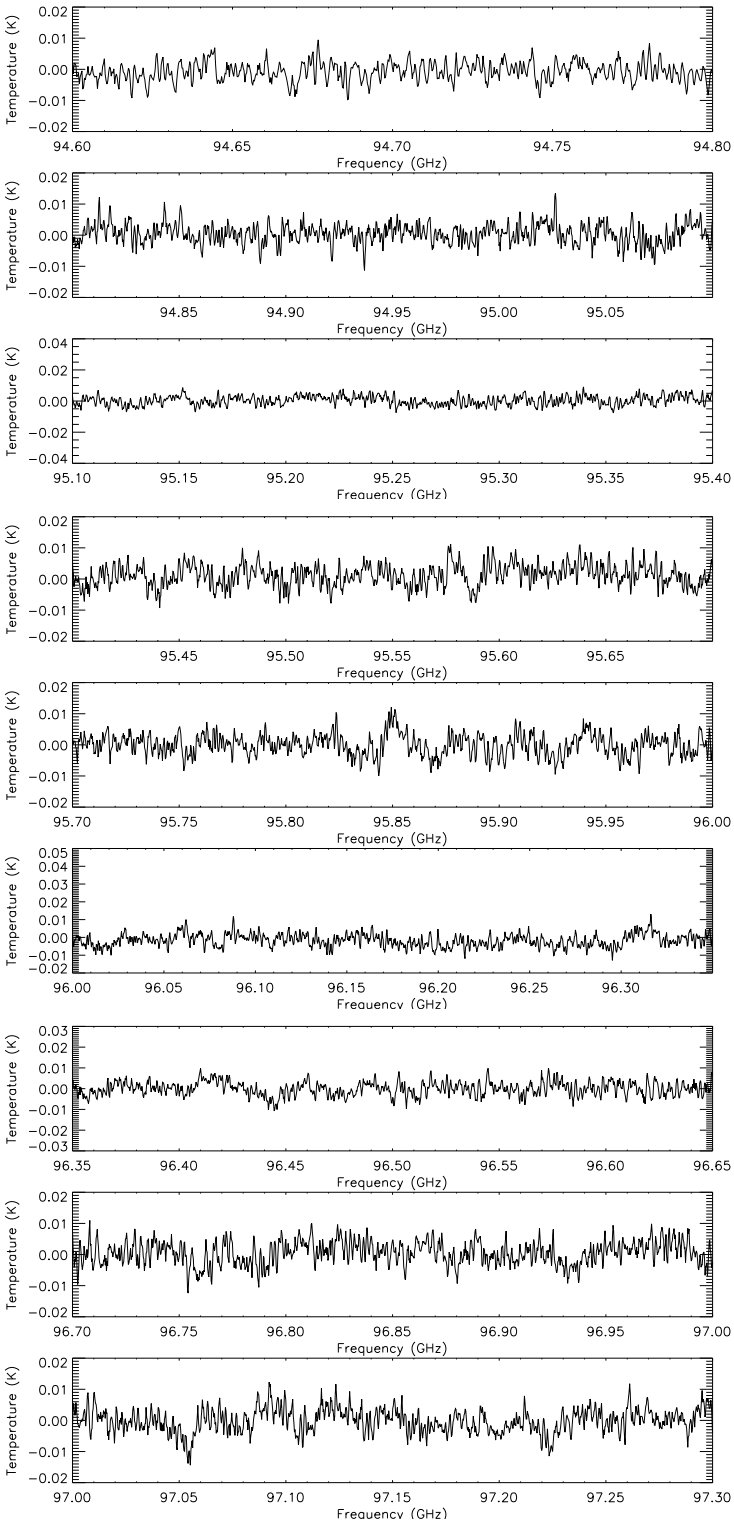

Figure A.3: – *continued.*

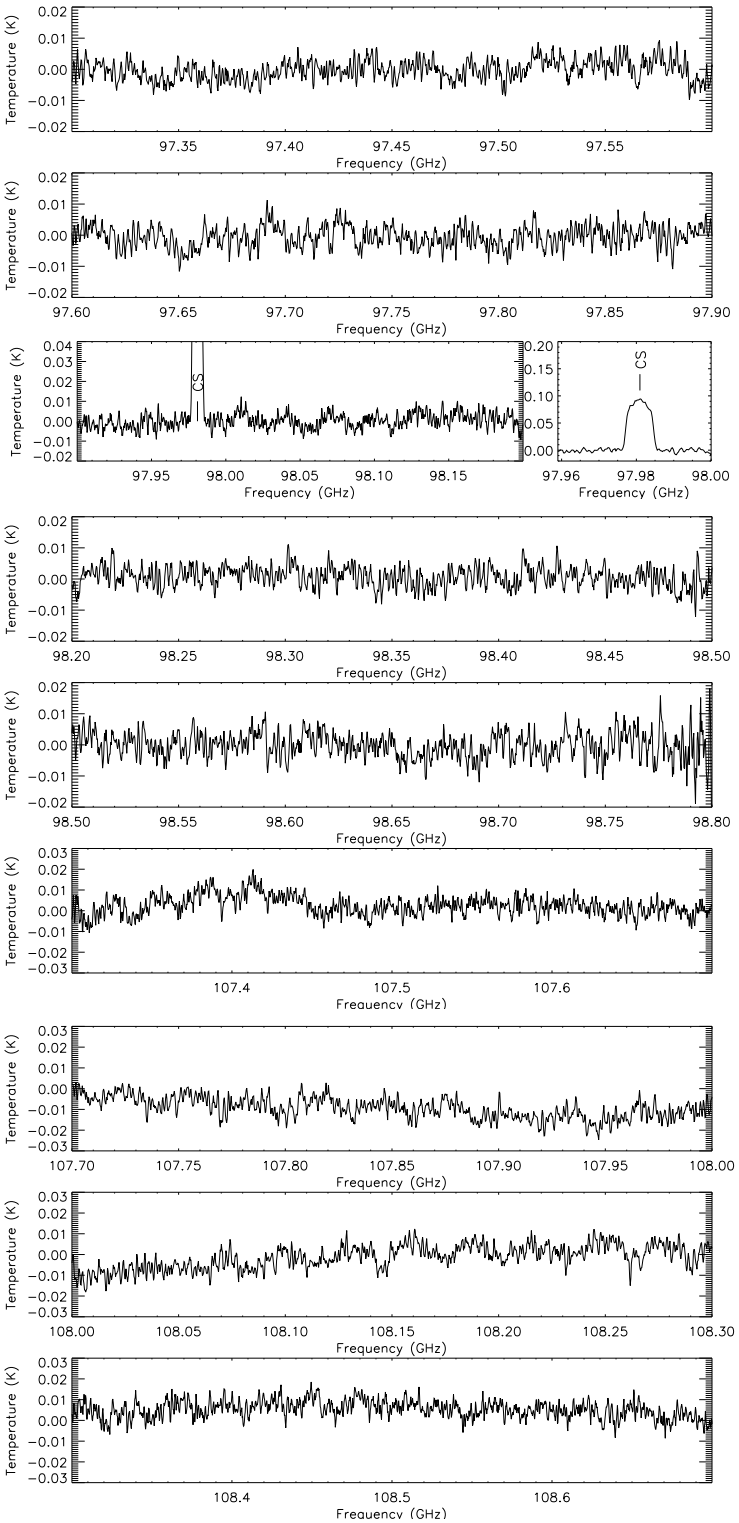

Figure A.3: – *continued.*

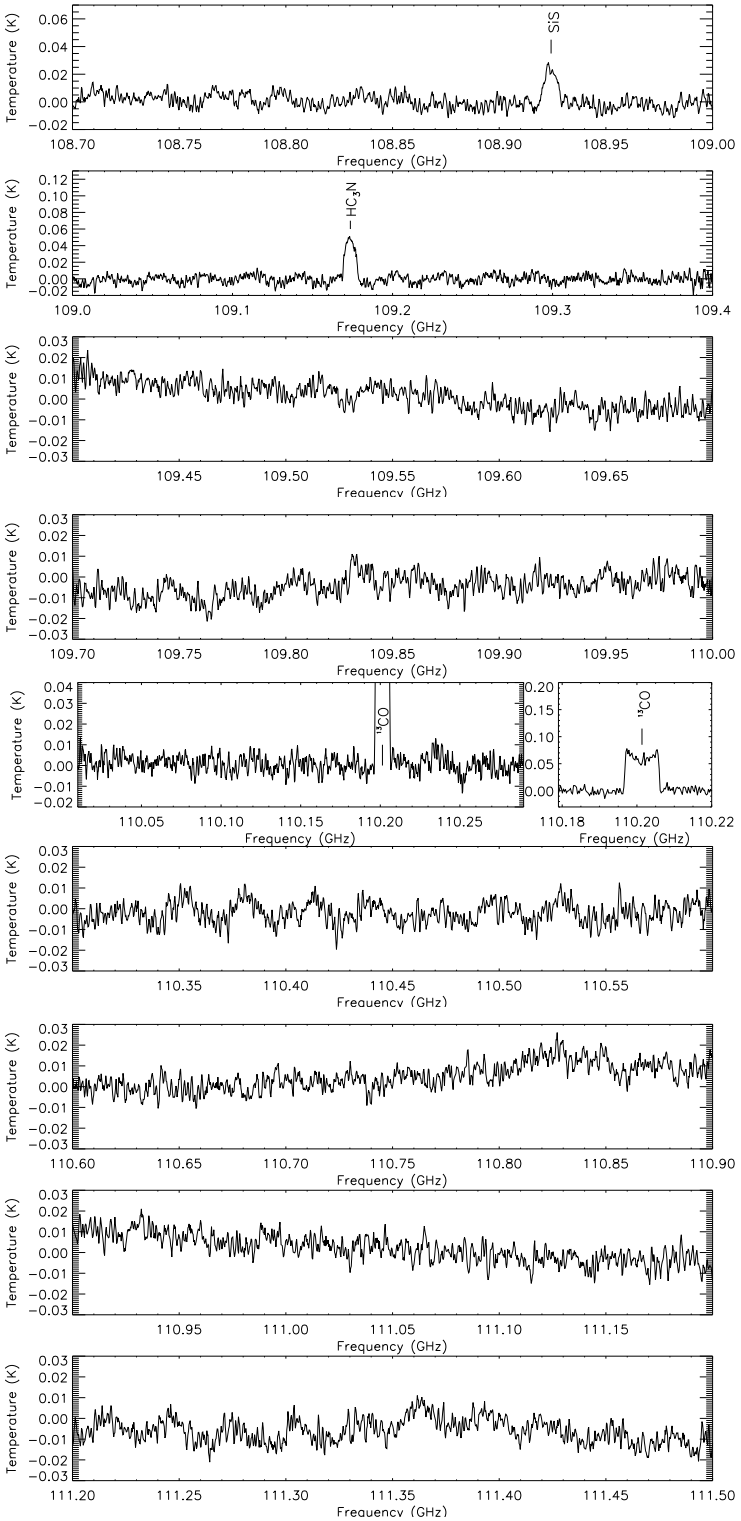

Figure A.3: – *continued.*

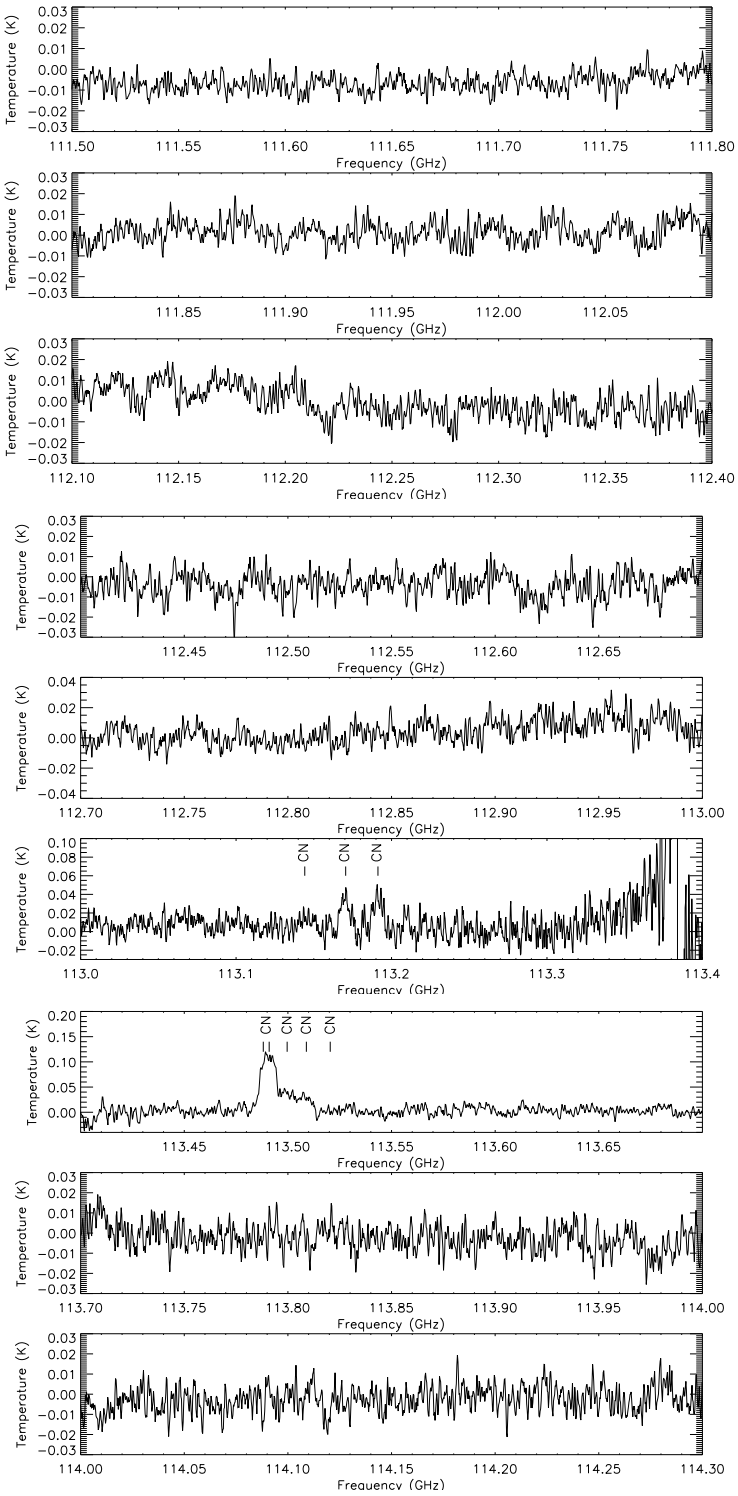

Figure A.3: – *continued.*

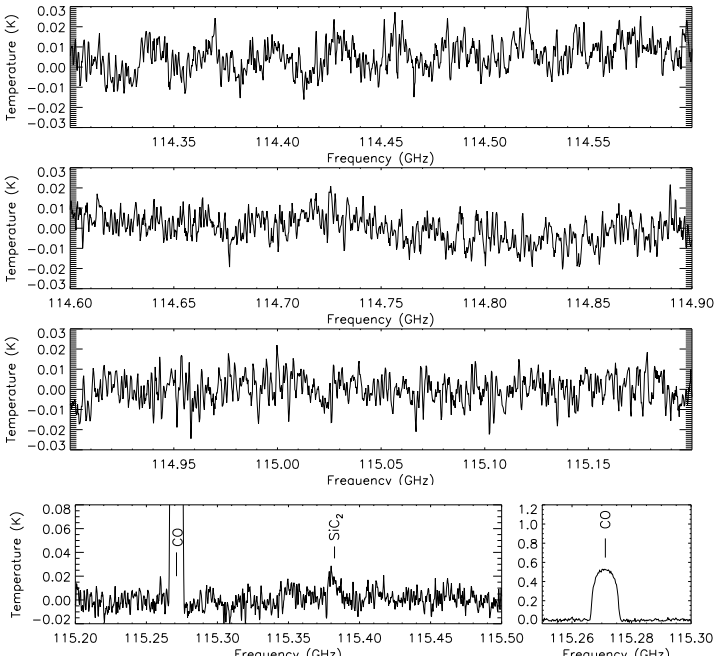

Figure A.3: – *continued.*

A.4 IC 4406

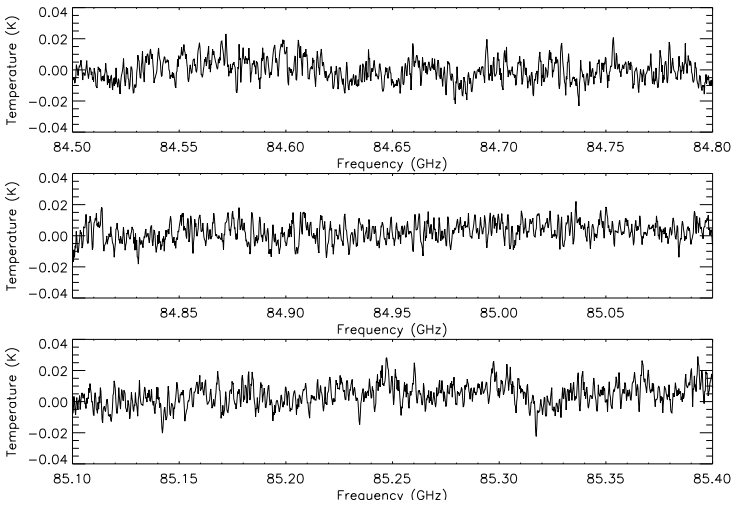

Figure A.4: Mopra spectrum of IC 4406.

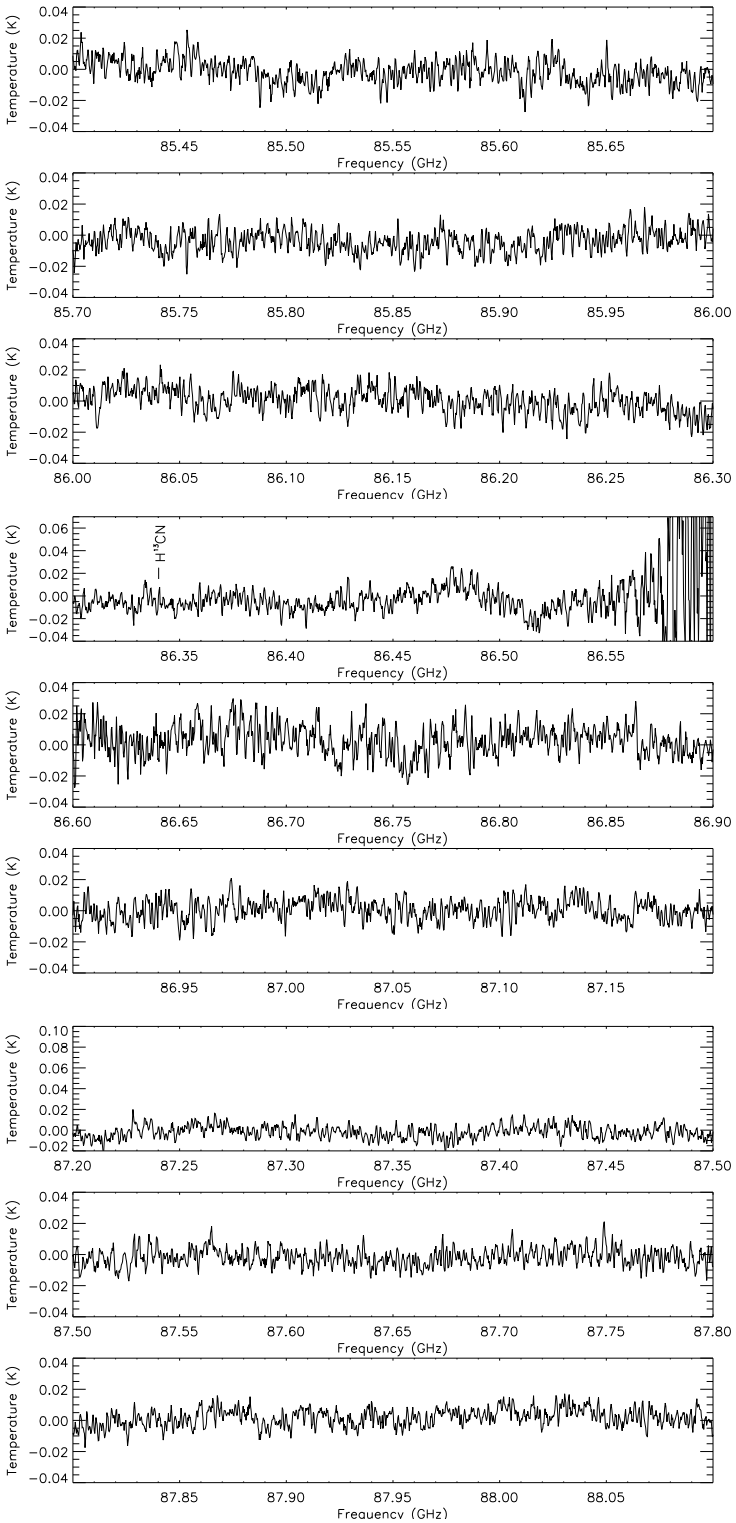

Figure A.4: – *continued.*

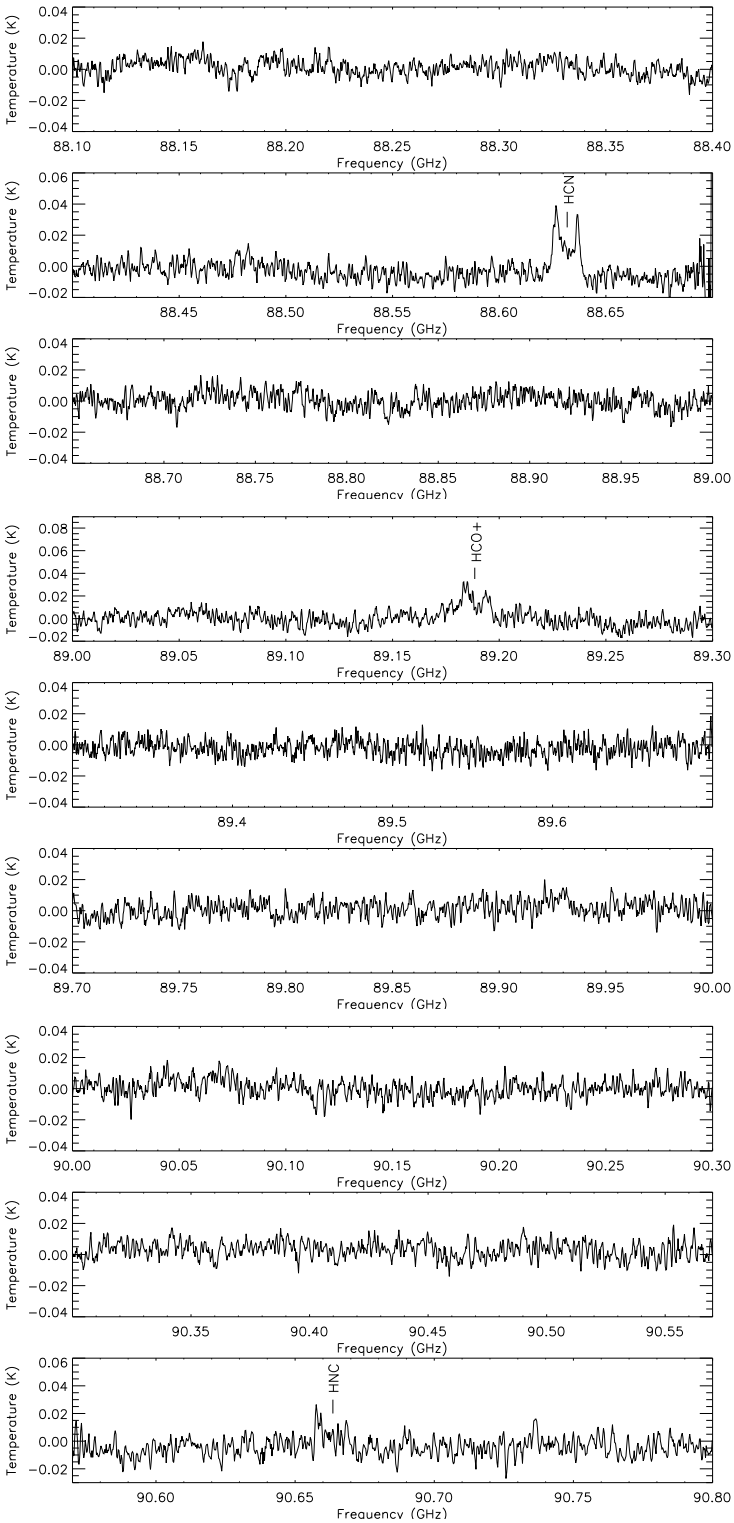

Figure A.4: – *continued.*

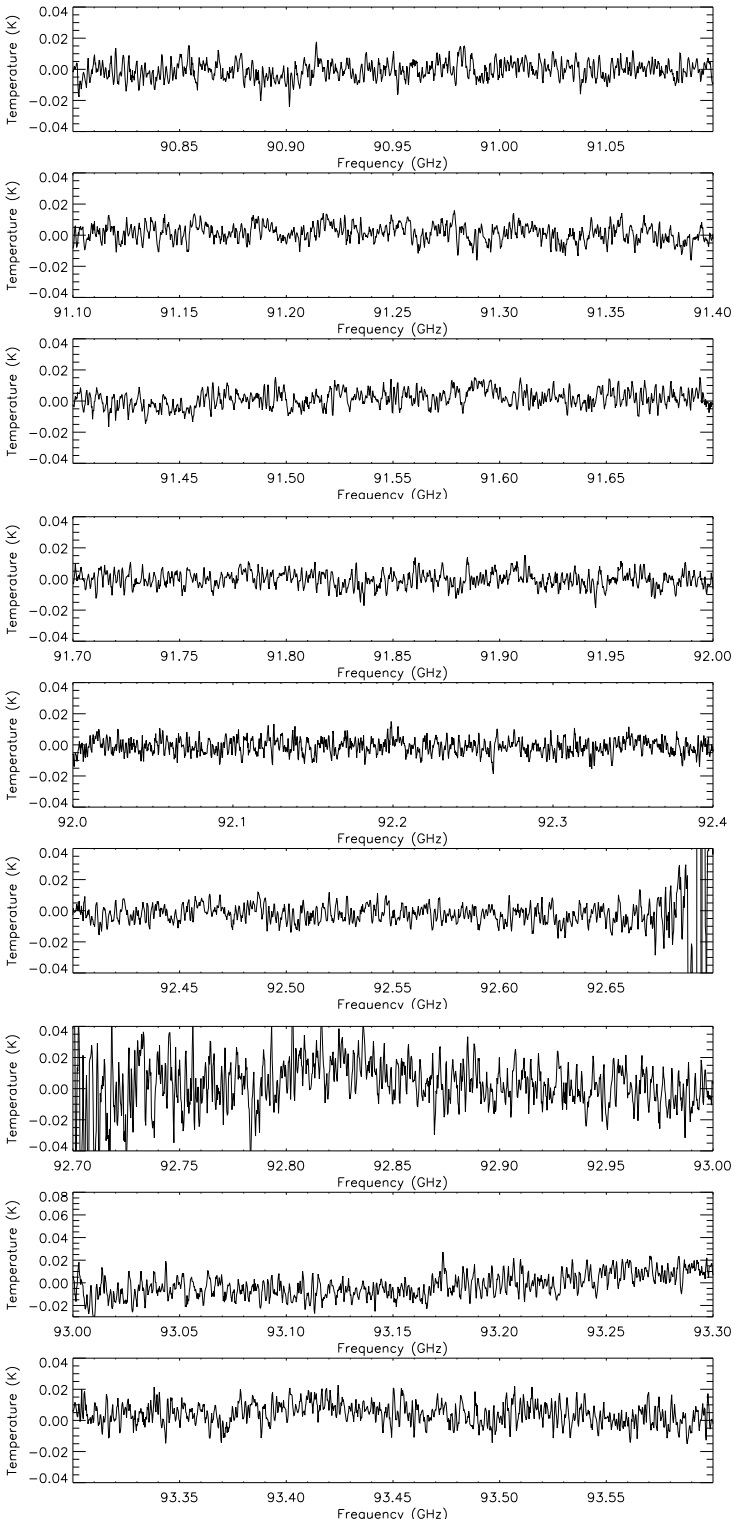

Figure A.4: – *continued.*

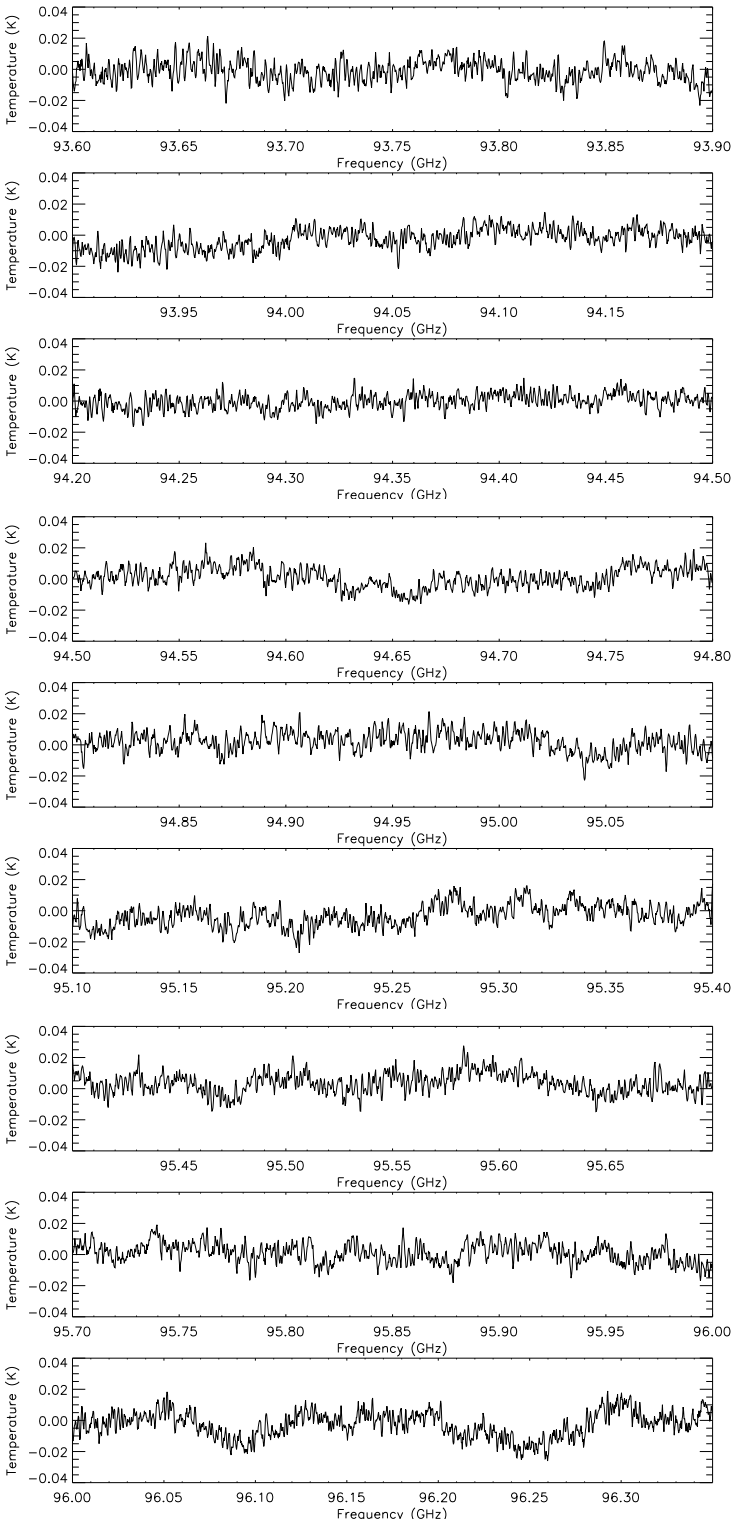

Figure A.4: – *continued.*

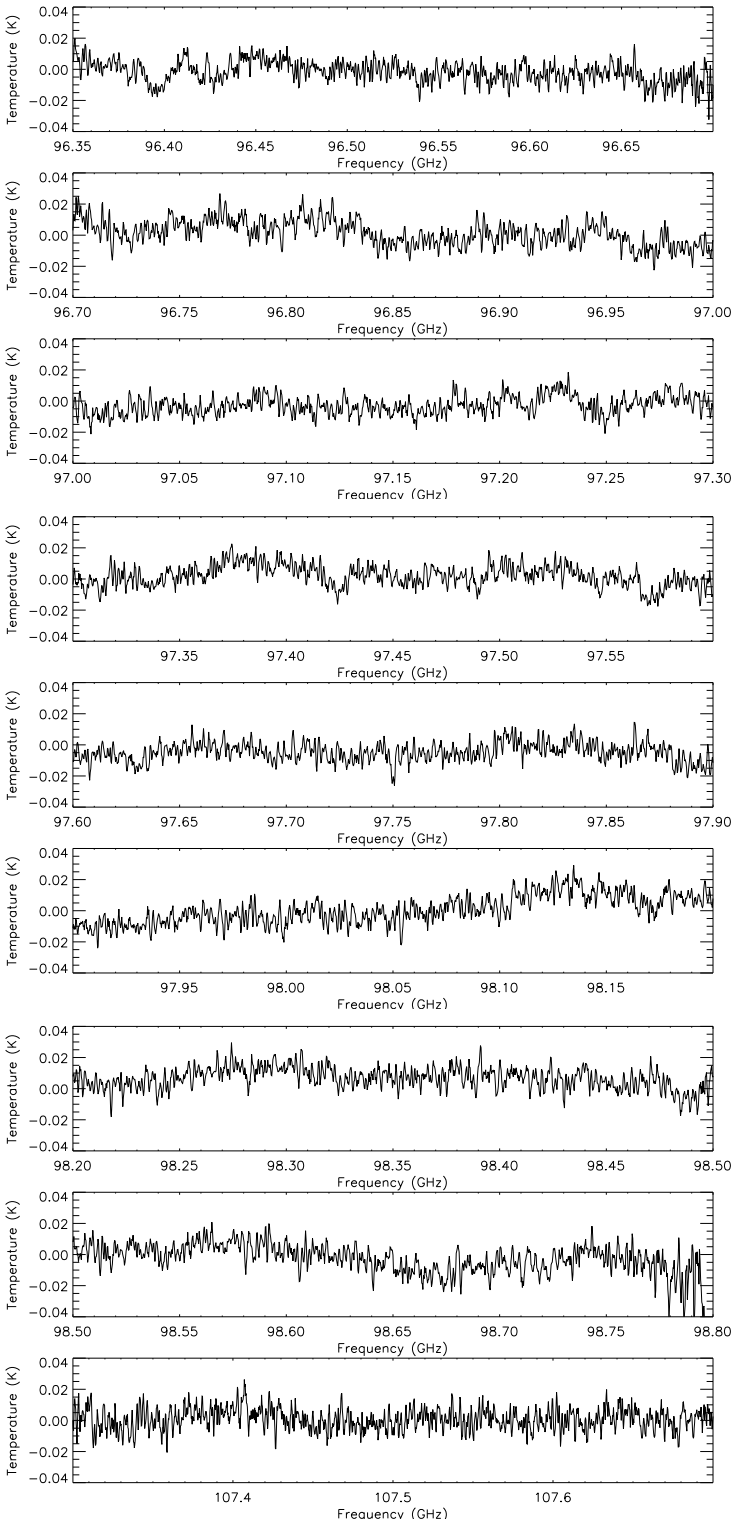

Figure A.4: – *continued.*

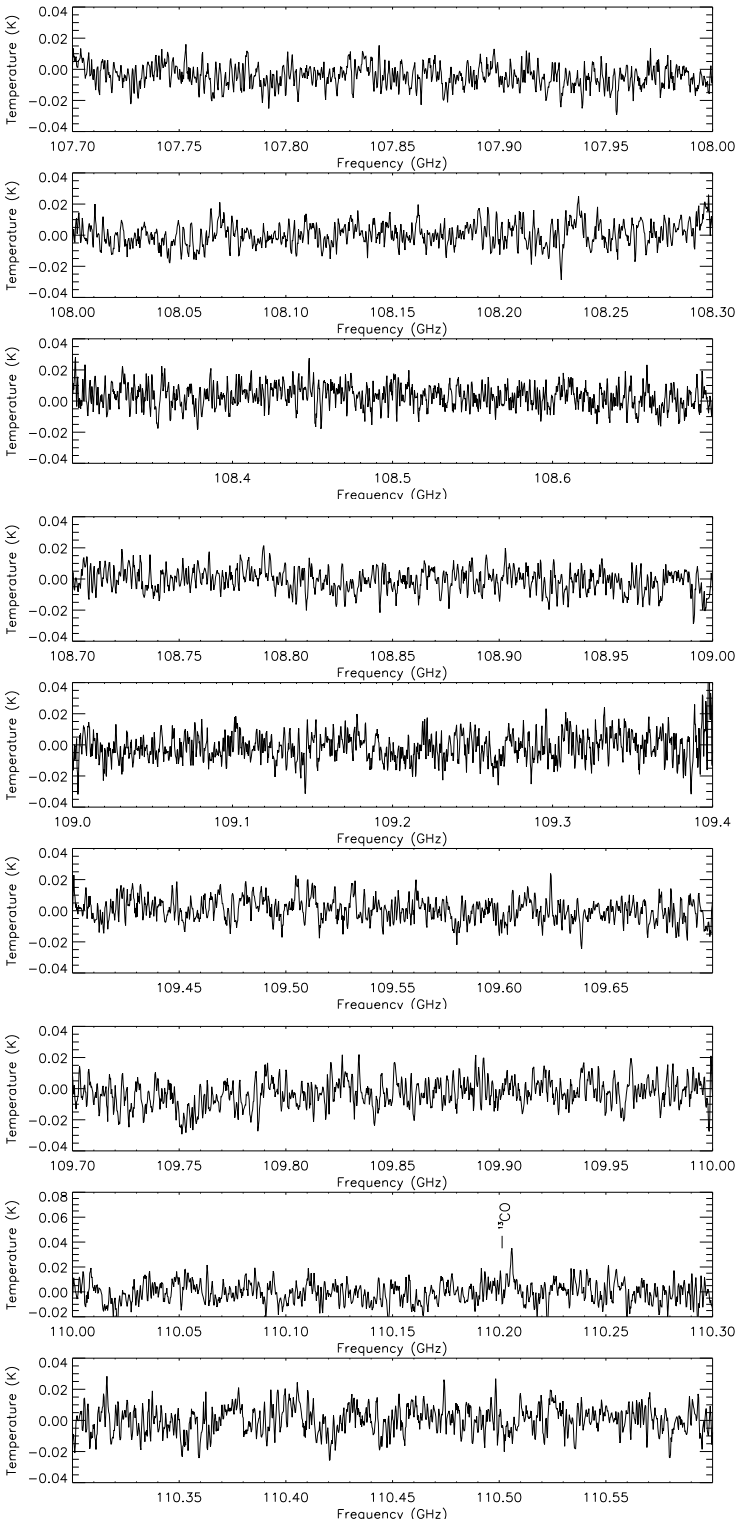

Figure A.4: – *continued.*

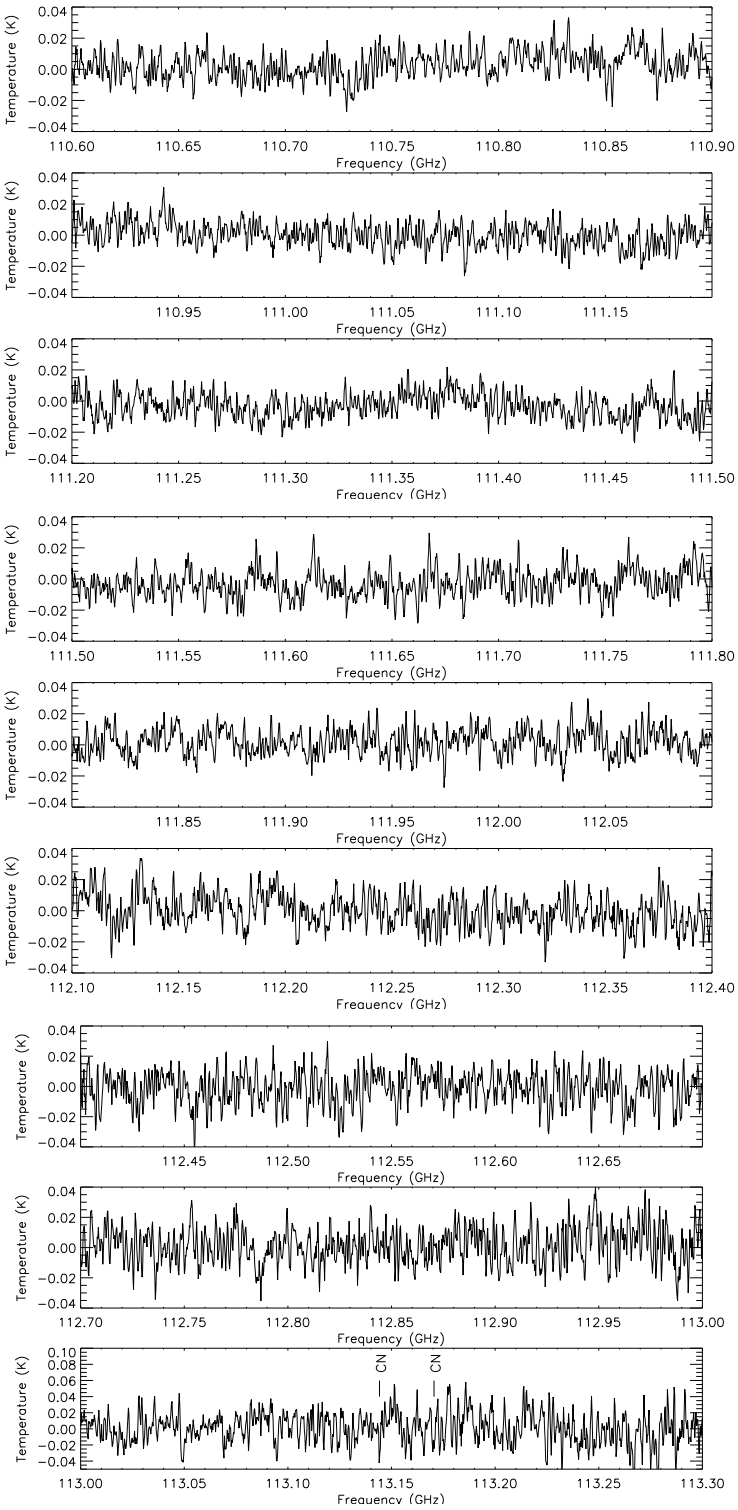

Figure A.4: – *continued.*

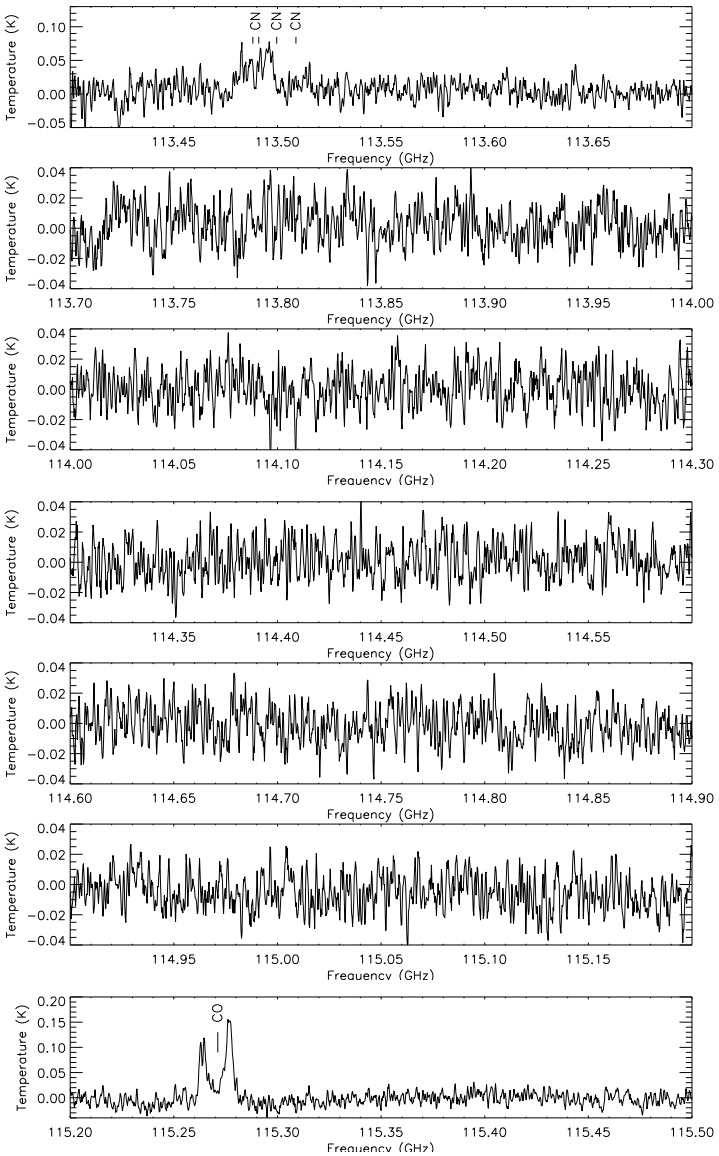

Figure A.4: – *continued.*

A.5 NGC 6537

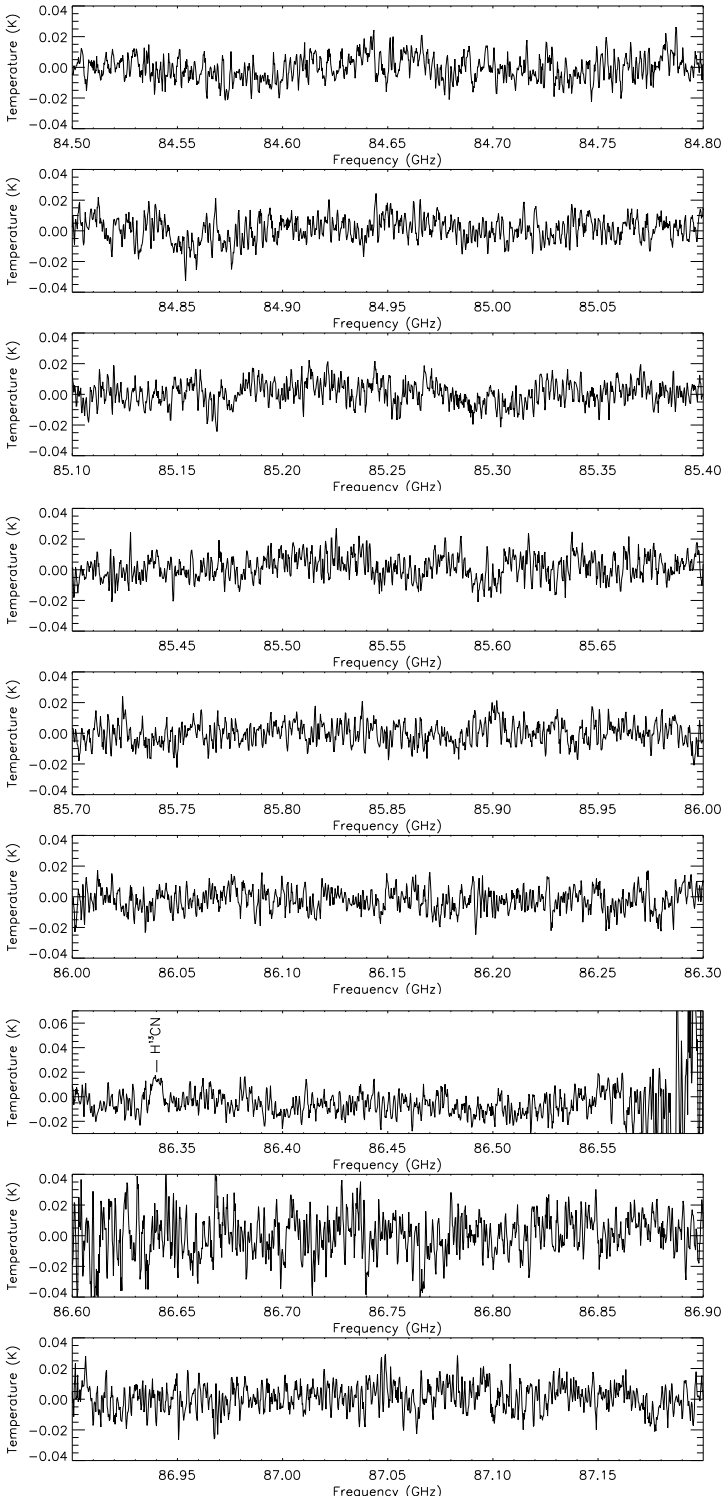

Figure A.5: Mopra spectrum of NGC 6537.

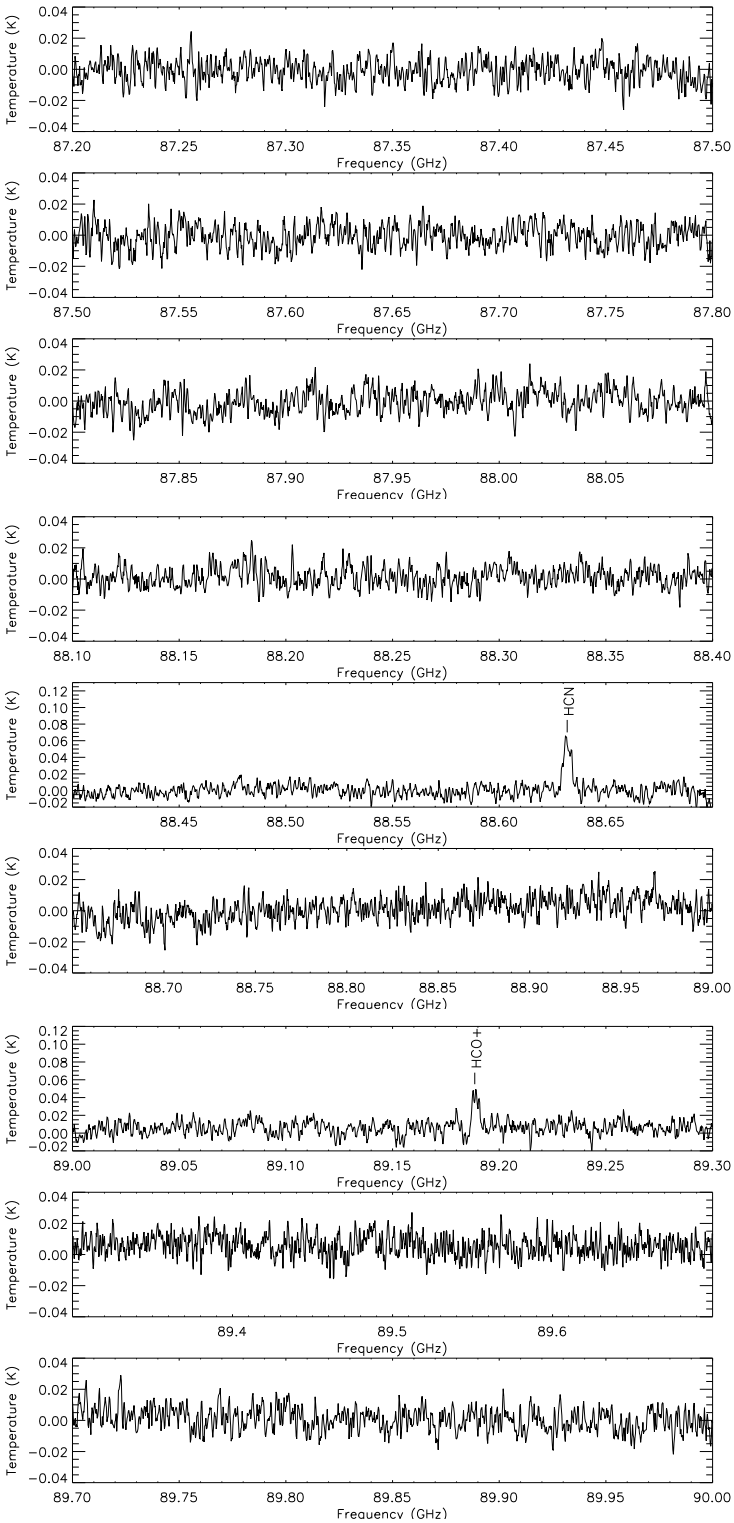

Figure A.5: – *continued.*

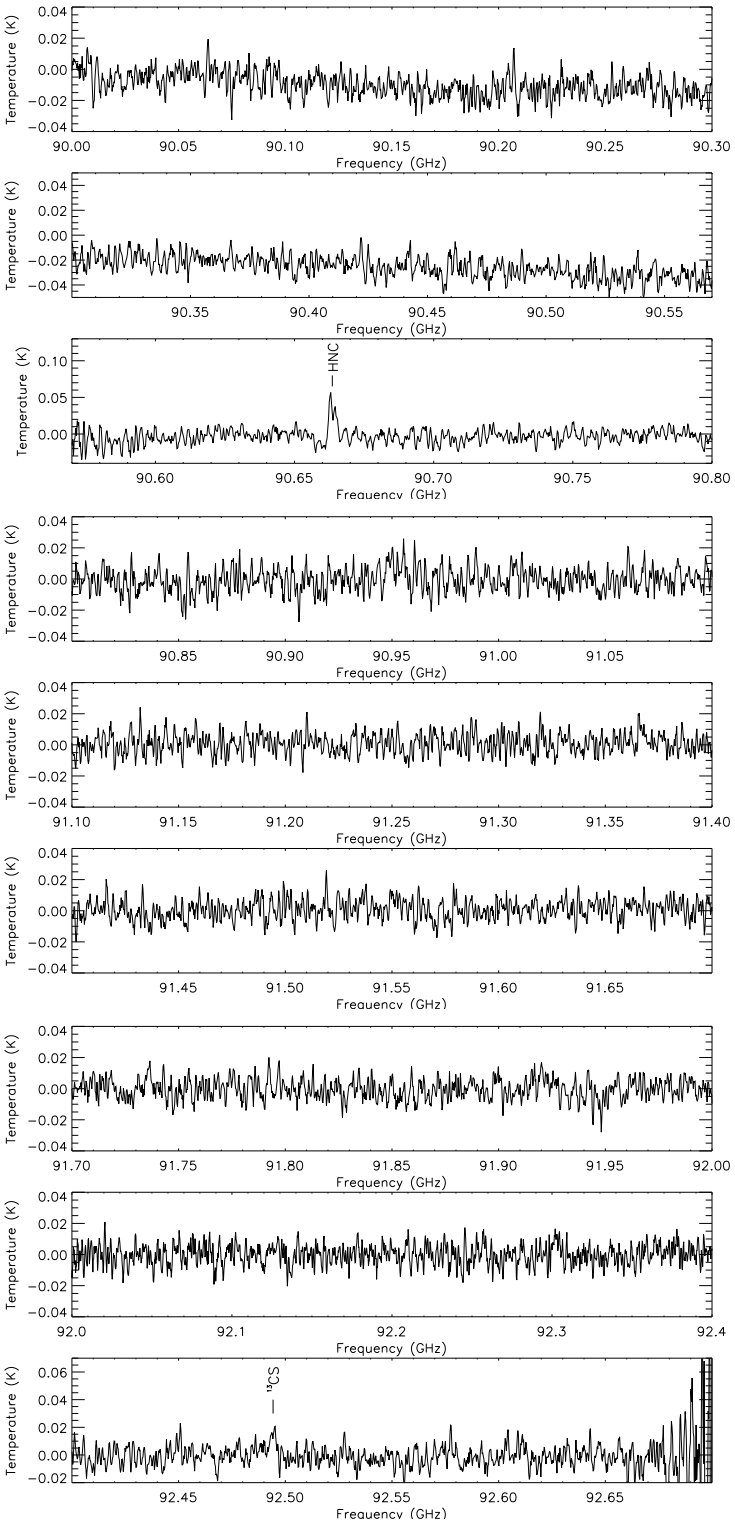

Figure A.5: – *continued.*

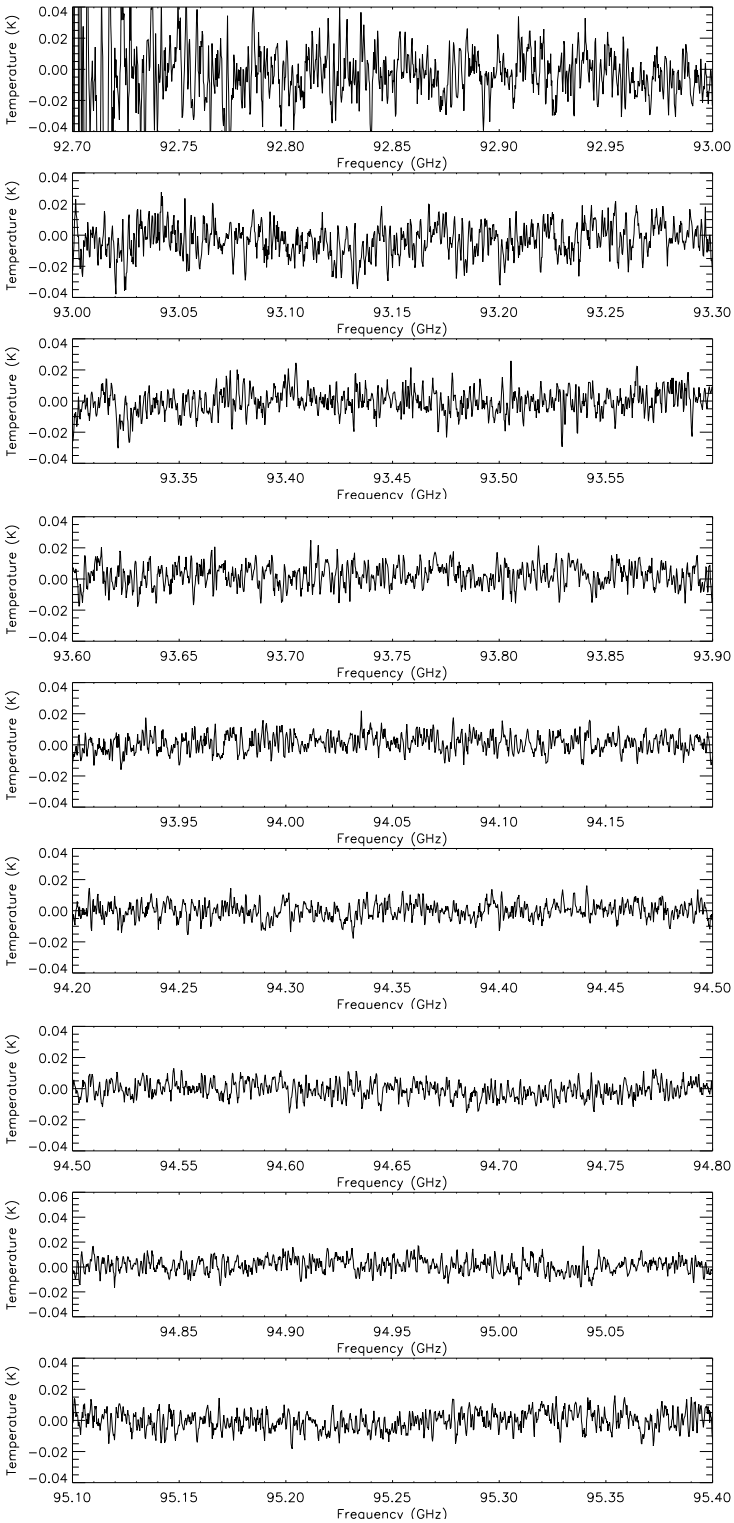

Figure A.5: – *continued.*

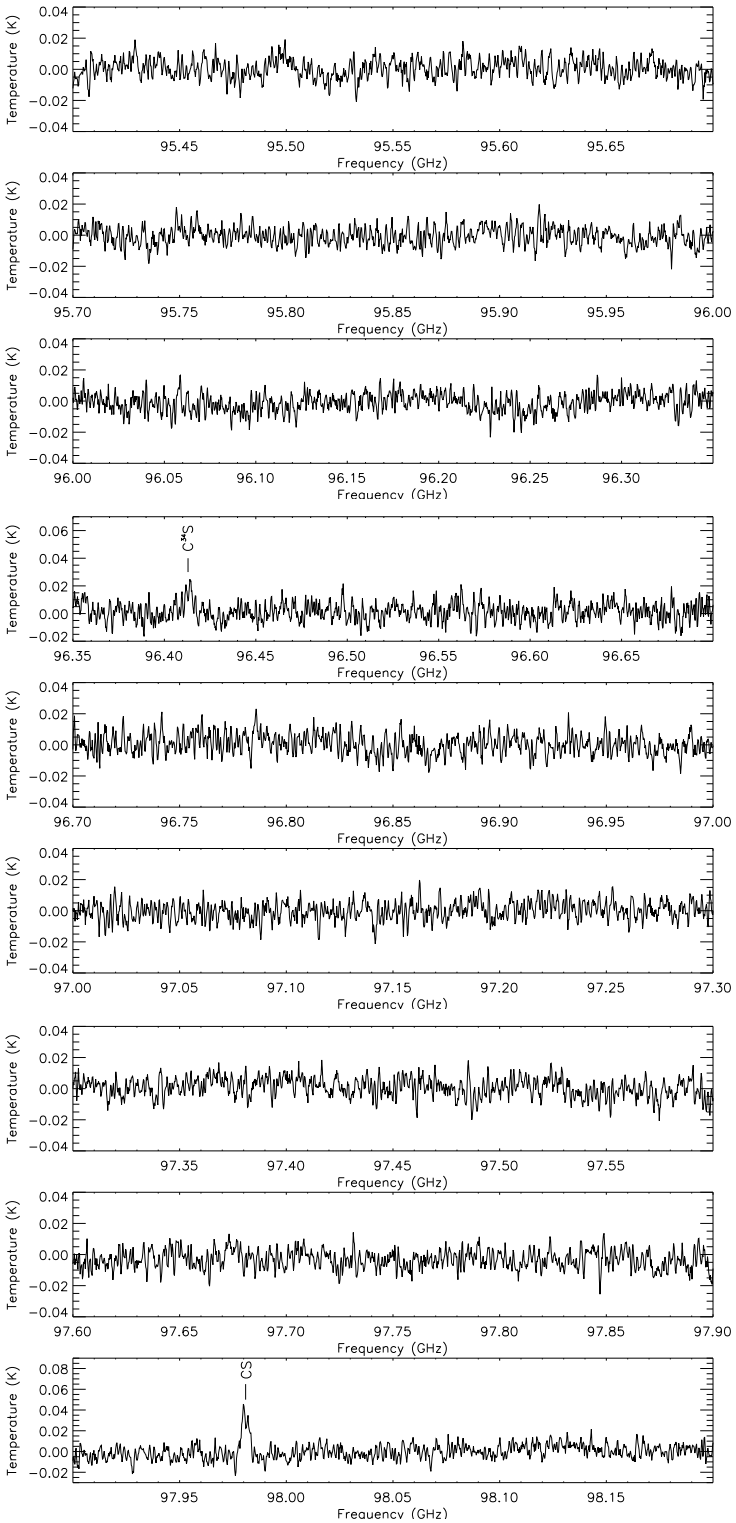

Figure A.5: – *continued.*

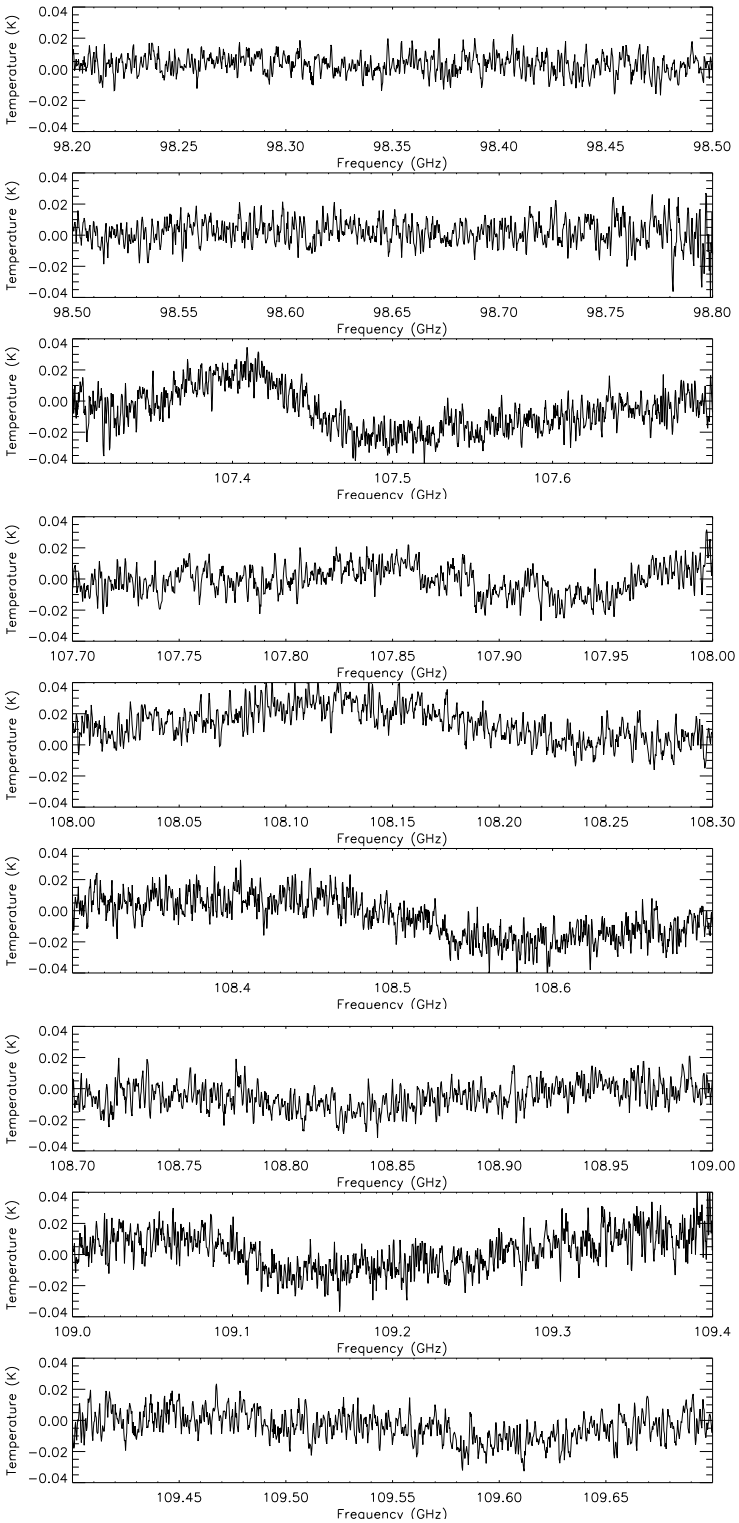

Figure A.5: – *continued.*

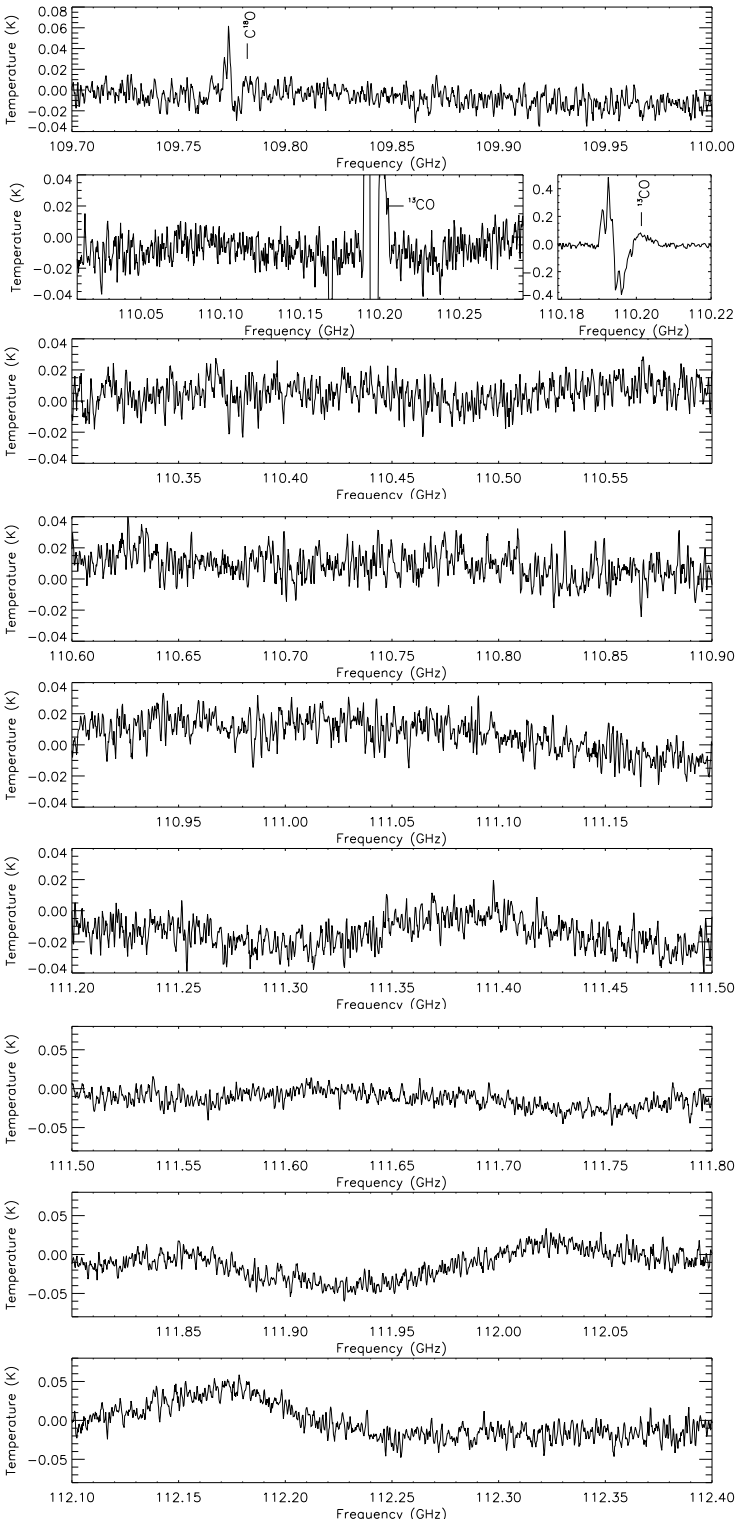

Figure A.5: – *continued.*

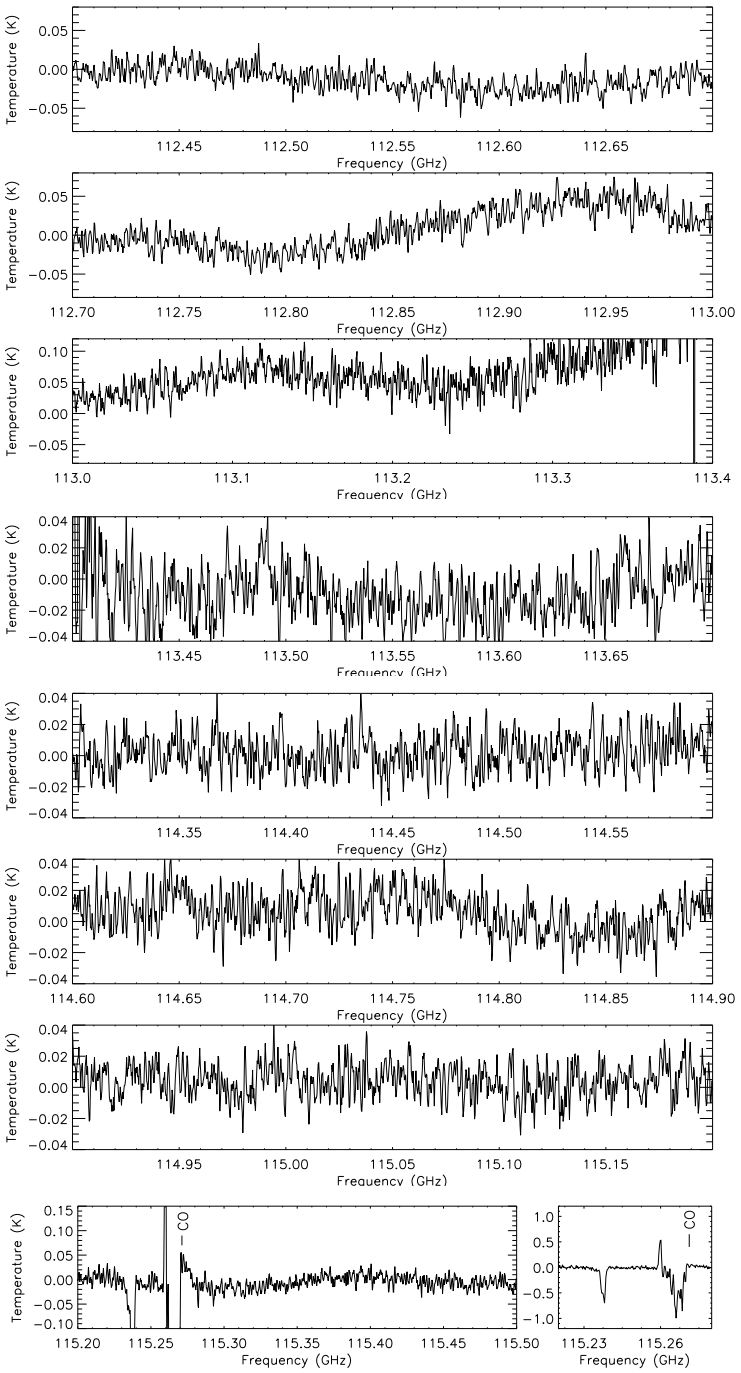

Figure A.5: – *continued.*

Appendix B

Constants and parameters

B.1 Table of constants for Mopra analysis

Table B.1: List of constants used in the analysis of column densities by both the direct calculation method and by the population diagram method. Constants are from the JPL and CDMS catalogues.

Molecule	g_u	ν_i (GHz)	a_i	$\log(A_{ul})$ ($\log(s^{-1})$)	E_u (K)	$\log(Q_{rot})$	T_{ex} (K)
CO	3	115.27120	...	-7.14246	5.53211	1.1429	37.50
						0.8526	18.75
^{13}CO	3	110.20135	...	-7.19843	5.28880	1.4630	37.50
						1.1722	18.75
HCN	3	88.63185	...	-4.61706	4.25362	1.7317	37.50
						1.4389	18.75
H^{13}CN	3	86.34018	...	-4.65256	4.14364	1.7428	37.50
						1.4498	18.75
HNC	3	90.66356	...	-4.57032	4.35114	1.2449	37.50
						0.9523	18.75
HN^{13}C	3	87.09086	...	-4.72878	4.17968	1.2620	37.50
						0.9691	18.75
CS	5	97.98095	...	-4.77628	7.05355	1.5084	37.50
						1.2119	18.75

Table B.1: – *continued.*

Molecule	g_u	ν_i (GHz)	a_i	$\log(A_{ul})$ ($\log(s^{-1})$)	E_u (K)	$\log(Q_{rot})$	T_{ex} (K)
^{13}CS	5	92.49431	...	-4.85003	6.65859	1.8342	37.50
						1.5374	18.75
C^{34}S	5	96.41295	...	-4.79698	6.24804	1.5153	37.50
						1.2187	18.75
C_2H	3	87.28416	0.043	-6.42627	4.19110	1.8628	37.50
		87.31693	0.417	-5.65605	4.19269	1.5699	18.75
		87.32862	0.208	-5.73675	4.19109		
		87.40200	0.208	-5.73568	4.19677		
		87.40717	0.083	-5.65473	4.19702		
		87.44651	0.043	-6.42386	4.19675		
C^{13}CH	3	85.22933	0.263	-5.84755	4.09883	2.1741	37.50
		85.23276	0.165	-5.87405	4.09741	1.8809	18.75
		85.24771	0.085	-5.85905	4.09122		
		85.25695	0.168	-5.86643	4.09166		
		85.30397	0.081	-5.88155	4.10241		
		85.30769	0.158	-5.89016	4.10259		
		85.31438	0.081	-5.8824	4.10133		
C_4H	19	85.63401	0.249	-5.58447	20.54582	2.8183	37.50
		85.63402	0.278	-5.58184	20.54539		
		85.67257	0.222	-5.58725	20.56292		
		85.67258	0.250	-5.58395	20.56336		
	21	95.15039	0.250	-5.44439	25.11223		
		95.15040	0.275	-5.44220	25.11180		
		95.18894	0.225	-5.44653	25.13120		
		95.18895	0.250	-5.44389	25.13164		
	23	114.18251	0.250	-5.20268	35.61531		
		114.18252	0.271	-5.20121	35.61487		
		114.22103	0.229	-5.20409	35.63802		
		114.22104	0.250	-5.20230	35.63845		
c-C_3H_2	15	85.33889	...	-4.63413	6.44539	2.3050	18.75

Table B.1: – *continued.*

Molecule	g_u	ν_i (GHz)	a_i	$\log(A_{ul})$ ($\log(s^{-1})$)	E_u (K)	$\log(Q_{rot})$	T_{ex} (K)
CN	3	113.12337	0.012	-5.89067	5.43004	1.9280	37.50
		113.14419	0.099	-4.97760	5.43003		
		113.17050	0.097	-5.28862	5.43231		
		113.19128	0.126	-5.17514	5.43230		
		113.48812	0.126	-5.17159	5.44755	1.6376	18.75
		113.49097	0.333	-4.92358	5.44668		
		113.49964	0.099	-4.97352	5.44810		
		113.50891	0.097	-5.28482	5.44754		
		113.52043	0.012	-5.88624	5.44809		
^{13}CN	3	108.78020	0.204	-4.97885	5.24750	1.9556	18.75
		108.78237	0.107	-5.11071	5.24883		
		108.78698	0.048	-5.24304	5.24873		
C_3N	19	89.04558	0.158	-4.50547	21.36592	3.3243	75.00
		89.04558	0.175	-4.50492	21.36577		
		89.04559	0.195	-4.50002	21.36592		
		89.06434	0.139	-4.50941	21.37444		
		89.06435	0.156	-4.50866	21.37444		
		89.06435	0.176	-4.50262	21.37444	2.9803	37.50
	23	108.83425	0.159	-4.23802	31.33756	2.6774	18.75
		108.83425	0.174	-4.23771	31.33742		
		108.83460	0.190	-4.23437	31.33742		
		108.85301	0.144	-4.24044	31.34781		
		108.85302	0.159	-4.24003	31.34767		
		108.85302	0.174	-4.23602	31.34781		
HC_3N	21	90.97902	...	−4.23627	24.01410	2.2358	37.50
	25	109.17363	...	−3.99469	34.05715	1.9356	18.75
						1.6363	9.375
$H^{13}CCCN$	21	88.16683	...	-4.27653	23.27241	1.6498	9.375
	23	96.98300	...	-4.15052	27.92694		
$HC^{13}CCN$	21	90.59306	...	-4.24119	23.91285	1.6381	9.375
$HCC^{13}CN$	21	90.60178	...	-4.24108	23.91528	1.6380	9.375
HC_5N	65	85.20134	...	-4.17752	67.46992	2.7688	37.50
						2.4680	18.75
HCO^+	3	89.18853	...	-4.38103	4.28035	1.2519	37.50

Table B.1: – *continued.*

Molecule	g_u	ν_i (GHz)	a_i	$\log(A_{ul})$ ($\log(s^{-1})$)	E_u (K)	$\log(Q_{rot})$	T_{ex} (K)
SiO	5	86.84696	...	-4.53354	6.25203	1.5602	37.50
						1.2632	18.75
^{29}SiO	5	85.75920	...	-4.54997	6.17364	1.2686	18.75
^{30}SiO	5	84.74617	...	-4.56540	6.10071	1.2736	18.75
SiS	11	90.77156	...	-4.92407	13.06907	1.6373	18.75
	13	108.92430	...	-4.67991	18.29671	1.3396	9.375
SiC_2	9	93.06300	...	-4.62380	11.22969		
	9	94.24539	...	-4.73063	19.12424	2.8113	75.00
	9	95.57938	...	-4.71223	19.22063	1.9104	18.75
	11	115.38239	...	-4.33485	16.76704		

Appendix C

PACS model spectra

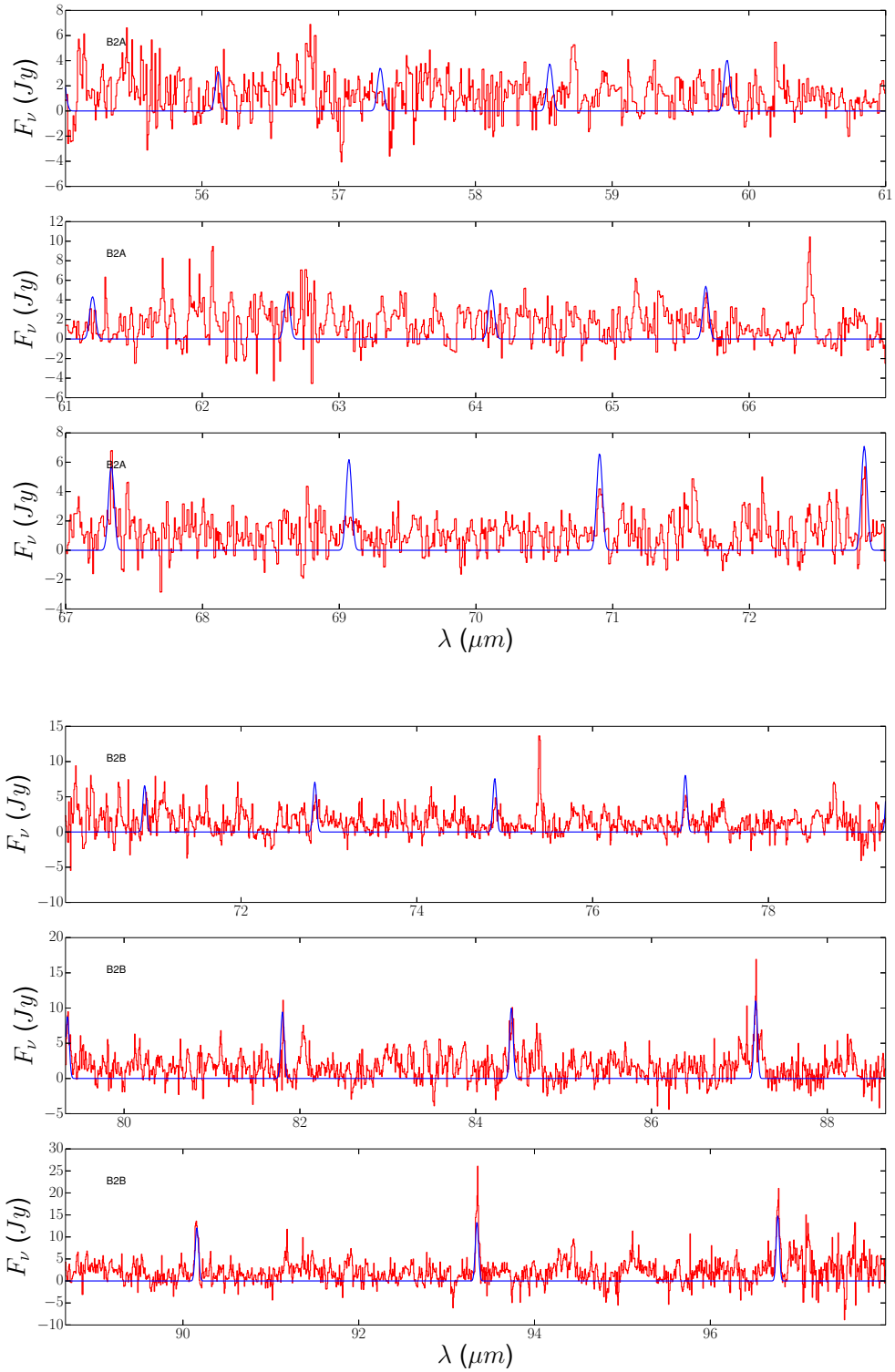

Figure C.1: Model PACS spectrum of the AC model.

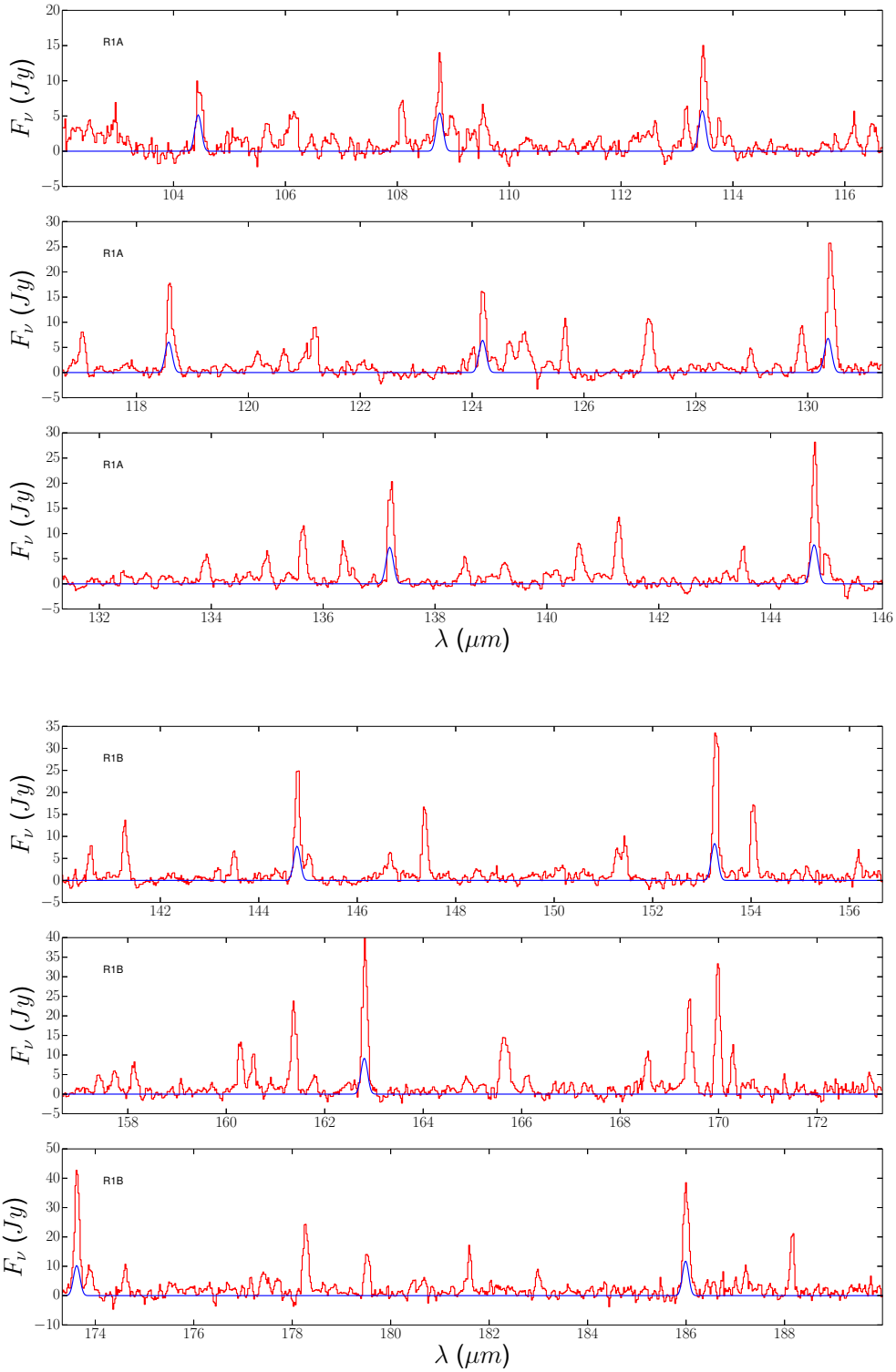

Figure C.1: – *continued*

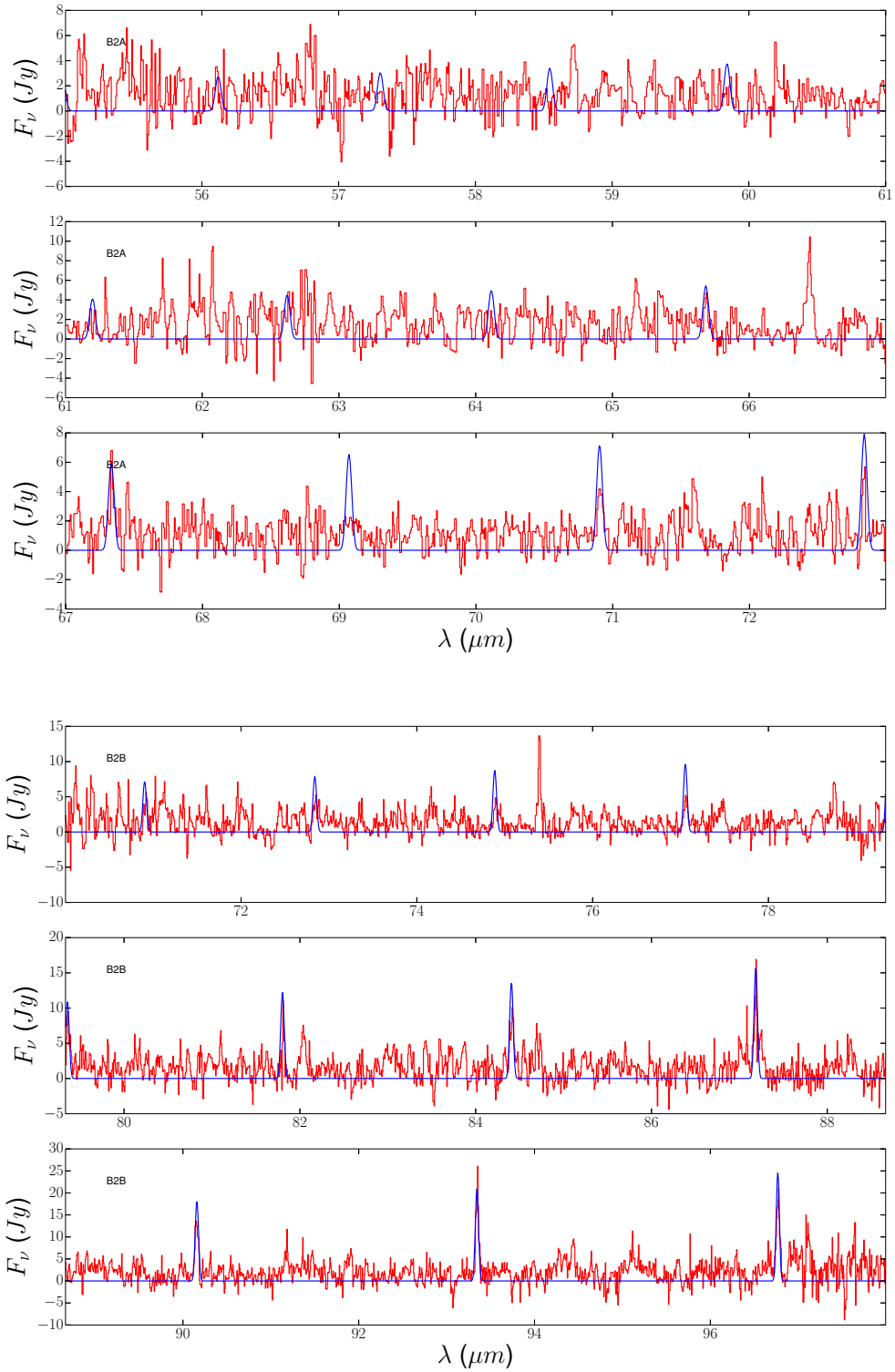

Figure C.2: Model PACS spectrum of the PE model.

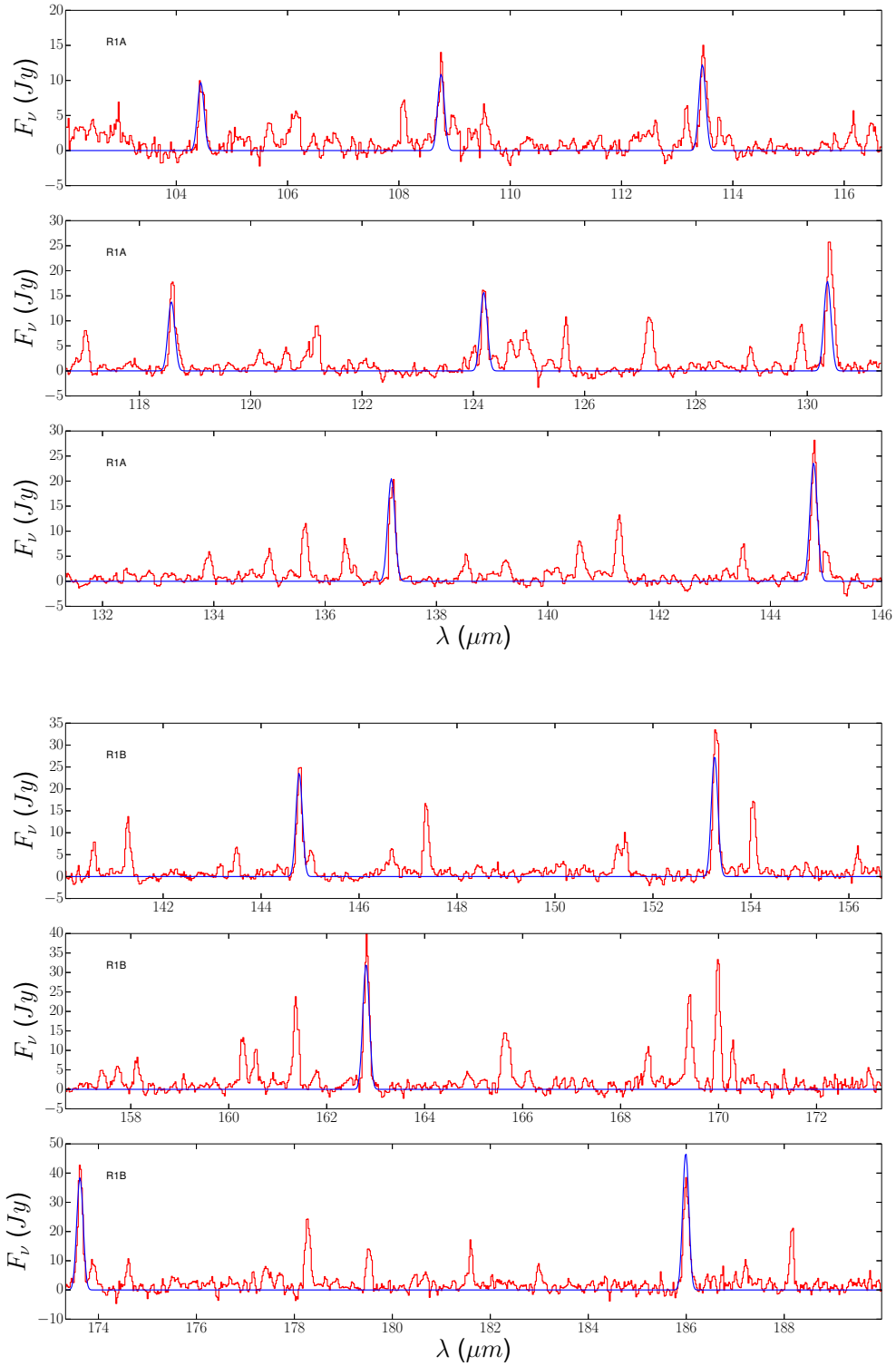

Figure C.2: – *continued*

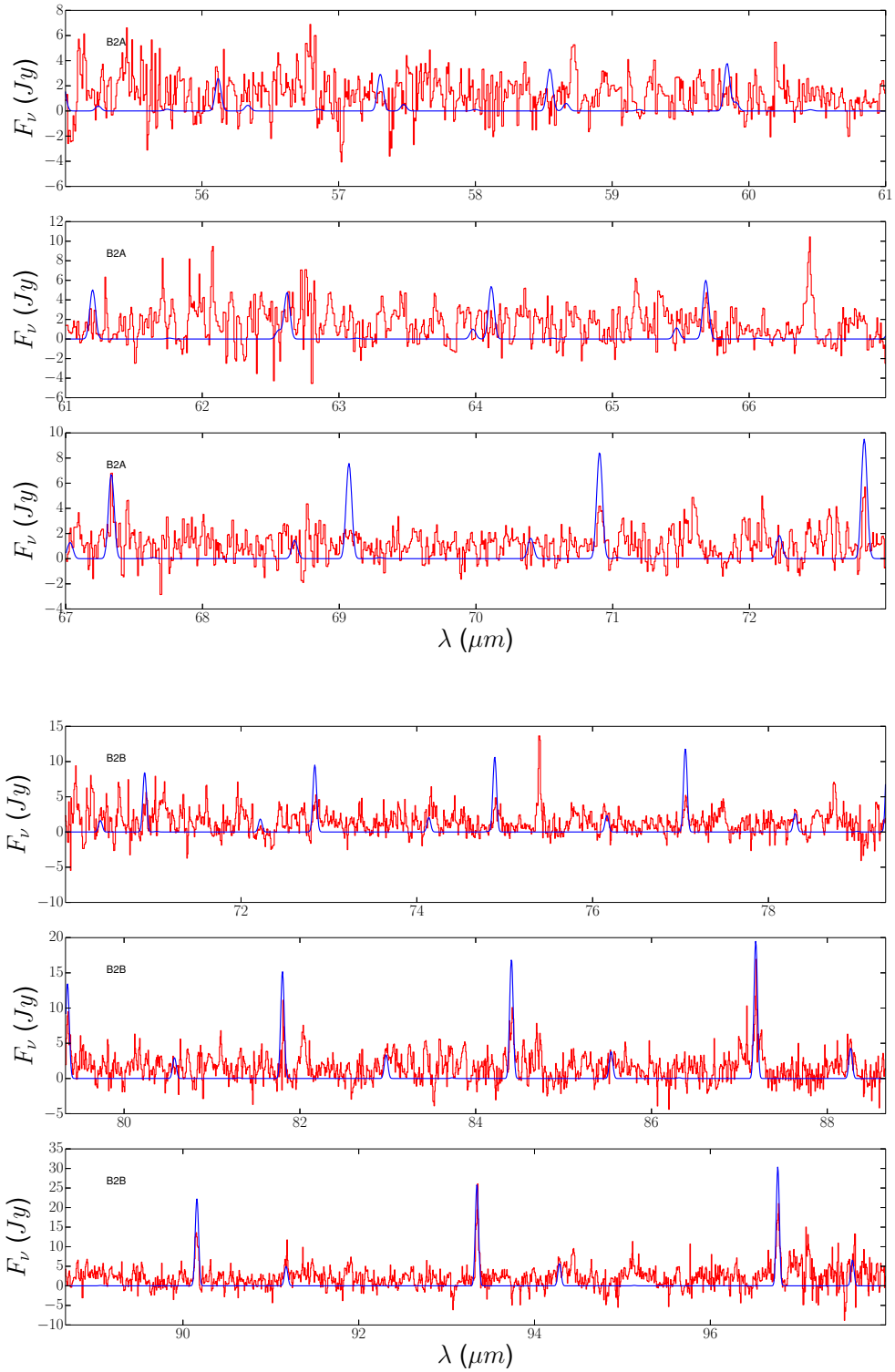

Figure C.3: Model PACS spectrum of the DTM model.

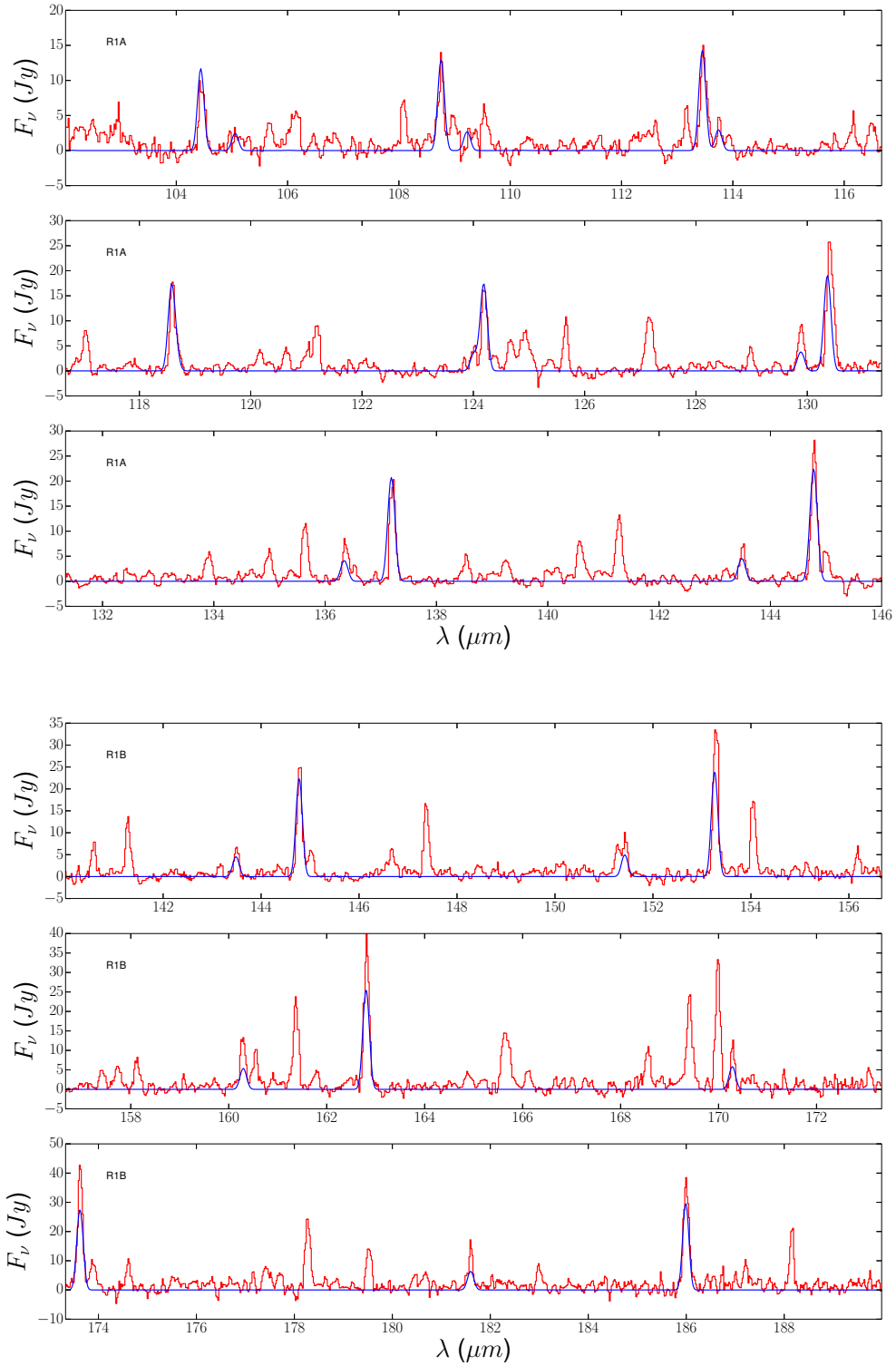

Figure C.3: – *continued*

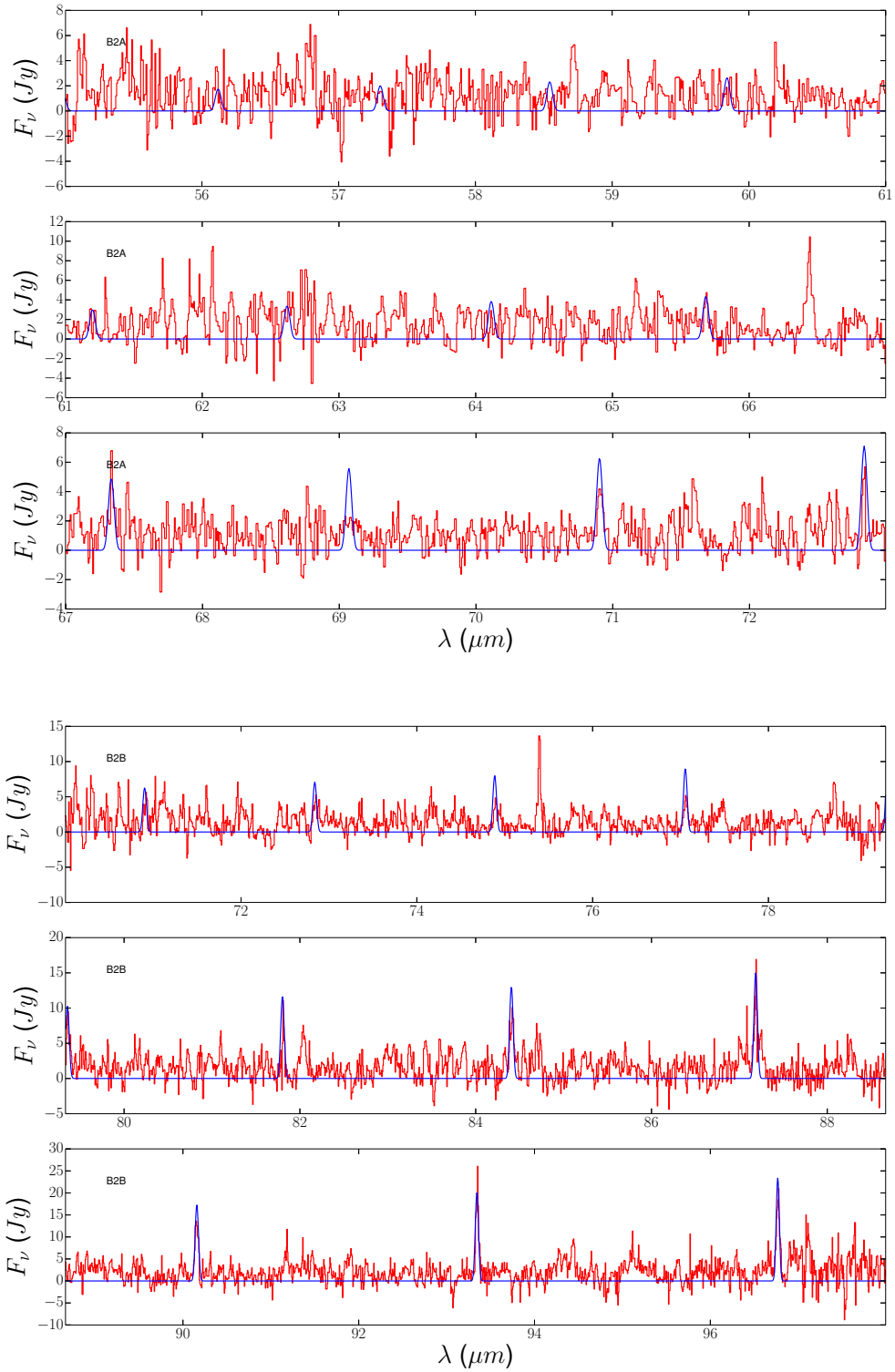

Figure C.4: Model PACS spectrum of the VMM model.

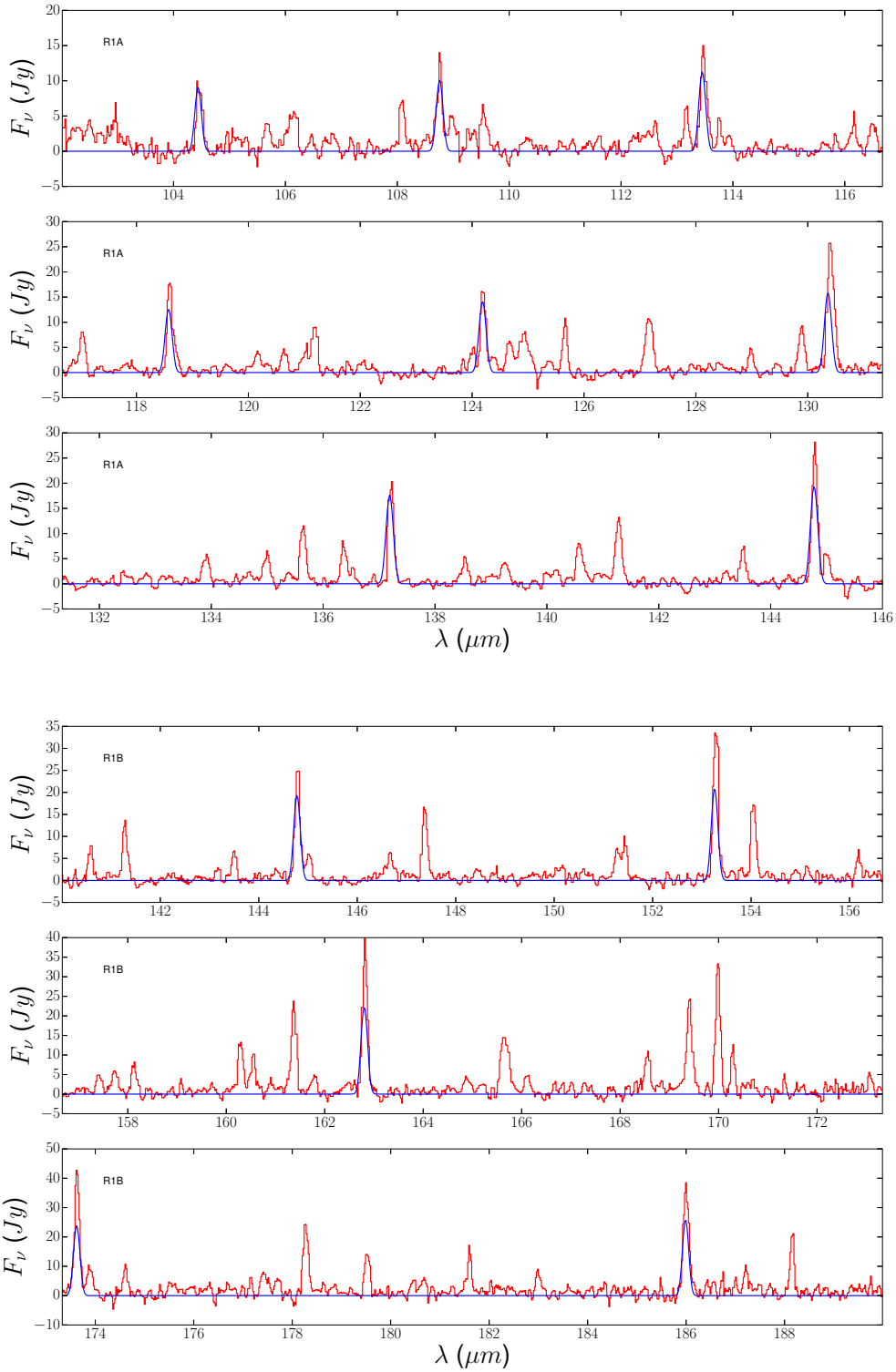

Figure C.4: – *continued*

References

Acke B. et al., 2013, A&A, 551, A76

Acker A., Marcout J., Ochsenbein F., Stenholm B., Tylenda R., Schohn C., 1992, The Strasbourg-ESO Catalogue of Galactic Planetary Nebulae. Parts I, II.

Adelberger E. G., Balantekin A. B., Bemmerer D., Bertulani C. A., Chen J., et al., 2010, ArXiv e-prints

Agúndez M., Cernicharo J., Pardo J. R., Fonfría Expósito J. P., Guélin M., Tenenbaum E. D., Ziurys L. M., Apponi A. J., 2008, Ap&SS, 313, 229

Alcolea J., Pardo J. R., Bujarrabal V., et. al, 1999, A&AS, 139, 461

Ali A., 2006, Journal of Astrophysics and Astronomy, 27, 399

Alksnis A., 1995, Baltic Astronomy, 4, 79

Aoki W., Tsuji T., Ohnaka K., 1999, A&A, 350, 945

Asplund M., Grevesse N., Sauval A. J., Scott P., 2009, ARA&A, 47, 481

Assaf K. A., Diamond P. J., Richards A. M. S., Gray M. D., 2013, MNRAS, 431, 1077

Balick B., Frank A., 2002, ARA&A, 40, 439

Balser D. S., McMullin J. P., Wilson T. L., 2002, ApJ, 572, 326

Bergeat J., Chevallier L., 2005, A&A, 429, 235

Bjorkman J. E., Wood K., 2001, ApJ, 554, 615

Blöcker T., Herwig F., Driebe T., 2000, Mem. Soc. Astron. Italiana, 71, 711

Bodner Research Web page, 2011, Quantum numbers and electron configurations, http://chemed.chem.purdue.edu/genchem/topicreview/bp/ch6/quantum.php.

Booth R. S. et al., 1989, A&A, 216, 315

Brown J., Carrington A., 2003, Rotational spectroscopy of diatomic molecules,

Cambridge molecular science series. Cambridge University Press

Bujarrabal V., Nguyen-Q-Rieu, 1981, A&A, 102, 65

Busso M., Wasserburg G. J., Nollett K. M., Calandra A., 2007, ApJ, 671, 802

Carlstrom J. E., Welch W. J., Goldsmith P. F., Lis D. C., 1990, AJ, 100, 213

Caswell J. L., Vaile R. A., Forster J. R., 1995, MNRAS, 277, 210

Cernicharo J., Agúndez M., Kahane C., Guélin M., Goicoechea J. R., Marcelino N., De Beck E., Decin L., 2011, A&A, 529, L3

Cernicharo J., Guélin M., Kahane C., 2000, A&AS, 142, 181

Cernicharo J., Yamamura I., González-Alfonso E., de Jong T., Heras A., Escribano R., Ortigoso J., 1999, ApJL, 526, L41

Chabay R., Sherwood B., 2010, Matter and Interactions, Matter and Interactions. John Wiley & Sons

Charbonneau P., 1995, ApJS, 101, 309

Charbonnel C., 1994, A&A, 282, 811

Chen Y. Q., Nissen P. E., Zhao G., 2004, A&A, 425, 697

Cherchneff I., 1996, in IAU Symposium, Vol. 178, Molecules in Astrophysics: Probes & Processes, van Dishoeck E. F., ed., p. 469

Clayton D., 2003, Handbook of Isotopes in the Cosmos: Hydrogen to Gallium, Cambridge Planetary Science. Cambridge University Press

Cooke S. A., Ohring P., 2012, ArXiv e-prints

Cotton W. D., Perrin G., Lopez B., 2008, A&A, 477, 853

Cox P., Omont A., Huggins P. J., Bachiller R., Forveille T., 1992, A&A, 266, 420

Cuisinier F., Maciel W. J., Köppen J., Acker A., Stenholm B., 2000, A&A, 353, 543

Cuntz M., Muchmore D. O., 1994, ApJ, 433, 303

Cutri R. M., Skrutskie M. F., van Dyk S., et al., 2003a, 2MASS All Sky Catalog of point sources.

Cutri R. M., Skrutskie M. F., van Dyk S., et. al, 2003b, 2MASS All Sky Catalog of point sources.

Cutri R. M., Wright E. L., Conrow T., et al., 2012, VizieR Online Data Catalog, 2311, 0

De Beck E., Decin L., de Koter A., Justtanont K., Verhoelst T., Kemper F., Menten K. M., 2010, A&A, 523, A18

De Beck E. et al., 2012, A&A, 539, A108

Decin L., Cherchneff I., Hony S., Dehaes S., De Breuck C., Menten K. M., 2008, A&A, 480, 431

Decin L. et al., 2010, A&A, 516, A69

Decin L., Hony S., de Koter A., Justtanont K., Tielens A. G. G. M., Waters L. B. F. M., 2006, A&A, 456, 549

Delgado-Inglada G., Rodríguez M., 2014, ApJ, 784, 173

Delgado Inglada G., Rodríguez M., Mampaso A., Viironen K., 2009, ApJ, 694, 1335

DENIS Consortium, 2005, VizieR Online Data Catalog, 2263, 0

Dinerstein H. L., Geballe T. R., 2001, ApJ, 562, 515

Dyson J., Williams D., 1997, The physics of the interstellar medium, The graduate series in astronomy. Institute of Physics Pub.

Edwards J. L., Ziurys L. M., 2013, ApJL, 770, L5

Epchtein N., Le Bertre T., Lepine J. R. D., 1990, A&A, 227, 82

Evans T., Murdin P., 2002, Red Giant Stars, Encyclopedia of Astronomy and Astrophysics

Exter K. M., Barlow M. J., Walton N. A., 2004, MNRAS, 349, 1291

Faes D. M., Costa R. D. D., Morisset C., 2011, in Revista Mexicana de Astronomia y Astrofisica Conference Series, Vol. 40, Revista Mexicana de Astronomia y Astrofisica Conference Series, pp. 233–234

Feast M. W., Whitelock P. A., Marang F., 2003, MNRAS, 346, 878

Ferland G. J. et al., 2013, Rev. Mex. Astronomy and Astrophysics, 49, 137

Fish V. L., 2007, in IAU Symposium, Vol. 242, IAU Symposium, Chapman J. M., Baan W. A., eds., pp. 71–80

Fleck, Jr. J. A., Canfield E. H., 1984, Journal of Computational Physics, 54, 508

Fouque P., Le Bertre T., Epchtein N., Guglielmo F., Kerschbaum F., 1992, A&AS, 93, 151

Fuller G. A., Myers P. C., 1993, ApJ, 418, 273

Gail H., Zhukovska S. V., Hoppe P., Trieloff M., 2009, ApJ, 698, 1136

Gesicki K., Zijlstra A. A., 2007, A&A, 467, L29

Gesicki K., Zijlstra A. A., Szyszka C., Hajduk M., Lagadec E., Guzman Ramirez L., 2010, A&A, 514, A54

Goldsmith P. F., Langer W. D., 1999, ApJ, 517, 209

Goldsmith P. F., Lis D. C., Omont A., Guilloteau S., Lucas R., 1988, ApJ, 333, 873

González Delgado D., Olofsson H., Kerschbaum F., Schöier F. L., Lindqvist M., Groenewegen M. A. T., 2003, A&A, 411, 123

Goorvitch D., Chackerian, Jr. C., 1994, ApJS, 91, 483

Goriely S., Siess L., 2005, in IAU Symposium, Vol. 228, From Lithium to Uranium: Elemental Tracers of Early Cosmic Evolution, Hill V., Francois P., Primas F., eds., pp. 451–460

Górny S. K., Chiappini C., Stasińska G., Cuisinier F., 2009, A&A, 500, 1089

Górny S. K., Stasińska G., Escudero A. V., Costa R. D. D., 2004, A&A, 427, 231

Gray M. D., Wittkowski M., Scholz M., Humphreys E. M. L., Ohnaka K., Boboltz D., 2009, Monthly Notices of the Royal Astronomical Society, 394, 51

Groenewegen M. A. T., Sevenster M., Spoon H. W. W., Pérez I., 2002, A&A, 390, 511

Gruenwald R., Viegas S. M., Broguiere D., 1997, ApJ, 480, 283

Guandalini R., Busso M., Ciprini S., Silvestro G., Persi P., 2006, A&A, 445, 1069

Guilloteau S., Omont A., Lucas R., 1987, A&A, 176, L24

Gutenkunst S., Bernard-Salas J., Pottasch S. R., Sloan G. C., Houck J. R., 2008, ApJ, 680, 1206

Habing H., Olofsson H., 2012, Asymptotic Giant Branch Stars, Astronomy and Astrophysics Library. Springer

Habing H. J., Olofsson H., eds., 2004, Asymptotic Giant Branch Stars. Astronomy and Astrophysics Library, Springer

He J. H., Dinh-V-Trung, Kwok S., Müller H. S. P., Zhang Y., Hasegawa T., Peng T. C., Huang Y. C., 2008, ApJS, 177, 275

Helou G., Walker D. W., eds., 1988, Infrared astronomical satellite (IRAS) catalogs and atlases. Volume 7: The small scale structure catalog, Vol. 7

Henden A. A., 2013, Observations from the AAVSO International Database, private communication

Herwig F., 2005, ARA&A, 43, 435

Herzberg G., Spinks J. W. T., 1944, Atomic spectra and atomic structure, Dover books on chemistry, physical chemistry, biochemistry. Dover

Hirano N. et al., 2004, ApJL, 616, L43

Höfner S., 2009, in Astronomical Society of the Pacific Conference Series, Vol. 414, Cosmic Dust - Near and Far, Henning T., Grün E., Steinacker J., eds., p. 3

Höfner S., Gautschy-Loidl R., Aringer B., Jørgensen U. G., 2003a, A&A, 399, 589

Höfner S., Gautschy-Loidl R., Aringer B., Jørgensen U. G., 2003b, A&A, 399, 589

Hoppe P., Leitner J., Grner E., Marhas K. K., Meyer B. S., Amari S., 2010, The Astrophysical Journal, 719, 1370

Hughes G. L., Gibson B. K., Carigi L., Sánchez-Blázquez P., Chavez J. M., Lambert D. L., 2008, MNRAS, 390, 1710

Hyung S., Aller L. H., Feibelman W. A., Lee S.-J., 2001, ApJ, 563, 889

Jones T. J., Bryja C. O., Gehrz R. D., Harrison T. E., Johnson J. J., Klebe D. I., Lawrence G. F., 1990, ApJS, 74, 785

Josselin E., Bachiller R., 2003, A&A, 397, 659

Karakas A. I., 2010, MNRAS, 403, 1413

Karakas A. I., Campbell S. W., Stancliffe R. J., 2010, ApJ, 713, 374

Karakas A. I., van Raai M. A., Lugaro M., Sterling N. C., Dinerstein H. L., 2009, The Astrophysical Journal, 690, 1130

Kerschbaum F., Groenewegen M. A. T., Lazaro C., 2006, A&A, 460, 539

Khouri T. et al., 2014, A&A, 561, A5

Kimura R. K., Gruenwald R., Aleman I., 2012, A&A, 541, A112

Kingsburgh R. L., Barlow M. J., 1994, MNRAS, 271, 257

Kippenhahn R., Weigert A., 1994, Stellar Structure and Evolution. Astronomy and Astrophysics Library

Kippenhahn R., Weigert A., Weiss A., 2012, Stellar Structure and Evolution, Astronomy and astrophysics library. Springer

Kondratyeva L. N., 2003, Astronomical and Astrophysical Transactions, 22, 181

Kwok S., 1993, ARA&A, 31, 63

Kwok S., 2000, The Origin and Evolution of Planetary Nebulae

Kwok S., Murdin P., 2000, Protoplanetary Nebulae, Nature Publishing Group, Institute of Physics Publishing

Kwon Y.-J., Suh K.-W., 2010, Journal of Astronomy and Space Sciences, 27, 279

Larsson B., Liseau R., Men'shchikov A. B., 2002, A&A, 386, 1055

Lattanzio J. C., Boothroyd A. I., 1997, in American Institute of Physics Conference Series, Vol. 402, American Institute of Physics Conference Series, T. J. Bernatowicz & E. Zinner, ed., pp. 85–114

Lattanzio J. C., Lugaro M. A., 2005, Nuclear Physics A, 758, 477

Le Bertre T., 1992, A&AS, 94, 377

Likkel L., Dinerstein H. L., Lester D. F., Kindt A., Bartig K., 2006, AJ, 131, 1515

Lis D. C., Goldsmith P. F., Predmore C. R., 1989, ApJ, 341, 823

Lo K. Y., 2005, ARA&A, 43, 625

Lockett P., Elitzur M., 1992, ApJ, 399, 704

Lodders K., Fegley B., 1998, The Planetary Scientist's Companion. Oxford University Press, USA

Lombaert R., 2013, PhD thesis, Katholieke Universiteit Leuven, Belgium

Lombaert R. et al., 2013, A&A, 554, A142

Loup C., Forveille T., Omont A., Paul J. F., 1993, A&AS, 99, 291

Lovas F. J., 1992, Journal of Physical and Chemical Reference Data, 21, 181

Lucas R., Cernicharo J., 1989, A&A, 218, L20

Lucas R., Guilloteau S., 1992, A&A, 259, L23

Lucas R., Omont A., Guilloteau S., 1988, A&A, 194, 230

Lucas R., Omont A., Guilloteau S., Nguyen-Q-Rieu, 1986, A&A, 154, L12

Lugaro M., van Raai M., 2008, Journal of Physics G Nuclear Physics, 35, 014007

Lykou F., 2013, Dusty Discs Around Evolved Stars. University of Manchester

Maercker M. et al., 2012, Nature, 490, 232

Mamon G. A., Glassgold A. E., Huggins P. J., 1988, ApJ, 328, 797

Markwardt C. B., 2009, in Astronomical Society of the Pacific Conference Series, Vol. 411, Astronomical Data Analysis Software and Systems XVIII, Bohlender D. A., Durand D., Dowler P., eds., p. 251

Markwick-Kemper A. J., Remijan A. J., Fomalont E., 2006, in Bulletin of the American Astronomical Society, Vol. 38, American Astronomical Society Meeting Abstracts #208, p. 130

Matsuura M. et al., 2005, A&A, 434, 691

McDonald I., Sloan G. C., Zijlstra A. A., Matsunaga N., Matsuura M., Kraemer K. E., Bernard-Salas J., Markwick A. J., 2010, ApJL, 717, L92

Menzies J. W., Feast M. W., Whitelock P. A., 2006, MNRAS, 369, 783

Milam S. N., Woolf N. J., Ziurys L. M., 2009, ApJ, 690, 837

Min M., Dullemond C. P., Dominik C., de Koter A., Hovenier J. W., 2009, A&A, 497, 155

Moorwood A., Cuby J.-G., Biereichel P., et al., 1998, The Messenger, 94, 7

Morris M., 1975, ApJ, 197, 603

Morton D. C., 1975, ApJ, 197, 85

Müller H. S., Schlöder F., Stutzki J., Winnewisser G., 2005, Journal of Molecular Structure, 742, 215

Nguyen-Q-Rieu, Epchtein N., Truong-Bach, Cohen M., 1987, A&A, 180, 117

Nguyen-Quang-Rieu, Deguchi S., Izumiura H., Kaifu N., Ohishi M., Suzuki H., Ukita N., 1988, ApJ, 330, 374

Nyman L.-Å., Olofsson H., 1995, Ap&SS, 224, 527

Nyman L.-A., Olofsson H., Johansson L. E. B., Booth R. S., Carlstrom U., Wolstencroft R., 1993, A&A, 269, 377

Nyman L.-A., Thaddeus P., Bronfman L., Cohen R. S., 1987, ApJ, 314, 374

Olofsson H., 1997, Astrophysics and Space Science, 251, 31

Olofsson H., Maercker M., Eriksson K., Gustafsson B., Schöier F., 2010, A&A, 515, A27

Patzer A. B. C., 2004, in Astronomical Society of the Pacific Conference Series,

Vol. 309, Astrophysics of Dust, Witt A. N., Clayton G. C., Draine B. T., eds., p. 301

Peng T.-C. et al., 2013, A&A, 559, L8

Pérez-Sánchez A. F., Vlemmings W. H. T., 2013, A&A, 551, A15

Pickett H. M., Poynter R. L., Cohen E. A., Delitsky M. L., Pearson J. C., Müller H. S. P., 1998, J. Quant. Spec. Radiat. Transf., 60, 883

Pottasch S. R., Beintema D. A., Feibelman W. A., 2000, A&A, 363, 767

Pottasch S. R., Bernard-Salas J., 2006, A&A, 457, 189

Pottasch S. R., Bernard-Salas J., 2010, A&A, 517, A95

Prialnik D., 2009, An Introduction to the Theory of Stellar Structure and Evolution. Cambridge University Press

Price S. D., Smith B. J., Kuchar T. A., Mizuno D. R., Kraemer K. E., 2010, ApJS, 190, 203

Prochaska J. X., Naumov S. O., Carney B. W., McWilliam A., Wolfe A. M., 2000, AJ, 120, 2513

Quievy D., Charbonneau P., Michaud G., Richer J., 2009, A&A, 500, 1163

Ramstedt S., Olofsson H., 2014, A&A, 566, A145

Reid M. J., Menten K. M., 2007, ApJ, 671, 2068

Remijan A. J., Markwick-Kemper A., ALMA Working Group on Spectral Line Frequencies, 2007, in Bulletin of the American Astronomical Society, Vol. 39, American Astronomical Society Meeting Abstracts, p. 132.11

Rich R. M., 1998, in Astronomical Society of the Pacific Conference Series, Vol. 147, Abundance Profiles: Diagnostic Tools for Galaxy History, Friedli D., Edmunds M., Robert C., Drissen L., eds., p. 36

Richards A. M. S., Etoka S., Gray M. D., Lekht E. E., Mendoza-Torres J. E., Murakawa K., Rudnitskij G., Yates J. A., 2012, A&A, 546, A16

Risacher C., van der Tak F., 2009, Allegro Memo No. 2: AGB stars as calibrators for HIFI and ALMA. Technical memo, SRON Netherlands Institute for Space Research

Rosseland S., 1924, MNRAS, 84, 720

Rybicki G., Lightman A., 2008, Radiative Processes in Astrophysics, Physics textbook. Wiley

Ryde N., Schöier F. L., Olofsson H., 1999, A&A, 345, 841

Sabin L., Zijlstra A. A., Greaves J. S., 2007, MNRAS, 376, 378

Sahai R., Wootten A., Schwarz H. E., Clegg R. E. S., 1991, A&A, 251, 560

Saito Y.-J., Takada-Hidai M., Honda S., Takeda Y., 2009, PASJ, 61, 549

Savage B. D., Sembach K. R., 1996, ARA&A, 34, 279

Schilke P., Menten K. M., 2003, ApJ, 583, 446

Schoenberg K., Hempe K., 1986, A&A, 163, 151

Schöier F. L., Olofsson H., 2001, A&A, 368, 969

Schöier F. L., Olofsson H., Lundgren A. A., 2006, A&A, 454, 247

Schöier F. L., Ramstedt S., Olofsson H., Lindqvist M., Bieging J. H., Marvel K. B., 2013, A&A, 550, A78

Schöier F. L., Ryde N., Olofsson H., 2002, A&A, 391, 577

Shenavrin V. I., Taranova O. G., Nadzhip A. E., 2011, Astronomy Reports, 55, 31

Shields G. A., 1975, ApJ, 195, 475

Shinnaga H. et al., 2009, in Astronomical Society of the Pacific Conference Series, Vol. 417, Submillimeter Astrophysics and Technology: a Symposium Honoring Thomas G. Phillips, Lis D. C., Vaillancourt J. E., Goldsmith P. F., Bell T. A., Scoville N. Z., Zmuidzinas J., eds., p. 301

Sivanandam S., Deepa S., 2007, Introduction to Genetic Algorithms. Springer

Skatrud D. D., de Lucia F. C., Blake G. A., Sastry K. V. L. N., 1983, Journal of Molecular Spectroscopy, 99, 35

Sloan G. C., Kraemer K. E., Price S. D., Shipman R. F., 2003, ApJS, 147, 379

Smith B. J., Price S. D., Moffett A. J., 2006, AJ, 131, 612

Smith C. L., Zijlstra A. A., Dinerstein H. L., 2014, MNRAS, 441, 3161

Smith C. L., Zijlstra A. A., Fuller G. A., 2014, MNRAS, 440, 172

Sneden C., Gratton R. G., Crocker D. A., 1991, A&A, 246, 354

Sobolev V. V., 1960, Soviet Ast., 4, 1

Soker N., 2006, PASP, 118, 260

Stanghellini L., Haywood M., 2010, ApJ, 714, 1096

Sterling N. C., Dinerstein H. L., Bowers C. W., Redfield S., 2005, ApJ, 625, 368

Storey P. J., Hummer D. G., 1995, MNRAS, 272, 41

Teyssier D. et al., 2014, in Why Galaxies Care about AGB Stars III: A Closer Look in Space and Time, Astronomical Society of the Pacific Conference Series, to appear

Tielens A., 2005, The physics and chemistry of the interstellar medium. Cambridge University Press

Umeda H., Nomoto K., 2002, ApJ, 565, 385

van Winckel H., 2003, ARA&A, 41, 391

Ventura P. et al., 2012, MNRAS, 424, 2345

Walter F. M., 2000, A Primer on Quantum Numbers and Spectroscopic Notation, www.astro.sunysb.edu/fwalter/AST341/qn.html

Wang W., Liu X.-W., 2007, MNRAS, 381, 669

Wehrse R., Baschek B., von Waldenfels W., 2000, A&A, 359, 780

Welty D. E., Hobbs L. M., Lauroesch J. T., Morton D. C., Spitzer L., York D. G., 1999, ApJS, 124, 465

Wesson R., Stock D. J., Scicluna P., 2012, MNRAS, 422, 3516

Whitelock P. A., Feast M. W., Marang F., Groenewegen M. A. T., 2006, VizieR Online Data Catalog, 736, 90751

Woo J., Demarque P., 2001, AJ, 122, 1602

Woods P. M., Schöier F. L., Nyman L.-Å., Olofsson H., 2003, A&A, 402, 617

Woosley S. E., Weaver T. A., 1995, ApJS, 101, 181

Xiong G. Z., Chen P. S., Gao H., 1994, A&AS, 108, 661

Yang X., Chen P., He J., 2004, A&A, 414, 1049

Zahn J., 1992, A&A, 265, 115

Zhang H.-Y., Sun J., Ping J.-S., 2000, caa, 24, 309

Zhang Y., Liu X.-W., Luo S.-G., Péquignot D., Barlow M. J., 2005, A&A, 442, 249

Zijlstra A. A., 2006, in IAU Symposium, Vol. 234, Planetary Nebulae in our Galaxy and Beyond, Barlow M. J., Méndez R. H., eds., pp. 55–62

Zijlstra A. A., 2007, Baltic Astronomy, 16, 79

Zinner E., Nittler L. R., Gallino R., Karakas A. I., Lugaro M., Straniero O.,

Lattanzio J. C., 2006, The Astrophysical Journal, 650, 350

Zinner E. K., 2003, Treatise on Geochemistry, 1, 17

Ziurys L. M., Turner B. E., 1986, ApJL, 300, L19

Zuckerman B., 1987, in Spectroscopy of Astrophysical Plasmas, Dalgarno A., Layzer D., eds., pp. 185–209

...and there was much rejoicing.

– Monty Python